

¹ Observation of the Higgs boson in the WW^*
² channel and search for Higgs boson pair
³ production in the $b\bar{b}b\bar{b}$ channel with the
⁴ ATLAS detector

⁵ A DISSERTATION PRESENTED
⁶ BY
⁷ TOMO LAZOVICH
⁸ TO
⁹ THE DEPARTMENT OF PHYSICS

¹⁰ IN PARTIAL FULFILLMENT OF THE REQUIREMENTS
¹¹ FOR THE DEGREE OF
¹² DOCTOR OF PHILOSOPHY
¹³ IN THE SUBJECT OF
¹⁴ PHYSICS

¹⁵ HARVARD UNIVERSITY
¹⁶ CAMBRIDGE, MASSACHUSETTS
¹⁷ MAY 2016

¹⁸ ©2016 – TOMO LAZOVICH

¹⁹ ALL RIGHTS RESERVED.

²⁰ **Observation of the Higgs boson in the WW^* channel and search
²¹ for Higgs boson pair production in the $b\bar{b}b\bar{b}$ channel with the
²² ATLAS detector**

²³ ABSTRACT

²⁴ This dissertation presents the observation and measurement of the Higgs boson in the $H \rightarrow WW^* \rightarrow$
²⁵ $\ell\nu\ell\nu$ channel at $\sqrt{s} = 7$ TeV and $\sqrt{s} = 8$ TeV and a search for Higgs pair production in the $HH \rightarrow$
²⁶ $b\bar{b}b\bar{b}$ channel at $\sqrt{s} = 13$ TeV with the ATLAS detector in pp collisions at the Large Hadron Collider.

²⁷ First, the discovery of a particle consistent with the Higgs boson in 4.8 fb^{-1} at $\sqrt{s} = 7$ TeV and
²⁸ 5.8 fb^{-1} at $\sqrt{s} = 8$ TeV is discussed. Then, the measurement of the Higgs boson signal strength
²⁹ and cross section in both the gluon fusion and vector boson fusion (VBF) production modes using
³⁰ 20.3 fb^{-1} of $\sqrt{s} = 8$ TeV data combined with 4.8 fb^{-1} of 7 TeV data is shown. The combined signal
³¹ strength is measured to be $\mu = 1.09^{+0.23}_{-0.21}$. The total observed significance of the $H \rightarrow WW^*$ process
³² is observed to be 6.1σ (with 5.8σ expected). Advanced methods for background reduction and estima-
³³ tion, particularly in same-flavor lepton final states, are shown. The VBF signal strength is measured to
³⁴ be $\mu_{\text{VBF}} = 1.27^{+0.53}_{-0.45}$ with an observed significance of 3.2σ (with 2.7σ expected). In the VBF chan-
³⁵ nel, a selection requirement based method, the precursor to the final multivariate technique used for the
³⁶ result, is detailed.

³⁷ Finally, a search for Higgs pair production in the $b\bar{b}b\bar{b}$ final state with 3.2 fb^{-1} at $\sqrt{s} = 13$ TeV is
³⁸ presented. A particular focus is placed on a tailored signal region for resonant production of Higgs pairs
³⁹ at high masses. No significant excesses are observed, and upper limits on cross sections are placed for
⁴⁰ spin-2 Randall Sundrum gravitons (RSG) and narrow spin-0 resonances. The cross section of $\sigma(pp \rightarrow$
⁴¹ $G_{\text{KK}}^* \rightarrow hh \rightarrow b\bar{b}b\bar{b})$ with $k/\bar{M}_{\text{Pl}} = 1$ is constrained to be less than 70 fb for masses in the range
⁴² $600 < m_{G_{\text{KK}}^*} < 3000$ GeV. The cross section upper limits for $\sigma(pp \rightarrow H \rightarrow hh \rightarrow b\bar{b}b\bar{b})$ ranges
⁴³ from 30 to 300 fb in the mass range of $500 < m_H < 3000$ GeV.

Contents

44

45	o INTRODUCTION	I
46	I Theoretical and Experimental Background	5
47	I THE PHYSICS OF THE HIGGS BOSON	6
48	1.1 The Standard Model of Particle Physics	6
49	1.2 Electroweak Symmetry Breaking and the Higgs	8
50	1.3 Higgs Boson Production and Decay	10
51	1.4 Higgs Pair Production in the Standard Model	15
52	1.5 Higgs Pair Production in Theories Beyond the Standard Model	16
53	1.6 Conclusion	20
54	2 THE ATLAS DETECTOR AND THE LARGE HADRON COLLIDER	22
55	2.1 The Large Hadron Collider	23
56	2.2 The ATLAS Detector	25
57	2.3 The ATLAS Muon New Small Wheel Upgrade	36
58	2.4 Object Reconstruction in ATLAS	40
59	II Observation and measurement of Higgs boson decays to WW^* in LHC	
60	Run 1 at $\sqrt{s} = 7$ and 8 TeV	49
61	3 $H \rightarrow WW^* \rightarrow \ell\nu\ell\nu$ ANALYSIS STRATEGY	50
62	3.1 Introduction	50
63	3.2 The $H \rightarrow WW^* \rightarrow \ell\nu\ell\nu$ signal in ATLAS	51
64	3.3 Background processes	52
65	3.4 Shared signal region selection requirements	55
66	3.5 Background reduction in same-flavor final states	59
67	3.6 Parameters of interest and statistical treatment	63
68	4 THE DISCOVERY OF THE HIGGS BOSON AND THE ROLE OF THE $H \rightarrow WW^* \rightarrow \ell\nu\ell\nu$ CHANNEL	69
69	4.1 Introduction	69

71	4.2	Data and simulation samples	70
72	4.3	$H \rightarrow WW \rightarrow e\nu\mu\nu$ search	70
73	4.4	$H \rightarrow \gamma\gamma$ search	75
74	4.5	$H \rightarrow ZZ \rightarrow 4\ell$ search	76
75	4.6	Combined results	77
76	4.7	Conclusion	79
77	5	OBSERVATION OF VECTOR BOSON FUSION PRODUCTION OF $H \rightarrow WW^* \rightarrow \ell\nu\ell\nu$	82
78	5.1	Introduction	82
79	5.2	Data and simulation samples	83
80	5.3	Object selection	87
81	5.4	Analysis selection	90
82	5.5	Background estimation	99
83	5.6	Systematic uncertainties	109
84	5.7	Results	112
85	6	COMBINED RUN I $H \rightarrow WW^* \rightarrow \ell\nu\ell\nu$ RESULTS	117
86	6.1	Introduction	117
87	6.2	Results of gluon fusion $H \rightarrow WW^* \rightarrow \ell\nu\ell\nu$ search	118
88	6.3	Signal strength measurements in ggF and VBF production	120
89	6.4	Measurement of Higgs couplings to vector bosons and fermions	123
90	6.5	Higgs production cross section measurement	124
91	6.6	Conclusion	125
92	III	Search for Higgs pair production in the $HH \rightarrow b\bar{b}b\bar{b}$ channel in LHC	
93		Run 2 at $\sqrt{s} = 13$ TeV	127
94	7	SEARCH FOR HIGGS PAIR PRODUCTION IN BOOSTED $b\bar{b}b\bar{b}$ FINAL STATES	128
95	7.1	Introduction	128
96	7.2	Motivation	129
97	7.3	Data and simulation samples	131
98	7.4	Event reconstruction and object selection	133
99	7.5	Event selection	136
100	7.6	Data-driven background estimation	141
101	7.7	Systematic uncertainties	147
102	7.8	Results	150

103	8 COMBINED LIMITS FROM BOOSTED AND RESOLVED SEARCHES	152
104	8.1 Introduction	152
105	8.2 Resolved results	153
106	8.3 Search technique and results	153
107	8.4 Limit setting	154
108	IV Looking ahead	158
109	9 CONCLUSION	159
110	APPENDIX A <i>b</i>-TAGGING PERFORMANCE AT HIGH p_T	163
111	A.1 Changes in MV2 score at high p_T	163
112	A.2 Effect of multiple <i>b</i> -quarks inside one jet	165
113	A.3 Changes in track quality at high p_T	167
114	REFERENCES	170

Listing of figures

116	I.1	The particles of the Standard Model and their properties [6].	7
117	I.2	The four most common Higgs boson production modes at the LHC: (a) gluon-gluon fusion, (b) vector boson fusion, (c) $W/Z + H$ production, (d) $t\bar{t}H$ production	11
118	I.3	Higgs production cross sections as a function of center of mass energy (\sqrt{s}) at a pp collider [18].	12
119	I.4	Higgs boson branching ratios as a function of m_H [18].	14
120	I.5	The two leading diagrams for Standard Model di-Higgs production at the LHC: (a) box diagram, (b) Higgs self coupling	15
121	I.6	Diagrams with new vertices for non-resonant Higgs pair production arising in composite Higgs models	17
122	I.7	Generic Feynman diagram for resonant Higgs pair production in BSM theories	17
123	I.8	Branching ratios for a spin-2 Randall-Sundrum graviton as a function of mass computed in MadGraph with the CP ₃ -Origins implementation [24, 30]	18
124	I.9	$\sigma \times \text{BR}(HH)$ for RSG as a function of mass computed in MadGraph with the CP ₃ -Origins implementation [24, 30]	19
125	I.10	RSG width as a function of mass computed in MadGraph with the CP ₃ -Origins implementation [24, 30]	20
126	I.11	Branching ratios for heavy Higgs H in Type I (left) and Type II (right) 2HDM models with $\tan \beta = 1.5$ and $\cos(\beta - \alpha) = 0.1(0.01)$ for Type I (Type II). [28]	21
135	2.1	A schematic view of the LHC ring [36]	23
136	2.2	A full diagram of the ATLAS detector [32]	26
137	2.3	The ATLAS coordinate system	27
138	2.4	Layout of the ATLAS Inner Detector system [40]	28
139	2.5	Layout of the ATLAS calorimeter system [32]	30
140	2.6	Layout of the ATLAS muon system [32]	32
141	2.7	Predicted field integral as a function of $ \eta $ for the ATLAS magnet system [32]	34
142	2.8	ATLAS trigger rates for Level-1 triggers as a function of instantaneous luminosity in 2012 and 2015 operation. These are single object triggers for electromagnetic clusters (EM), muons (MU), jets (J), missing energy (XE), and τ leptons (TAU). The threshold of the trigger is given in the name in GeV. [42]	35

146	2.9	Instantaneous luminosity as a function of time for data recorded by ATLAS at different center of mass energies [43, 44]	36
148	2.10	MDT tube hit (solid) and segment (dashed) efficiency as a function of hit rate per tube [45]	37
149	2.11	Trigger rate as a function of p_T threshold with and without the NSW upgrade [45]	38
150	2.12	Illustrations of the geometry (left) and operating principle (right) of the micromegas detector [45]	39
152	2.13	Geometry of the sTGC detector [45]	39
153	2.14	Illustration of particle interactions in ATLAS [48]	41
154	2.15	Electron performance: (a) reconstruction efficiency as a function of electron E_T [50] (b) energy resolution in simulation as a function of $ \eta $ for different energy electrons [51]	42
155	2.16	Muon performance: (a) reconstruction efficiency as a function of muon p_T (b) dimuon mass resolution as a function of average p_T [52]	43
158	2.17	Jet energy response after calibration as a function of true p_T in simulation [56]	45
159	2.18	Summary of the inputs to the MV2 b -tagging algorithm	46
160	2.19	Light jet rejection (1/efficiency) vs. b -jet efficiency for MV1 and its input algorithms (a) [57] and MV2 (b) [58] in simulated $t\bar{t}$ events. The numbers in the algorithm names in (b) refer to the fraction of charm events used in the MV2 training.	46
163	2.20	Resolution of E_T^{miss} components as a function of $\sum E_T$ before pileup suppression with different pileup techniques [60]	48
165	3.1	Branching ratios for a WW system. q refers to quarks. ℓ can be either an electron or muon, and the leptonic branching ratios of the τ are included. For example, the $\ell\nu qq$ final state includes one W decaying to $e\nu$, $\mu\nu$, or $\tau\nu$. τ_h refer to hadronic decays of the τ	52
168	3.2	Feynman diagram for Standard Model WW production	53
169	3.3	Feynman diagrams for top pair production (left) and Wt production (right)	53
170	3.4	An example Feynman diagram of W +jets production	54
171	3.5	An example Feynman diagram of Z +jets production	55
172	3.6	An illustration of the unique analysis signal regions [61]. The most sensitive regions for both gluon fusion and vector boson fusion production are underlined.	56
174	3.7	A graphical illustration of the $E_{T,\text{rel}}^{\text{miss}}$ calculation	57
175	3.8	Predicted backgrounds (compared with data) as a function of n_j (a and b) and n_b (c) after pre-selection requirements	58
177	3.9	An event display of a Z/γ^* + jets event illustrating the effect of pileup interactions	60
178	3.10	The RMS of different missing transverse momentum definitions as a function of the average number of interactions per bunch crossing	60
180	3.11	The difference between the true and reconstructed values of the missing transverse momentum (a) and m_T (b) in a gluon fusion signal sample	62

182	3.12	Comparison of f_{recoil} distributions for $Z/\gamma^* + \text{jets}$, $H \rightarrow WW^*$, and other backgrounds with real neutrinos.	63
183			
184	3.13	Signal significance as a function of required value for f_{recoil} and $p_{\text{T},\text{rel}}^{\text{miss}(\text{trk})}$ in the ggF $H \rightarrow WW^*$ with $n_j = 0$	64
185			
186	4.1	Jet multiplicity distribution in data and MC after applying lepton, jet, and $E_{\text{T},\text{rel}}^{\text{miss}}$ selections. The WW and top backgrounds have been normalized using control samples, and the hashed band indicates the total uncertainty on the prediction. [1]	71
187			
188	4.2	Comparison of m_{T} between data and simulation in the $n_j = 0$ WW (a) and $n_j = 1$ top (b) control samples [1]	73
189			
190	4.3	m_{T} distribution in the $H \rightarrow WW \rightarrow e\nu\mu\nu$ $n_j \leq 1$ channels for 8 TeV data [1].	75
191			
192	4.4	Diphoton mass spectrum in 7 and 8 TeV data. Panel a) shows the unweighted data distribution superimposed on the background fit, while panel c) shows the data where each event category is weighted by its signal to background ratio. Panels b) and d) show the respective distributions with background subtracted [1].	76
193			
194	4.5	Four lepton invariant mass spectrum ($m_{4\ell}$) in 7 and 8 TeV data compared to background estimate. A 125 GeV SM Higgs signal is shown in blue [1].	77
195			
196	4.6	Local p_0 distribution as a function of hypothesized Higgs mass for the $H \rightarrow ZZ^* \rightarrow 4\ell$ (a), $H \rightarrow \gamma\gamma$ (b), and $H \rightarrow WW^* \rightarrow \ell\nu\ell\nu$ (c) channels. Dashed curves show expected results, while solid curves show observed. Red curves are from 7 TeV data, blue curves from 8 TeV, and black curved combined [1].	79
197			
198	4.7	Combined 95% CL limits (a), local p_0 values (b), and signal strength measurement (c) as a function of Higgs mass [1].	80
199			
200	4.8	Comparison of measured signal strength μ for a 126 GeV Higgs in the 7 and 8 TeV datasets [1].	81
201			
202	4.9	Two dimensional likelihood as a function of signal strength μ and Higgs mass m_H [1].	81
203			
204	5.1	A comparison of the subleading lepton p_{T} spectrum between VBF $H \rightarrow WW^*$ production and $t\bar{t}$ background	84
205			
206	5.2	Leading jet η in VBF $H \rightarrow WW^*$ (red) and $t\bar{t}$ (black)	92
207			
208	5.3	Distributions of (a) m_{jj} , (b) Δy_{jj} , (c) $C_{\ell 1}$, and (d) $\Sigma m_{\ell j}$, for the VBF analysis. The top panels compare simulation and data, while the bottom panels show normalized distributions for all background processes and signal [61].	94
209			
210	5.4	A cartoon of the WW final state. Momenta are represented with thin arrows, spins with thick arrows. [61]	95
211			
212	5.5	Event display of a VBF candidate event [61].	97
213			
214	5.6	Distributions of $m_{\ell\ell}$ (top left), $\Delta\phi_{\ell\ell}$ (top right), and m_{T} (bottom), Higgs topology variables used in the selection requirements of the cut-based signal region and as inputs to the BDT result. These are plotted after all of the BDT pre-training selection cuts [61].	98
215			
216			
217			

218	5.7 Distributions of m_{jj} (top left), Δy_{jj} (top right), $\sum C_\ell$ (bottom), VBF topology variables used in the selection requirements of the cut-based signal region and as inputs to the BDT result. These are plotted after all of the BDT pre-training selection cuts [61].	99
219		
220		
221	5.8 Distributions of m_{jj} (a) and O_{BDT} (b) in the VBF $n_b = 1$ top CR [61].	102
222		
223	5.9 Comparison of m_{jj} shape in a same flavor $Z \rightarrow \ell\ell$ control region and the VBF cut-based signal region.	103
224		
225	5.10 General illustration of the ABCD region definitions for $Z/\gamma^* \rightarrow \ell\ell$ background estimation.	104
226		
227	5.11 Distribution of $m_{\text{T}2}$ in the WW validation region of the VBF analysis [61].	106
228		
229	5.12 Extrapolation factors for the $W + \text{jets}$ estimate derived for muons (a) and electrons (b) as a function of lepton p_T [61].	108
230		
231	5.13 Background composition in final VBF signal region [61].	109
232		
233	5.14 Variations in the top background extrapolation factor in the cut-based analysis due to PDF uncertainties, binned in m_{T}	III
234		
235	5.15 Variations in the top background extrapolation factor in the cut-based analysis due to QCD scale uncertainties, binned in m_{T}	III
236		
237	5.16 Post-fit distributions in the cut-based VBF analysis. Panel (a) shows the one-dimensional m_{T} distribution, while (b) shows the data candidates split into the bins of m_{T} and m_{jj} used in the final fit [61].	II4
238		
239	5.17 Postfit distributions in the BDT VBF analysis [61].	II5
240		
241	5.18 Overlap between cut-based and BDT VBF signal region candidates in the m_{jj} - m_{T} plane.	II6
242		
243		
244		
245	6.1 Post-fit m_{T} distribution in the $n_j \leq 1$ regions [61].	II9
246		
247	6.2 Best fit signal strength $\hat{\mu}$ as a function of hypothesized m_H [61].	121
248		
249	6.3 Local p_0 as a function of m_H [61].	121
250		
251	6.4 Likelihood as a function of $\mu_{\text{VBF}}/\mu_{\text{ggF}}$ [61].	122
252		
253	6.5 Likelihood scan as a function of μ_{VBF} and μ_{ggF} [61].	123
254		
255	6.6 Likelihood scan as a function of κ_F and κ_V [61].	124
256		
257	6.7 Comparison of signal strength measurements in different Higgs decay channels on ATLAS [90].	126
258		
259		
260		
261		
262		
263		
264		
265	7.1 Parton luminosity ratios as a function of resonance mass M_X for 13/8 TeV and 7/8 TeV [91].	129
266		
267	7.2 Summary of HH branching ratios [92].	130
268		
269	7.3 Minimum ΔR between B decay vertices for different RSG masses in a $G_{\text{KK}}^* \rightarrow HH \rightarrow 4b$ sample with $c = 1$	131
270		
271		
272		
273		
274		
275		
276		
277		
278		
279		
280		
281		
282		
283		
284		
285		
286		
287		
288		
289		
290		
291		
292		
293		
294		
295		
296		
297		
298		
299		
300		
301		
302		
303		
304		
305		
306		
307		
308		
309		
310		
311		
312		
313		
314		
315		
316		
317		
318		
319		
320		
321		
322		
323		
324		
325		
326		
327		
328		
329		
330		
331		
332		
333		
334		
335		
336		
337		
338		
339		
340		
341		
342		
343		
344		
345		
346		
347		
348		
349		
350		
351		
352		
353		
354		
355		
356		
357		
358		
359		
360		
361		
362		
363		
364		
365		
366		
367		
368		
369		
370		
371		
372		
373		
374		
375		
376		
377		
378		
379		
380		
381		
382		
383		
384		
385		
386		
387		
388		
389		
390		
391		
392		
393		
394		
395		
396		
397		
398		
399		
400		
401		
402		
403		
404		
405		
406		
407		
408		
409		
410		
411		
412		
413		
414		
415		
416		
417		
418		
419		
420		
421		
422		
423		
424		
425		
426		
427		
428		
429		
430		
431		
432		
433		
434		
435		
436		
437		
438		
439		
440		
441		
442		
443		
444		
445		
446		
447		
448		
449		
450		
451		
452		
453		
454		
455		
456		
457		
458		
459		
460		
461		
462		
463		
464		
465		
466		
467		
468		
469		
470		
471		
472		
473		
474		
475		
476		
477		
478		
479		
480		
481		
482		
483		
484		
485		
486		
487		
488		
489		
490		
491		
492		
493		
494		
495		
496		
497		
498		
499		
500		
501		
502		
503		
504		
505		
506		
507		
508		
509		
510		
511		
512		
513		
514		
515		
516		
517		
518		
519		
520		
521		
522		
523		
524		
525		
526		
527		
528		
529		
530		
531		
532		
533		
534		
535		
536		
537		
538		
539		
540		
541		
542		
543		
544		
545		
546		
547		
548		
549		
550		
551		
552		
553		
554		
555		
556		
557		
558		
559		
560		
561		
562		
563		
564		
565		
566		
567		
568		
569		
570		
571		
572		
573		
574		
575		
576		
577		
578		
579		
580		
581		
582		
583		
584		
585		
586		
587		
588		
589		
590		
591		
592		
593		
594		
595		
596		
597		
598		
599		
600		
601		
602		
603		
604		
605		
606		
607		
608		
609		
610		
611		
612		
613		
614		
615		
616		
617		
618		
619		
620		
621		
622		
623		
624		
625		
626		
627		
628		
629		
630		
631		
632		
633		
634		
635		
636		
637		
638		
639		
640		
641		
642		
643		
644		
645		
646		
647		
648		
649		
650		
651		
652		
653		
654		
655		
656		
657		
658		
659		
660		
661		
662		
663		
664		
665		
666		
667		
668		
669		
670		
671		
672		
673		
674		
675		
676		
677		
678		
679		
680		
681		
682		
683		
684		
685		
686		
687		
688		
689		
690		
691		
692		
693		
694		
695		
696		
697		
698		
699		
700		
701		
702		
703		
704		
705		
706		
707		
708		

254	7.5	Comparison of untrimmed and trimmed jet masses for large radius jets in a RSG sample with $m_{G_{\text{KK}}^*} = 1 \text{ TeV}$. JES (JMS) refers to the standard jet energy (mass) scale calibration for ATLAS [56].	134
255			
256	7.6	Efficiency of finding two b -jets from each Higgs in an RSG event using calorimeter jets with $R = 0.3$ or different track jet radii [105]	135
257			
258	7.7	Illustration of the boosted selection requirements on Higgs candidates. Each large-radius calorimeter jet (Higgs candidate) must contain two track jets	137
259			
260	7.8	Estimated significance as a function of signal mass for RSG $c = 1$ models in the $3b$ (a) and $4b$ (b) regions for different b -tagging efficiency working points	138
261			
262	7.9	Acceptance \times efficiency as a function of mass for (a) RSG and (b) narrow heavy scalar signal models [108].	139
263			
264	7.10	Efficiency of requiring 3 or 4 b -tagged track jets vs. RSG mass. The efficiency quoted is relative to the previous selection requirements (rather than an absolute efficiency).	140
265			
266	7.11	MV2c20 b -tagging efficiency for each of the four track jets in the boosted $4b$ selection as a function of RSG mass for $c = 1$ models.	141
267			
268	7.12	M_J^{sublead} vs. M_J^{lead} in a $2 b$ -tag data sample. The signal region is defined by the inner black contour ($X_{hh} < 1.6$) and the sideband region is defined by the outer contour ($R_{hh} >$ 35.8 GeV). The region between the black contours is the control region. The mass region which is enriched in $t\bar{t}$ background is also shown for illustration. [108]	142
269			
270	7.13	An illustration of the data-driven background estimation technique for the boosted analysis	144
271			
272	7.14	Leading large-R jet mass in the $3b$ (a) and $4b$ (b) sideband regions. The multijet and $t\bar{t}$ backgrounds are estimated using the data-driven methods described above. Because their normalizations are derived in the sideband region, the total background normalization is constrained by default to match the normalization of the data [108].	145
273			
274	7.15	Di-jet invariant mass (M_{2J}) in the $3b$ (a) and $4b$ (b) control regions. The multijet and $t\bar{t}$ backgrounds are estimated using the data-driven methods described above [108].	146
275			
276	7.16	Di-jet invariant mass (M_{2J}) in the $3b$ (a) and $4b$ (b) signal regions. The multijet and $t\bar{t}$ backgrounds are estimated using the data-driven methods described above. In the $3b$ re- gion, a graviton signal with $m_{G_{\text{KK}}^*} = 1.8 \text{ TeV}$ and $c = 1$ is overlaid, with the cross section multiplied by a factor of 50 so that the signal is visible. In the $4b$ region, signals with $m_{G_{\text{KK}}^*} = 1.0 \text{ TeV}$ and $m_{G_{\text{KK}}^*} = 1.5 \text{ TeV}$ are overlaid, both with $c = 1$ and the yields multiplied by factors of 2 and 5 respectively [108].	151
277			
278	8.1	Di-jet invariant mass (M_{2J}) in the resolved signal region. A graviton signal with $m_{G_{\text{KK}}^*} =$ 800 GeV and $c = 1$ is overlaid. [108].	154
279			
280	8.2	Expected and observed upper limit as a function of mass for G_{KK}^* in the RSG model with (a) $c = 1$ and (b) $c = 2$, as well as (c) H with fixed $\Gamma_H = 1 \text{ GeV}$, at the 95% confidence level in the CL_s method. [108]	157
281			

291	9.1	Combined ATLAS and CMS measurements in Run 1 for (a) Higgs signal strength in gluon		
292		fusion and VBF and (b) Higgs couplings normalized to their SM predictions	161	
293	9.2	Discovery significance for RSG models at the HL-LHC in three different budget scenar-		
294		ios [115]. Systematic uncertainties on the background prediction (σ_B) of 2.5% and 5.0%		
295		are both tested.	162	
296	A.1	p_T of the leading track jet in the leading calorimeter jet for different signal masses in RSG		
297		$c = 1$ models	164	
298	A.2	MV _{2c2o} score for the leading track jet (a) and subleading track jet (b) of the leading calorime-		
299		ter jet for different signal masses in RSG $c = 1$ models	164	
300	A.3	IP _{3D} log-likelihood ratio ($\log(p_b/p_u)$) of the leading track jet in the leading calorimeter		
301		jet for different signal masses in RSG $c = 1$ models	165	
302	A.4	Mass (a) and number of tracks (b) for the secondary vertices computed with the SV1 algo-		
303		rithm. When no secondary vertex is found, the quantities are assigned to default negative		
304		values.	166	
305	A.5	Mass (a) and number of tracks (b) for vertices computed with the JetFitter algorithm.		
306		When no vertices are found, the quantities are assigned to default negative values.	166	
307	A.6	MV _{2c2o} score (a) and SV1 mass (b) for leading track jets with two truth b quarks ($n_{tb,lead} =$		
308		2) compared to those with only one truth b ($n_{tb,lead} = 1$).	167	
309	A.7	Track fit χ^2/n_{DOF} (a) and number of pixel detector hits (b) for the leading track of the		
310		leading track jet in different mass RSG $c = 1$ samples	168	
311	A.8	MV _{2c2o} score (a) and SV1 mass (b) for leading track jets whose leading track jet has at least		
312		four pixel hits ($N_{pix} \geq 4$) compared to those which do not ($N_{pix} < 4$).	169	

Listing of tables

313

314	1.1	Production cross sections for a 125 GeV Higgs boson at $\sqrt{s} = 8$ TeV with scale and PDF uncertainties [18].	13
315	1.2	Branching ratios for a 125 GeV Higgs boson [18].	14
316	1.3	Possible channels for Higgs searches. Checkmarks denote the most sensitive production modes [5].	15
317	1.4	Production cross sections for pair production of a 125 GeV Higgs boson at $\sqrt{s} = 14$ TeV with total uncertainty [19]. The uncertainties include QCD scale and PDF variations as well as uncertainties on α_S	16
318			
319	2.1	Evolution of LHC machine conditions [38, 39]	25
320	2.2	Performance requirements for the ATLAS detector [32].	36
321	2.3	Signal efficiencies for WH production with $H \rightarrow b\bar{b}$ and $H \rightarrow WW^* \rightarrow \mu\nu qq$ under different trigger configurations [45].	40
322			
323	3.1	A summary of backgrounds to the $H \rightarrow WW^* \rightarrow \ell\nu\ell\nu$ signal	55
324			
325	4.1	Monte carlo generators used to model signal and background for the Higgs search [1].	70
326	4.2	Normalization factors (ratio of data and MC yields in a control sample) for the Standard Model WW and top backgrounds in the $H \rightarrow WW^* \rightarrow \ell\nu\ell\nu$ analysis [1]. Only statistical uncertainties are shown.	73
327			
328	4.3	Data and expected yields for signal and background in the final $H \rightarrow WW^* \rightarrow \ell\nu\ell\nu$ signal region. Uncertainties shown are both statistical and systematic. [1]	74
329			
330	4.4	Summary of the expected and observed significance and measured signal strengths in the combined 7 and 8 TeV datasets for the Higgs discovery analysis [1].	78
331			
332	5.1	Single lepton triggers used for electrons and muons. A logical “or” of the triggers listed for each lepton type is taken. Units are in GeV, and the i denotes an isolation requirement in the trigger.	84
333	5.2	Di-lepton triggers used for different flavor combinations. The two thresholds listed refer to leading and sub-leading leptons, respectively. The di-muon trigger only requires a single lepton at level-1.	84
334			
335			
336			
337			
338			
339			
340			

341	5.3	Trigger efficiency for signal events and relative gain of adding a dilepton trigger on top of the single lepton trigger selection. The first lepton is the leading, while the second is the sub-leading. Efficiencies shown here are for the ggF signal in the $n_j = 0$ category but are comparable for the VBF signal.	85
342	5.4	Monte Carlo samples used to model the signal and background processes [61].	86
343	5.5	p_T dependent isolation requirements for muons. Muons are required to have the amount of calorimeter or track based cone sums be less than this fraction of their p_T	88
344	5.6	p_T dependent requirements for electrons. Electrons are required to have the amount of calorimeter or track based cone sums be less than this fraction of their E_T	89
345	5.7	Summary of event selection for the $n_j \geq 2$ VBF analysis in the 8 TeV cut-based analy- sis [61].	96
346	5.8	Background composition after each requirement in the $n_j \geq 2$ VBF analysis in the 8 TeV cut-based analysis [61].	96
347	5.9	Top normalization factors computed at each stage of the cut-based selection. Uncertainties are statistical only.	101
348	5.10	Top normalization factors computed for each bin of O_{BDT} . Uncertainties are statistical only.	101
349	5.11	$Z/\gamma^* \rightarrow \tau\tau$ correction factors for the VBF cut-based analysis. Uncertainties are statistical only.	104
350	5.12	$Z/\gamma^* \rightarrow \ell\ell$ normalization factors for cut-based and BDT analyses. Uncertainties are statistical only.	105
351	5.13	Systematic uncertainties for various processes in the cut-based VBF analysis, given in units of % change in yield. Values are given for the low m_{jj} signal region.	110
352	5.14	Composition of the post-fit uncertainties (in %) on the total signal (N_{sig}), total back- ground (N_{bkg}), and individual background yields in the VBF analysis [61].	113
353	5.15	Event selection for the VBF BDT analysis. The event yields in (a) are shown after the pre- selection and the additional requirements applied before the BDT classification (see text). The event yields in (b) are given in bins in O_{BDT} after the classification [61].	113
361	6.1	All signal regions definitions input into final statistical fit [61].	118
362	6.2	Post-fit yields in the different ggF and VBF dedicated signal regions [61].	119
371	7.1	Summary of requirements on objects used in the $X \rightarrow HH \rightarrow b\bar{b}b\bar{b}$ search	136
372	7.2	Effect of boosted selection on data, RSG signal models, $t\bar{t}$, and $Z+\text{jets}$. The numbers from simulation are normalized with the MC generator cross section and do not take into account the data driven estimates described in section 7.6 [109].	141
374	7.3	Mass region definitions used for background estimation	143

376	7.4	Parameters derived for exponential fit to background M_{2J} shape in the $3b$ and $4b$ signal regions [109]	145
377	7.5	The number of events in data and predicted background events in the boosted 3-tag and 4-tag sideband and control regions. The uncertainties shown are statistical only. [108] . . .	146
378	7.6	Summary of systematic uncertainties in the total background and signal event yields (expressed in %) in the boosted 3-tag and 4-tag signal regions. Systematic uncertainties on the signal normalization are shown for models with $m_{G_{KK}^*} = 1.5$ TeV and both $c = 1$ and $c = 2$ as well as a narrow width heavy scalar.	148
379	7.7	Alternate fit functions used to model the M_{2J} distribution in the QCD multijet background. In the equations, $x = M_{2J}/\sqrt{s}$	149
380	7.8	Observed yields in the 3-tag and 4-tag signal regions for the boosted analysis compared to the predicted number of background events Errors correspond to the total uncertainties in the predicted event yields. The yields for a graviton with $m_{G_{KK}^*} = 1$ TeV and $c = 1$ are also shown. [108]	150
381	8.1	Observed yields in the resolve selection 4-tag signal region compared to the predicted number of background events Errors correspond to the total uncertainties in the predicted event yields. The yields for a graviton with $m_{G_{KK}^*} = 800$ GeV and $c = 1$ are also shown. [108]	153
382			
383			
384			
385			
386			
387			
388			
389			
390			
391			
392			
393			

Acknowledgments

396 I have been a member of the Harvard ATLAS group for many years now, first as an undergraduate and
397 then as a graduate student. As a result, I have had the privilege of interacting with many amazing people
398 there over the years and have accumulated a large list of folks to thank.

399 First and foremost, I must thank the two people who have effectively been my academic parents since I
400 started in the Harvard group: João Guimarães da Costa and Melissa Franklin. Melissa Franklin and João
401 Guimarães da Costa. They have both been so important to both my academic and personal development
402 that I can't even put one before the other. João has been an excellent PhD advisor, showing me how to
403 look at the big picture and helping me navigate the sometimes complicated politics of ATLAS. He got me
404 started on my first projects with ATLAS as a young college sophomore before there was even beam in the
405 LHC (go cosmic ray muons!). He has also been a constant source of advice and support, even when we
406 have been on different continents. Melissa gave me my start in HEP as a summer student on CDF and
407 has been an unbelievable mentor throughout my time at Harvard. I still remember our weekly chalkboard
408 particle physics lessons after that first summer. She also graciously took me on as a co-advisee after João
409 moved on to his new position at IHEP. I am incredibly lucky to have had both of them as advisors.

410 Another mentor who was essential to my development as a graduate student is Paolo Giromini. His un-
411 canny knowledge and intuition about detectors is unmatched and I am very grateful to have had the chance
412 to work with him on the micromegas for the ATLAS New Small Wheel upgrade project. I owe essentially
413 all my practical knowledge about detectors (and building things in general) to him. I also appreciated his
414 unique sense of humor which made sometimes difficult tasks much easier to get through.

415 I am grateful to John Huth and Masahiro Morii for their helpful advice as the other professors in the
416 Harvard ATLAS group as well. I especially thank John for helping me get started on the micromegas
417 trigger project and being a great professor to TF particle physics for. Additionally I thank Howard Georgi
418 for serving as my third committee member and offering me feedback throughout my graduate career.

419 I also owe enormous thanks to Hugh Skottowe, the postdoc that I worked most closely with in my early
420 years as a graduate student. He was always able to help me through complicated tasks in everything from
421 writing code to understanding difficult physics concepts. I particularly enjoyed walking down to his office
422 in Palfrey at random times and talking through whatever problem I was tackling on that day.

423 Alex Tuna, the second postdoc that I worked closely with at Harvard, deserves great thanks as well. He
424 helped me push through to the end of my graduate career and offered great advice along the way.

425 Being at Harvard, I have seen an incredible array of graduate students graduate before me: Ben Smith,
426 Verena Martinez Outschoorn, Srivas Prasad, Michael Kagan, Giovanni Zevi Della Porta, Laura Jeanty,
427 Kevin Mercurio, William Spearman, and Andy Yen. I want to thank them all for showing me what a good
428 physicist looks like and for patiently answering my questions and offering insightful advice about physics
429 and life.

430 Getting through graduate school would not have been possible without the support and friendship of
431 the other students in our group. Thanks to Emma Tolley for geeking out with me about cool comput-
432 ing stuff, going to taste delicious beers with me, and helping start the Palfrey tradition of Taco Tuesdays.
433 Thanks to Brian Clark for being a great friend and housing companion both in Kirkland House and in our
434 tiny summer apartment in Geneva (and thanks to his partner Allison Goff for the same reasons!). Thanks
435 to Siyuan Sun for giving me my first aikido lesson and always being there for great conversations, big and
436 small. Tony (Baojia) Tong deserves special recognition for working with me on the $4b$ analysis and putting
437 up with my sometimes strange requests (and giving me rides to the Val Thoiry Migros so I wouldn't have
438 to pay exorbitant Geneva grocery prices!). Stephen Chan is probably the only student in the group who
439 both understands my references to the Sopranos and makes some of his own. To the younger graduate
440 students - Karri Di Petrillo, Jennifer Roloff, Julia Gonski, and Ann Wang - I want to say thank you for
441 making the group a fun and lively place to be and giving all of us energy that the older graduate students
442 like myself can sometimes lack.

443 I'd like to thank Annie Wei and Gray Putnam, the two undergraduates I have worked with as a graduate
444 student. Their unbelievable intuition and quickness in picking up difficult particle physics concepts is
445 inspiring.

446 I would also like to thank all of the postdocs that I have interacted with in my time in the Harvard group:
447 Kevin Black, Alberto Belloni (who would always ask me “Do you have it?”...I can now say that I do!),
448 Shulamit Moed, Corrinne Mills, Geraldine Conti, David Lopez Mateos, Chris Rogan, Valerio Ippolito,
449 and Stefano Zambito.

450 There are many people on ATLAS who have helped me get to this point as well. In the *WW* group, I
451 have to thank Jonathan Long, Joana Machado Miguens, Ben Cerio, Philip Chang, Bonnie Chow, Richard
452 Polifka, Heberth Torres, Tae Min Hong, and Jennifer Hsu for being wonderful colleagues and making the
453 entire analysis run smoothly. In the *4b* group, I have to thank Qi Zeng, Tony Tong, Alex Tuna, Michael
454 Kagan, Max Bellomo, John Alison, and Patrick Bryant.

455 Kirkland House was my home for the last three years of graduate school and was an wonderful envi-
456 ronment and support system. I want to thank my fellow tutors, especially Brian Clark and Allison Goff
457 (again), Zach Abel, Kelly Bodwin, Alex Lupsasca, John and Pam Park, Luke and Erin Walczewski, and
458 Philip Gant for their friendship and support. I also want to thank Kate Drizos Cavell, Bob Butler, and the
459 Faculty Deans Tom and Verena Conley.

460 There are still a few friends that haven’t been covered yet and deserve great thanks. Jake Connors and
461 Meredith MacGregor have been absolutely wonderful friends and I thank them in particular for the many
462 home-cooked meals and great conversations we’ve had in their apartment. Nihar Shah has been my friend
463 and confidant since we were both wee freshmen in Harvard Yard. Gareth Kafka, though he sits on the
464 “neutrino” side of Palfrey House, has made days there more fun and has also been an enthusiastic partici-
465 pant in the Palfrey Taco Tuesdays.

466 Being at Harvard necessarily means having to navigate through bureaucracy at some point or another.
467 I thank Lisa Cacciabuado, Carol Davis, and Jacob Barandes for always having open doors and being the
468 most kind, helpful people in the Physics department.

469 I thank Venky Narayananuriti for putting on a great SPU course that I was proud to be a part of and
470 TF for. I’d also like to thank Jim Waldo for offering me much advice about working in Computer Science
471 and giving me a fun data project to be a part of in my free time.

472 I grew up in a very tight knit Serbian community on the south side of Chicago which helped make me

473 the person I am today. I would like to thank all of the people at St. Simeon Mirotochivi Serbian Orthodox
474 Church who have always been sources of enthusiasm and support in my life.

475 I would not be here without the unconditional love and constant support and encouragement of my
476 family. To my pokojni Deda Branko and Miloje, my pokojni Baba Milka, and my Baba Desa, I want to
477 say thank you for instilling in me at an early age the love of curiosity and storytelling that I have carried
478 throughout my life. To my sister Angelina, I want to say thank you for always loving me and being my
479 partner in crime throughout our childhoods. To my parents, Miroljub and Nada, Tata and Mama, I really
480 cannot express how grateful I am to you and how much I owe you. As I look back now I see how I am a
481 combination of both of your best qualities and every day I am in situations where I understand more and
482 more the lessons you made sure to teach me and the sacrifices you made to make sure I got the best possible
483 education. I love you all.

484 Finally, I have to thank my soul mate, the one person in my life who understands me more than anyone
485 else, my fiancée Kelly Brock. You are my sounding board, my support system, my cheerleader (figuratively
486 and literally!), my best friend, my role model, and my everything. I would not have gotten through grad-
487 uate school without you and my life would not be the same without you. I cannot wait to start our new
488 lives together as the married doctors, tackling whatever comes our way with the same zeal with which we
489 tackled graduate school. I love you with all my heart and soul.

0

490

491

Introduction

492 The Higgs boson is often described as one of the cornerstones of the Standard Model. Since the concep-
493 tion of the Higgs mechanism as the source of electroweak symmetry breaking in the early 1960s, countless
494 collider experiments have searched for this elusive particle. This dissertation presents the story of the Higgs
495 boson from its discovery to its use as a tool in the search for physics beyond the Standard Model with the
496 ATLAS detector at the Large Hadron Collider (LHC).

497 One of the first priorities of the early LHC was the search for the Higgs boson. This search was first
498 tackled in three main channels: $H \rightarrow \gamma\gamma$, $H \rightarrow ZZ^*$, and $H \rightarrow WW^*$. Each channel has its own
499 merits, but the WW^* is particularly suited to searching over a wide range of masses. The $H \rightarrow WW^*$
500 branching ratio is large and it is the primary decay channel above the $2m_W$ mass threshold.

501 While the rate of events produced in $H \rightarrow WW^*$ is large, the channel poses some challenges. First,
502 the most common mode of study for this channel is $H \rightarrow WW^* \rightarrow \ell\nu\ell\nu$. With neutrinos in the
503 final state, it is not possible to fully reconstruct the invariant mass of the parent Higgs like the $\gamma\gamma$ and

504 $ZZ \rightarrow 4\ell$ channels. Second, the final state topology is mimicked by a wide variety of backgrounds that
505 need to be properly estimated. This means tailored selection requirements for background reduction and
506 robust background estimation techniques must both be developed.

507 In 2012, the ATLAS and CMS experiments announced the discovery of a new particle consistent with
508 the Higgs boson [1, 2]. In ATLAS, this discovery was made with 4.8 fb^{-1} collected at $\sqrt{s} = 7 \text{ TeV}$ and
509 5.8 fb^{-1} at $\sqrt{s} = 8 \text{ TeV}$. The $H \rightarrow WW^* \rightarrow \ell\nu\ell\nu$ analysis played an important role in this discovery.
510 After the discovery, measurement of the properties of the newly discovered particle and confirmation of its
511 consistency with the Standard Model Higgs were the main priorities. The WW^* channel is also uniquely
512 suited to these types of measurements. Because of its good rate, it offers some of the best cross section
513 measurements available among the various Higgs decay modes. It is also suited for measurement of mul-
514 tiple Higgs production modes, like the vector boson fusion (VBF) mode, where incoming quarks radiate
515 W/Z bosons which fuse to make a Higgs. In VBF production with the WW^* decay channel, the coupling
516 of the Higgs to the W boson is present in both the production and decay which allows for more precise
517 measurements of this coupling than other channels which rely on gluon fusion production (where gluons
518 couple to the Higgs through a top loop in the production). The measurement of VBF carries the addi-
519 tional challenge that its cross section is an order of magnitude smaller than that of gluon fusion, meaning
520 that the large branching ratio to WW^* offers an additional advantage in isolating this production mode.
521 In the final ATLAS Run 1 results, combining 20.3 fb^{-1} taken at $\sqrt{s} = 8 \text{ TeV}$ with the 4.8 fb^{-1} collected
522 at $\sqrt{s} = 7 \text{ TeV}$, the WW^* channel achieved its first observation of VBF production of the Higgs.

523 After Run 1 of the LHC, with the existence of the Higgs now firmly established, the focus shifted to
524 searches for physics beyond the Standard Model. In particular, searches for high mass resonances benefit
525 from the LHC's increase to $\sqrt{s} = 13 \text{ TeV}$ in Run 2. The cross section for a generic gluon-initiated reso-
526 nance with a mass of 2 TeV increases tenfold in Run 2, making searches for high mass resonances a high
527 priority. The newly discovered Higgs can be used as a tool in these searches. After the discovery, the Higgs
528 boson provides a large swath of unmeasured phase space where new physics could be discovered. Higgs
529 pair production in the Standard Model has a low cross section that requires large datasets (on the order of
530 the LHC's lifetime) for full measurement. However, new physics can modify this cross section, especially

531 through new resonances which decay to two Higgs bosons. Such high mass resonances also produce diffi-
532 cult to recognize final state topologies due to the merging of decay products from high momentum Higgs
533 bosons. A search for Higgs pair production in the $HH \rightarrow b\bar{b}b\bar{b}$ final state was performed with 3.2 fb^{-1}
534 collected with ATLAS at $\sqrt{s} = 13 \text{ TeV}$ in 2015. The results are presented in this dissertation with a focus
535 on a dedicated signal region for boosted final states. This signal region uses new techniques for recognizing
536 jet substructure and b -tagging to the improve signal acceptance of high mass resonances.

537 This dissertation begins by discussing the discovery of the Higgs and the role of the $H \rightarrow WW^* \rightarrow$
538 $\ell\nu\ell\nu$ channel. It then discusses the first observation of the VBF production mode in $H \rightarrow WW^* \rightarrow$
539 $\ell\nu\ell\nu$ with the full ATLAS Run 1 dataset, as well as the final combined Run 1 measurements from this
540 channel. Finally, it presents a search for Higgs pair production in the $HH \rightarrow b\bar{b}b\bar{b}$ channel. It is organized
541 into four parts.

542 Part 1 presents the theoretical and experimental background required for the subsequent parts. Chap-
543 ter 1 gives an overview of Higgs physics, particularly single and double Higgs production in the Standard
544 Model and beyond. Chapter 2 presents details regarding the Large Hadron Collider and the ATLAS exper-
545 iment. The evolution of machine conditions, descriptions of the ATLAS sub-detectors, and an overview
546 of object reconstruction in ATLAS are all shown. A brief interlude on the ATLAS Muon New Small
547 Wheel upgrade is also given, as this upgrade has been a focus of my graduate work and will have important
548 impact on ATLAS' ability to study the Higgs at the High Luminosity LHC.

549 Part 2 discusses the observation and measurement of the Higgs in the $H \rightarrow WW^* \rightarrow \ell\nu\ell\nu$ channel
550 in the ATLAS Run 1 dataset at $\sqrt{s} = 7$ and 8 TeV . Because I worked in this channel from before the
551 discovery through to the final analysis of the Run 1 dataset, Part 2 is organized in such a way to allow easy
552 presentation of multiple analyses on different subsets of the full Run 1 dataset. Chapter 3 presents a general
553 overview of the $H \rightarrow WW^*$ analysis strategy and defines many of the variables and common elements
554 used in the rest of Part 2. Chapter 4 presents the discovery of the Higgs boson, focusing on the role of the
555 WW^* channel in this discovery. Chapter 5 presents the first observation of the VBF production mode of
556 the Higgs in the WW^* channel, a study which was done on the full Run 1 ATLAS dataset. In this chapter,
557 the focus is mainly on the selection cut-based VBF analysis. The cut-based analysis was an important first

558 step to the final VBF result which used a Boosted Decision Tree (BDT). Where appropriate, connections
559 between the cut-based and BDT analyses are shown and their compatibility is discussed. Finally, the VBF
560 analysis was an important input into the combined Run 1 $H \rightarrow WW^* \rightarrow \ell\nu\ell\nu$ result, which used
561 both the gluon fusion and VBF channels in a combined fit to infer properties of the Higgs, including its
562 couplings to the gauge bosons and its production cross section. This is the topic of Chapter 6.

563 Part 3 presents a search for Higgs pair production in the $HH \rightarrow b\bar{b}b\bar{b}$ channel. Chapter 7 presents
564 an overview of this search in the boosted regime, where the Higgs pairs are the result of the decay of a
565 heavy resonance. Chapter 8 shows the combined results between the boosted regime and the resolved
566 regime, which is sensitive to lower mass resonances and non-resonant Higgs pair production. Finally, Part
567 4 presents a conclusion and brief outlook of future Higgs physics with ATLAS.

Part I

Theoretical and Experimental Background

In modern physics, there is no such thing as “nothing.”

Richard Morris

1

570

571

The Physics of the Higgs Boson

572 This chapter presents an overview of the Standard Model of Particle Physics and in particular the physics
573 of the Higgs boson. First, a brief overview of the Standard Model and its history are presented. Then, a
574 description of the Higgs mechanism of electroweak symmetry breaking is given. Next, the physics of single
575 Higgs boson production and decay is described. The Standard Model also allows for production of two
576 Higgs bosons and this is detailed as well. Finally, di-Higgs production in two beyond the Standard Model
577 (BSM) theories - Randall-Sundrum gravitons (RSG) and Two Higgs Doublet Models (2HDM) - is shown.

578 **I.I THE STANDARD MODEL OF PARTICLE PHYSICS**

579 The Standard Model (SM) of Particle Physics is a quantum field theory describing the fundamental
580 particles of nature and the forces that govern their interactions. Several comprehensive treatments of the
581 SM already exist in the literature [3–8] and this section will not rehash those. Rather, this section presents
582 a brief overview of the SM particles and forces in order to define them for subsequent discussions.

583 The Standard Model consists of two primary categories of fundamental particles: fermions (spin 1/2
 584 particles) and bosons (integer spin particles). The SM also describes three forces: electromagnetism, the
 585 weak nuclear force, and the strong nuclear force. Gravity is not included in the theory and is largely irrele-
 586 evant at the scales currently probed by collider experiments. Within the fermions, there are both quarks
 587 (which interact via all three forces) and the leptons. The charged leptons interact via electromagnetic and
 588 weak interactions, while neutrinos (neutral leptons) interact only via the weak force. Within the bosons,
 589 there are the W^\pm and Z bosons (the mediators of the weak force), the gluon (g , the mediator of the strong
 590 force), and the photon (γ), the mediator of the electromagnetic force. Finally, there is the Higgs boson,
 591 a fundamental spin-0 particle resulting from the Higgs mechanism of electroweak symmetry breaking.

592 Figure 1.1 summarizes the fermions and bosons of the SM.

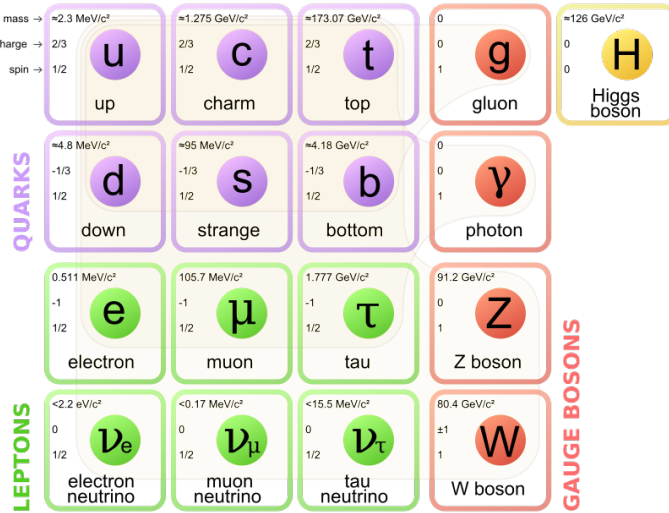


Figure 1.1: The particles of the Standard Model and their properties [6].

593 The Standard Model coalesced into a unified theoretical framework in the 1960s through the work
 594 of Glashow, Weinberg, Salam, and others on the theory of electroweak interactions [9–12]. This theory
 595 characterized both the electromagnetic and weak interactions as unified under a single gauge symmetry
 596 group, namely $SU(2) \times U(1)$. At low enough energy scales (on the order of the W and Z masses, the
 597 electroweak symmetry is broken, as evidenced by the fact that the weak bosons have mass while the photon
 598 does not. The discovery of the Higgs boson in 2012 confirmed the Higgs mechanism as the most likely
 599 candidate for this electroweak symmetry breaking [1, 2]. The electroweak theory is then combined with

600 the theory of quantum chromodynamics (which models the strong sector as a non-Abelian $SU(3)$ gauge
 601 group) to form the complete SM [13].

602 **I.2 ELECTROWEAK SYMMETRY BREAKING AND THE HIGGS**

603 In the Standard Model Lagrangian, it is difficult to include mass terms for the W and Z bosons without
 604 breaking the fundamental gauge symmetry of the Lagrangian. A traditional mass term does not preserve
 605 the $SU(2) \times U(1)$ symmetry. Additionally, scattering of massive W and Z bosons violate unitarity and
 606 these diagrams diverge at high energy scales. In the 1960s, Higgs, Brout, Englert, Guralnik, Kibble, and
 607 Hagen developed a mechanism for spontaneous symmetry breaking via the addition of a complex scalar
 608 doublet to the SM. Three of the four real degrees of freedom of this complex field would go to the lon-
 609 gitudinal modes of the W^\pm and Z , thus allowing them to have mass [14–17]. The remaining degree of
 610 freedom would manifest as an additional scalar, known now as the Higgs boson.

611 The mechanism works by introducing a Lagrangian for the newly introduced field that still respects the
 612 symmetry of the Standard Model inherently, but with a minimum at a non-zero vacuum expectation value
 613 for the field. In this minimum of the potential, the electroweak symmetry is broken. Specifically, consider
 614 a complex scalar doublet Φ with four degrees of freedom, as shown in equation I.1.

$$\Phi = \begin{pmatrix} \phi^+ \\ \phi^0 \end{pmatrix} = \frac{1}{\sqrt{2}} \begin{pmatrix} \phi_1^+ + i\phi_2^+ \\ \phi_1^0 + i\phi_2^0 \end{pmatrix} \quad (\text{I.1})$$

615 The minimal potential of a self-interacting Higgs that still respects the SM symmetry is given in equa-
 616 tion I.2.

$$V(\Phi) = \mu^2 \Phi^\dagger \Phi + \lambda (\Phi^\dagger \Phi)^2 \quad (\text{I.2})$$

617 If the μ^2 term of this potential is positive, then the potential has a minimum at $\Phi = 0$ and the SM
 618 symmetry is preserved. However, if instead $\mu^2 < 0$, then the minimum is at a finite value of Φ , namely

$$\Phi_{\min} = \frac{1}{\sqrt{2}} \begin{pmatrix} 0 \\ v \end{pmatrix} \quad (\text{I.3})$$

⁶¹⁹ where $v = \sqrt{\mu^2/\lambda}$. Because this is the location of the minimum, it corresponds to the vacuum expecta-
⁶²⁰ tion value for the field ($\langle \Phi \rangle = \Phi_{\min}$). The excitations of the Higgs can then be parameterized as

$$\Phi = \frac{1}{\sqrt{2}} \begin{pmatrix} 0 \\ v + H \end{pmatrix} \quad (1.4)$$

⁶²¹ The full scalar Lagrangian, including the kinetic term, is then given as

$$\mathcal{L}_s = (D^\mu \Phi)^\dagger (D_\mu \Phi) - V(\Phi) \quad (1.5)$$

⁶²² where the covariant derivative is defined as

$$D_\mu = \partial_\mu + \frac{ig}{2} \tau^a W_\mu^a + ig' Y B_\mu \quad (1.6)$$

⁶²³ and W^1, W^2, W^3 and B are the $SU(2)$ and $U(1)$ gauge fields of the electroweak theory, respectively. g
⁶²⁴ and g' are the corresponding coupling constants. With the scalar Lagrangian in place, the physical gauge
⁶²⁵ fields can then be written as

$$W_\mu^\pm = \frac{1}{\sqrt{2}} (W_\mu^1 \mp i W_\mu^2) \quad (1.7)$$

⁶²⁶

$$Z_\mu = \frac{-g'B_\mu + gW_\mu^3}{\sqrt{g^2 + g'^2}} \quad (1.8)$$

⁶²⁷

$$A_\mu = \frac{gB_\mu + g'W_\mu^3}{\sqrt{g^2 + g'^2}} \quad (1.9)$$

⁶²⁸ Equation 1.7 corresponds to the charged W^+ and W^- bosons, equation 1.8 corresponds to the neutral Z
⁶²⁹ boson, and equation 1.9 corresponds to the neutral photon. The masses of the particles also arise from the
⁶³⁰ Lagrangian. The photon has zero mass, while the masses of the W and Z bosons are given in equation 1.10.

⁶³¹

$$M_W^2 = \frac{1}{4} g^2 v^2$$

$$M_Z^2 = \frac{1}{4} (g^2 + g'^2) v^2 \quad (1.10)$$

632 The fermion masses also arise through a coupling with the Higgs via the Yukawa interaction (for a detailed
633 description, see [8]). In this case the coupling between the Higgs and the fermions goes as

$$g_{Hf\bar{f}} = \frac{m_f}{v} \quad (\text{i.ii})$$

634 The full Lagrangian of Higgs interactions can be written as

$$\mathcal{L}_{\text{Higgs}} = -g_{Hf\bar{f}}\bar{f}fH + \frac{g_{HHH}}{6}H^3 + \frac{g_{HHHH}}{24}H^4 + \delta_V V_\mu V^\mu \left(g_{HV}VH + \frac{g_{HHV}}{2}H^2 \right) \quad (\text{i.12})$$

635 with

$$\begin{aligned} g_{HV} &= \frac{2m_V^2}{v} & g_{HHV} &= \frac{2m_V^2}{v^2} \\ g_{HHH} &= \frac{3m_H^2}{v} & g_{HHHH} &= \frac{3m_H^2}{v^2} \end{aligned} \quad (\text{i.13})$$

636 Here, V refers to the W^\pm and Z , and $\delta_W = 1$ while $\delta_Z = 1/2$. Phenomenologically, there are a few
637 features of this Lagrangian that are useful to note. First, note that the Higgs mass is a free parameter of the
638 theory that must be determined experimentally. Second, note that the coupling of the Higgs to the vector
639 bosons and fermions scales with the masses of these particles, a fact that is important when considering
640 both the production and decays of the particle. Also note that the branching ratio of the Higgs to W
641 bosons will be twice that of the branching ratio to Z if the Higgs mass is large enough to produce the
642 particles on shell because of the extra symmetry factor associated with the W coupling. Finally, note the
643 presence of the cubic and quartic Higgs self interaction terms, which can lead to final states with multiple
644 Higgs bosons produced.

645 1.3 HIGGS BOSON PRODUCTION AND DECAY

646 This section discusses the properties of Higgs production and decay mechanisms. The details presented
647 here will focus on the properties of a 125 GeV Higgs boson, as this is the mass closest to that of the newly
648 discovered Higgs.

649 1.3.1 HIGGS PRODUCTION

650 The Higgs is produced by four main production modes at the Large Hadron Collider - gluon-gluon
 651 fusion (ggF), vector boson fusion (VBF), associated production with a W or Z boson, or associated pro-
 652 duction with top quarks ($t\bar{t}H$). Figure 1.2 shows the Feynman diagrams for these four modes.

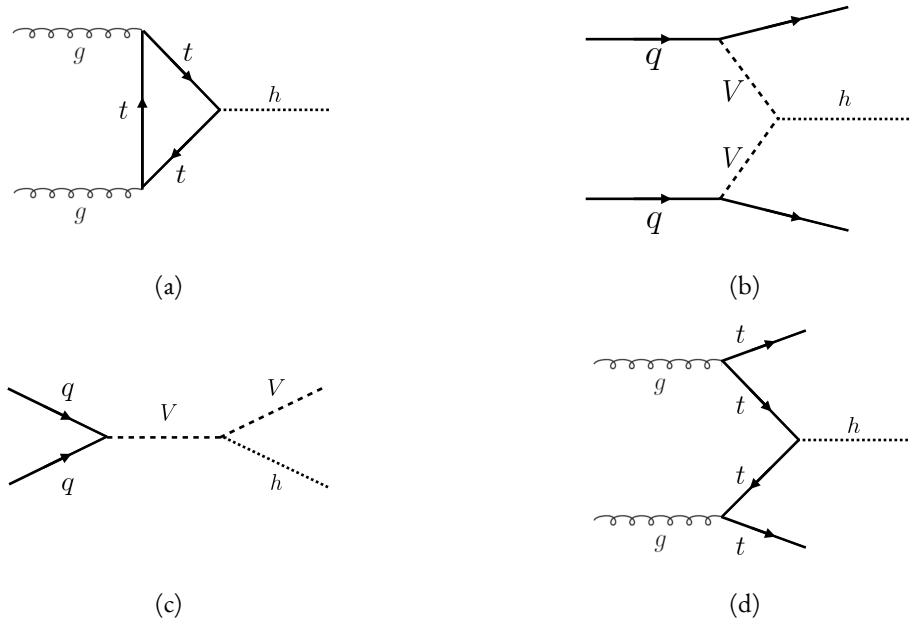


Figure 1.2: The four most common Higgs boson production modes at the LHC: (a) gluon-gluon fusion, (b) vector boson fusion, (c) $W/Z + H$ production, (d) $t\bar{t}H$ production

653 In gluon-gluon fusion, gluons from the incoming protons fuse via a top-quark loop to produce a Higgs.
 654 The top quark is the dominant contribution in the loop due to its heavy mass and the fact that the Higgs-
 655 fermion coupling constant scales with fermion mass. In vector boson fusion, the incoming quarks each
 656 radiate a W or Z boson which fuse to produce the Higgs. This production mode results in a final state
 657 with a Higgs boson and two additional jets which tend to be forward because they carry the longitudinal
 658 momentum of the incoming partons. The Higgs can also be produced in association with a W or Z boson.
 659 The W/Z is produced normally and then radiates a Higgs (this mode is also sometimes known as “Higgs-
 660 strahlung”). Finally, the Higgs can be produced in association with two top quarks. Each incoming gluon
 661 splits into a $t\bar{t}$ pair, and one of the top pairs combines to create a Higgs. Figure 1.3 shows the production
 662 cross section for a 125 GeV Higgs boson in each of these modes at a pp collider as a function of center of

663 mass energy.

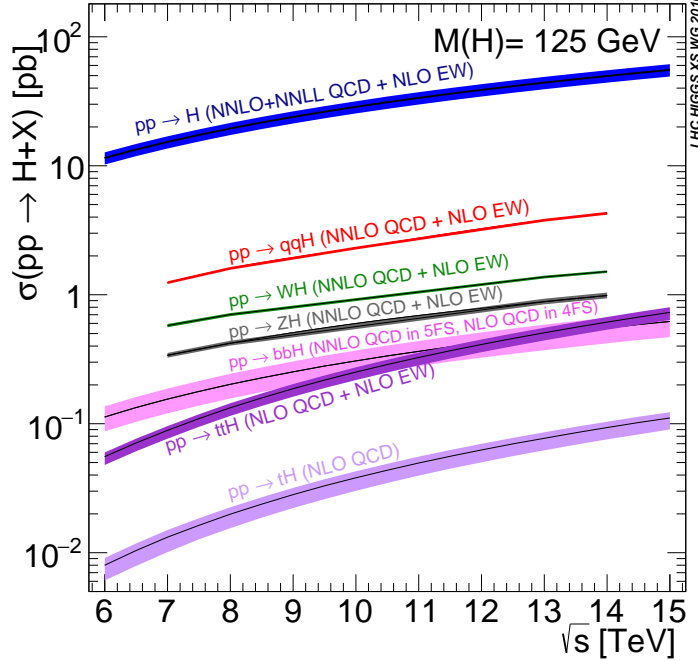


Figure 1.3: Higgs production cross sections as a function of center of mass energy (\sqrt{s}) at a pp collider [18].

664 In figure 1.3, note that gluon fusion has the largest cross section, while VBF is the second largest at
 665 approximately a factor of 10 smaller. The figure also includes the less commonly studied $b\bar{b}H$ and tH
 666 modes. The $b\bar{b}H$ and tH modes are not studied as commonly as $t\bar{t}H$ due to the larger background con-
 667 tributions and lower cross sections, respectively. At $\sqrt{s} = 8$ TeV, ggF production of a 125 GeV Higgs
 668 has a cross section of 19.47 pb, while VBF has a cross section of 1.601 pb [18]. The cross sections of all of
 669 the main Higgs production modes at this center of mass energy, as well as their uncertainties from varying
 670 the renormalization and factorization scales and PDFs, are summarized in table 1.1 for a 125 GeV Higgs.

671 1.3.2 HIGGS BRANCHING RATIOS

672 The fact that the Higgs couples more strongly to more massive particles is crucial for understanding its
 673 branching ratios. The width for Higgs decays to fermions is given in equation 1.14 [5].

$$\Gamma(H \rightarrow f\bar{f}) = \frac{N_c \sqrt{2} G_F m_f^2 m_H}{8\pi} \quad (1.14)$$

Production mode	σ (pb)	QCD scale uncert. (%)	PDF + α_s uncert. (%)
Gluon fusion	19.47	+7.3/ - 8.0	3.1
Vector boson fusion	1.601	+0.3/ - 0.2	2.2
WH	0.7026	+0.6/ - 0.9	2.0
ZH	0.4208	+2.9/ - 2.4	1.7
$t\bar{t}H$	0.1330	+4.1/ - 9.2	4.3
bbH	0.2021	+20.7/ - 22.3	
tH (t -channel)	0.01869	+7.3/ - 16.5	4.6
tH (s -channel)	1.214×10^{-3}	+2.8/ - 2.4	2.8

Table 1.1: Production cross sections for a 125 GeV Higgs boson at $\sqrt{s} = 8$ TeV with scale and PDF uncertainties [18].

In this case, N_c is the number of colors, G_F is the Fermi constant, m_f is the mass of the fermion, and m_H is the mass of the Higgs. Note that the width scales with the square of the fermion mass. (This also assumes that the Higgs mass is large enough to decay with both the fermions on shell.)

The decay width to WW is given in equation 1.15 [5].

$$\Gamma(H \rightarrow W^+W^-) = \frac{\sqrt{2}G_FM_W^2m_H}{16\pi} \frac{\sqrt{1-x_W}}{x_W} (3x_W^2 - 4x_W + 4) \quad (1.15)$$

where m_W is the mass of the W and $x_W = 4M_W^2/m_H^2$. To get the branching ratio to ZZ , the equation is divided by 2 to account for identical particles in the final state, and x_W is replaced with $x_Z = 4M_Z^2/m_H^2$. This is shown in equation 1.16 [5].

$$\Gamma(H \rightarrow ZZ) = \frac{\sqrt{2}G_FM_Z^2m_H}{32\pi} \frac{\sqrt{1-x_Z}}{x_Z} (3x_Z^2 - 4x_Z + 4) \quad (1.16)$$

These formulas can also be visualized as a function of Higgs mass. Figure 1.4 shows the branching ratios as a function of the Higgs mass. There are a few interesting features to note in this figure. First, note that at high Higgs masses, once on-shell production of both W and Z bosons is possible, these two decays are the dominant ones due to the large masses of the W/Z . Also note that the branching ratio to W s is twice that of Z s at these large masses due to the δ_V symmetry factor noted previously. At 125 GeV, the Higgs is accessible through many different decay modes. The largest branching ratio is the decay $H \rightarrow b\bar{b}$

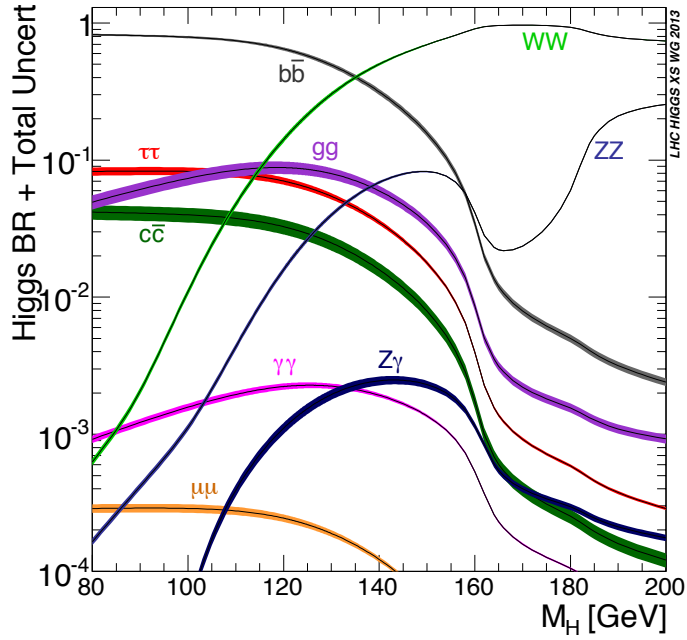


Figure 1.4: Higgs boson branching ratios as a function of m_H [18].

at 58.24% [18]. This branching is larger than the WW/ZZ decays because one of the two bosons must be produced off-shell for $m_H = 125$ GeV. The second largest branching ratio is to WW^* at 21.37 % (before taking into account the branching ratios of the W). Table 1.2 summarizes the branching ratios for a 125 GeV Higgs. Note that there is in fact a Higgs branching ratio to $\gamma\gamma$ even though photons are massless. This decay happens through a loop (the largest contributions to the loop are top and W) which suppresses the branching ratio.

Decay	Branching ratio (%)
$b\bar{b}$	58.24
WW^*	21.37
gg	8.187
$\tau\tau$	6.272
$cc\bar{c}$	2.891
ZZ^*	2.619
$\gamma\gamma$	0.2270
$Z\gamma$	0.1533
$\mu\mu$	0.02176

Table 1.2: Branching ratios for a 125 GeV Higgs boson [18].

693 Note that the branching ratios alone do not tell the full story of which Higgs channels are the most
 694 sensitive. For example, a $H \rightarrow b\bar{b}$ search in gluon fusion production is incredibly difficult due to the
 695 large QCD dijet background at the LHC. However, in associated production of the Higgs, where a W
 696 or Z gives additional final state particles that can be used to reduce background, a search for $H \rightarrow b\bar{b}$
 697 can be sensitive. The combinations of production and decay modes that are most commonly studied are
 698 summarized in table 1.3 [5].

Decay	Inclusive (incl. ggF)	VBF	WH/ZH	$t\bar{t}H$
$H \rightarrow \gamma\gamma$	✓	✓	✓	✓
$H \rightarrow b\bar{b}$			✓	✓
$H \rightarrow \tau^+\tau^-$		✓		
$H \rightarrow WW^* \rightarrow \ell\nu\ell\nu$	✓	✓	✓	
$H \rightarrow ZZ \rightarrow 4\ell$	✓			
$H \rightarrow Z\gamma \rightarrow \ell\ell\gamma$	very low			

Table 1.3: Possible channels for Higgs searches. Checkmarks denote the most sensitive production modes [5].

699 1.4 HIGGS PAIR PRODUCTION IN THE STANDARD MODEL

700 The Standard Model also allows for processes that produce two Higgs bosons in the final state, known
 701 as Higgs pair production or di-Higgs production. The two main production mechanisms are shown in
 figure 1.5. The two diagrams in figure 1.5 interfere destructively with one another, resulting in a low overall

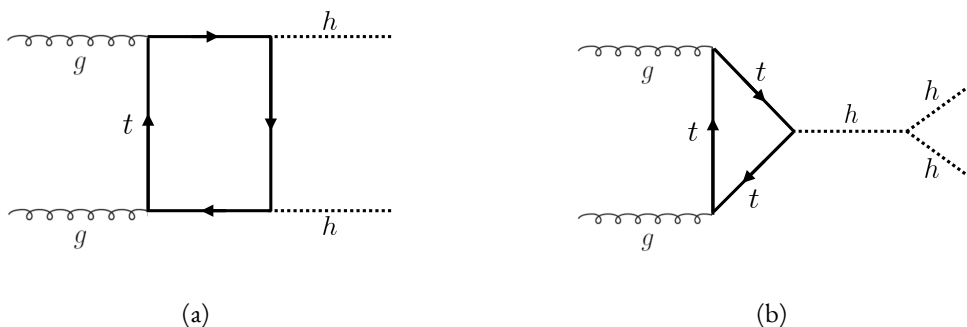


Figure 1.5: The two leading diagrams for Standard Model di-Higgs production at the LHC: (a) box diagram, (b) Higgs self coupling

702
 703 cross section for di-Higgs production at the LHC. Nevertheless, Higgs pair production is quite interesting

704 to study because it gives direct access to the λ parameter of the Higgs potential, also known as the Higgs
705 self coupling. The diagram in figure 1.5(b) is sensitive to this coupling through the triple Higgs vertex.

706 One can substitute the gluon fusion production of diagram 1.5(b) with any of the other production
707 modes previously discussed. These other modes do not suffer from interference with the box diagram in
708 figure 1.5(a) due to the presence of additional particles in the final state. They still have a lower cross section
709 than the gluon fusion mode, however. The cross sections for di-Higgs production in the different modes,
710 as well as their uncertainties, are shown in table 1.4 [19]. These are shown for $\sqrt{s} = 14$ TeV as the higher
711 center of mass energy is more sensitive to this process. Note that the scale of cross section quoted is now
in fb rather than pb.

Production mode	σ (fb)	Total uncert. (%)
Gluon fusion	33.89	+37.2 / - 27.8
Vector boson fusion	2.01	+7.6 / - 5.1
$W H H$	0.57	+3.7 / - 3.3
$Z H H$	0.42	+7.0 / - 5.5
$t \bar{t} H$	1.02	-

Table 1.4: Production cross sections for pair production of a 125 GeV Higgs boson at $\sqrt{s} = 14$ TeV with total uncertainty [19]. The uncertainties include QCD scale and PDF variations as well as uncertainties on α_S .

712

713 1.5 HIGGS PAIR PRODUCTION IN THEORIES BEYOND THE STANDARD MODEL

714 The Standard Model Higgs pair production cross section is rather small, and datasets on the scale of
715 the full lifetime of the LHC will be required to obtain sensitive measurements of the Higgs self-coupling.
716 However, the discovery of the Higgs also gives particle physicists a new tool that can be exploited in the
717 search for new physics beyond the Standard Model. In particular, Higgs pair production is a promising
718 channel in the search for new physics. The cross section for di-Higgs production can be altered through
719 both resonant and non-resonant production of Higgs pairs. In non-resonant production, di-Higgs pro-
720 duction vertices can arise from the presence of a new strong sector and additional colored particles [20–22].
721 Figure 1.6 shows examples of the types of vertices that can arise. In the resonant case, new heavy particle
722 can decay to Higgs pairs. Such new particles can include heavy Higgs bosons arising in two Higgs doublet

723 models (2HDM) or Higgs portal models as well as heavy gravitons in Randall-Sundrum theories [20, 23–
 724 29]. Figure 1.7 shows a generic diagram for a heavy resonance decaying to two Higgs bosons. In the 2HDM,
 725 X corresponds to the heavy CP-even scalar H . In the Randall-Sundrum model, X corresponds to a heavy
 spin-2 graviton G . The next sections provide more detail on the phenomenology of resonant Higgs pro-

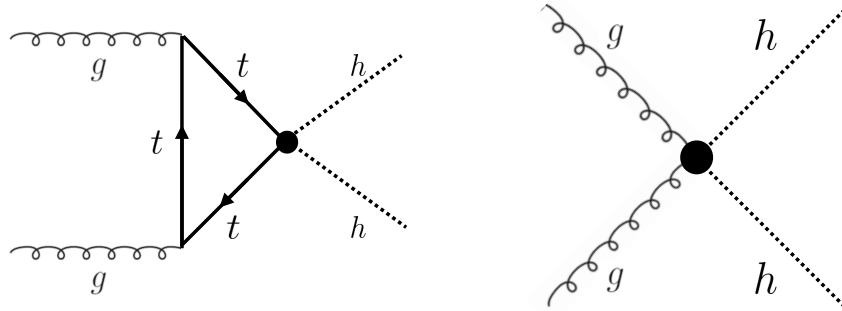


Figure 1.6: Diagrams with new vertices for non-resonant Higgs pair production arising in composite Higgs models

726
 727 duction in Randall-Sundrum and 2HDM models, as these models will later be tested in a dedicated search
 for resonant production of boosted Higgs pairs.

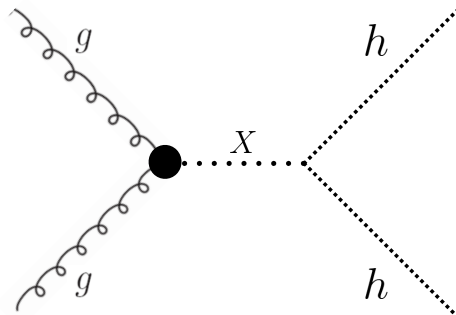


Figure 1.7: Generic Feynman diagram for resonant Higgs pair production in BSM theories

728

729 1.5.1 RANDALL-SUNDRUM GRAVITONS

730 The Randall-Sundrum model is a proposed solution to the hierarchy problem that posits a five-dimensional
 731 warped spacetime that contains two branes: one where the force of gravity is very strong and a second brane
 732 at the TeV scale corresponding to the known Standard Model sector [23]. In the theory, the branes are

733 weakly coupled and the graviton probability function drops exponentially going from the gravity brane
 734 to the SM brane, rendering gravity weak on the SM brane. The experimental consequence of this theory
 735 is a tower of widely spaced (in mass) Kaluza-Klein graviton resonances. In theories where the fermions
 736 are localized to the SM brane, production of gravitons from fermion pairs is suppressed and the primary
 737 mode of production is gluon fusion [24]. These gravitons have a substantial branching fraction to Higgs
 738 pairs, ranging from 6.43% for gravitons with a mass of 500 GeV to 7.66% at 3 TeV. Figure 1.8 shows the
 739 branching ratios of the spin-2 Randall Sundrum graviton (RSG) as a function of its mass. The predomi-
 740 nant decays are to $t\bar{t}$ above the mass threshold for that channel.

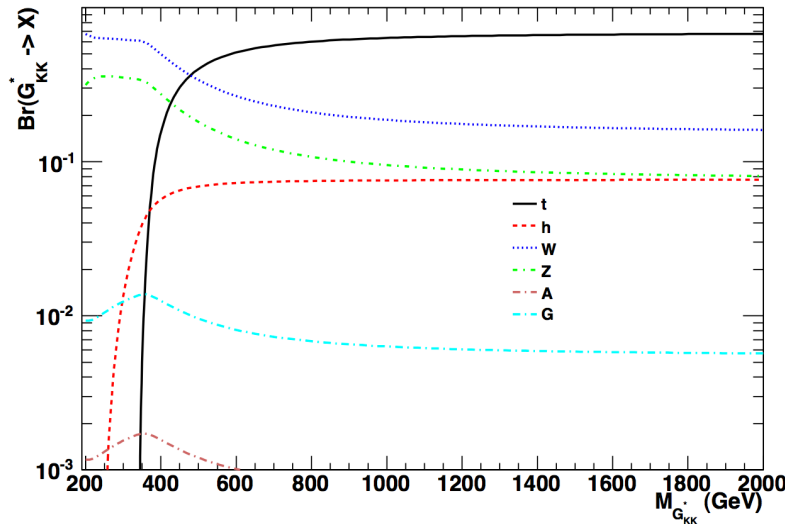


Figure 1.8: Branching ratios for a spin-2 Randall-Sundrum graviton as a function of mass computed in MadGraph with the CP3-Origins implementation [24, 30]

741 These models have two free parameters - the mass of the graviton and a curvature parameter k . Typically,
 742 rather than k , the theory is parameterized using $c \equiv k/\bar{M}_{\text{pl}}$, where \bar{M}_{pl} is the reduced Planck mass. The
 743 cross section for production of the RSG decreases as a function of mass and is strongly dependent on the
 744 gluon PDF. The increase in center of mass energy from 8 to 13 TeV in LHC Run 2 greatly increases the
 745 cross section at higher mass. Figure 1.9 shows the cross section as a function of graviton mass at $\sqrt{s} =$
 746 13 TeV for RSG models with $c = 1.0$ and $c = 2.0$.

747 Another interesting feature of the theory is that the width of the graviton increases with both c and m_G .
 748 Figure 1.10 shows the graviton width for both $c = 1.0$ and $c = 2.0$ as a function of mass. In $c = 1.0$,

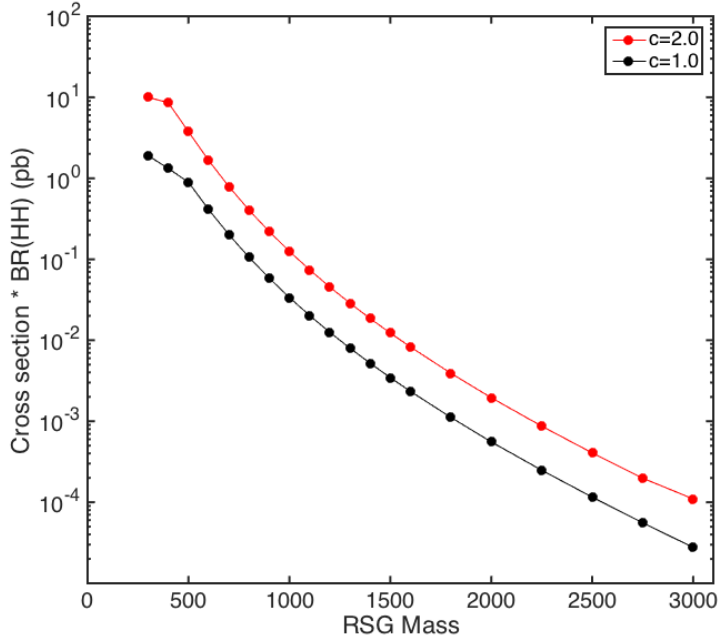


Figure 1.9: $\sigma \times \text{BR}(HH)$ for RSG as a function of mass computed in MadGraph with the CP3-Origins implementation [24, 30]

the width starts at 8.365 GeV for a mass of 300 GeV and increases to 187.2 GeV at a mass of 3 TeV. Similarly, with $c = 2.0$, the width starts at 33.46 GeV for $m_G = 300$ GeV and increases to 748.8 GeV at a mass of 3 TeV.

1.5.2 Two Higgs Doublet Models

In Two Higgs Doublet Models (2HDM), a second complex scalar doublet is added to SM [26–28]. In this case, all four degrees of freedom in the second doublet correspond to new particles, meaning that there are five total scalars from the two Higgs doublets - h (light CP-even Higgs), H (heavy CP-even Higgs), A (heavy CP-odd Higgs), and H^\pm (charged Higgs). The model is parameterized by two main parameters. The first, $\tan \beta \equiv \frac{v_2}{v_1}$, is the ratio of the vacuum expectation values of the two Higgs doublets (where v_1 corresponds to the v in the SM Higgs model described above). The second parameter is α , a mixing angle between the heavy and light Higgs fields. Models are also often parameterized with $\cos(\beta - \alpha)$ rather than α directly. The limit where $\cos(\beta - \alpha) = 0$ is called the alignment limit, and it is in this limit that

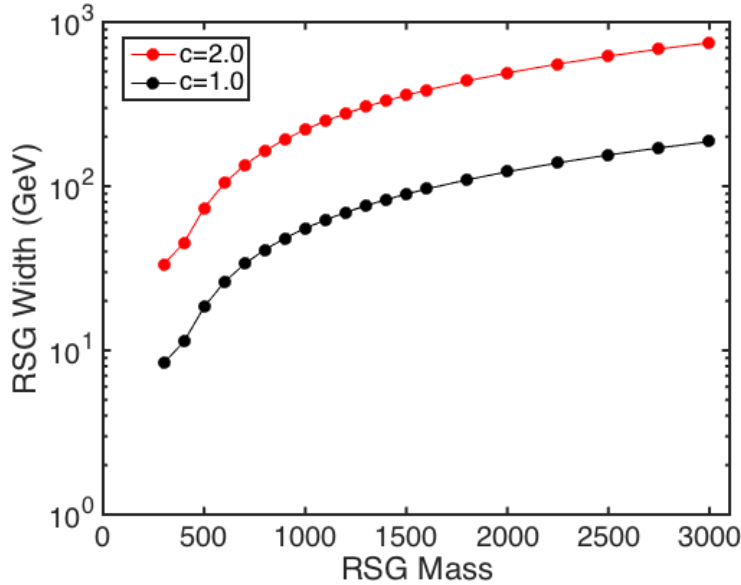


Figure 1.10: RSG width as a function of mass computed in MadGraph with the CP3-Origins implementation [24, 30]

761 the light Higgs h has the same couplings as a Standard Model Higgs.

762 2HDM models are usually separated into two main types - Type I and Type II. In Type I models, the
 763 charged fermions only couple to the second Higgs doublet, leading to a fermiophobic light Higgs. In
 764 Type II models, up-type quarks couple to the first doublet while down-type quarks couple to the second
 765 doublet. One specific realization of a Type II 2HDM is the Minimal Supersymmetric Standard Model
 766 (MSSM).

767 Resonant di-Higgs production in this model can proceed through decays of the heavy CP-even Higgs
 768 $H \rightarrow hh$. The branching ratio for $H \rightarrow hh$ depends on the model type as well as the values of $\tan \beta$ and
 769 $\cos \beta - \alpha$. Figure 1.11 shows the branching ratios as a function of the mass of the heavy scalar H for both
 770 Type I and Type II models. Depending on the type of model hh can be a substantial fraction of the decays
 771 of H .

772 **1.6 CONCLUSION**

773 Studying the Higgs sector is essential for understanding the details of how mass arises in the Standard
 774 Model and how the electroweak symmetry is broken. The discovery of the Higgs boson also opens the

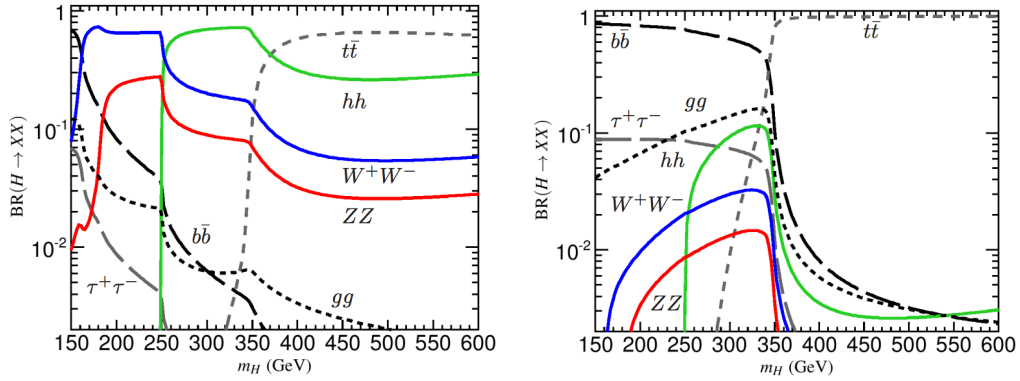


Figure 1.II: Branching ratios for heavy Higgs H in Type I (left) and Type II (right) 2HDM models with $\tan \beta = 1.5$ and $\cos(\beta - \alpha) = 0.1(0.01)$ for Type I (Type II). [28]

775 door for its use as a tool to search for new physics, and Higgs pair production is an ideal candidate for
 776 this study. Even if no BSM physics is found in Higgs pair production, searches for Higgs pairs will put
 777 constraints on the Higgs self coupling and thus further knowledge of the Standard Model and the details
 778 of the Higgs potential.

*The enthusiasm and motivation to explore particle physics
at the high-energy frontier knows no borders between the
nations and regions of the planet.*

Peter Jenni

2

779

780

781

The ATLAS detector and the Large Hadron Collider

782 This chapter presents an overview of the experimental systems used to conduct the measurements pre-
783 sented in this thesis. First, a brief overview of the accelerator, the Large Hadron Collider, will be given.
784 In this section, the accelerator conditions relevant to data-taking are presented as well. Next, an overview
785 of the ATLAS experiment is given. The basics of each sub-detector's role are summarized, as well as the
786 details of the datasets accumulated. Then, a brief interlude on the ATLAS Muon New Small Wheel up-
787 grade is presented. While this new detector does not have a direct impact on any of the datasets taken so
788 far, it will have an impact on future analyses and the work done on it is briefly summarized here. Finally,
789 an overview of object reconstruction in ATLAS is given. While the details of all of the algorithms will not
790 be presented in detail, aspects of the reconstruction performance such as object resolutions are shown as
791 these are relevant to the two studies presented later in this thesis.

792 2.1 THE LARGE HADRON COLLIDER

793 The Large Hadron Collider (LHC) is a proton-proton collider at the CERN laboratory in Geneva,
794 Switzerland [31]. It is designed for a maximum collision center of mass energy of $\sqrt{s} = 14$ TeV and has a
795 circumference of 26.7 kilometers. Four main experiments are located at the interaction points (IP) of the
796 accelerator: ATLAS (A Toroidal LHC ApparatuS), CMS (the Compact Muon Solenoid), ALICE (A Large
797 Ion Collider Experiment), and LHCb [32–35]. The studies performed in this thesis were all completed with
798 the ATLAS detector. Figure 2.1 shows a schematic of the LHC ring and the various experiments.

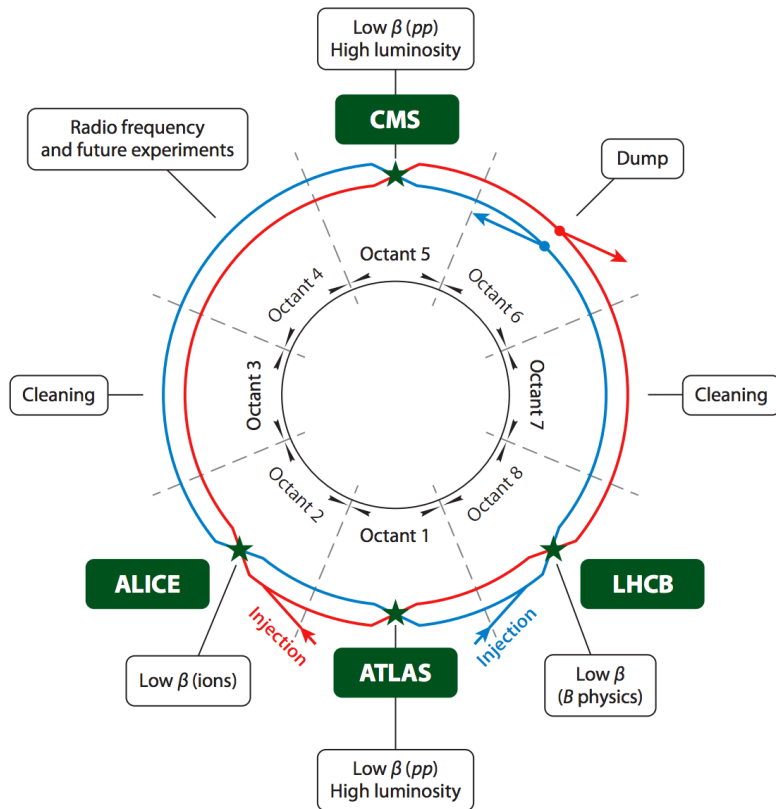


Figure 2.1: A schematic view of the LHC ring [36]

799 One of the most interesting features of the LHC is in its magnet design. Because the tunnel does not
800 have room for separate superconducting magnets for each of the beam pipes, the LHC employs a twin-bore
801 magnet design. Each magnet must hold an 8.3 Tesla magnetic field in order to bend the proton beams at
802 $\sqrt{s} = 14$ TeV. The superconducting magnets are cooled to a temperature of 1.9 Kelvin with superfluid

803 helium.

804 2.1.1 INSTANTANEOUS LUMINOSITY

805 The rate of physics events expected from the accelerator is dependent on the instantaneous luminosity
806 of the machine and the cross section of the physics process, $R_{\text{events}} = L\sigma$. Here, R_{events} is the number
807 of events per second, L is the instantaneous luminosity of the machine, and σ is the cross section for the
808 physics process being measured. The instantaneous luminosity of the LHC is determined by numerous
809 factors related to machine conditions. Equation 2.1 gives the equation for instantaneous luminosity of
810 Gaussian beam profile [36].

$$L = \frac{N_b^2 n_b f_{\text{rev}} \gamma_r}{4\pi \epsilon_n \beta^*} F \quad (2.1)$$

811 The LHC collides protons in bunches, and in the above equation N_b is the number of protons per bunch
812 while n_b is the number of bunches per beam. Nominally, the LHC can hold up to 2808 proton bunches.
813 f_{rev} is the revolution frequency. ϵ_n is the normalized transverse beam emittance, a measurement of the
814 average spread of the particles position-momentum space which has the dimension of length. β^* is the
815 value of the *beta* function for the beam at the interaction point. It relates the emittance to the Gaussian
816 width of the beam with $\sigma_{\text{beam}} = \sqrt{\epsilon \cdot \beta}$. F is a reduction factor that corrects for the fact that the beams
817 are colliding at an angle at the IP.

818 Another way of writing the instantaneous luminosity is shown in equation 2.2. In this case, the instanta-
819 neous luminosity is written as the ratio of the rate of inelastic collisions with the inelastic cross section [37].

820

$$L = \frac{R_{\text{inel}}}{\sigma_{\text{inel}}} = \frac{\mu n_b f_{\text{rev}}}{\sigma_{\text{inel}}} \quad (2.2)$$

821 In this case, μ is the average number of interactions per bunch crossing in the accelerator. μ is a use-
822 ful parameter for characterizing the amount of activity recorded in an experiment. As the instantane-
823 ous luminosity and thus μ increase, there are more interactions per bunch crossing and more activity in the
824 detector. This is often characterized with $\langle \mu \rangle$, the measured per bunch crossing μ value averaged over all
825 bunch crossings. The interactions inside each bunch crossing that are not the main physics process of in-

826 terest are often referred to as “pileup” interactions, and $\langle \mu \rangle$ is a measurement of the level of pileup in the
827 detector.

828 **2.1.2 EVOLUTION OF MACHINE CONDITIONS**

829 This thesis uses datasets taken at three different center of mass energies: $\sqrt{s} = 7\text{ TeV}$ data taken in the
830 year 2011, $\sqrt{s} = 8\text{ TeV}$ data taken in the year 2012, and $\sqrt{s} = 13\text{ TeV}$ data taken in the year 2015. In
831 addition to increasing center of mass energy, the instantaneous luminosity and parameters that determine
832 it were evolving. Table 2.1 summarizes that machine conditions in each of these datasets.

	2011	2012	2015	Design
$\sqrt{s} [\text{TeV}]$	7	8	13	14
Number of bunches	1380	1380	1825	2808
Max. protons per bunch	1.45×10^{11}	1.7×10^{11}	1.2×10^{11}	1.15×10^{11}
Bunch spacing [ns]	50	50	25	25
Max. instantaneous luminosity [$\text{cm}^{-2}\text{s}^{-1}$]	3.7×10^{33}	7.7×10^{33}	5×10^{33}	10^{34}
$\beta^* [\text{m}]$	1.0	0.6	0.8	0.55
$\langle \mu \rangle$	11.6	20.7	13.7	-

Table 2.1: Evolution of LHC machine conditions [38, 39]

833 **2.2 THE ATLAS DETECTOR**

834 The ATLAS detector is a multi-purpose particle detector experiment at the LHC’s Point 1 [32]. It has
835 nearly 4π coverage in solid angle around the interaction point. It consists of an inner detector for mea-
836 suring charged particles, electromagnetic and hadronic calorimeters, and a muon spectrometer. Figure 2.2
837 gives an overview of the detector.

838 **2.2.1 COORDINATE SYSTEM**

839 Before defining the properties of the individual detectors, it is important to establish the coordinate
840 system used. Figure 2.3 shows a schematic of the coordinate system. The azimuthal plane (perpendicular
841 to the beam line) is defined as the x - y plane. The angle in this plane is referred to as ϕ . The angle relative

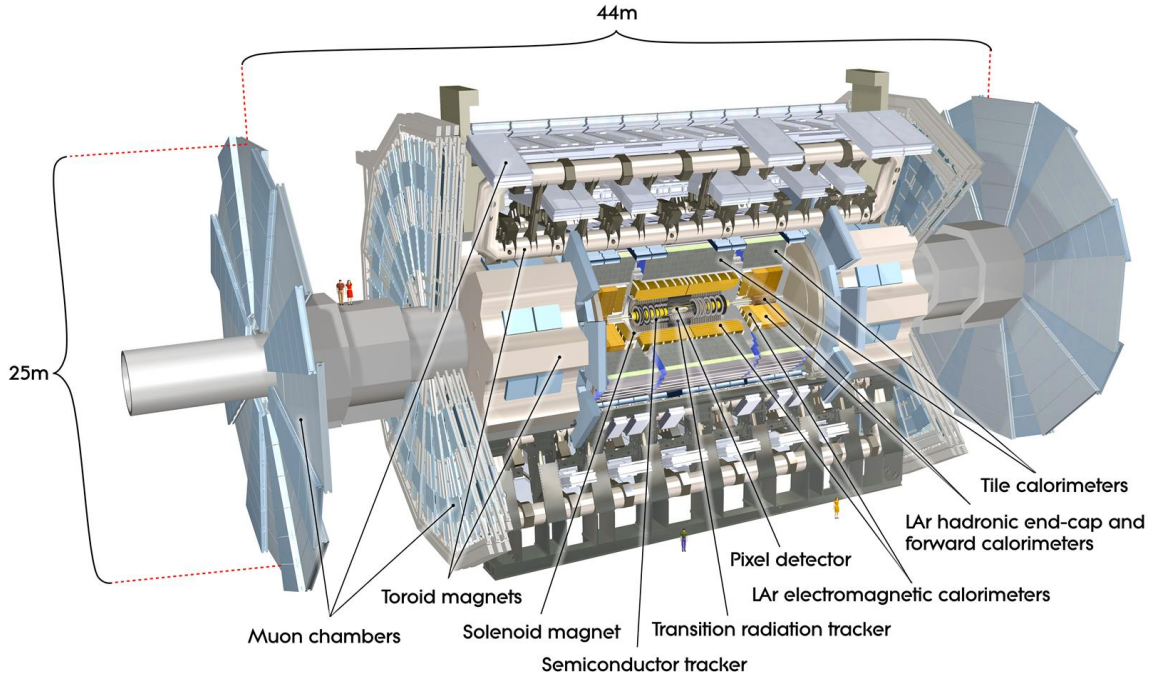


Figure 2.2: A full diagram of the ATLAS detector [32]

842 to the beam axis is referred to as θ . Rather than using θ directly as a coordinate, the experiment often uses
 843 the pseudorapidity η . η is defined in equation 2.3.

$$\eta = \ln \left(\tan \left(\frac{\theta}{2} \right) \right) \quad (2.3)$$

844 Pseudorapidity is the massless approximation of rapidity, the angle used to parameterize boosts in spe-
 845 cial relativity. This is important for two reasons. First, it means that differences in η are Lorentz invariant.
 846 Second, particle production is roughly constant in pseudorapidity. Particles with η close to zero are re-
 847 ferred to as “central”, while those at high $|\eta|$ are called “forward”. In general, two main detector topologies
 848 can be seen in figure 2.2. There are “barrel” elements, which surround the beam line cylindrically and are
 849 in the central region of the detector. In the forward region, there are “endcap” regions which are arranged
 850 as disks perpendicular to the beam line.

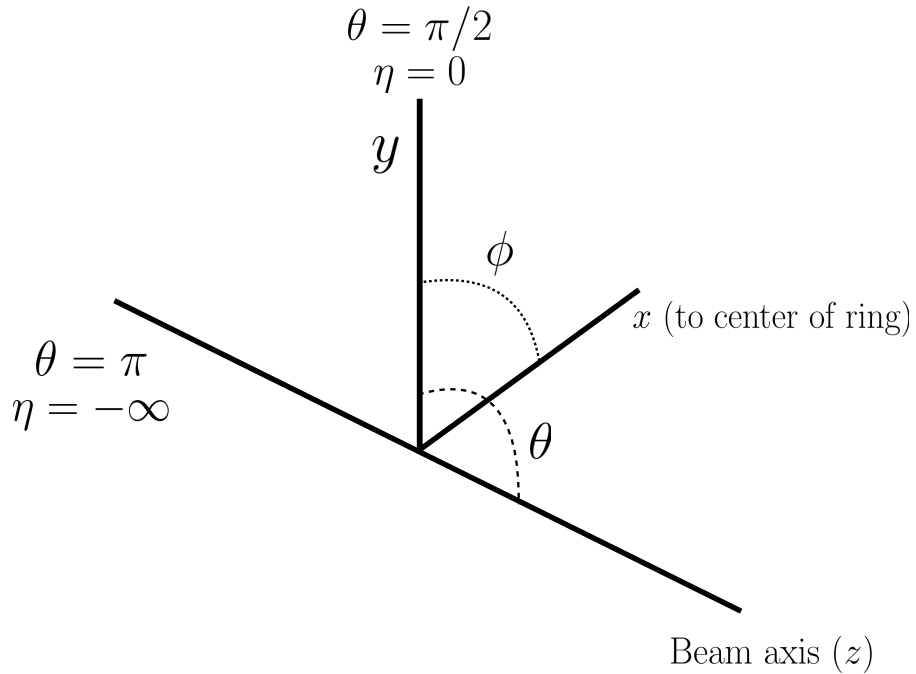


Figure 2.3: The ATLAS coordinate system

851 2.2.2 INNER DETECTOR

852 The ATLAS Inner Detector (ID) system is built for precision tracking of charged particles. It covers
 853 the range $|\eta| < 2.5$. In this range, approximately 1000 particles are generated every bunch crossing in the
 854 detector. This requires having fine granularity to achieve the resolutions required for good momentum
 855 measurement and vertex reconstruction.

856 The ID consists of three sub-components: the pixel detector, semiconductor tracker (SCT), and trans-
 857 sition radiation tracker (TRT). It is surrounded by a solenoid providing a 2 T axial magnetic field which
 858 bends particles in the transverse plane to allow for momentum measurement. Figure 2.4 shows the layout
 859 of each of these components.

860 PIXEL DETECTOR

861 The pixel detector is the first detector particles traverse after being generated in proton collisions and
 862 is the most granular detector. Its operation is crucial for precision tracking and vertex reconstruction as

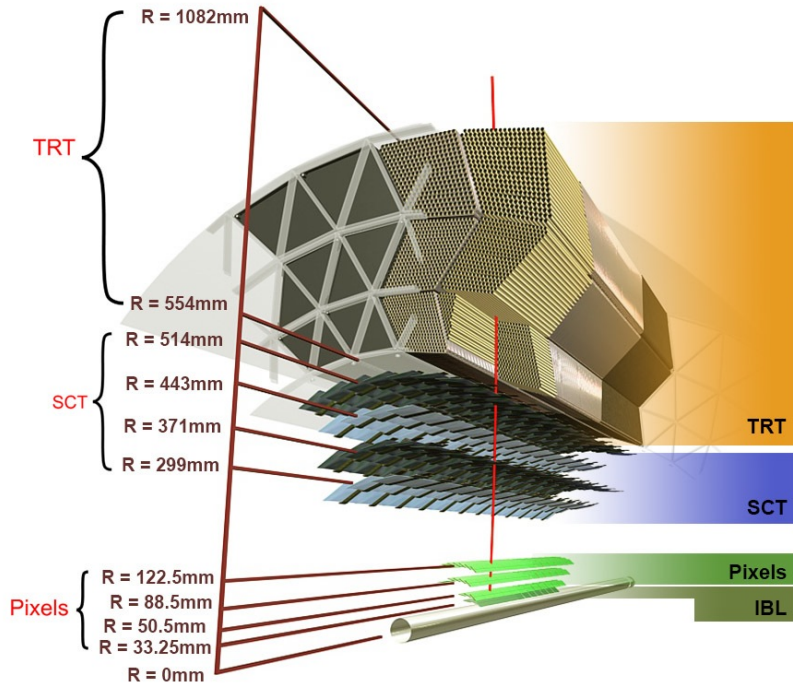


Figure 2.4: Layout of the ATLAS Inner Detector system [40]

well as higher level object reconstruction like tagging of jets from b -quarks. The basic sensing element in this subdetector is a silicon pixel detector. The operating principle for the silicon pixels is that of a p - n junction. When a charged particle passes through, it creates electron-hole pairs that are then separated by the electric field. The sensors are $250\ \mu\text{m}$ thick and use oxygenated n -type wafers with readout pixels on the n^+ side of the detector [32]. Overall, the pixel detector has 1744 sensors and 80.4 million readout channels.

In the barrel region, the pixel detector has three concentric layers of sensors surrounding the beamline. In the endcap region, it consists of disks perpendicular to the beam axis. The detector is segmented in the R - ϕ plane and in z . Usually, three pixel layers are crossed by a charged particle track. The intrinsic accuracies of the sensors are $10\ \mu\text{m}$ in R - ϕ and $115\ \mu\text{m}$ in z (or R for the endcap).

873 INSERTABLE B-LAYER

874 In Run 2, a new innermost pixel layer, known as the insertable B-layer (IBL), was added to the Inner
 875 Detector [41]. This layer was added to cope with the higher luminosities planned in LHC Run 2 and at the

876 high luminosity HL-LHC. Additionally it improves tracking position resolution which in turn improves
877 the vertexing and b -tagging capabilities in ATLAS. The detector sits directly on a new beam pipe, only
878 33.25 mm away from the collision points in the azimuthal plane.

879 **SEMICONDUCTOR TRACKER (SCT)**

880 The semiconductor tracker (SCT) consists of silicon microstrips and comprises the next four layers
881 of the ID. This sub-detector has 6.4cm long sensors that are daisy-chained into strips with a strip pitch
882 of $80\ \mu\text{m}$ [32]. Some of the strips have a small stereo angle to allow for measurement of both angular
883 coordinates. In total there are 6.3 million readout channels. The intrinsic accuracies are $17\ \mu\text{m}$ in $R\text{-}\phi$
884 and $580\ \mu\text{m}$ in z (or R in the endcap).

885 **TRANSITION RADIATION TRACKER (TRT)**

886 The transition radiation tracker (TRT) serves two purposes. First, it consists of 4mm diameter straw
887 tubes filled with a 70/27/3% gas mixture of xenon, carbon dioxide, and oxygen to provide tracking of
888 charged particles. Particles typically have 36 TRT straw tube hits per track. The material in between
889 the straws is designed to induce transition radiation which can be useful for particle identification. As
890 particles pass between media with different dielectric constants, they emit transition radiation that can
891 cause additional showers in the TRT. In particular it is useful for discrimination between electrons and
892 pions or other charged hadrons, as the amount of transition radiation is proportional to the Lorentz factor
893 of the particle.

894 **2.2.3 CALORIMETERS**

895 The calorimeter system consists of two main sub-components: a fine granularity electromagnetic calorime-
896 ter tailored for the measurement of photons and electrons and multiple coarser hadronic calorimeters ded-
897 icated to the measurement of hadronic showers [32]. The calorimeter system has broader coverage than
898 the inner detector, covering the region out to $|\eta| < 4.9$. It is also designed to deliver good containment of
899 showers so as to limit leakage into the muon system. Figure 2.5 shows the layout of the calorimeter system.

900 Both the electromagnetic and hadronic calorimeters are sampling calorimeters. They alternate active
901 material for energy measurement with passive material for energy absorption. The materials used for each
902 purpose vary based on the type of calorimeter and its location in the detector.

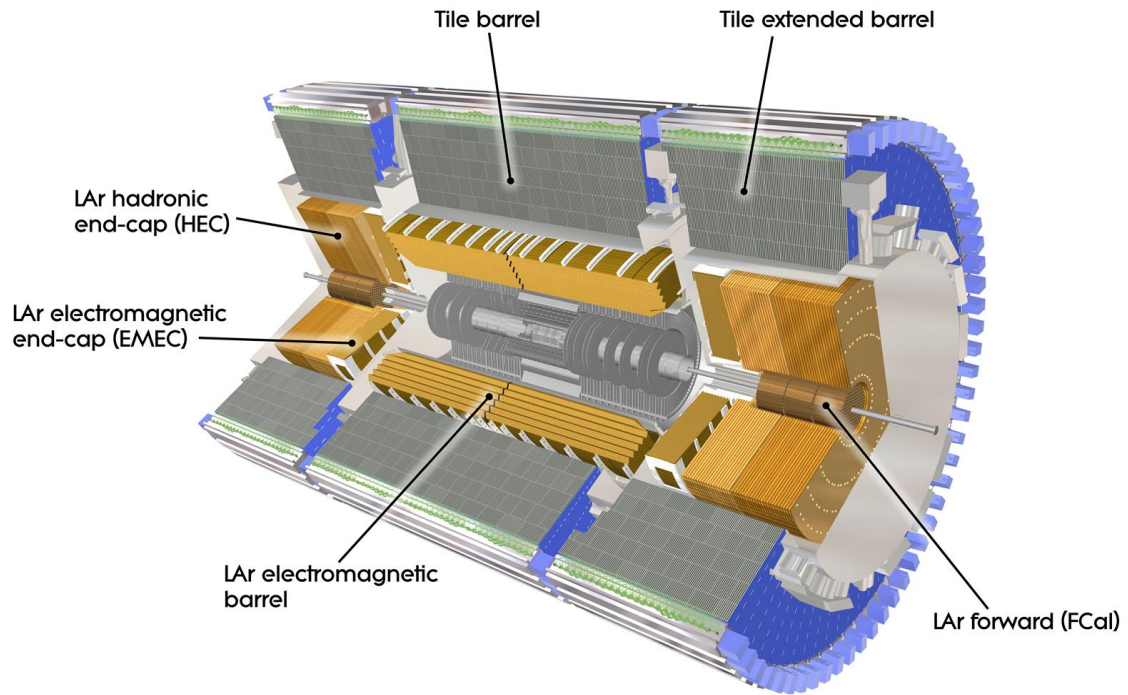


Figure 2.5: Layout of the ATLAS calorimeter system [32]

903 ELECTROMAGNETIC CALORIMETER

904 The electromagnetic calorimeter (EM calorimeter) use liquid Argon (LAr) as its active material and
905 lead as its passive material. It is arrange in an accordion geometry to increase the absorption area while still
906 allowing it to have no azimuthal cracks (complete symmetry in ϕ). The EM calorimeter is divided into a
907 barrel portion that extends to $|\eta| < 1.475$ and an endcap portion going from $1.375 < |\eta| < 3.2$. The
908 region where these two units overlap is called the “transition region”.

909 In order to provide good containment the calorimeter depth must be optimized. Typically, for elec-
910 tromagnetic calorimeters the depth is measured in radiation lengths. In general, the intensity of a par-
911 ticle beam attenuates exponentially in distance with a constant equal to the radiation length. That is,

₉₁₂ $I(x) = I_0 e^{-x/X_0}$, where I is the intensity, x is the distance traveled, and X_0 is the radiation length.
₉₁₃ The ATLAS EM calorimeter is designed to have > 22 radiation lengths in the barrel and > 24 in the
₉₁₄ endcap [32].

₉₁₅ **HADRONIC CALORIMETERS**

₉₁₆ There are three types of hadronic calorimeters present in ATLAS: the tile calorimeter (TileCal), hadronic
₉₁₇ endcap (HEC), and forward calorimeter (FCal). Each one is optimized for stopping of hadronic showers
₉₁₈ and the materials chosen are specific to their placement in the detector.

₉₁₉ The TileCal is a scintillating tile calorimeter placed directly outside the EM calorimeter. It uses steel as
₉₂₀ the absorber and plastic scintillator tiles as the active material. It has coverage in the barrel at $|\eta| < 1.0$
₉₂₁ and in the “extended barrel” region of $0.8 < |\eta| < 1.7$.

₉₂₂ The HEC had two wheels perpendicular to the beam line per endcap and is located directly behind the
₉₂₃ EM calorimeter endcap modules. The HEC covers the region from $1.5 < |\eta| < 3.2$, overlapping slightly
₉₂₄ with both the tile calorimeter and the forward calorimeter. Like the EM calorimeter, it uses liquid Argon
₉₂₅ as the active material, but it uses copper as the absorber.

₉₂₆ The FCal covers the most forward regions of the calorimeter system, extending to the region of $3.1 <$
₉₂₇ $|\eta| < 4.9$. It again uses liquid argon as its active material. For absorber, it consists of an innermost module
₉₂₈ made of copper followed by a module made of tungsten.

₉₂₉ The hadronic equivalent of radiation length is called the interaction length and is denoted as λ . In the
₉₃₀ barrel, the hadronic calorimeter depth is approximately 9.7λ , while in the endcap is 10λ . The outer
₉₃₁ supports contribute an additional 1.3λ . This is been shown to be sufficient to limit punch-through of
₉₃₂ showers to the muon system [32].

₉₃₃ **2.2.4 MUON SPECTROMETER**

₉₃₄ The muon spectrometer is dedicated to measuring the momentum and position of muons. It consists
₉₃₅ of tracking and trigger chambers which are unique in the barrel and endcap regions. The magnetic field
₉₃₆ for bending of muons is provided by a system of three large air-core toroid magnets (from which ATLAS

937 derives its name.) These magnets provide 1.5 to 5.5 Tm of bending power at $0 < |\eta| < 1.4$ and approx-
 938 imately 1 to 7.5 Tm in the endcap region of $1.6 < |\eta| < 2.7$. The entire muon system covers the range
 939 $0 < |\eta| < 2.7$. Monitored drift tubes (MDTs) are used for tracking in the barrel and the two outer layers
 940 of the endcap, while cathode strip chambers (CSCs) are used to provide tracking in the innermost endcap
 941 wheel. In the barrel, resistive plate chambers (RPCs) are used as trigger chambers while thin gap chambers
 942 (TGCs) are used in the endcap. Figure 2.6 shows the layout of the ATLAS muon system. The entire muon
 943 system is designed with the specification of providing a 10% momentum resolution for a 1 TeV muon.

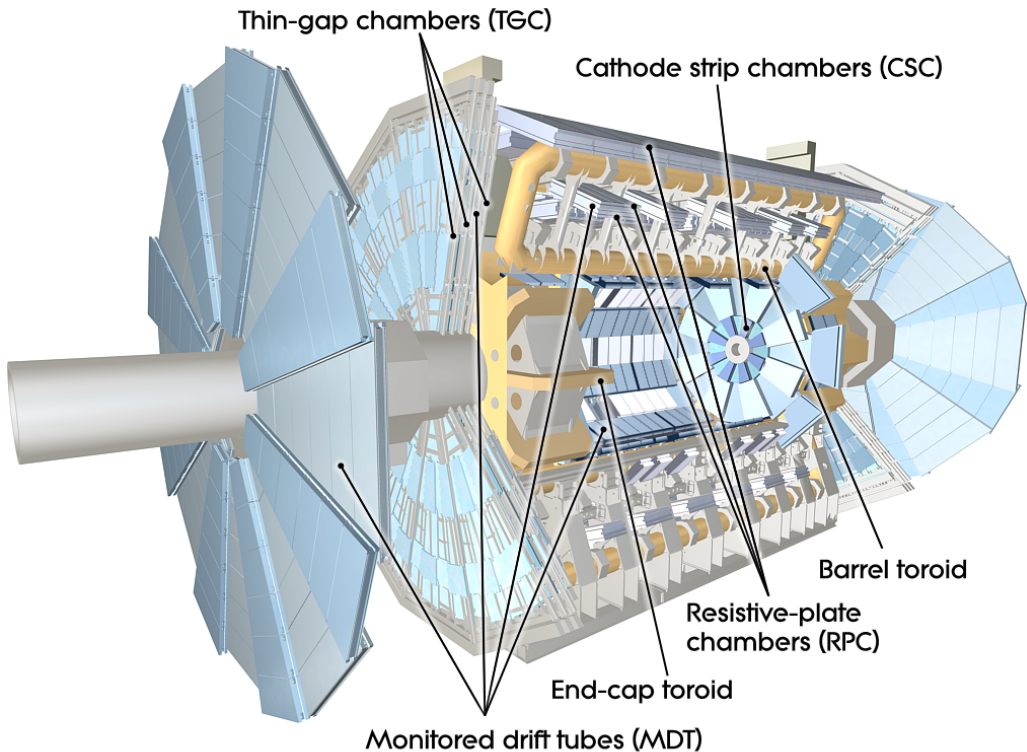


Figure 2.6: Layout of the ATLAS muon system [32]

944 MONITORED DRIFT TUBES (MDTs)

945 The monitored drift tubes (MDTs) are aluminum 3cm diameter tubes filled with a 93/7 % mixture of
 946 Argon and CO₂, with trace amounts of water. As a charged particle traverses the tube, it ionizes the gas
 947 and the ions drift to a wire at the center of the tube. The radial distance of traversal of the particle in the

948 tube is determined by the drift time of the electrons, allowing for fine position resolution. The tubes have
949 an average resolution of $80 \mu\text{m}$ per tube and a maximum drift time of approximately 700ns. The tubes
950 are oriented so that they give precision measurement in η and run along ϕ . They cover $|\eta| < 2.7$, except
951 in the innermost layer of the endcap where they only go to $|\eta| < 2.0$ [32].

952 CATHODE STRIP CHAMBERS (CSCs)

953 The cathode strip chambers cover a narrow window of the innermost endcap region at $2.0 < |\eta| <$
954 2.7. In this region the background rates in the cavern are particularly high and the CSCs are designed to
955 handle these higher rates. The CSCs are multiwire proportional chambers with wires pointing in the radial
956 direction (away from the beam pipe). The wire serves as an anode and there are two types of segmented
957 cathode strip, one perpendicular to the wires which gives the precision measurement and one parallel which
958 provides the transverse coordinate. It has an 80/20 gas mixture of Argon and CO₂ [32].

959 RESISTIVE PLATE CHAMBERS (RPCs)

960 The resistive plate chambers (RPCs) are gaseous electrode-plate detectors covering the region $|\eta| <$
961 1.05. They consist of two resistive plates separated by a distance of 2 mm. The gas mixture used is a
962 94.7/5/0.3% mixture of C₂H₂F₄, Iso-C₄H₁₀, and SF₆. It has readout strips with a pitch of 23-35 mm
963 for both η and ϕ measurement and thus provides measurement of the azimuthal coordinate in the barrel
964 that the MDTs do not. The thin gas gap allows for a quick response time which makes it ideal for use in the
965 trigger. There are three layers of RPCs which are referred to as the three trigger stations. They allow for
966 both a low p_T and high p_T trigger. The coincidence of hits in the innermost chambers allows for triggering
967 of muons between 6 and 9 GeV, while the outermost layer allows the trigger to select high momentum
968 tracks in the range of 9 to 35 GeV [32].

969 THIN GAP CHAMBERS (TGCs)

970 The thin gap chambers (TGCs) are multiwire proportional chambers where the wire to cathode dis-
971 tance (1.4mm) is smaller than the wire-to-wire distance (1.8 mm). They contain a gas mixture of CO₂
972 and *n*-pentane and use a high electric field to gain good time resolution. They serve two functions in the

973 end-cap system. First, they serve as the trigger chambers. Second, they also provide azimuthal coordinate
 974 measurement which the MDTs do not. They sit on the inner and middle layers of the endcap. The outer-
 975 most layer's azimuthal coordinate is determined by extrapolation [32].

976 2.2.5 MAGNET SYSTEM

977 As mentioned previously, there are two independent magnet systems in ATLAS. The first is a 2 T
 978 solenoid field in the inner detector which provides bending in the azimuthal plane. The second is an ap-
 979 proximately 0.5 T toroidal field in the muon system which provides bending in η . Figure 2.7 shows the
 980 predicted field integral as a function of $|\eta|$ [32].

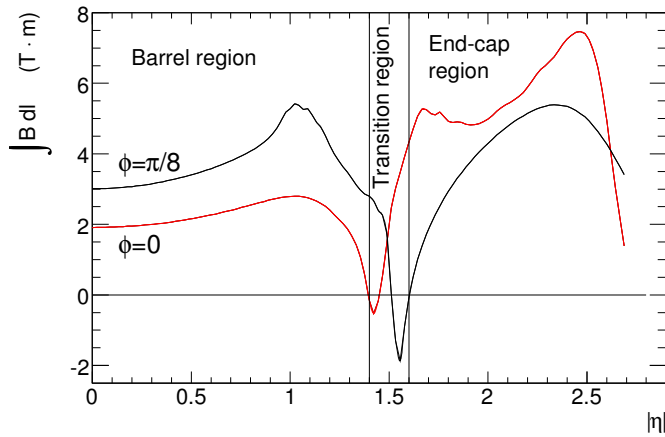


Figure 2.7: Predicted field integral as a function of $|\eta|$ for the ATLAS magnet system [32]

981 2.2.6 TRIGGER SYSTEM

982 The ATLAS trigger system searches for signatures of muons, electrons, photons, hadronically decaying
 983 τ leptons, and jets in order to save these events for further analysis. The trigger system in ATLAS is de-
 984 signed to reduce the maximum LHC event rate of 40 MHz to a more reasonable rate that can be recorded.
 985 The trigger first consists of a fast, hardware based system called the Level-1 (L1) trigger. The L1 trigger
 986 consists of independent dedicated detector sub-components that can seed regions of interest (RoIs) for
 987 further analysis downstream. For muons, the RPCs and TGCs are used, while in the calorimeter coarsely
 988 grained sections of calorimeter cells called towers are used. Once regions of interest are seeded, a software

989 based system called the High Level Trigger (HLT) is used to reconstruct objects and integrate information
 990 from different parts of the detector. In Run 1 of ATLAS, the HLT consisted of two separate stages: the
 991 level 2 (L2) trigger and the event filter (EF).

992 The maximum trigger rate that the L1 trigger can handle is 75 kHz. In the HLT, the rate of events
 993 written to disk is approximately 200 Hz. Figure 2.8 shows the trigger rates for different L1 triggers in 2012
 994 and 2015 for ATLAS [42].

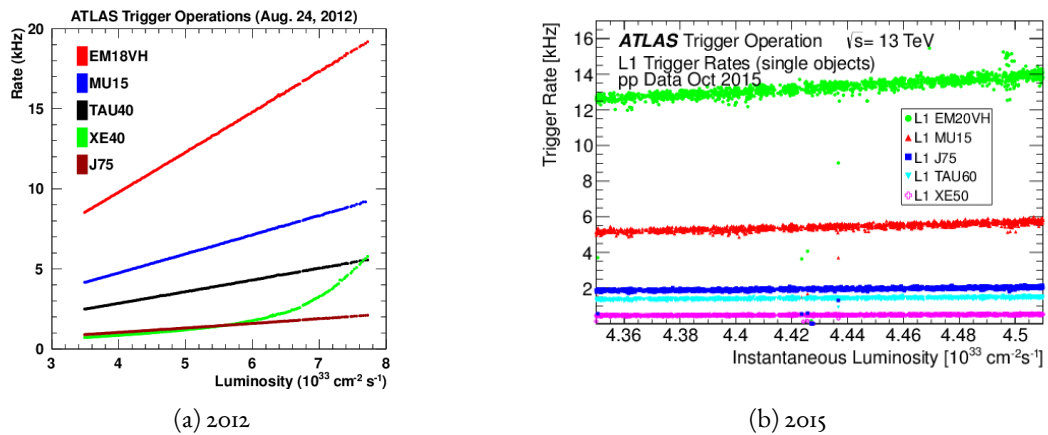


Figure 2.8: ATLAS trigger rates for Level-1 triggers as a function of instantaneous luminosity in 2012 and 2015 operation. These are single object triggers for electromagnetic clusters (EM), muons (MU), jets (J), missing energy (XE), and τ leptons (TAU). The threshold of the trigger is given in name in GeV. [42]

995 2.2.7 ATLAS DATASETS

996 ATLAS has collected data at center of mass energies of 7, 8, and 13 TeV. Figure 2.9 shows the integrated
 997 luminosity as a function of time for each of the three collected datasets. At $\sqrt{s} = 7$ TeV, ATLAS recorded
 998 5.08 fb^{-1} . Increased instantaneous luminosity in 2012 led to a larger dataset of 21.3 fb^{-1} recorded at
 999 $\sqrt{s} = 8$ TeV. After Long Shutdown 1 (LS1) of the LHC and a restart in 2015, ATLAS recorded 3.9 fb^{-1}
 1000 of data at $\sqrt{s} = 13$ TeV. [43, 44]

1001 2.2.8 DETECTOR PERFORMANCE

1002 Table 2.2 summarizes the design requirements for each of the different sub-detectors. This table shows
 1003 the energy and momentum resolution of each tracking, calorimetry, and muon measurements.

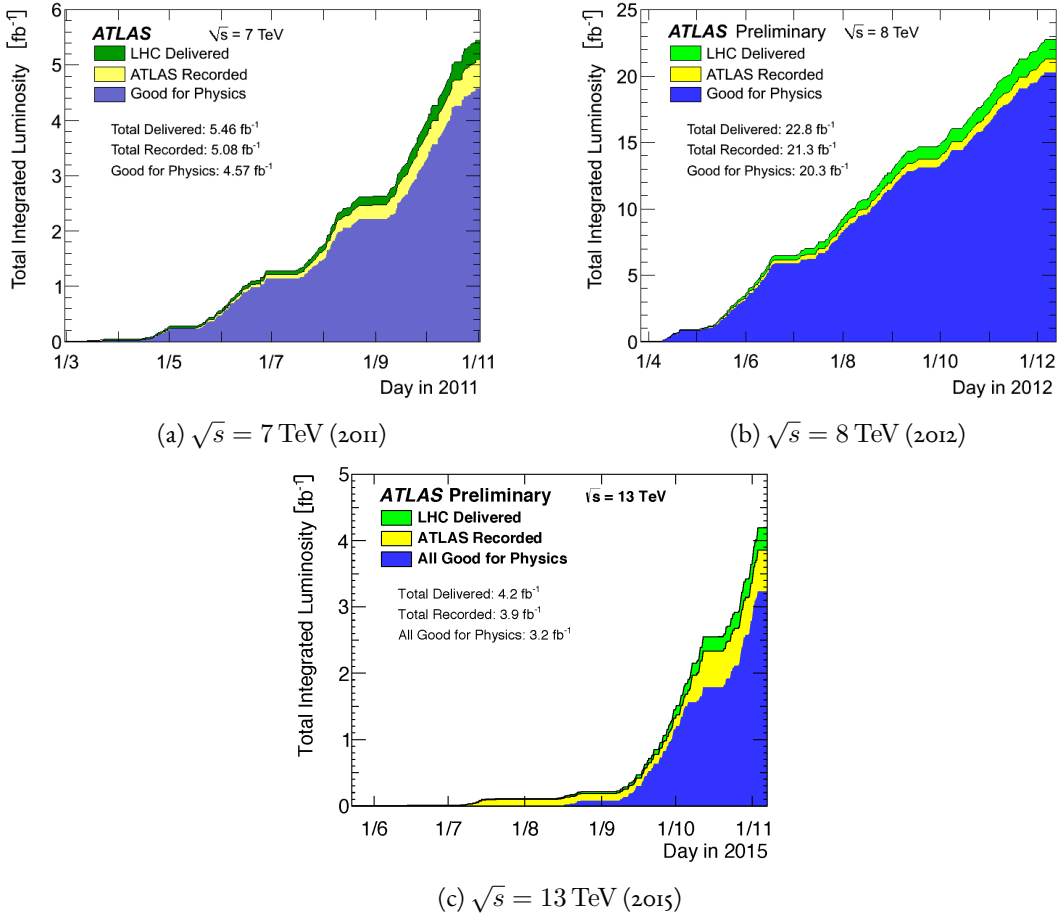


Figure 2.9: Instantaneous luminosity as a function of time for data recorded by ATLAS at different center of mass energies [43, 44]

	Required resolution
Tracking	$\sigma_{p_T}/p_T = 0.05\% p_T \oplus 1\%$
EM calorimetry	$\sigma_E/E = 10\%/\sqrt{E} \oplus 0.7\%$
Hadronic calorimetry	
Barrel and end-cap	$\sigma_E/E = 50\%/\sqrt{E} \oplus 3\%$
Forward	$\sigma_E/E = 100\%/\sqrt{E} \oplus 10\%$
Muon spectrometer	σ_{p_T}/p_T at $p_T = 1 \text{ TeV}$

Table 2.2: Performance requirements for the ATLAS detector [32].

¹⁰⁰⁴ 2.3 THE ATLAS MUON NEW SMALL WHEEL UPGRADE

¹⁰⁰⁵ As the LHC continues operation, it is scheduled to be upgraded in several phases to allow it to reach
¹⁰⁰⁶ higher instantaneous luminosities and thus collect larger datasets. These conditions will open new doors

1007 for study of rare physics processes but will also present interesting challenges that must be faced. ATLAS
 1008 will require new detector technologies to cope with the increased background rates in the cavern in these
 1009 high luminosity conditions. One such upgrade, scheduled to be installed during Long Shutdown 2 (LS2)
 1010 of the LHC in 2018, is the ATLAS Muon New Small Wheel (NSW) upgrade [45]. The NSW will replace
 1011 the innermost end-cap wheel of the muon system with new technologies, as this is the part of the muon
 1012 detector closest to the beam and thus suffers from the highest rates.

1013 2.3.1 MOTIVATION

1014 The motivation of the NSW is two-fold. First, the objective is to alleviate the decreased tracking ef-
 1015 ficiency that comes in a high rate environment. As figure 2.10, at the LHC design luminosity both the
 1016 efficiency of recording hits and reconstructing track segments in the MDTs decreases at the LHC design
 1017 luminosity.

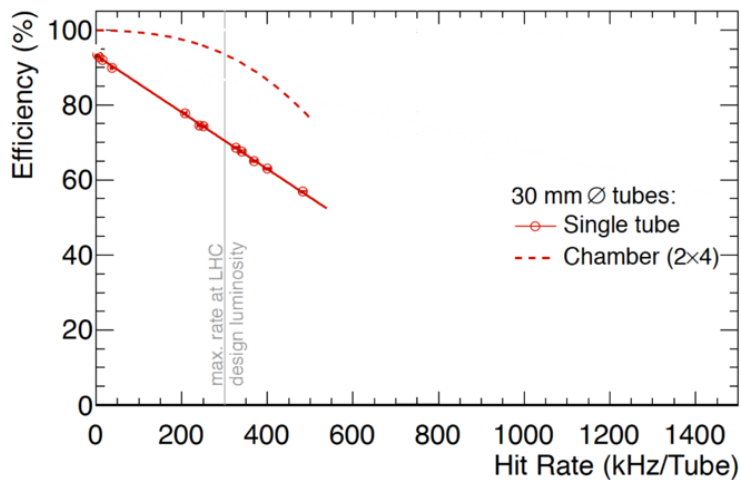


Figure 2.10: MDT tube hit (solid) and segment (dashed) efficiency as a function of hit rate per tube [45]

1018 Second, the NSW will work to alleviate the rate of fake triggers arising in the endcap. Figure 2.11 shows
 1019 the extrapolated trigger rates as a function of the p_T threshold with and without the NSW upgrade. As
 1020 the figure shows, the NSW upgrade will reduce the trigger rate by an order of magnitude compared to the
 1021 current endcap trigger system.

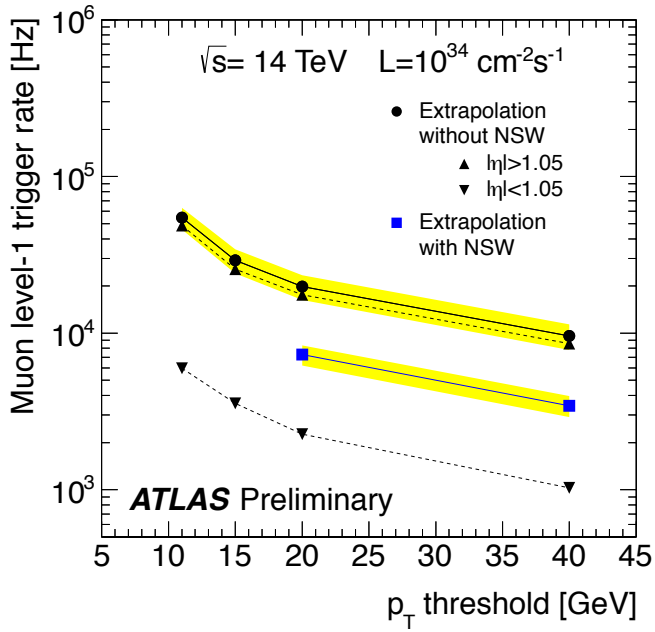


Figure 2.11: Trigger rate as a function of p_T threshold with and without the NSW upgrade [45]

1022 2.3.2 NSW DETECTOR TECHNOLOGIES

1023 The NSW will use two new detector technologies - micromesh gaseous structure detectors (micromegas)
 1024 and small-strip thin gap chambers (sTGCs) [45, 46]. Unlike the previous detectors, both of these detector
 1025 technologies can be used for tracking or trigger. However, the micromegas is more suited to tracking be-
 1026 cause of its good spatial resolution, while the sTGCs have better time resolution and are more suited for
 1027 the trigger. To maintain a fully redundant system, both technologies are used for both purposes.

1028 MICROMEGAS

1029 Micromegas detectors operate using a thin metallic mesh that sits approximately $100\ \mu\text{m}$ away from the
 1030 readout electrodes to create the amplification region. Above this mesh, there is a drift region on the order
 1031 of a few mm in length capped by a drift electrode. As a charged particle traverses the detector, it ionizes gas
 1032 and the electrons drift down towards readout strips. The timing of the drift can be used to reconstruct the
 1033 angle of traversal of the particle. This is illustrated in figure 2.12. The micromegas used in ATLAS will be
 1034 resistive micromegas, where the readout electrodes are topped with resistive strips [47]. This alleviates the

1035 risk of sparking in the large area detectors that ATLAS will use.

1036 In ATLAS, the micromegas drift gap will be 5 mm and the amplification gap will be $128 \mu\text{m}$. They are
1037 filled with the same gas mixture as the MDTs. They will be stacked in an octuplet in an XXUV-UVXX
1038 geometry, where X refers to straight strips and U and V refer to stereo strips at an angle of $\pm 1.5^\circ$. This
1039 arrangement allows for measurement of the azimuthal coordinate and gives a large lever arm between the
1040 straight strips for triggering purposes. Figure 2.12 shows the geometry of a single micromegas detector as
1041 well as its operating principle [45].

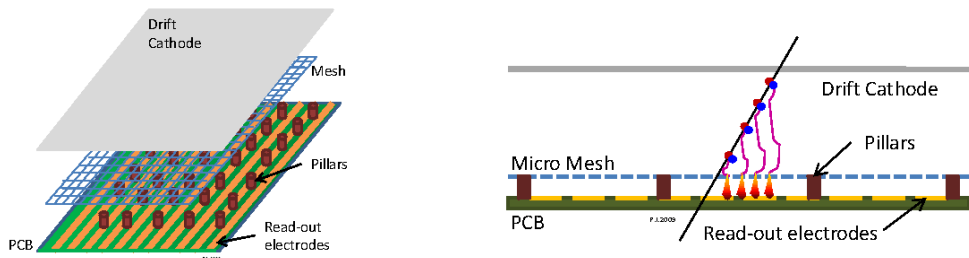


Figure 2.12: Illustrations of the geometry (left) and operating principle (right) of the micromegas detector [45]

1042 sTGCs

1043 The sTGCs are similar to the TGCs already described. They consist of gold-plated tungsten wires with a
1044 1.8 mm pitch between two cathode planes 1.4 mm away from the wire plane. One cathode plane consists
1045 of strips with a 3.2 mm pitch (much smaller pitch than the TGCs), while the other consists of coarser
1046 pads that are used for defining regions of interest in the sTGC trigger algorithm. Figure 2.13 shows the
1047 basic detector geometry.

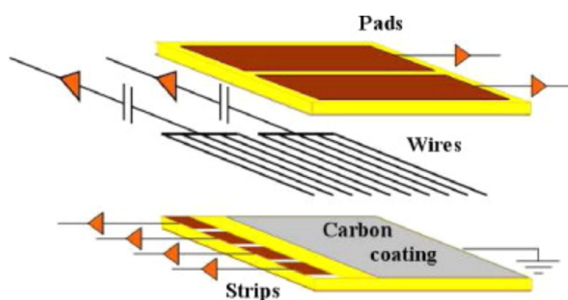


Figure 2.13: Geometry of the sTGC detector [45]

1048 2.3.3 PHYSICS IMPACT

1049 Maintaining low p_T thresholds for muons while still staying within the trigger rate budget at Level 1
1050 (20 kHz) for the muon system is crucial for physics analyses to be successful in high luminosity condi-
1051 tions. One realm where the lepton trigger threshold is especially important is in Higgs physics. In the
1052 $H \rightarrow WW^*$ analysis, one of the W bosons is off shell and tends to decay to soft leptons. In associated
1053 production of a Higgs with a W , the lepton is also important because the lepton provides the main han-
1054 dle which allows the event to be triggered. Table 2.3 shows the impact of increasing the trigger thresholds
1055 on these analyses. It shows that either raising the threshold or using only the barrel both have significant
1056 impacts on the signal efficiency. With the NSW, the signal efficiency is largely maintained and the triggers
1057 can be unprescaled.

Threshold	$H \rightarrow b\bar{b}$ (%)	$H \rightarrow WW^*$ (%)
$p_T > 20 \text{ GeV}$	93	94
$p_T > 40 \text{ GeV}$	61	75
$p_T > 20 \text{ GeV} (\text{barrel only})$	43	72
$p_T > 20 \text{ GeV} (\text{with NSW})$	90	92

Table 2.3: Signal efficiencies for WH production with $H \rightarrow b\bar{b}$ and $H \rightarrow WW^* \rightarrow \mu\nu qq$ under different trigger configurations [45].

1058 2.4 OBJECT RECONSTRUCTION IN ATLAS

1059 ATLAS analyses first start by requiring the presence of certain reconstructed physics objects in the event.
1060 This section will present a brief overview of the algorithms used to reconstruct electrons, muons, jets (in-
1061 cluding b -jets), and missing energy¹. The performance of object reconstruction and measurement will also
1062 be discussed as these are relevant to the analyses presented later. Figure 2.14 gives an overview of the differ-
1063 ent sub-detectors that each type of particle will interact with in ATLAS.

¹Reconstruction algorithms for other objects, such as photons and τ leptons, are not detailed here as these objects are not used in the presented studies.

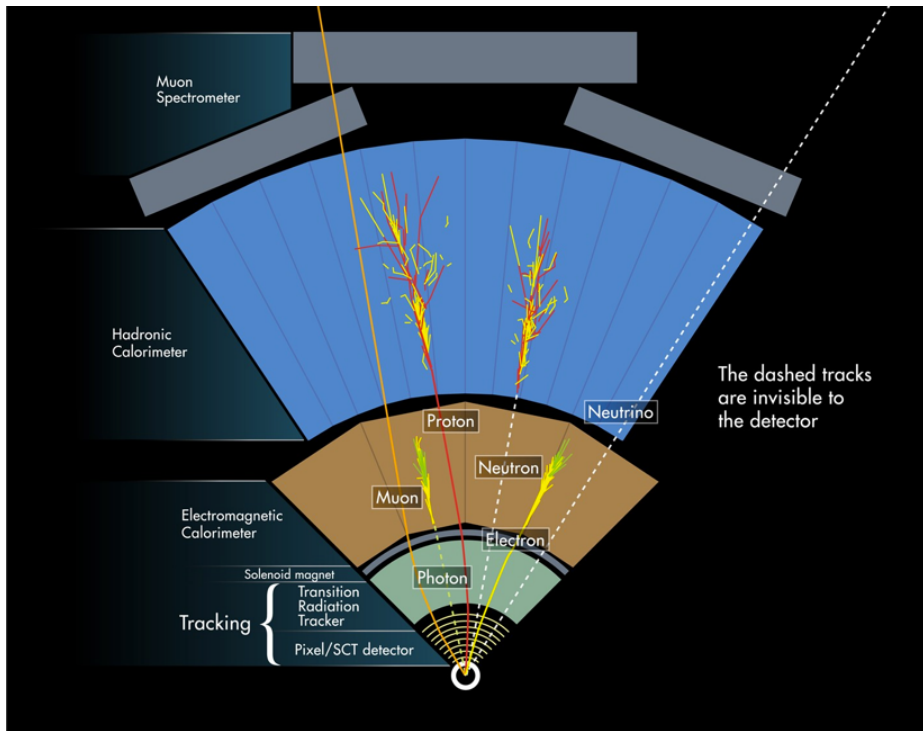


Figure 2.14: Illustration of particle interactions in ATLAS [48]

1064 2.4.I ELECTRONS

1065 Electrons in ATLAS will leave tracks in the inner detector and energy deposits in the electromagnetic
 1066 calorimeter. The algorithm for recognizing the signature of electrons proceeds in two steps: reconstruction
 1067 and identification.

1068 In reconstruction, an electron candidate is formed by matching EM calorimeter deposits with ID tracks.
 1069 The algorithm first chooses seed clusters in the EM calorimeter by using a sliding window algorithm that
 1070 searches for towers with transverse energy larger than 2.5 GeV. In addition to seed clusters, track candi-
 1071 dates must be identified in the ID. The algorithm selects seed tracks with $p_T > 1$ GeV that do not fit
 1072 well with a pion hypothesis. Once candidate tracks are selected, they are re-fit with a Gaussian Sum Filter
 1073 (GSF) algorithm to estimate electron parameters [49]. Finally, an electron candidate is formed if at least
 1074 one track matches to a seed cluster in the calorimeter. The full details of the reconstruction algorithm can
 1075 be found in reference [50].

1076 Once an electron candidate is present, identification criteria must be applied in order to reject fake elec-

1077 trons from background. Many different variables are used for this identification, most of them related to
 1078 the shower shape in the EM calorimeter and the amount of leakage into the hadronic calorimeter, as well
 1079 as information from the ID and in particular the TRT. There are both cut-based and likelihood-based
 1080 criteria that range from “loose” to “very tight”. For details, see reference [50].

1081 Figure 2.15 shows the algorithm’s reconstruction efficiency of true electrons for different identification
 1082 criteria as well as the electron energy resolution in simulation [50, 51]. The reconstruction efficiency is
 1083 measured using both Z and J/ψ tag and probe techniques.

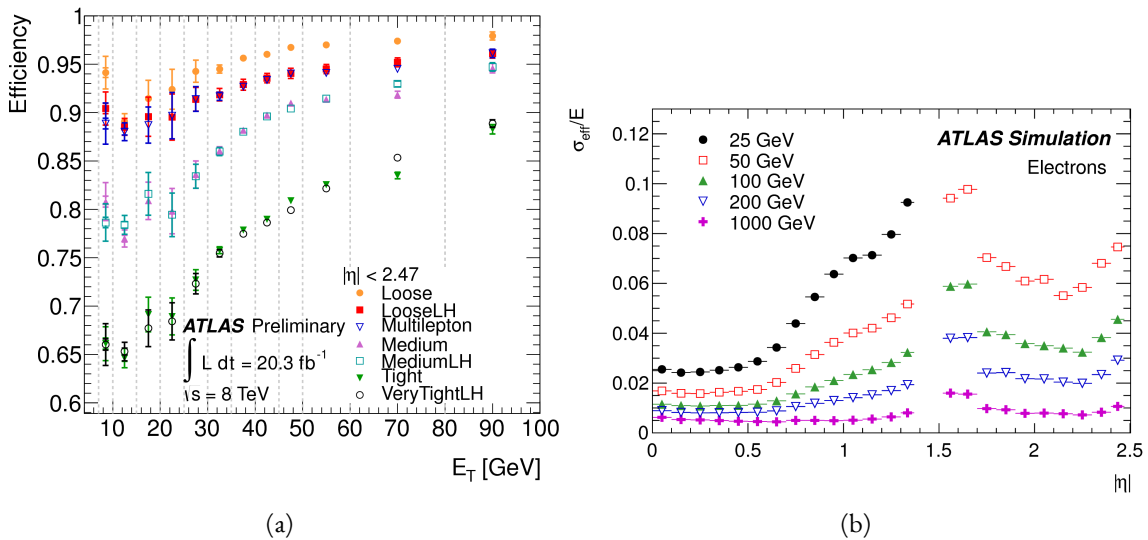


Figure 2.15: Electron performance: (a) reconstruction efficiency as a function of electron E_T [50] (b) energy
 resolution in simulation as a function of $|\eta|$ for different energy electrons [51]

1084 2.4.2 MUONS

1085 The ATLAS detector is designed to stop most particles before they reach the muon spectrometer. Muons,
 1086 however, are minimum ionizing particles, meaning that they will not lose a significant amount of energy
 1087 through interactions with the detector and will thus pass through. Therefore, the muon reconstruction
 1088 works to match tracks in the muon spectrometer with tracks in the inner detector.

1089 The first step of reconstruction is to reconstruct local straight line tracks, called segments, in each muon
 1090 chamber. Segments are then fit to larger tracks that traverse the entire muon spectrometer. Such muon
 1091 tracks are referred to as “standalone” tracks (SA) as they only use information from the muon spectrometer.

1092 The standalone tracks are then matched to tracks in the inner detector to form “combined” (CB) muons,
 1093 where the combined ID and MS fit are used to determine the momentum and direction of the muon. To
 1094 improve acceptance, segment-tagged and calorimeter-tagged muons are also reconstructed. In these cases,
 1095 ID tracks are matched to segments in the MS and calorimeter deposits consistent with a minimum ionizing
 1096 particle, respectively. The details of the reconstruction can be found in reference [52].

1097 As with electrons, once muon candidates are reconstructed they have identification criteria applied to
 1098 reduce background. These criteria include the χ^2 match between the ID and MS tracks, the number of
 1099 hits in the ID, overall ID and MS track fit quality, and additional variables [52]. The criteria range from
 1100 “loose” to “tight” as with electrons.

1101 Figure 2.16 shows the muon reconstruction efficiency (measured with Z and J/ψ tag and probe) and
 1102 invariant mass resolution [52].

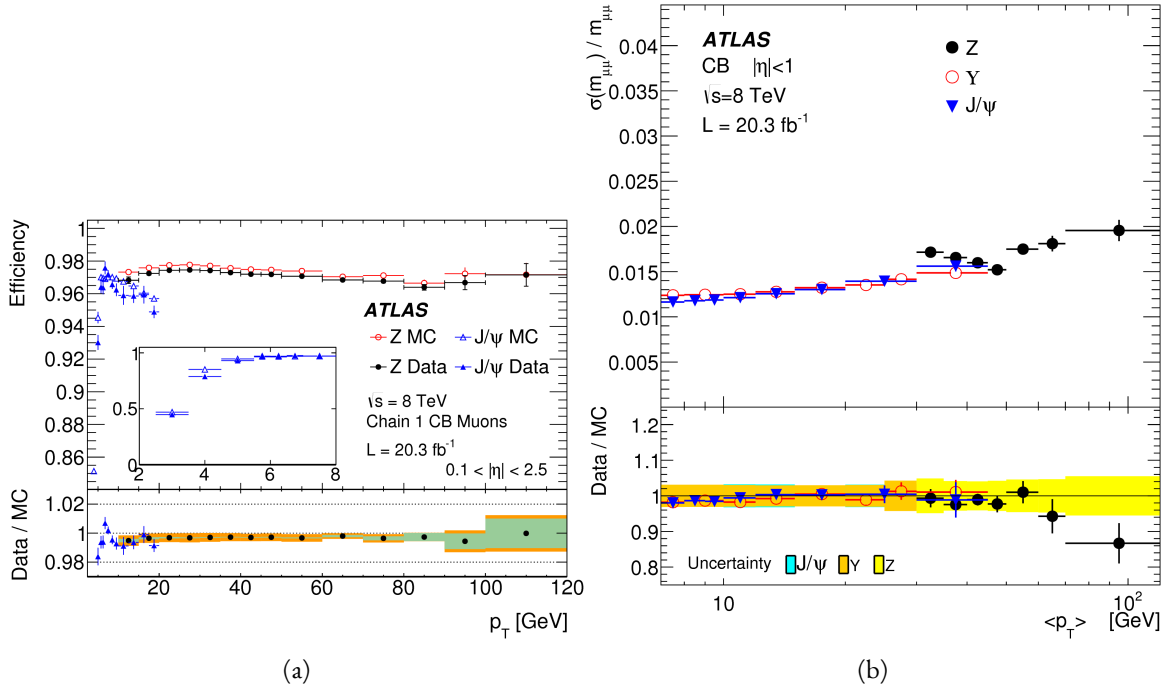


Figure 2.16: Muon performance: (a) reconstruction efficiency as a function of muon p_T (b) dimuon mass resolution as a function of average p_T [52]

1103 2.4.3 JETS

1104 When a quark or gluon is produced in collisions, it is not measured directly in ATLAS. Rather, due to
1105 QCD effects, it produces a collimated spray of hadrons in the direction of the original parton, which is
1106 known as a jet. Jets are reconstructed in ATLAS using energy deposits in the hadronic calorimeter. The
1107 first step is build “topological clusters” out of energy deposits in calorimeter cells [53, 54]. This is done
1108 using strategy where seed cells are chosen by picking cells whose energy measurements are four times the
1109 amount of noise expected for that cell. Adjacent cells with at least 2σ energy measurements are added to
1110 the cluster, then a final layer of clusters with energy above 0σ are added. Once calorimeter clusters are
1111 formed, they are clustered further into jet candidates using the anti- k_T jet clustering algorithm [55]. This
1112 algorithm uses a parameter R that appears in the denominator of the clustering distance metric and defines
1113 the radial size of the jet in η - ϕ space.

1114 The energy response of the calorimeter must be properly characterized in order to reconstruct jet energy.
1115 Calorimeter clusters can be calibrated either with the EM calibration, where each cluster is assumed to have
1116 come from the energy deposit of an electron or photon, or the LCW calibration, where local cluster weights
1117 are computed to allow for local calibration of clusters as hadronic or electromagnetic. The details of the
1118 jet energy calibration are not detailed here and are discussed in reference [56].

1119 Figure 2.17 shows the jet energy response after calibration in Monte Carlo as a function of the true p_T
1120 of the jet [56].

1121 2.4.4 b -TAGGING

1122 One important aspect of jet physics is the task of identifying the flavor of parton that produced the
1123 measured jet. While in general this is very difficult, jets from b -quarks offer an interesting case where such
1124 identification is possible. B mesons have a lifetime on the order of 10^{-12} seconds, which makes a $c\tau$ on
1125 the order of millimeters [6]. This type of displaced decay vertex can be identified in detectors like ATLAS
1126 and allows b -jets to be distinguished from other flavors of jets².

²Jets from charm quarks can also be detected in this way but they do not live quite as long so the displacement of the vertex is harder to distinguish

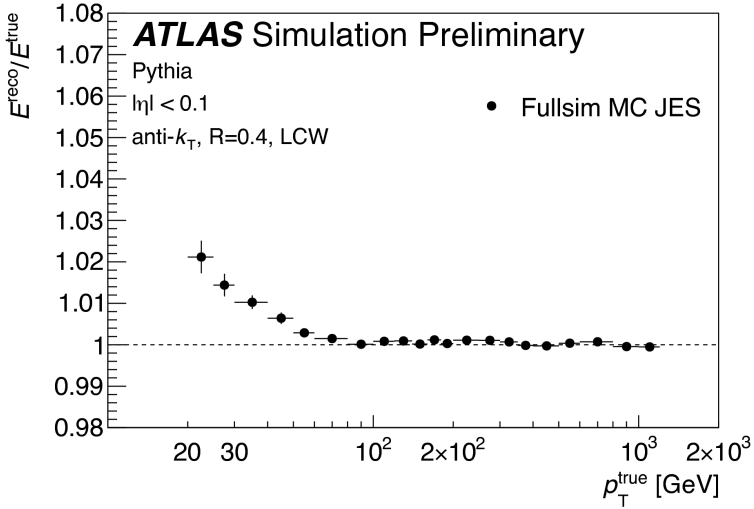


Figure 2.17: Jet energy response after calibration as a function of true p_T in simulation [56]

1127 ATLAS uses a multivariate machine learning algorithm to identify jets from b -quarks. The inputs to this
 1128 algorithm are determined from lower level reconstruction algorithms. There are three distinct algorithms
 1129 that reconstruct variables which are used as input to the multivariate technique.

1130 The first family is referred to as IPxD (where the x can either be 2 or 3). These algorithms use the trans-
 1131 verse and longitudinal impact parameters d_0 and z_0 of the tracks inside a jet to determine their consistency
 1132 with the primary vertex. They two or three dimensional (hence the x) templates for light flavor, charm,
 1133 and bottom jets and then evaluate the likelihood of the jet coming from each of these types. The likelihood
 1134 ratios are used as inputs to the multivariate algorithm.

1135 The next two algorithms used as input are referred to as the secondary vertex (SV) and JetFitter (JF)
 1136 algorithms. The SV algorithm uses tracks inside the jet to fit for vertices that are displaced from the pri-
 1137 mary vertex. The JF algorithm attempts to reconstruct the full flight path of the b by looking for multiple
 1138 displaced vertices along the same line (as B decays often result in subsequent c decays).

1139 In Run 1, the multivariate b -tagging algorithm used a neural network and was referred to as MV1.
 1140 The details of this algorithm and its inputs are given in reference [57]. In Run 2, the number of inputs
 1141 was simplified and a boosted decision tree with 24 input variables was used, referred to as MV2 [58]. The
 1142 MV2 algorithm is a boosted decision tree incorporating twenty-four input variables constructed from three

¹¹⁴³ lower level input algorithms described above. Figure 2.18 summarizes the inputs to MV2. Figure 2.19 shows
¹¹⁴⁴ the performance of each of these algorithms.

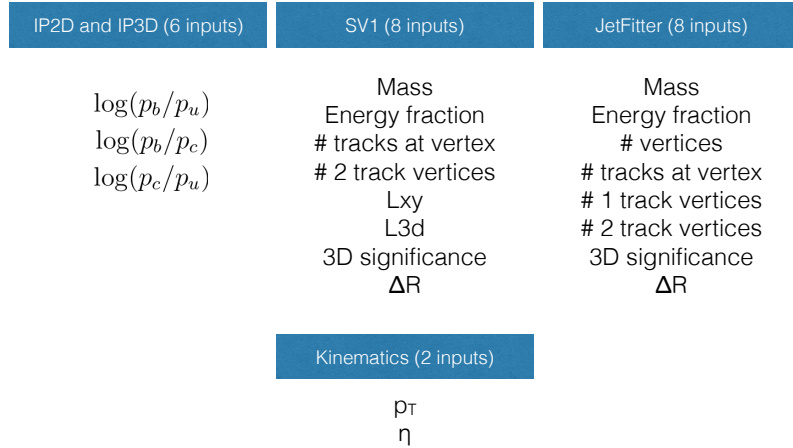


Figure 2.18: Summary of the inputs to the MV2 b -tagging algorithm

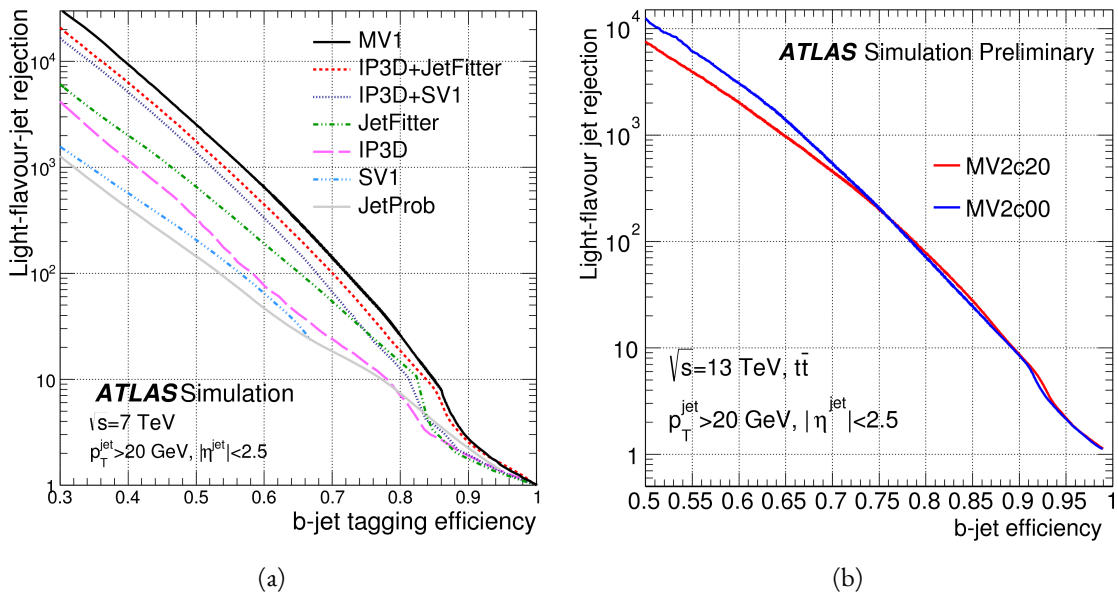


Figure 2.19: Light jet rejection (1/efficiency) vs. b -jet efficiency for MV1 and its input algorithms (a) [57] and MV2 (b) [58] in simulated $t\bar{t}$ events. The numbers in the algorithm names in (b) refer to the fraction of charm events used in the MV2 training.

1145 2.4.5 MISSING TRANSVERSE ENERGY

1146 As noted in figure 2.14, neutrinos produced in ATLAS will pass through the detector without interact-
1147 ing. The only way of detecting the presence of particles like neutrinos (or BSM particles that are long-lived)
1148 is to use missing transverse momentum. The basic principle of missing transverse energy is to use the mo-
1149 mentum balance of the incoming protons to infer the presence of missing particles. The net longitudinal
1150 momentum of the incoming partons that collide is not known (since each carries an unknown fraction of
1151 the proton's momentum). However, the protons (and thus incoming partons) have no net momentum
1152 in the plane transverse to the beam line (the x - y) plane. Therefore, if there are no un-measured particles
1153 in the final state, the transverse momenta of all of the final state particles should balance. The magnitude
1154 of this imbalance is known as missing transverse momentum (E_T^{miss}).

1155 The basic calculation of missing transverse momentum from calorimeter cells is given in equation 2.4 [59].

1156

$$\begin{aligned} E_x^{\text{miss}} &= -\sum_{i=1}^{N_{\text{cell}}} E_i \sin \theta_i \cos \phi_i \\ E_y^{\text{miss}} &= -\sum_{i=1}^{N_{\text{cell}}} E_i \sin \theta_i \sin \phi_i \end{aligned} \quad (2.4)$$

1157 The E_T^{miss} calculation is separated into different terms based on the objects that the calorimeter clusters
1158 are associated with. This way, each cell's contribution is calibrated appropriately according to the object.
1159 This separation of terms is shown in equation 2.5 [59].

$$\begin{aligned} E_{x(y)}^{\text{miss,calo}} &= E_{x(y)}^{\text{miss},e} + E_{x(y)}^{\text{miss},\gamma} + E_{x(y)}^{\text{miss},\tau} + E_{x(y)}^{\text{miss,jets}} \\ &\quad + E_{x(y)}^{\text{miss,softjets}} + E_{x(y)}^{\text{miss},\mu} + E_{x(y)}^{\text{miss,CellOut}} \end{aligned} \quad (2.5)$$

1160 The CellOut term of the above equation corresponds to calorimeter cells with energy deposits that are
1161 not associated with other objects. The soft jets term comes from cells associated to jets with p_T between
1162 7 and 20 GeV, while the jets term comes from jets with $p_T > 20$ GeV. Because muons do not deposit
1163 significant energy in the calorimeter, the muon momentum is used for the muon term [59]. The final
1164 E_T^{miss} is calculated using equation 2.6.

$$E_T^{\text{miss}} = \sqrt{(E_x^{\text{miss}})^2 + (E_y^{\text{miss}})^2} \quad (2.6)$$

1165 Figure 2.20 shows the resolution of the components of the E_T^{miss} under different pileup suppression techniques [60].

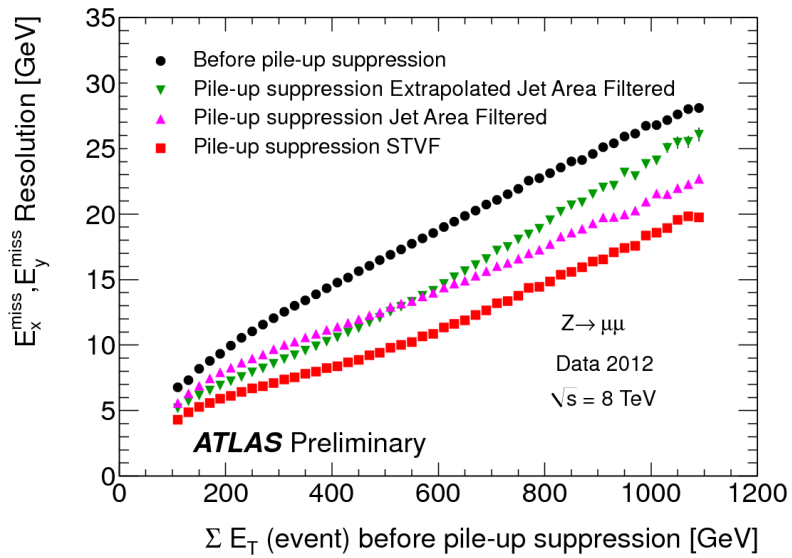


Figure 2.20: Resolution of E_T^{miss} components as a function of $\sum E_T$ before pileup suppression with different pileup techniques [60]

1166

Part II

1167

Observation and measurement of Higgs

1168

boson decays to WW^* in LHC Run I at

1169

$\sqrt{s} = 7$ and 8 TeV

1170

*Basic research is what I am doing when I don't know what
I am doing.*

Wernher von Braun

3

1171

1172 $H \rightarrow WW^* \rightarrow \ell\nu\ell\nu$ Analysis Strategy

1173 3.1 INTRODUCTION

1174 This chapter presents an overview of the strategy for searching for a Higgs boson in the $H \rightarrow WW^* \rightarrow$
1175 $\ell\nu\ell\nu$ decay topology. Its purpose is to define in broad terms how the search and measurement are under-
1176 taken, before going into details on the specific sub-categories within the larger analysis. First, the properties
1177 of the Higgs signal are discussed and the associated backgrounds are presented. Next, the observables used
1178 to enhance the signal to background ratio are defined. Finally, the parameters of interest in the search
1179 and measurement will be shown, along with a brief overview of the statistical treatment of the final Higgs
1180 candidates.

1181 Following this chapter, the results of three different studies within the $H \rightarrow WW^* \rightarrow \ell\nu\ell\nu$ channel
1182 are shown. Chapter 4 presents a search for Higgs boson production in gluon fusion mode and the role of
1183 the $H \rightarrow WW^*$ channel in its discovery. Chapter 5 shows the search and first observation in ATLAS of
1184 the Vector Boson Fusion (VBF) production mode of the Higgs in the $H \rightarrow WW^*$ decay channel. Finally,

1185 chapter 6 shows the combined Run 1 $H \rightarrow WW^*$ results for the measurement of the Higgs cross section
1186 and relative coupling strengths to other SM particles.

1187 3.2 THE $H \rightarrow WW^* \rightarrow \ell\nu\ell\nu$ SIGNAL IN ATLAS

1188 The signal studied in this and subsequent chapters is the Higgs boson in the WW^* final state, where
1189 each W boson subsequently decays into a charged lepton and a neutrino. In the simplest decay path, the
1190 final state consists of two neutrinos and two charged leptons, each of which can be either an electron or a
1191 muon. If a W decays to a τ lepton, only leptonic decays of the τ are considered. The τ lepton produce
1192 additional neutrinos in the final state but still yield two charged leptons (where each lepton is an electron or
1193 muon). Neutrinos are not detected in ATLAS, so the final state ultimately consists of two reconstructed
1194 leptons and missing transverse momentum (denoted as E_T^{miss}). Final states where both of the charged
1195 leptons are electrons or muons are referred to as the “same flavor” ($ee/\mu\mu$) final states, while those with
1196 one electron and one muon are referred to as “different flavor” ($e\mu$ or μe).

1197 There can be additional jets produced in association with the Higgs boson. As described in detail in
1198 Chapter 1, if the Higgs is produced via vector boson fusion production, there will be two additional forward
1199 jets in the event. In gluon fusion, one or more jets can be produced through initial state radiation from
1200 the incoming gluons. Because of the varying background composition as a function of jet multiplicity,
1201 each bin in this variable has its own dedicated requirements applied in the search and measurement. The
1202 $n_j = 0$ and $n_j = 1$ bins are dedicated to gluon fusion production, while the $n_j \geq 2$ bin has separate
1203 dedicated searches for ggF and VBF production.

1204 Figure 3.1 shows the relative branching fractions for the $H \rightarrow WW^*$ process, calculated from the Par-
1205 ticle Data Group values for the W and τ branching ratios [6]. The largest branching ratio corresponds
1206 to both W bosons decaying to quark pairs at 45.44%. The second largest ratio is for one W decaying lep-
1207 tonically and the other decaying to quarks, a branching ratio of 34.18%. In all cases, ℓ denotes either an
1208 electron or muon, and the leptonic branching ratios of the τ are included. For example, the $\ell\nu qq$ final
1209 state includes one W decaying to $e\nu$, $\mu\nu$, or $\tau\nu$. In the case of the $W \rightarrow \tau\nu$ decay, the τ lepton then
1210 decays to an electron or muon via $\tau \rightarrow \nu_\tau \ell \nu_\ell$. Final states with a τ_h refer to hadronic decays of the τ . The

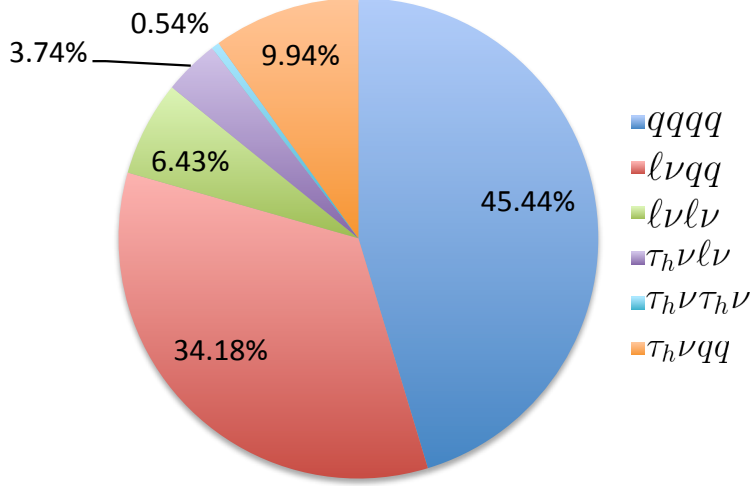


Figure 3.1: Branching ratios for a WW system. q refers to quarks. ℓ can be either an electron or muon, and the leptonic branching ratios of the τ are included. For example, the $\ell\nu qq$ final state includes one W decaying to $e\nu$, $\mu\nu$, or $\tau\nu$. τ_h refer to hadronic decays of the τ .

branching ratio of the $\ell\nu\ell\nu$ final state is 6.43%.

While the $\ell\nu\ell\nu$ final state is not a large fraction of the branching ratio, there are significant advantages to using this channel in an analysis. First, both the $qqqq$ and $\ell\nu qq$ channels suffer from a large QCD multijet background, which is often difficult to model. Second, events in the the $\ell\nu\ell\nu$ channel in data can be triggered more efficiently due to the presence of two leptons.

3.3 BACKGROUND PROCESSES

Many processes from the Standard Model can also produce a final state with two leptons and missing transverse momentum. This section describes the dominant backgrounds to Higgs production and further explains how they can be reduced. Table 3.1 summarizes the different background processes.

3.3.1 STANDARD MODEL WW PRODUCTION

Non-resonant Standard Model diboson production, as shown in figure 3.2, is an irreducible background to Higgs boson production in the WW final state. It produces the same exact final state objects, namely

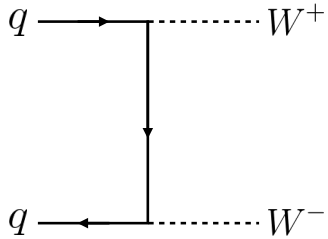


Figure 3.2: Feynman diagram for Standard Model WW production

leptonically decaying W bosons. There are no additional objects in the final state that allow for background reduction. Therefore the analysis solely relies on the correlations between the leptons to reduce this background.

3.3.2 TOP QUARK PRODUCTION

Top quark production can mimic the Higgs in the WW^* final state as well. Top quarks can be produced either in pairs ($t\bar{t}$ production) or singly (s -channel, t -channel, or associated production Wt). The dominant top background are $t\bar{t}$ and Wt production.

Because top quarks decay via $t \rightarrow Wb$, top pair production can produce a final state with two W bosons that then decay leptonically. In Wt production, there are two real W bosons produced, as with $t\bar{t}$. In both cases, there is at least one b -jet in the final state. By vetoing on the presence of b -jets, these top quark backgrounds can be reduced. Figure 3.3 shows the Feynman diagrams for $t\bar{t}$ and Wt production.

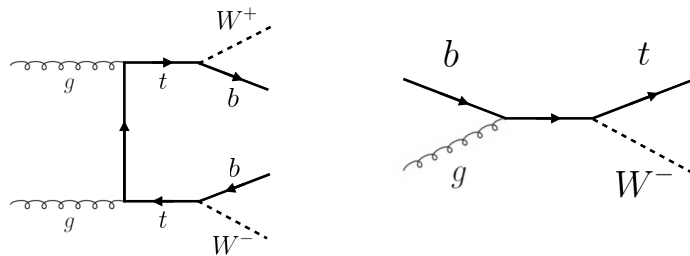


Figure 3.3: Feynman diagrams for top pair production (left) and Wt production (right)

1234 3.3.3 W +JETS BACKGROUND

1235 Single W boson production in association with jets is a unique background to Higgs production. The
1236 other backgrounds considered thus far have all included two prompt leptons, each decaying from a W
1237 boson, in the final state. In W +jets production, however, only one reconstructed lepton originates from
1238 a W . The second reconstructed lepton is either an algorithmic “fake” or the result of non-prompt decays.
1239 In the first case, the lepton is a jet misidentified as a lepton by either the electron or muon reconstruction
1240 algorithms. In the second case, the lepton may be a real lepton but coming from semi-leptonic decays of
1241 particles inside the shower of the jet. This background can be reduced by requiring that the reconstructed
1242 lepton have little activity in the surrounding region of the calorimeter (also known as an “isolation”). Fig-
1243 ure 3.4 shows the Feynman diagram for W +jets production.

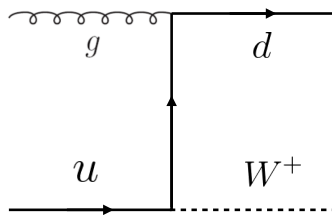


Figure 3.4: An example Feynman diagram of W +jets production

1244 3.3.4 Z/γ^* +JETS BACKGROUND

1245 Production of a Z boson or virtual photon (also known as Drell-Yan and denoted with Z/γ^*) in as-
1246 sociation with jets is also a background to Higgs production. The Z boson decays to two leptons of the
1247 same flavor. When the Z/γ^* decays directly to electrons or muons, the background enters the same flavor
1248 final state. When the Z decays to two τ leptons the background can enter the different flavor final state as
1249 well. Figure 3.5 shows the production of a Z in association with one jet. Because there are no neutrinos in
1250 this final state, variables like E_T^{miss} can be used to reduce the background¹.

¹The E_T^{miss} cut is much more effective for the reduction of Z/γ^* production in the same flavor final state. If the background enters the different flavor final state through τ decays, there will be neutrinos present. Other requirements on the lepton invariant mass are made to reduce the $Z/\gamma^* \rightarrow \tau\tau$ background.

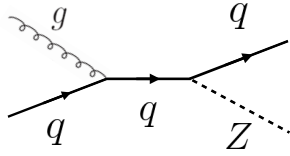


Figure 3.5: An example Feynman diagram of $Z + \text{jets}$ production

1251 3.3.5 SUBDOMINANT BACKGROUNDS

1252 There are additional processes which contribute to the background composition. These backgrounds
 1253 are subdominant and contribute less to the total background estimate than those discussed previously.
 1254 The first process is referred to as VV or “Other diboson” processes and includes multiple Standard Model
 1255 diboson processes, including WZ , ZZ , $W\gamma$, $W\gamma^*$, and $Z\gamma$ production. Additionally, there is a back-
 1256 ground contribution from QCD multijet production. While the cross section for this process is large, its
 1257 contribution to the WW^* final state is small because two jets must be misidentified as leptons.

Category	Process	Description
SM WW	$WW \rightarrow \ell\nu\ell\nu$	Real leptons and neutrinos
Top quark production	$t\bar{t} \rightarrow WbWb \rightarrow \ell\nu b\bar{\nu} b$	Real leptons, untagged b s
	$tW \rightarrow WbW \rightarrow \ell\nu\ell\nu b$	Real leptons, untagged b
	$t\bar{b}, t\bar{q}\bar{b}$	Untagged b , jet misidentified as lepton
Drell-Yan	$Z/\gamma^* \rightarrow ee, \mu\mu$	“Fake” E_T^{miss}
	$Z/\gamma^* \rightarrow \tau\tau \rightarrow \ell\nu\ell\nu\nu$	Real leptons and neutrinos
Other dibosons	$ZZ \rightarrow \ell\ell\nu\nu$	Real leptons and neutrinos
	$W\gamma^*, WZ \rightarrow \ell\nu\ell\ell, ZZ \rightarrow \ell\ell\ell\ell$	Unreconstructed leptons
	$W\gamma, Z\gamma$	γ reconstructed as e , unreconstructed lepton
$W + \text{jets}$	$Wj \rightarrow \ell\nu j$	Jet reconstructed as lepton
QCD multijet	jj	Jets reconstructed as leptons

Table 3.1: A summary of backgrounds to the $H \rightarrow WW^* \rightarrow \ell\nu\ell\nu$ signal

1258 3.4 SHARED SIGNAL REGION SELECTION REQUIREMENTS

1259 As presented in section 3.2, there are many different combinations of physics objects that can define a
 1260 $H \rightarrow WW^* \rightarrow \ell\nu\ell\nu$ final state. The multiplicity of jets and the flavor combinations of the leptons

1261 both lead to many potential signal regions. Additionally, signal regions can be optimized separately to be
 1262 sensitive to the distinct production modes of the Higgs. Gluon fusion, vector boson fusion, and associated
 1263 production of a Higgs all lead to unique final state topologies. Figure 3.6 delineates the different signal
 1264 regions used in the gluon fusion and vector boson fusion $H \rightarrow WW^*$ analyses. While there are different
 1265 optimizations possible in each signal region, there are also some commonly shared selections that will be
 1266 described here.

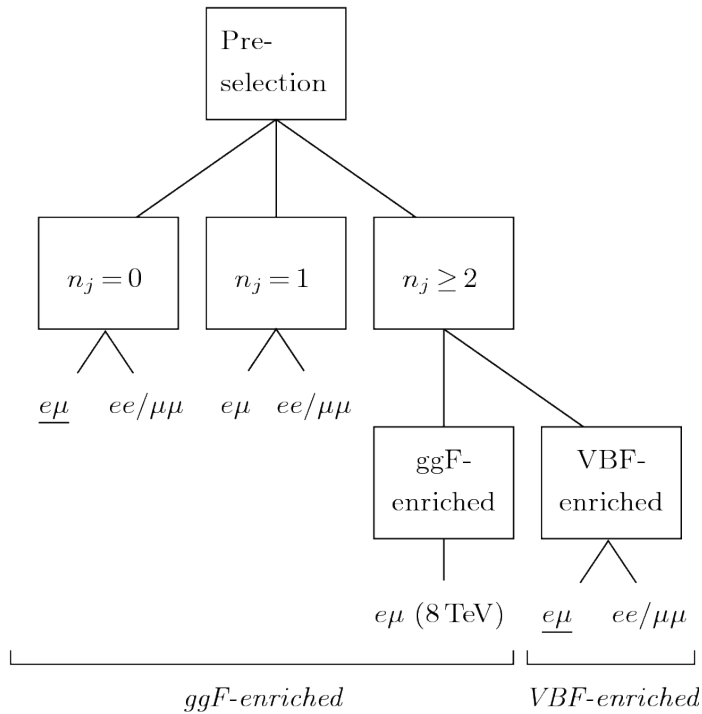


Figure 3.6: An illustration of the unique analysis signal regions [61]. The most sensitive regions for both gluon fusion and vector boson fusion production are underlined.

1267 3.4.1 EVENT PRE-SELECTION

1268 Before being sorted into the distinct signal regions, basic requirements are applied to the reconstructed
 1269 objects in the event to select Higgs-like event candidates. First, two oppositely charged leptons are required.
 1270 Once the leptons are selected, the last requirement for event pre-selection is the presence of neutrinos. As
 1271 neutrinos cannot be detected directly in ATLAS, E_T^{miss} can be used as a proxy for the combined neutrino
 1272 momentum in the transverse plane.

1273 In general, it is expected that the signal should have a harder E_T^{miss} spectrum than backgrounds, espe-
 1274 cially if these backgrounds do not contain neutrinos in the final state. When using E_T^{miss} , it is possible
 1275 mis-measurements of objects in the detector can lead to imbalances in the transverse plane. When such a
 1276 mis-measurement occurs, the E_T^{miss} vector in the transverse plane will often point in the same direction as
 1277 the mis-measured object. Therefore, a new variable, $E_{T,\text{rel}}^{\text{miss}}$, is used in the pre-selection. $E_{T,\text{rel}}^{\text{miss}}$ is defined
 1278 in equation 3.1.

$$E_{T,\text{rel}}^{\text{miss}} = \begin{cases} E_T^{\text{miss}} \sin \Delta\phi_{\text{near}} & \text{if } \Delta\phi_{\text{near}} < \pi/2 \\ E_T^{\text{miss}} & \text{otherwise,} \end{cases} \quad (3.1)$$

1279 If the closest object to the E_T^{miss} vector is within $\pi/2$ radians in the transverse plane, the E_T^{miss} is projected
 1280 away from this object. Otherwise, the normal E_T^{miss} vector is used. Figure 3.7 shows a graphical illustration
 of this concept.

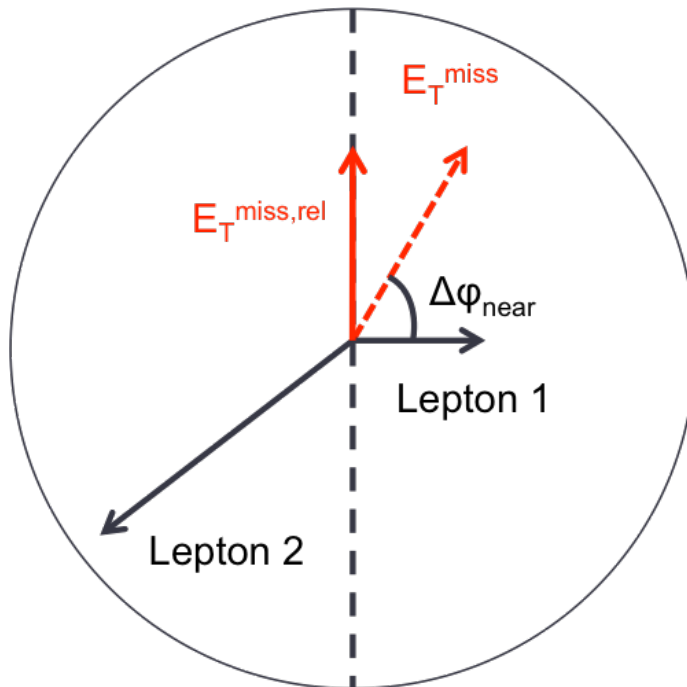


Figure 3.7: A graphical illustration of the $E_{T,\text{rel}}^{\text{miss}}$ calculation

1281 Once the lepton and E_T^{miss} pre-selections are made, the analysis is divided into different regions accord-
 1282 ing to jet multiplicity.
 1283

1284 3.4.2 JET MULTIPLICITY

1285 Jet multiplicity, denoted as n_j , is used to sub-divide the analysis into distinct signal regions. By creating
 1286 separate signal regions, each bin in jet multiplicity becomes sensitive to different modes of Higgs produc-
 1287 tion and different backgrounds.

1288 For example, the $n_j \geq 2$ region is more sensitive to VBF production because of the two high momen-
 1289 tum jets produced at matrix element level. For gluon fusion production to enter this bin, two initial state
 1290 radiation jets must be emitted.

1291 Figure 3.8 shows the jet multiplicity in both the different flavor and same flavor regions after the pre-
 1292 selection. It also shows the background composition in the bins of n_b . A few trends from this distribution
 1293 are worth noting. The first is that the Drell-Yan background dominates in the same flavor channels for
 1294 $n_j \leq 1$. Second, the top background becomes a clear contributor to the total background for $n_j \geq$
 1295 1. Lastly, the SM WW production dominates in the $n_j = 0$ bin, as it is an irreducible background to
 1296 $H \rightarrow WW^*$ production. Because of these distinct features, each jet multiplicity bin is treated separately.

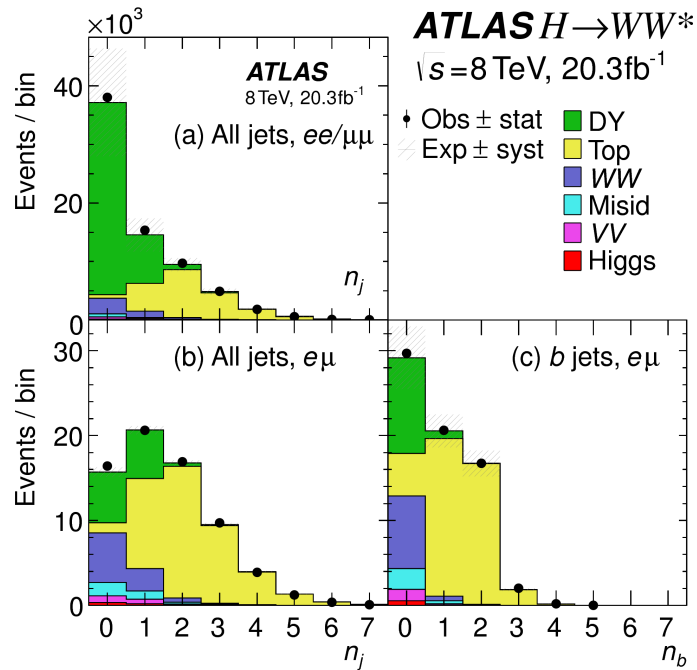


Figure 3.8: Predicted backgrounds (compared with data) as a function of n_j (a and b) and n_b (c) after pre-selection requirements

1297 3.5 BACKGROUND REDUCTION IN SAME-FLAVOR FINAL STATES

1298 As described in section 3.4.2, the background composition of the same flavor final states is different
1299 from that of the different flavor states. In particular, Drell Yan processes play a much larger role because
1300 the Z/γ^* decays to same flavor leptons. Because real neutrinos are absent in the Z/γ^* decays to ee and $\mu\mu$,
1301 a requirement on E_T^{miss} should largely reduce the background. However, as this section will demonstrate,
1302 with increasing pileup conditions the resolution of the calorimeter-based E_T^{miss} degrades greatly. There-
1303 fore, two new variables for Z/γ^* background reduction are constructed and described in this section.

1304 3.5.1 PILEUP AND E_T^{miss} RESOLUTION

1305 Secondary interactions of protons in the colliding bunches of the LHC (known as pileup interactions,
1306 described in detail in Chapter 2) deposit energy into the ATLAS calorimeter in addition to the energy that
1307 comes from the hard scatter process of interest. The calculation of E_T^{miss} is fundamentally Poissonian.
1308 Summing up all of the energy deposits in individual calorimeter cells or clusters is similar to a counting
1309 experiment. The error on a mean of N in a Poisson distribution is \sqrt{N} , so the energy resolution scales
1310 as \sqrt{E} . As more energy is deposited in the calorimeter, the E_T^{miss} resolution degrades, meaning that the
1311 E_T^{miss} resolution is particularly sensitive to LHC instantaneous luminosity conditions.

1312 Figure 3.9 shows an event display of a $Z/\gamma^* + \text{jets}$ event candidate with the twenty-five reconstructed
1313 primary vertices. This display illustrates that while the interaction of interest only has tracks coming from
1314 the hardest primary vertex, all of the secondary interactions deposit energy in the calorimeter as well.

1315 Figure 3.10 shows the RMS of the E_T^{miss} distribution in $Z \rightarrow \mu\mu$ events (where there are no real neu-
1316 trinos) as a function of the number of the average number of interactions. Under 2011 LHC conditions,
1317 this RMS was approximately 9 GeV, while under 2012 running conditions the resolution worsened to 12
1318 GeV. The increase in pileup dilutes the E_T^{miss} variable's ability to reduce the Z/γ^* background.

1319 3.5.2 TRACK-BASED DEFINITIONS OF MISSING TRANSVERSE MOMENTUM

1320 Because the increasing number of secondary proton-proton interactions degrades calorimeter-based
1321 E_T^{miss} resolution, a new variable using only contributions from the primary interaction vertex is necessary

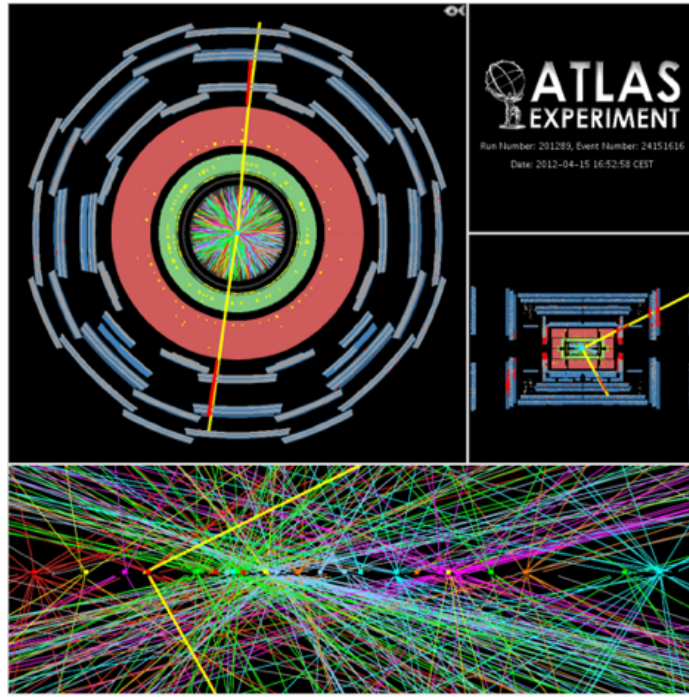


Figure 3.9: An event display of a Z/γ^* + jets event illustrating the effect of pileup interactions

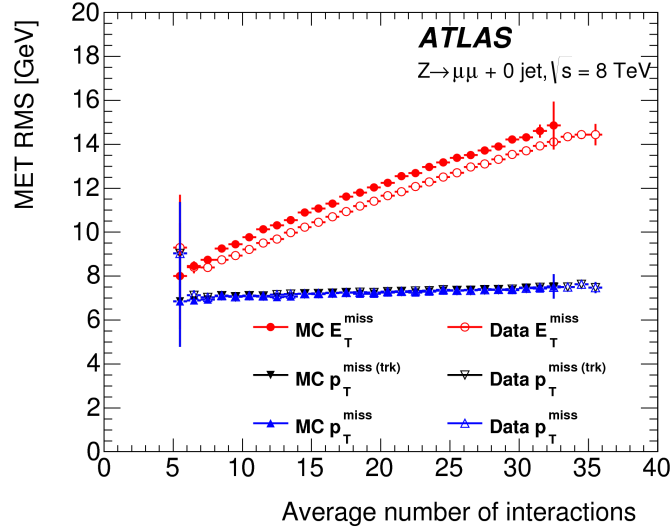


Figure 3.10: The RMS of different missing transverse momentum definitions as a function of the average number of interactions per bunch crossing

¹³²² to further reduce the Z/γ^* background. While it is not possible to associate calorimeter energy deposits
¹³²³ with a particular vertex, individual charged particle tracks in the Inner Detector are associated to unique
¹³²⁴ vertices. Thus, two track-based definitions of missing transverse momentum , using only tracks coming

1325 from the primary vertex in the event, are used in the analysis. The simplest variable, $p_T^{\text{miss}(\text{trk})}$, is the vec-
 1326 torial sum of the p_T of all of the tracks from the primary vertex and the selected leptons (excluding the
 1327 tracks associated with the selected leptons to avoid double counting). Equation 3.2 defines $p_T^{\text{miss}(\text{trk})}$.

$$p_T^{\text{miss}(\text{trk})} = - \left(\sum_{\text{selected leptons}} p_T + \sum_{\text{other tracks}} p_T \right), \quad (3.2)$$

1328 To further improve the resolution on the missing transverse momentum, the variable p_T^{miss} is used as de-
 1329 fined in equation 3.3. For selected leptons and jets, the nominal p_T measurements are used. Tracks are used
 1330 to estimate the soft component of the missing transverse momentum instead of calorimeter measurements.

1331

$$p_T^{\text{miss}} = - \left(\sum_{\text{selected leptons}} p_T + \sum_{\text{selected jets}} p_T + \sum_{\text{other tracks}} p_T \right), \quad (3.3)$$

1332 Figure 3.10 illustrates that these two new variables accomplish their intended purpose. The resolution as a
 1333 function of mean number of interactions for both $p_T^{\text{miss}(\text{trk})}$ and p_T^{miss} is much flatter than the dependence
 1334 for E_T^{miss} . Figure 3.11a shows the difference between the true and reconstructed values of missing transverse
 1335 momentum using both the track-based p_T^{miss} and calorimeter based E_T^{miss} . The RMS of the distribution
 1336 improves by 3.5 GeV when using p_T^{miss} .

1337 3.5.3 DISTINGUISHING Z/γ^* +JETS AND $H \rightarrow WW^*$ TOPOLOGIES

1338 In addition to measuring missing transverse momentum, another variable can be constructed to exploit
 1339 kinematic and topological differences between the Z/γ^* background and $H \rightarrow WW^*$ signal. Because
 1340 there are no real neutrinos in the final state (in the case of $Z/\gamma^* \rightarrow ee, \mu\mu$ decays), the dilepton system will
 1341 be balanced with the jets produced in the hard scatter. A new variable, f_{recoil} , is constructed to estimate
 1342 the balance between the dilepton system and recoiling jets and is defined in equation 3.4. The transverse
 1343 plane is divided into four sections, or quadrants, with one quadrant centered on the dilepton vector. The
 1344 numerator of f_{recoil} is the magnitude of the vectorial sum of the p_T of jets in the quadrant opposite the
 1345 dilepton system, weighted by each jet's Jet Vertex Fraction (JVF, described in chapter 2). The denominator

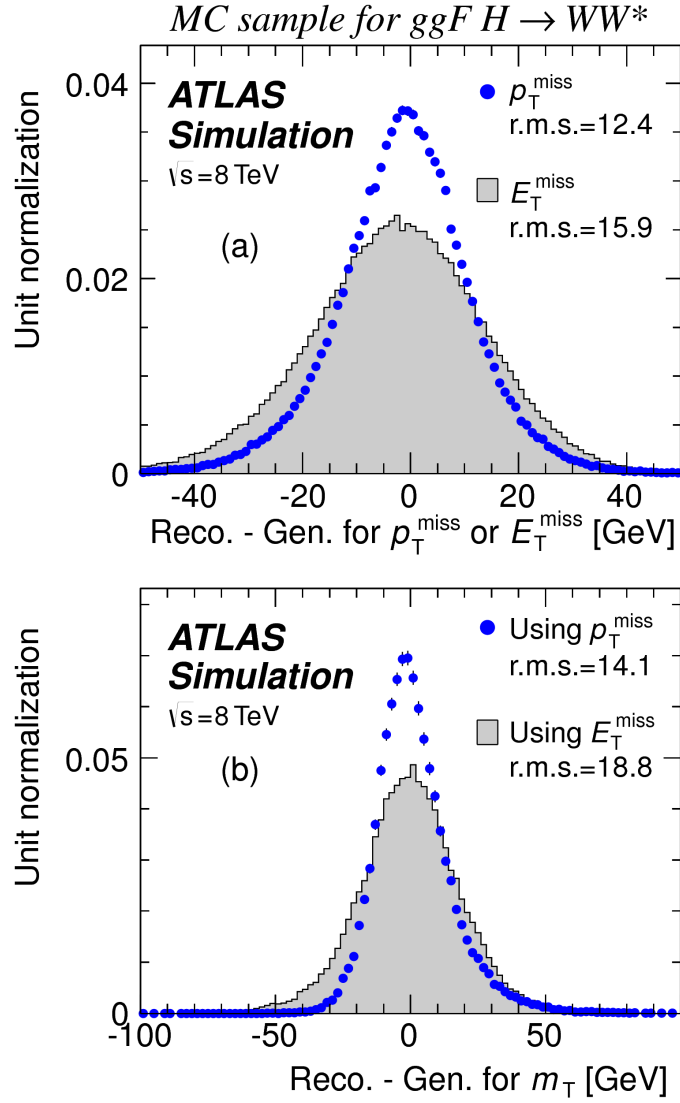


Figure 3.11: The difference between the true and reconstructed values of the missing transverse momentum (a) and m_T (b) in a gluon fusion signal sample

¹³⁴⁶ is the magnitude of the dilepton p_T .

$$f_{\text{recoil}} = \left| \sum_{\text{jets } j \text{ in } \wedge} \text{JVF}_j \cdot \mathbf{p}_T^j \right| / p_T^{\ell\ell}. \quad (3.4)$$

¹³⁴⁷ Figure 3.12 shows a shape comparison of the f_{recoil} distribution in a simulated $Z/\gamma^* + \text{jets}$ sample, a
¹³⁴⁸ $H \rightarrow WW^*$ signal sample, and other backgrounds that contain real neutrinos. The $Z/\gamma^* + \text{jets}$ events

1349 tend to be more balanced between the dilepton system and recoiling jets, while the processes containing
 1350 real neutrinos are less balanced in the transverse plane. Thus, a requirement on f_{recoil} will reduce the Z/γ^*
 1351 + jets background while maintaining a good signal efficiency.

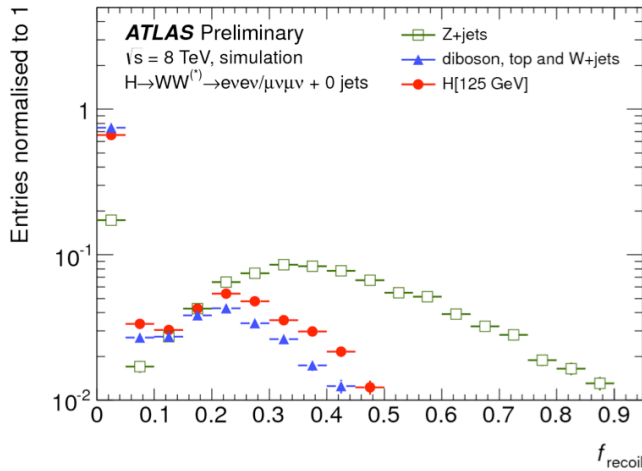


Figure 3.12: Comparison of f_{recoil} distributions for $Z/\gamma^* + \text{jets}$, $H \rightarrow WW^*$, and other backgrounds with real neutrinos.

1352 3.5.4 OPTIMIZING BACKGROUND REDUCTION SELECTION REQUIREMENTS

1353 The requirements on $p_T^{\text{miss}(\text{trk})}$ and f_{recoil} used to reduce the $Z + \text{jets}$ background must be optimized
 1354 to maximize expected signal significance in the same flavor channels. Figure 3.13 shows an optimization of
 1355 the combination of the two requirements in the gluon fusion zero jet bin. Each bin shows the expected
 1356 signal significance if the $p_{T,\text{rel}}^{\text{miss}(\text{trk})}$ is required to be greater than the left edge of the bin and the f_{recoil} is
 1357 required to be less than the top edge of the bin. The figure shows that the best signal significance comes
 1358 from requiring low values of f_{recoil} (< 0.05) and $p_{T,\text{rel}}^{\text{miss}(\text{trk})}$ values greater than 45 GeV.

1359 3.6 PARAMETERS OF INTEREST AND STATISTICAL TREATMENT

1360 As with any search or measurement, there are particular parameters of the Higgs that the $H \rightarrow WW^*$
 1361 analysis is interested in measuring. In this case, the parameters of interest are the mass of the Higgs boson
 1362 and its production cross section. Because the $H \rightarrow WW^* \rightarrow \ell\nu\ell\nu$ process does not have a closed final

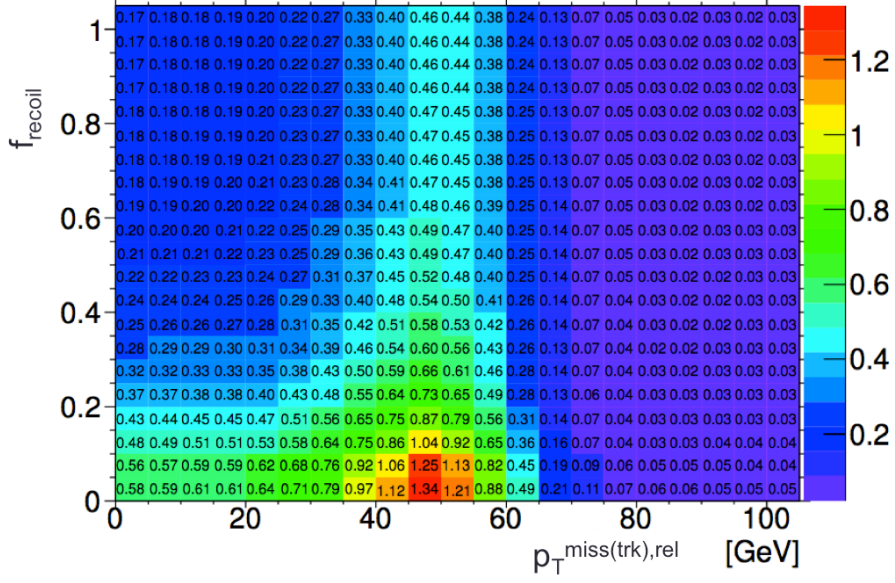


Figure 3.13: Signal significance as a function of required value for f_{recoil} and $p_{T,\text{rel}}^{\text{miss}(\text{trk})}$ in the ggF $H \rightarrow WW^*$ with $n_j = 0$

state, it is not possible to measure the full invariant mass of the particle that may have produced the final state. However, a proxy for the invariant mass is defined using transverse plane information and detailed in section 3.6.1. The second parameter of interest is the ratio of the measured cross section to that expected from the Standard Model Higgs, which is denoted a μ . This is defined in equation 3.5.

$$\mu = \frac{\sigma}{\sigma_{\text{SM}}} \quad (3.5)$$

All of the likelihoods used in the statistical analysis of the final signal region events are parameterized as a function of μ . μ is a natural variable for hypothesis testing, as $\mu = 0$ corresponds to a background only hypothesis and $\mu = 1$ corresponds exactly to a Standard Model Higgs.

3.6.1 TRANSVERSE MASS

The $H \rightarrow WW^* \rightarrow \ell\nu\ell\nu$ analysis cannot reconstruct the full invariant mass of the Higgs because of the neutrinos in the final state. The transverse mass serves as a proxy for the full invariant mass by

1373 exploiting information from the transverse plane. The transverse mass is defined in equation 3.6.

$$m_T = \sqrt{(E_T^{\ell\ell} + p_T^{\text{miss}})^2 - |\vec{p}_T^{\ell\ell} + \vec{p}_T^{\text{miss}}|^2}, \quad (3.6)$$

1374 Here the $E_T^{\ell\ell}$ and $p_T^{\ell\ell}$ are the transverse energy and momentum of the dilepton system, while p_T^{miss} is a
1375 proxy for the transverse momentum of the di-neutrino system. The track-based p_T^{miss} is used in the m_T
1376 rather than the calorimeter based E_T^{miss} because it has a better resolution on the true transverse mass.
1377 Figure 3.11b shows the improvement in the RMS of the difference between the true and reconstructed
1378 transverse mass in a ggF signal sample. The RMS improves by 4.7 GeV using p_T^{miss} in the m_T calculation.

1379 **3.6.2 STATISTICAL TREATMENT²**

1380 **LIKELIHOOD FUNCTION**

1381 The statistical analysis of final event candidates is framed as a hypothesis test, where the null hypoth-
1382 esis is background-only (no Standard Model Higgs). The first step in the analysis is to form a likelihood
1383 function for the data. In its simplest form, this likelihood is the probability of observing the number of
1384 events seen in the final signal region given knowledge of the signal strength. Because observation of events
1385 is fundamentally a Poisson counting experiment, this simple likelihood can be expressed as a Poisson prob-
1386 ability of observing N events given a total number of predicted signal and background events. This basic
1387 likelihood is shown in equation 3.7.

$$\mathcal{L}(\mu) = P(N|\mu S + B) \quad (3.7)$$

1388 Here, P is the Poisson probability density function, N is the total number of observed events, μ is the
1389 signal strength, S is the predicted number of signal events, and B is the predicted number of background
1390 events.

1391 In particle physics, certain background estimates are commonly normalized in so-called “control” re-
1392 gions and those predictions are scaled by the same normalization factor in the signal region. This leads to a

²Many thanks to Aaron Armbruster, whose thesis [62] inspired parts of this section.

1393 slightly more complicated likelihood, which is a function of both the signal strength and the background
1394 normalization. This is shown in equation 3.8.

$$\mathcal{L}(\mu, \theta) = P(N|\mu S + \theta B) P(N_{\text{CR}}|\theta B_{\text{CR}}) \quad (3.8)$$

1395 Here, θ serves as a “nuisance parameter”, or a parameter that is not of primary interest but still enters the
1396 likelihood. The second Poisson term enforces that the background normalization be consistent with the
1397 number of observed events in data in the control region, N_{CR} .

1398 So far, these two formulations of likelihoods have assumed a single signal region and do not take into
1399 account any shape information of potential discriminating variables. The $H \rightarrow WW^*$ analysis is divided
1400 into many different categories, the counting experiment described above can be performed in each individ-
1401 ual category. As mentioned in section 3.6.1, the transverse mass is used as the primary discriminating vari-
1402 able in many of the $H \rightarrow WW^*$ sub-analyses. The same counting experiment can be performed in each
1403 bin of the m_T distribution to incorporate some shape information. Thus, the total likelihood becomes a
1404 product over signal regions and bins of the m_T distribution. Finally, there are usually many backgrounds
1405 that are normalized in control regions. The new formulation of the likelihood takes this into account by
1406 including a product over control regions in the second Poisson term. All of these modifications are shown
1407 in equation 3.9.

$$\mathcal{L}(\mu, \theta) = \prod_{\substack{\text{SRs } i \\ \text{bins } b}} P\left(N_{ib} \middle| \mu S_{ib} + \sum_{\text{bkg } k} \theta_k B_{kib}\right) \prod_{\text{CRs } l} P\left(N_l \middle| \sum_{\text{bkg } k} \theta_k B_{kl}\right) \quad (3.9)$$

1408 The final step to obtain the full likelihood used in the analysis is to add nuisance parameters for the
1409 systematic uncertainties. In cases where the uncertainty does not affect the shape of m_T bin-by-bin, each
1410 systematic uncertainty ϵ is allowed to affect the expected event yields through a linear response function
1411 of the nuisance parameter, namely $\nu(\theta) = (1 + \epsilon)\theta$. If instead the uncertainty does affect the shape, the
1412 effect is instead parameterized by $\nu_b(\theta) = 1 + \epsilon_b\theta$. The value of the nuisance parameters for the systematic
1413 uncertainty are constrained with a Gaussian term that is added to the likelihood as well. This is of the form
1414 $g(\delta|\theta) = e^{-(\delta-\theta)^2/2}/\sqrt{2\pi}$, where δ is the central value and θ is a nuisance parameter. Finally, a last term is

¹⁴¹⁵ added to account for the statistical uncertainty in the Monte Carlo samples used, which adds an additional
¹⁴¹⁶ poisson term. The full likelihood used in the final statistical analysis is defined in equation 3.10.

$$\begin{aligned} \mathcal{L}(\mu, \boldsymbol{\theta}) = & \prod_{\substack{\text{SRs i} \\ \text{bins b}}} P \left(N_{ib} \middle| \mu S_{ib} \cdot \prod_{\substack{\text{sig.} \\ r}} \nu_{br}(\theta_r) + \sum_{\text{bkg k}} \theta_k B_{kib} \cdot \prod_{\substack{\text{bkg.} \\ s \\ \text{syst.}}} \nu_{bs}(\theta_s) \right) \\ & \cdot \prod_{\text{CRs l}} P \left(N_l \middle| \sum_{\text{bkg k}} \theta_k B_{kl} \right) \\ & \cdot \prod_{\substack{\text{syst} \\ t}} g(\delta_t | \theta_t) \cdot \prod_{\text{bkg k}} P(\xi_k | \zeta_k \theta_k) \end{aligned} \quad (3.10)$$

¹⁴¹⁷ The fourth term of the equation quantifies the uncertainty due to finite Monte Carlo sample size. Here,
¹⁴¹⁸ ξ represents the central value of the background prediction, θ is the associated nuisance parameter, $\zeta =$
¹⁴¹⁹ $(B/\delta B)^2$, where δB is the statistical uncertainty of B .

¹⁴²⁰ The best fit value of the signal strength μ is determined by finding the values of μ and $\boldsymbol{\theta}$ that maximize
¹⁴²¹ the likelihood, while setting $\delta = 0$ and $\xi = \zeta$. Once the likelihood is defined, a test statistic must be built
¹⁴²² for use in hypothesis testing.

¹⁴²³ TEST STATISTIC

¹⁴²⁴ To distinguish whether the data match a background only or background and signal hypothesis, a test
¹⁴²⁵ statistic must be used. The $H \rightarrow WW^*$ analysis uses the profile likelihood technique [63]. The first step
¹⁴²⁶ in formulating this test statistic is to define the profile likelihood ratio, shown in equation 3.11.

$$\lambda(\mu) = \frac{\mathcal{L}(\mu, \hat{\theta}_\mu)}{\mathcal{L}(\hat{\mu}, \hat{\theta})} \quad (3.11)$$

¹⁴²⁷ Here $\hat{\theta}_\mu$ is the value of θ that maximizes the likelihood for the choice of μ being tested. Additionally, $\hat{\theta}$
¹⁴²⁸ and $\hat{\mu}$ represent the values of θ and μ that gives the overall maximum value of the likelihood.

¹⁴²⁹ Once this is defined, a test statistic q_μ is constructed. This is shown in equation 3.12.

$$q_\mu = -2 \ln \lambda(\mu) \quad (3.12)$$

¹⁴³⁰ A higher value of q_μ indicates that the data are more incompatible with the hypothesized value of μ , and
¹⁴³¹ q_0 then corresponds to the value of the test statistic for the background only hypothesis. A p_0 value is
¹⁴³² then defined to quantify the compatibility between the data and the null hypothesis. The p_0 value is the
¹⁴³³ probability of obtaining a value of q_0 larger than the observed value, and this is shown in equation 3.13.

$$p_0 = \int_{q_0^{\text{obs}}}^{\infty} f(q_\mu | \mu = 0) dq_\mu \quad (3.13)$$

¹⁴³⁴ Here $f(q_\mu)$ is the probability distribution function of the test statistic. Finally, the p_0 value can be con-
¹⁴³⁵ verted into a signal significance, using the formula in equation 3.14, or the one-sided tail of the Gaussian
¹⁴³⁶ distribution.

$$Z_0 = \sqrt{2} \operatorname{erf}^{-1}(1 - 2p_0) \quad (3.14)$$

¹⁴³⁷ The threshold for discovery used in particle physics is $Z_0 \geq 5$, more commonly known as a value of 5σ .

The real voyage of discovery consists not in seeking new landscapes, but in having new eyes.

Marcel Proust

4

1438

1439 The discovery of the Higgs boson and the role

1440

of the $H \rightarrow WW^* \rightarrow \ell\nu\ell\nu$ channel

1441

4.1 INTRODUCTION

1442

This chapter presents the results of the search for the Higgs boson in 4.8 fb^{-1} collected at $\sqrt{s} = 7 \text{ TeV}$ and 5.8 fb^{-1} at $\sqrt{s} = 8 \text{ TeV}$. The results of three searches at $\sqrt{s} = 8 \text{ TeV}$ in the $H \rightarrow WW^* \rightarrow \ell\nu\ell\nu$, $H \rightarrow \gamma\gamma$, and $H \rightarrow ZZ \rightarrow 4\ell$ channels are combined with results of searches at $\sqrt{s} = 7 \text{ TeV}$ in the same search channels (as well as the $H \rightarrow \tau\tau$ production and associated production searches for $H \rightarrow b\bar{b}$). The results of this combination are a 5.9σ detection of a new particle consistent with a Higgs boson. Rather than going into detail for all of the different Higgs decay searches, this chapter will discuss the three most sensitive channels and in particular focus on $H \rightarrow WW^* \rightarrow \ell\nu\ell\nu$. While the focus is on WW^* , some of the ZZ^* and $\gamma\gamma$ results are shown for completeness. The results not discussed here can

1450 be found in the ATLAS Higgs discovery publication [1].

1451 **4.2 DATA AND SIMULATION SAMPLES**

1452 The data sample used for the following results was taken in 2011 and 2012 at center of mass energies
1453 of 7 and 8 TeV, respectively, with 4.8 fb^{-1} collected at 7 TeV and 5.8 fb^{-1} collected at 8 TeV. Higgs
1454 production in the gluon fusion and vector boson fusion modes is modeled with **POWHEG** for the hard
1455 scattering event and **PYTHIA** for the showering and hadronization. Associated production of a Higgs with a
1456 vector boson or top quarks is modeled via **PYTHIA**. Table 4.1 shows the Monte Carlo generators used for
1457 modeling the signal and background processes relevant for the three analyses to be discussed.

Process	Generator
ggF, VBF H	POWHEG + PYTHIA
$WH, ZH, t\bar{t}H$	PYTHIA
$W + \text{jets}, Z/\gamma^* + \text{jets}$	ALPGEN + HERWIG
$t\bar{t}, tW, tb$	MC@NLO + HERWIG
tqb	ACERMC + PYTHIA
$q\bar{q} \rightarrow WW$	MC@NLO + HERWIG
$gg \rightarrow WW$	GG2WW+ HERWIG
$q\bar{q} \rightarrow ZZ$	POWHEG + PYTHIA
$gg \rightarrow ZZ$	GG2ZZ+ HERWIG
WZ	MADGRAPH+ PYTHIA , HERWIG
$W\gamma + \text{jets}$	ALPGEN + HERWIG
$W\gamma^*$	MADGRAPH+ PYTHIA
$q\bar{q}/gg \rightarrow \gamma\gamma$	SHERPA

Table 4.1: Monte carlo generators used to model signal and background for the Higgs search [1].

1458 **4.3 $H \rightarrow WW \rightarrow e\nu\mu\nu$ SEARCH**

1459 The $H \rightarrow WW \rightarrow e\nu\mu\nu$ search is unique compared to the ZZ and $\gamma\gamma$ channels. The Higgs mass
1460 cannot be fully reconstructed due to the presence of neutrinos in the final state, so the transverse mass m_T
1461 is used as the final discriminating variable. Compared to the other channels, there are more backgrounds
1462 here as well, as discussed in chapter 3. The same flavor final states are excluded from this search due to high
1463 pileup in the 8 TeV dataset.

1464 4.3.I EVENT SELECTION

1465 The analysis requires two opposite charge isolated leptons, with the leading (sub-leading) lepton required
 1466 to have $p_T > 25(15)$ GeV. The events are separated into different signal regions depending on which
 1467 flavor of lepton is leading ($e\mu$ for leading electron, μe for leading muon). Strict lepton quality cuts are
 1468 applied to the sample to reduce backgrounds from fake leptons.

1469 Jets are reconstructed with the anti- k_T algorithm with a radius parameter $R = 0.4$. The jets are re-
 1470 quired to have $p_T > 25$ GeV and $|eta| < 4.5$, with jets in the tracking volume required to have a jet
 1471 vertex fraction of 0.5 and jets in the forward region required to have $p_T > 30$ GeV. The analysis is sepa-
 1472 rated into three different signal regions based on jet multiplicity: $n_j = 0, 1, \geq 2$.

1473 To indicate the presence of neutrinos in the event, a requirement of $E_{T,\text{rel}}^{\text{miss}} > 25$ GeV is made¹. This
 1474 requirement significantly reduces the QCD multijet and $Z/\gamma^* + \text{jets}$ backgrounds. Figure 4.1 shows the
 1475 distribution of n_j in data and simulation after applying these “pre-selection” requirements.

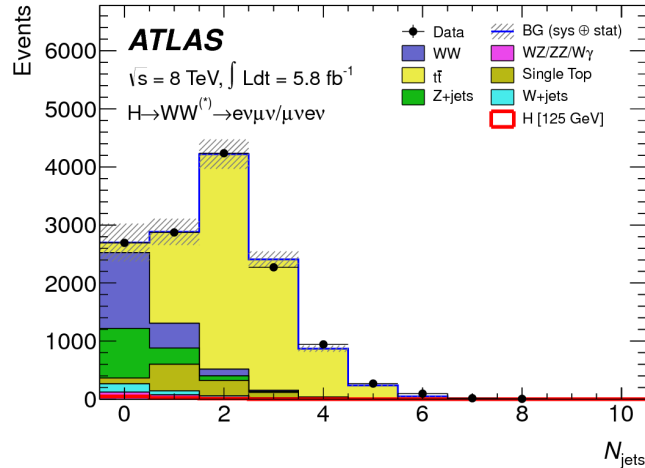


Figure 4.1: Jet multiplicity distribution in data and MC after applying lepton, jet, and $E_{T,\text{rel}}^{\text{miss}}$ selections. The WW and top backgrounds have been normalized using control samples, and the hashed band indicates the total uncertainty on the prediction. [1]

1476 Additional selections are applied to require the dilepton topology to correspond to that of a SM Higgs.
 1477 The requirements are presented here - more detailed discussion on the motivation for each requirement is
 1478 saved for Chapter 5. In all of the jet multiplicity channels, the dilepton system is required to have a small

¹For the definition of $E_{T,\text{rel}}^{\text{miss}}$, see chapter 3

1479 gap in azimuthal angle, $\Delta\phi_{\ell\ell} < 1.8$. Similarly, the $m_{\ell\ell}$ is required to be less than 50 GeV in the lower jet
1480 multiplicity channels and less than 80 GeV in the $n_j \geq 2$ channel. In the $n_j = 0$ channel, the magnitude
1481 of the dilepton p_T , $p_T^{\ell\ell}$, is required to be greater than 30 GeV.

1482 In the higher jet multiplicity channels ($n_j \geq 1$), the top background is a more important component
1483 and must be reduced. The total transverse momentum p_T^{sum} is thus required to be less than 30 GeV. Ad-
1484 ditionally, the di- τ invariant mass $m_{\tau\tau}$ (dilepton mass computed under the assumption that the neutrinos
1485 from the τ decay are emitted collinear to the charged leptons) is used to reject $Z \rightarrow \tau\tau$ events by requiring
1486 $|m_{\tau\tau} - m_Z| > 25$ GeV. These variables are also discussed in more detail in Chapter 5.

1487 In the $n_j \geq 2$ channel, requirements are made to isolate the VBF contribution to Higgs production.
1488 The kinematics of the two leading jets are used to make these requirements. In particular, the event must
1489 have $\Delta y_{jj} > 3.8$ and $m_{jj} > 500$ GeV, along with a veto on having any additional jets with rapidity
1490 between the two leading jets.

1491 4.3.2 BACKGROUND ESTIMATION

1492 The details of the background estimation techniques used in the $H \rightarrow WW^* \rightarrow \ell\nu\ell\nu$ analysis are
1493 discussed in section 5.5. As that section refers to a later iteration of the analysis, a general discussion is given
1494 here for completeness. The dominant backgrounds are SM WW production and top (both pair and
1495 single) production, and these backgrounds have their normalizations estimated from dedicated control
1496 regions while their shapes are taken from simulation.

1497 The control sample for the Standard Model WW background is defined by making the same require-
1498 ments as the signal region with the $m_{\ell\ell}$ requirement inverted (now requiring $m_{\ell\ell} > 80$ GeV) and remov-
1499 ing the $\Delta\phi_{\ell\ell}$ requirement. This creates a control sample that is 70% (40%) pure in the 0(1)-jet region. The
1500 correction to the pure MC-based background estimate is quantified by defining a normalization factor β
1501 which is the ratio of the data yield to the MC yield ($N_{\text{data}}/N_{\text{MC}}$) in this control sample. Table 4.2 shows
1502 the WW normalization factors in the $n_j = 0$ and $n_j = 1$ bins (the $n_j \geq 2$ estimate is taken directly
1503 from MC).

1504 The top background estimate is also computed separately in each jet multiplicity bin. In the $n_j = 0$

n_j	β_{WW}	β_t
= 0	1.06 ± 0.06	1.11 ± 0.06
= 1	0.99 ± 0.15	1.11 ± 0.05
≥ 2	-	1.01 ± 0.26

Table 4.2: Normalization factors (ratio of data and MC yields in a control sample) for the Standard Model WW and top backgrounds in the $H \rightarrow WW^* \rightarrow \ell\nu\ell\nu$ analysis [1]. Only statistical uncertainties are shown.

channel, the background is first normalized using data after pre-selection requirements with no selection on n_j . Then, a dedicated b -tagged control sample is used to evaluate the ratio of one-jet to two-jet events in data. The details of this technique are shown in reference [64]. In the $n_j = 1$ and the $n_j \geq 2$ regions, the top background is normalized in a control sample where the signal region selections are applied, but the b -jet veto is reversed and the Higgs topology requirements on $m_{\ell\ell}$ and $\Delta\phi_{\ell\ell}$ are removed. The resulting normalization factors for these techniques are shown in table 4.2.

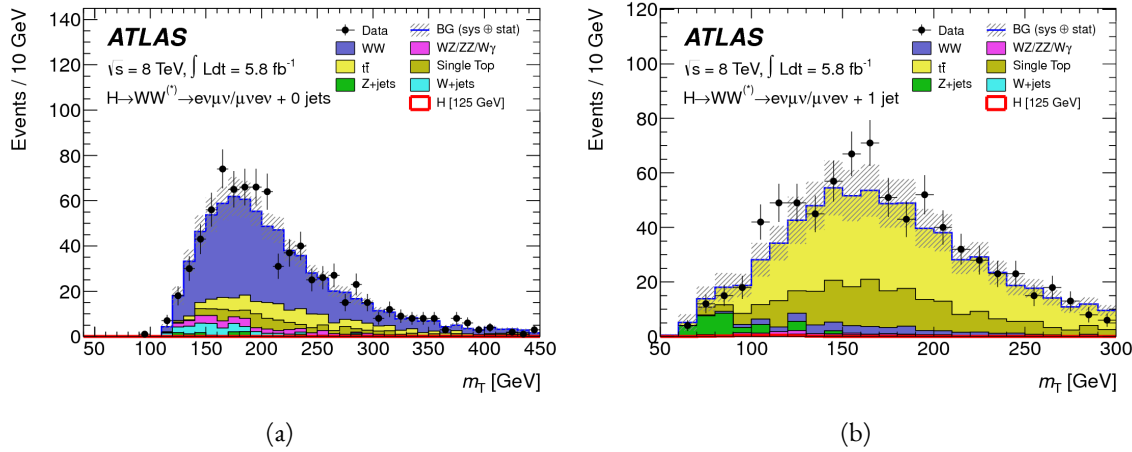


Figure 4.2: Comparison of m_T between data and simulation in the $n_j = 0$ WW (a) and $n_j = 1$ top (b) control samples [1]

The control samples which are used for background normalization can also be used to validate the modeling of the m_T distribution for each background. Figure 4.2 shows the comparison between data and MC for the m_T distribution after correcting the normalization of the backgrounds in the WW and top control regions. Good agreement between data and simulation is seen in both cases.

The $W + \text{jets}$ background estimate is taken entirely from data using a control sample with one well reconstructed lepton and one anti-identified lepton. All other backgrounds are taken purely from simulation.

1517 4.3.3 SYSTEMATIC UNCERTAINTIES

1518 The systematic uncertainties that have the largest impact on the analysis are the theoretical uncertainties
 1519 associated with the signal cross section, and these are shared with the ZZ^* and $\gamma\gamma$ channels. The uncer-
 1520 tainties resulting from variations of the QCD scale are $+7\%/-8\%$ on the final singal yield. Those coming
 1521 from variations of the parton distribution function (PDF) used in the simulation add a $\pm 8\%$ uncertainty
 1522 on the yield. The uncertainties on the branching ratios of the Higgs are $\pm 5\%$.

1523 The main experimental uncertainties come from variations of the jet energy scale (JES), jet energy reso-
 1524 lution, pile-up, E_T^{miss} , b -tagging efficiency, W +jets background estimate, and integrated luminosity. For
 1525 more details, see reference [1].

1526 4.3.4 RESULTS

1527 Table 4.3 shows the signal and background yields in the final signal region after normalizing the back-
 1528 grounds according to the methods described above.

	$n_j = 0$	$n_j = 1$	$n_j \geq 2$
Signal	20 ± 4	5 ± 2	0.34 ± 0.07
WW	101 ± 13	12 ± 5	0.10 ± 0.14
Other dibosons	12 ± 3	1.9 ± 1.1	0.10 ± 0.10
$t\bar{t}$	8 ± 2	6 ± 2	0.15 ± 0.10
Single top	3.4 ± 1.5	3.7 ± 1.6	-
$Z/\gamma^* + \text{jets}$	1.9 ± 1.3	0.10 ± 0.10	-
$W + \text{jets}$	15 ± 7	2 ± 1	-
Total background	142 ± 16	26 ± 6	0.35 ± 0.18
Observed in data	185	38	0

Table 4.3: Data and expected yields for signal and background in the final $H \rightarrow WW^* \rightarrow \ell\nu\ell\nu$ signal region.
 Uncertainties shown are both statistical and systematic. [1]

1529 Figure 4.3 shows the m_T distribution in the $n_j \leq 1$ channels for 8 TeV data. (No events are observed
 1530 in data in the $n_j \geq 2$ channels in this dataset). The excess shown here relatively flat as a function of
 1531 hypothesized Higgs mass. The combined 7 and 8 TeV data gives an excess with local significance of 2.8σ
 1532 with an expected significance of 2.3σ , corresponding to a μ measurement of 1.3 ± 0.5 .

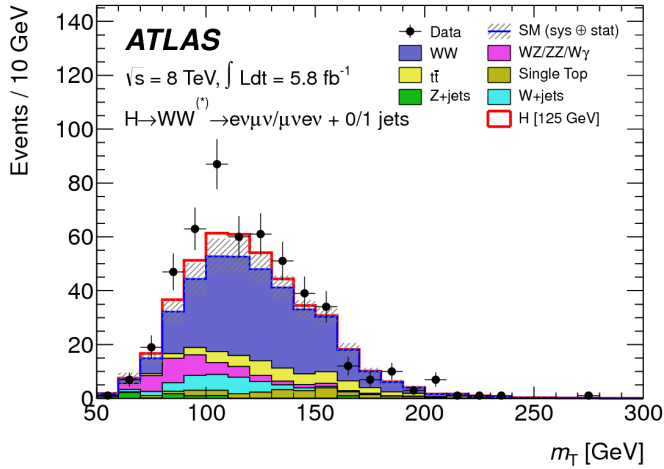


Figure 4.3: m_T distribution in the $H \rightarrow WW \rightarrow e\nu\mu\nu n_j \leq 1$ channels for 8 TeV data [1].

1533 4.4 $H \rightarrow \gamma\gamma$ SEARCH

1534 The $H \rightarrow \gamma\gamma$ search is in essence a search for a peaked excess above the falling SM diphoton mass
 1535 spectrum, with $m_{\gamma\gamma}$ as the ultimate discriminating variable. Events are selected by requiring two isolated
 1536 photons, with the leading (sub-leading) photon required to have $E_T > 40(30)$ GeV. In the 8 TeV data,
 1537 the photons are required to pass cut-based identification criteria consistent with a photon in the electro-
 1538 magnetic calorimeter and little leakage in the hadronic calorimeter.

1539 The main challenges for this analysis are accurate mass reconstruction and background estimation. In
 1540 order to accurately reconstruct the invariant mass of the di-photon system, both the energy and direction
 1541 of the photons must be measured well. Therefore, the identification of the primary vertex of the hard
 1542 interaction is particularly important, and is done using a multivariate likelihood which combines informa-
 1543 tion about the photon direction and vertex position. The background is modeled with a falling spectrum
 1544 in $m_{\gamma\gamma}$ that is parameterized by different functions depending on the category of the event.

1545 4.4.1 RESULTS

1546 The resulting diphoton mass spectrum is shown in figure 4.4. The best fit mass value in the $\gamma\gamma$ channel
 1547 alone in the combined 7 and 8 TeV data is 126.5 GeV. The local significance at this point is 4.5σ , with
 1548 an expected significance of 2.5σ . Therefore, the measured signal strength μ is 1.8 ± 0.5 in this channel.

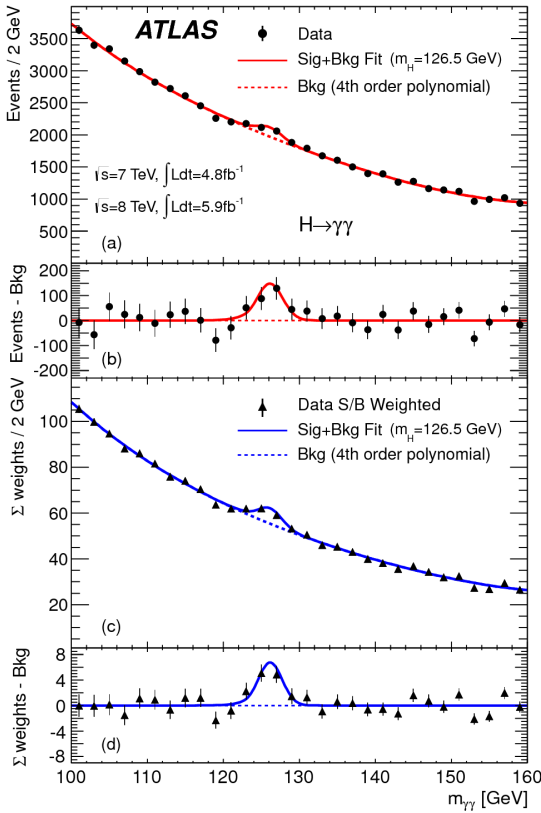


Figure 4.4: Diphoton mass spectrum in 7 and 8 TeV data. Panel a) shows the unweighted data distribution superimposed on the background fit, while panel c) shows the data where each event category is weighted by its signal to background ratio. Panels b) and d) show the respective distributions with background subtracted [1].

1549 4.5 $H \rightarrow ZZ \rightarrow 4\ell$ SEARCH

1550 The $H \rightarrow ZZ \rightarrow 4\ell$ analysis searches for a Standard Model Higgs boson decaying to two Z bosons,
 1551 each of which decays to a pair of same flavor, opposite charge isolated leptons. The ultimate discriminating
 1552 variable is $m_{4\ell}$, or the invariant mass of the four selected leptons. The ℓ denotes an e or μ as with the
 1553 $H \rightarrow WW^* \rightarrow \ell\nu\ell\nu$ analysis.

1554 Four distinct signal regions are constructed depending on the flavors of the final state, additionally sep-
 1555 arated by the flavor of the leading lepton pair. These are referred to as $4e$, $2e2\mu$, $2\mu2e$, 4μ .

1556 The main backgrounds in the $H \rightarrow ZZ \rightarrow 4\ell$ search are continuum ZZ^* production, $Z +$ jets pro-
 1557 duction, and $t\bar{t}$. The $m_{4\ell}$ distribution for background is estimated from simulation. The normalization
 1558 of the SM ZZ^* background is also taken from MC simulation, while the $Z +$ jets and $t\bar{t}$ normalizations are

1559 taken from data-driven methods.

1560 **4.5.1 RESULTS**

1561 Figure 4.5 shows the $m_{4\ell}$ spectrum measured in the 7 and 8 TeV datasets. The total number of events
1562 observed in the window between 120 and 130 GeV is 13, with 6 events in the 4μ channel, 2 events in
1563 the $4e$ channel, and 5 events in the $2e2\mu/2\mu2e$. The best fit μ value in the combined 7 and 8 TeV data
1564 occurs at 125 GeV and is measured to be 1.2 ± 0.6 . The observed significance at this mass is 3.6σ , with
1565 an expected significance of 2.7σ .

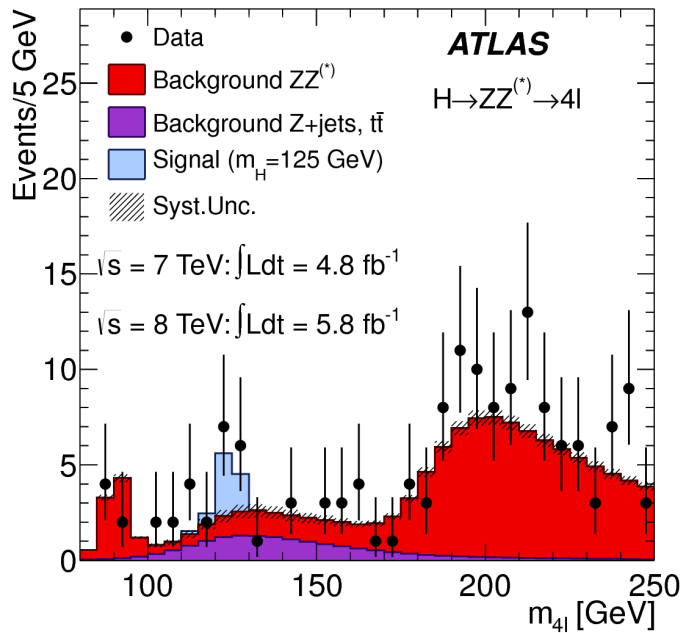


Figure 4.5: Four lepton invariant mass spectrum ($m_{4\ell}$) in 7 and 8 TeV data compared to background estimate. A 125 GeV SM Higgs signal is shown in blue [1].

1566 **4.6 COMBINED RESULTS**

1567 The statistical interpretation of the combined results is undertaken as described in section 3.6.2, with a
1568 hypothesis test based on a likelihood ratio parameterized by the Higgs signal strength μ . The null hypoth-
1569 esis corresponds to $\mu = 0$, while the SM Higgs corresponds to $\mu = 1$.

1570 Table 4.4 summarizes the properties of the individual channels as well as the significances of the excesses
 1571 seen. The most significant observed local excess comes from the $\gamma\gamma$ channel. Figure 4.6 shows a compari-
 1572 son of the observed local p_0 values as a function of hypothesized mass for the three different search chan-
 1573 nels. Both the ZZ^* and $\gamma\gamma$ channels have very peaked excesses, while the WW^* excess can be seen as very
 1574 broad because the m_T distribution does not provide detailed information about the true Higgs mass.

Channel	Fit var.	Observed Z_l	Expected Z_l	$\hat{\mu}$
$H \rightarrow ZZ^* \rightarrow 4\ell$	$m_{4\ell}$	3.6	2.7	1.2 ± 0.6
$H \rightarrow \gamma\gamma$	$m_{\gamma\gamma}$	4.5	2.5	1.8 ± 0.5
$H \rightarrow WW^* \rightarrow e\nu\mu\nu$	m_T	2.8	2.3	1.3 ± 0.5
Combined	-	6.0	4.9	1.4 ± 0.3

Table 4.4: Summary of the expected and observed significance and measured signal strengths in the combined 7 and 8 TeV datasets for the Higgs discovery analysis [1].

1575 Figure 4.7 shows the combined exclusion limit, p_0 , and signal strength. The highest local excess comes
 1576 at a value of 126.5 GeV and corresponds to a 6.0σ observed excess.

1577 Figure 4.8 shows a comparison of the measured signal strengths between the different Higgs search
 1578 channels. All measured μ are consistent with unity within their uncertainty, and the combined μ mea-
 1579 surement is 1.4 ± 0.3 .

1580 The likelihood can also be computed in a two-dimensional plane of m_H and μ , and this is shown in
 1581 figure 4.9. The figure shows that while the $\gamma\gamma$ and ZZ^* channels have very good mass resolution, the
 1582 excess in WW^* covers a broad mass range. The banana shape of the WW^* result is due to the fact that
 1583 the excess in this channel can either be explained by increasing the signal strength or by changing the mass
 1584 (and thus the cross section). The two parameters are correlated due to the lack of mass sensitivity in this
 1585 channel.

1586 Because multiple Higgs mass points are searched for, the local significance must be corrected for a look-
 1587 elsewhere effect to compute a true global significance. The global significance for finding a Higgs anywhere
 1588 in the mass range of 110 GeV to 600 GeV is 5.1σ . This increases slightly to 5.3σ if only mass range from
 1589 110 to 150 GeV.

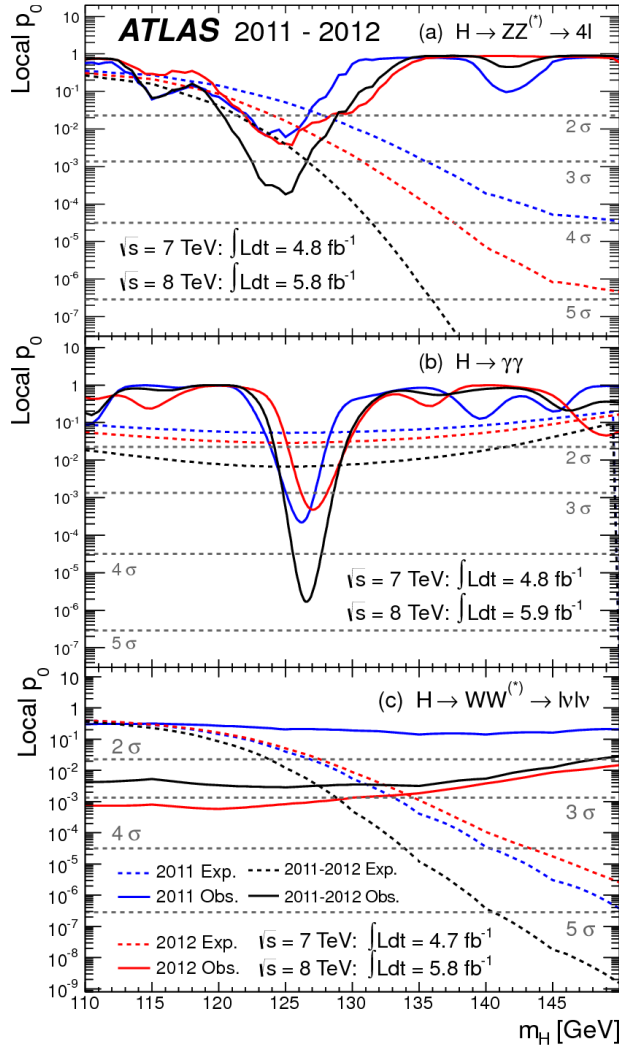


Figure 4.6: Local p_0 distribution as a function of hypothesized Higgs mass for the $H \rightarrow ZZ^* \rightarrow 4\ell$ (a), $H \rightarrow \gamma\gamma$ (b), and $H \rightarrow WW^* \rightarrow \ell\nu\ell\nu$ (c) channels. Dashed curves show expected results, while solid curves show observed. Red curves are from 7 TeV data, blue curves from 8 TeV, and black curved combined [1].

1590 4.7 CONCLUSION

1591 A search for the production of a Standard Model Higgs boson was conducted in 4.8 fb^{-1} collected at
 1592 $\sqrt{s} = 7 \text{ TeV}$ and 5.8 fb^{-1} at $\sqrt{s} = 8 \text{ TeV}$. A new particle consistent with the Higgs boson was observed,
 1593 with a mass of 126.5 GeV and a global (local) significance of $5.1(6.0)\sigma$. This is the first discovery level
 1594 observation of a particle consistent with the Higgs.

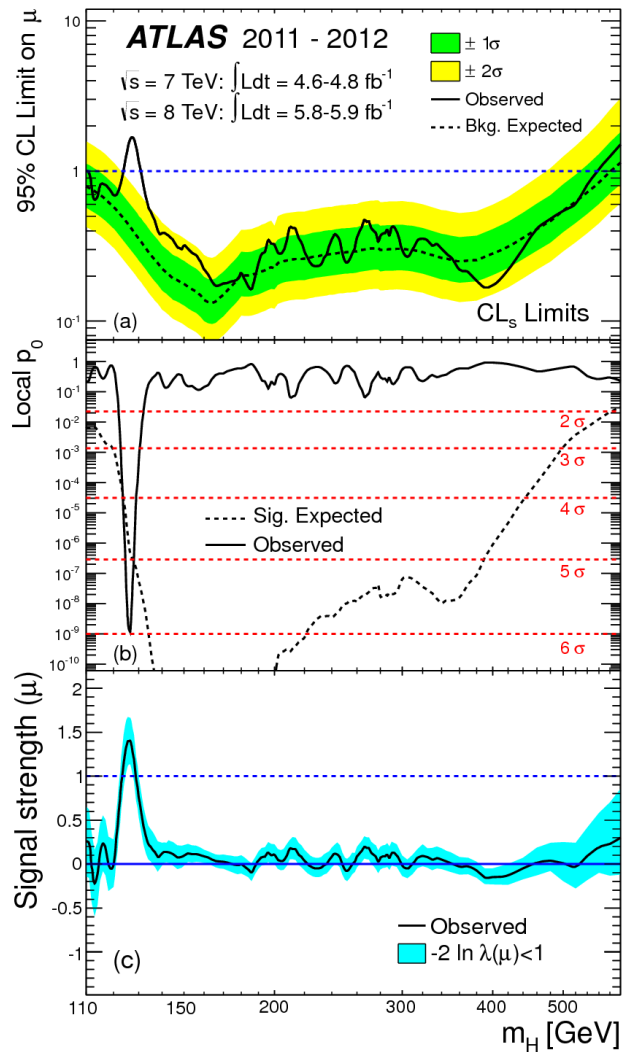


Figure 4.7: Combined 95% CL limits (a), local p_0 values (b), and signal strength measurement (c) as a function of Higgs mass [1].

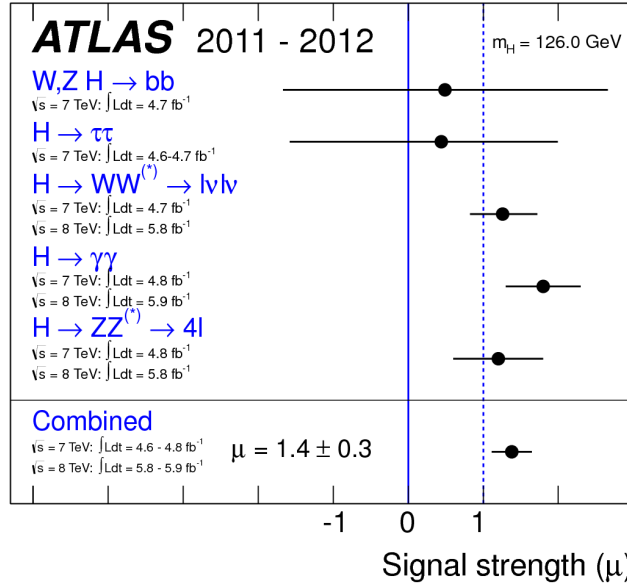


Figure 4.8: Comparison of measured signal strength μ for a 126 GeV Higgs in the 7 and 8 TeV datasets [1].

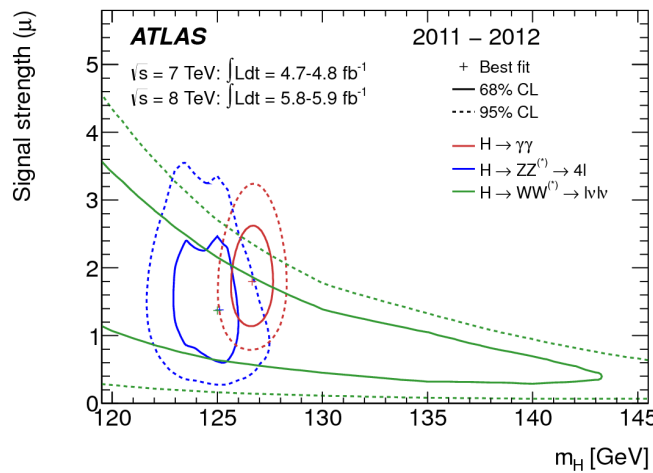


Figure 4.9: Two dimensional likelihood as a function of signal strength μ and Higgs mass m_H [1].

*The imagination of nature is far, far greater than the
imagination of man.*

Richard Feynman

1595

5

1596

Observation of Vector Boson Fusion

1597

production of $H \rightarrow WW^* \rightarrow \ell\nu\ell\nu$

1598

5.1 INTRODUCTION

1599

After the discovery of a particle consistent with the Higgs boson, the $H \rightarrow WW^*$ analysis had two main goals. The first goal was to increase the sensitivity of the analysis to fully confirm that the $H \rightarrow WW^*$ process did indeed exist. The second goal was to characterize the particle as much as possible, including searching for the lower cross-section production modes, in order to confirm that it was indeed a Higgs boson. This chapter presents a dedicated search for Vector Boson Fusion (VBF) production of a Higgs boson decaying via the $H \rightarrow WW^* \rightarrow \ell\nu\ell\nu$ mode. First, basics of the topology of VBF production are presented. Then, the details of the analysis are shown, including signal region definition, background estimation techniques, and systematic uncertainties. Finally, the results of the analysis are presented. As

1607 will be shown, this analysis is the first and most sensitive observation of the VBF production mode of the
1608 Higgs on ATLAS.

1609 In the VBF channel, there are both a selection requirement based signal region analysis (known as the
1610 “cut-based”) and a multivariate analysis which uses a boosted decision tree (known as the BDT analysis).
1611 The focus of this chapter will be on the cut-based signal region, as this is an important component of the
1612 VBF analysis and in particular acts as strong validation for the final BDT result. Connections between the
1613 cut-based and BDT analyses will be discussed where appropriate.

1614 5.2 DATA AND SIMULATION SAMPLES

1615 The results presented here are with 20.3 fb^{-1} taken at $\sqrt{s} = 8 \text{ TeV}$ and 4.5 fb^{-1} taken at $\sqrt{s} = 7 \text{ TeV}$.
1616 The details of the LHC and detector conditions during this period are given in Chapter 2. The trigger
1617 selection defining the dataset is discussed in section 5.2.1. The simulation samples used for signal and back-
1618 ground modeling are given in section 5.2.2.

1619 5.2.1 TRIGGERS

1620 The analysis uses a combination of single lepton and dilepton triggers to allow lowering of the p_T
1621 thresholds and increased signal acceptance. The p_T threshold on the leptons is a particularly important
1622 consideration for this signal. Because the second W produced in the decay can be off-shell, it tends to pro-
1623 duce lower momentum leptons. Thus, being able to lower the p_T threshold while still maintaining a low
1624 background rate is critical. Figure 5.1 shows an example of the subleading lepton p_T for a VBF $H \rightarrow WW^*$
1625 signal compared to the corresponding $t\bar{t}$ background. Note that the lepton p_T spectrum is considerably
1626 softer in the signal sample.

1627 As discussed in Chapter 2, there are multiple levels in the ATLAS trigger system, and there are different
1628 p_T thresholds imposed for the leptons at each level. Additionally, some triggers have a loose selection
1629 on the isolation of the lepton (looser than that applied offline in the analysis object selection). Table 5.1
1630 shows the thresholds used for single lepton triggers, while table 5.2 shows the thresholds coming from
1631 di-lepton triggers. The single lepton trigger efficiency for muons that pass the analysis object selection is

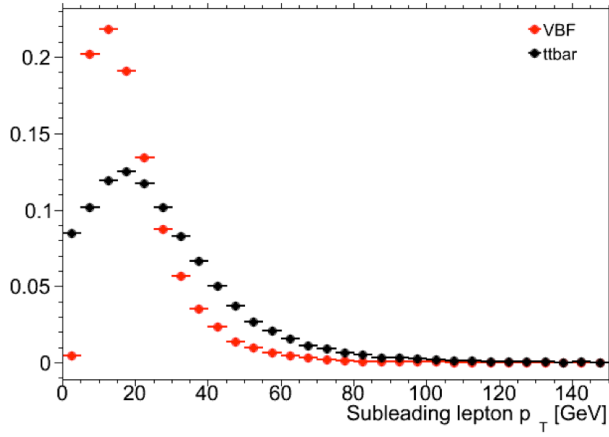


Figure 5.1: A comparison of the subleading lepton p_T spectrum between VBF $H \rightarrow WW^*$ production and $t\bar{t}$ background

1632 70% for muons in the barrel region ($|\eta| < 1.05$) and 90% in the endcap region. The electron trigger
 1633 efficiency increases with electron p_T but the average is approximately 90%. These efficiencies are measured
 1634 by combined performance and trigger signature groups [65, 66].

	Level-1 threshold	High-level threshold
Electron	18	$24i$
	30	60
Muon	15	$24i$
		36

Table 5.1: Single lepton triggers used for electrons and muons. A logical “or” of the triggers listed for each lepton type is taken. Units are in GeV, and the i denotes an isolation requirement in the trigger.

	Level-1 threshold	High-level threshold
ee	10 and 10	12 and 12
$\mu\mu$	15	18 and 8
$e\mu$	10 and 6	12 and 8

Table 5.2: Di-lepton triggers used for different flavor combinations. The two thresholds listed refer to leading and sub-leading leptons, respectively. The di-muon trigger only requires a single lepton at level-1.

1635 The combination of all triggers shown gives good efficiency for signal events. This efficiency is sum-
 1636 marized in table 5.3. The relative improvement in efficiency by adding the dilepton triggers is also shown

1637 in the same table. The largest gain comes in the $\mu\mu$ channel. Overall the trigger selection shows a good
1638 efficiency for $H \rightarrow WW^*$ signal events.

Channel	Trigger efficiency	Gain from 2ℓ trigger
ee	97%	9.1%
$\mu\mu$	89%	18.5%
$e\mu$	95%	8.3%
μe	81%	8.2%

Table 5.3: Trigger efficiency for signal events and relative gain of adding a dilepton trigger on top of the single lepton trigger selection. The first lepton is the leading, while the second is the sub-leading. Efficiencies shown here are for the ggF signal in the $n_j = 0$ category but are comparable for the VBF signal.

1639 **5.2.2 MONTE CARLO SAMPLES**

1640 Modeling of signal and background processes in the signal region, in particular for the m_T distribution,
1641 is an important consideration for the final interpretation of the analysis. Therefore, careful consideration
1642 must be paid to which Monte Carlo (MC) generators are used for specific processes. With the exception of
1643 the $W + \text{jet}$ and multijet backgrounds, the m_T shape used as the final discriminant is taken from simulation.
1644 (Many backgrounds are normalized from data, as described in section 5.5).

1645 Table 5.4 shows the MC generators used for the signal and background processes, as well as their cross
1646 sections. In order to include corrections up to next-to-leading order (NLO) in the QCD coupling constant
1647 α_s , the **POWHEG** [67] generator is often used. In some cases, only leading order generators like **ACERMC**
1648 [68] and **GG2VV** [69] are available for the process in question. If the process requires good modeling for
1649 very high parton multiplicities, the **SHERPA** [70] and **ALPGEN** [71] generators are used to provide merged
1650 calculations for five or fewer additional partons. These matrix element level calculations must then be
1651 additionally matched to models of the underlying event, hadronization, and parton shower. There are
1652 four possible generators for this: **SHERPA**, **PYTHIA 6** [72], **PYTHIA 8** [73], or **HERWIG** [74] + **JIMMY** [75].
1653 The simulation additionally requires an input parton distribution function (PDF). The **CT10** [76] PDFs
1654 are used for **SHERPA** and **POWHEG** simulated samples, while **CTEQ6Li** [77] is used for **ALPGEN + HERWIG**
1655 and **ACERMC** simulations. The Drell-Yan samples are reweighted to the **MRST** [78] PDFs, as these are
1656 found to give the best agreement between data and simulation.

Process	MC generator	$\sigma \cdot \mathcal{B}$ (pb)
Signal		
ggF $H \rightarrow WW^*$	POWHEG +PYTHIA 8	0.435
VBF $H \rightarrow WW^*$	POWHEG +PYTHIA 8	0.0356
VH $H \rightarrow WW^*$	PYTHIA 8	0.0253
WW		
$q\bar{q} \rightarrow WW$ and $qg \rightarrow WW$	POWHEG +PYTHIA 6	5.68
$gg \rightarrow WW$	GG2VV +HERWIG	0.196
$(q\bar{q} \rightarrow W) + (q\bar{q} \rightarrow W)$	PYTHIA 8	0.480
$q\bar{q} \rightarrow WW$	SHERPA	5.68
VBS $WW + 2$ jets	SHERPA	0.0397
Top quarks		
$t\bar{t}$	POWHEG +PYTHIA 6	26.6
Wt	POWHEG +PYTHIA 6	2.35
$t\bar{q}\bar{b}$	ACERMC +PYTHIA 6	28.4
$t\bar{b}$	POWHEG +PYTHIA 6	1.82
Other dibosons (VV)		
$W\gamma$ ($p_T^\gamma > 8$ GeV)	ALPGEN +HERWIG	369
$W\gamma^*$ ($m_{\ell\ell} \leq 7$ GeV)	SHERPA	12.2
WZ ($m_{\ell\ell} > 7$ GeV)	POWHEG +PYTHIA 8	12.7
VBS $WZ + 2$ jets	SHERPA	0.0126
($m_{\ell\ell} > 7$ GeV)		
$Z\gamma$ ($p_T^\gamma > 8$ GeV)	SHERPA	163
$Z\gamma^*$ (min. $m_{\ell\ell} \leq 4$ GeV)	SHERPA	7.31
ZZ ($m_{\ell\ell} > 4$ GeV)	POWHEG +PYTHIA 8	0.733
$ZZ \rightarrow \ell\ell\nu\nu$ ($m_{\ell\ell} > 4$ GeV)	POWHEG +PYTHIA 8	0.504
Drell-Yan		
Z ($m_{\ell\ell} > 10$ GeV)	ALPGEN +HERWIG	16500
VBF $Z + 2$ jets	SHERPA	5.36
($m_{\ell\ell} > 7$ GeV)		

Table 5.4: Monte Carlo samples used to model the signal and background processes [61].

Once the basic hard scattering process is simulated, it must be passed through a detector simulation and additional pile-up events must be overlaid. The pile-up events are modeled with PYTHIA 8, and the ATLAS detector is simulated with GEANT4 [79]. Because of the unique phase space of the $H \rightarrow WW^*$

1660 analysis, events are sometimes filtered at generator level to allow for more efficient generation of relevant
1661 events. The efficiency of the trigger in MC simulation does not always match the measured efficiency in
1662 data, so trigger scale factors are applied to correct the MC efficiency to the data. These are derived by the
1663 combined performance groups [65, 66].

1664 **5.3 OBJECT SELECTION**

1665 In order to define the signal region, the analysis must first select the objects to be considered. The details
1666 of the object reconstruction algorithms are discussed in Chapter 2, while this section gives specific selection
1667 cuts used in the $H \rightarrow WW^*$ analysis.

1668 The first step in this process is to select a primary vertex candidates. The event’s primary vertex is the
1669 vertex with the largest sum of p_T^2 for associated tracks and is required to have at least three tracks with
1670 $p_T > 450$ MeV. Many of the object selection cuts are then made relative to this chosen primary vertex.

1671 **5.3.1 MUONS**

1672 The analysis uses combined muon candidates, where a track in the Inner Detector has been matched to
1673 a standalone track in the Muon Spectrometer. The track parameters are combined statistically in the muon
1674 reconstruction algorithm [52]. The muons are required to be within $|\eta| < 2.5$ and have a $p_T > 10$ GeV.
1675 To reduce backgrounds coming from mis-reconstructed leptons, there are requirements on the impact
1676 parameter of the muon relative to the primary vertex. The transverse impact parameter d_0 is required to
1677 be small relative to its estimated uncertainty, the exact cut value being $d_0/\sigma_{d_0} < 3$. The longitudinal
1678 impact parameter z_0 must satisfy $|z_0 \sin \theta| < 1$ mm.

1679 As discussed previously, the muons must also be isolated. There are two types of lepton isolations that
1680 are calculated: track-based and calorimeter-based. For muons, the track-based isolation is defined using the
1681 scalar sum $\sum p_T$ for tracks with $p_T > 1$ GeV (excluding the muon’s track) within a cone of $\Delta R = 0.3$
1682 (0.4) for muon with $p_T > 15$ GeV ($10 < p_T < 15$ GeV). The final isolation requirement is made my
1683 requiring that this scalar sum be no more than a certain fraction of the muon’s p_T . This requirement varies
1684 with muon p_T and the exact cuts are defined in table 5.5.

1685 The calorimeter-based muon isolation is defined using as a $\sum E_T$ calculated from calorimeter cells us-
 1686 ing the same cone size as the track-based isolation but excluding cells with $\Delta R < 0.05$ around the muon.
 1687 This requirement is also defined as a cut on the ratio of the sum to the muon p_T and varies with muon p_T .
 1688 The cut values are also given in table 5.5.

 1689 The isolation requirements loosen as a function of p_T to allow for larger signal acceptance. At low p_T ,
 1690 the isolation is tightened to reduce the $W + \text{jets}$ background which arises from a misidentified lepton.

p_T range (GeV)	Calorimeter isolation	Track isolation
10 – 15	0.06	0.06
15 – 20	0.12	0.08
20 – 25	0.18	0.12
> 25	0.30	0.12

Table 5.5: p_T dependent isolation requirements for muons. Muons are required to have the amount of calorimeter or track based cone sums be less than this fraction of their p_T .

1691 5.3.2 ELECTRONS

1692 Electrons are identified by matching reconstructed clusters in the electromagnetic calorimeter with tracks
 1693 in the inner detector. The electrons are identified using a likelihood based method [49, 50] which takes
 1694 into account the shower shapes in the calorimeter, the matching of tracks to clusters, and the amount of
 1695 transition radiation in the TRT. The electrons are required to have $|\eta| < 2.47$, and candidates in the
 1696 transition region between the barrel and endcap ($1.37 < |\eta| < 1.52$) are excluded. As the muons, the
 1697 electrons are required to have transverse impact parameter significance < 3 , while in the longitudinal di-
 1698 rection they must have $|z_0 \sin \theta| < 0.4$ mm. Some electron requirements also vary with electron E_T , and
 1699 these requirements are summarized in table 5.6.

1700 The isolation for electrons are defined similarly to the muons but with unique cuts on the objects in-
 1701 cluded. The track-based isolation is defined using tracks with $p_T > 400$ MeV with cone sizes as defined
 1702 previously. The calorimeter-based isolation also uses the same cone size as the muon, but here the cells
 1703 within a 0.125×0.175 area in $\eta \times \phi$ around the electron cluster's barycenter are excluded. The other
 1704 difference with respect to muons is that the denominator of the isolation ratio is the electron's E_T rather
 1705 than p_T . The isolation cuts very with electron E_T and are defined in table 5.6.

1706 The electron is also required to not be consistent with a vertex coming from a photon conversion.

p_T range (GeV)	Quality cut	Calorimeter isolation	Track isolation
10 – 15	Very tight LH	0.20	0.06
15 – 20	Very tight LH	0.24	0.08
20 – 25	Very tight LH	0.28	0.10
> 25	Medium	0.28	0.10

Table 5.6: p_T dependent requirements for electrons. Electrons are required to have the amount of calorimeter or track based cone sums be less than this fraction of their E_T .

1707 5.3.3 JETS

1708 Jets are clustered with the anti- k_T reconstruction algorithm using a radius parameter of $R = 0.4$. They
1709 are required to have a jet vertex fraction (JVF) of at least 50%, meaning that half of the tracks associated with
1710 the jet originated from the primary vertex. Jets with no tracks associated (i.e. those outside the acceptance
1711 of the ID) do not have this requirement applied. Jets are required to have $p_T > 25$ GeV if they are within
1712 the tracking acceptance ($|\eta| < 2.4$). Jets with $2.4 < |\eta| < 4.5$ are required to have $p_T > 30$ GeV.
1713 This tighter requirement reduces jets from pileup in the region where JVF requirements cannot be applied.
1714 The two highest p_T jets in the event are referred to as the “VBF” jets and used to compute various analysis
1715 selections later.

1716 Identification of b -jets is done using the MV1 algorithm and is limited to the acceptance of the ID ($|\eta| <$
1717 2.5). The operating point of MV1 that is used is the one that is 85% efficient for identifying true b -jets. This
1718 operating point has a 10.3% of mis-tagging a light quark jet as a b -jet. In order to improve the rejection of b -
1719 jets, a lower threshold than the nominal p_T threshold described above is used. For the purposes of counting
1720 the number of b -jets, jets with p_T down to 20 GeV are used.

1721 5.3.4 OVERLAP REMOVAL

1722 There are some cases where certain reconstructed objects will overlap and one will have to be chosen
1723 (for example, an electron and a jet in the calorimeter). First, the case of lepton overlap is dealt with. If
1724 an electron candidate extends into the muon spectrometer, it is removed. If a muon or electron have a
1725 $\Delta R < 0.1$, the electron is removed and the muon is kept. If two electron candidates overlap within the

1726 same radius, then the higher E_T electron is kept. Next, the overlap between leptons and jets is considered.
1727 If an electron and jet are within $\Delta R < 0.3$ of one another, the electron is kept and the jet is removed.
1728 However, if a muon and jet overlap within $\Delta R < 0.3$, the jet is kept (as it is likely that the muon is the
1729 result of a semileptonic decay inside the jet).

1730 Once the overlap removal is complete, the final set of objects used in the analysis is defined.

1731 5.4 ANALYSIS SELECTION

1732 The VBF analysis uses two distinct selections. The first is a more standard selection, referred to as “cut-
1733 based”, that applies requirements on the VBF variables and uses m_T as the final discriminating variable.
1734 The second is a looser selection that uses a Boosted Decision Tree (BDT) score as the final discriminator in
1735 order to take advantage of the detailed correlations between the VBF variables. While the BDT analysis is
1736 ultimately more sensitive, the cut-based serves as an important component of the analysis. First, the cut-
1737 based allows for confirming the modeling and validity of many variables used as input to the BDT. Second,
1738 because this is the first use of such an MVA technique in the $H \rightarrow WW^*$ analysis, the cut-based selection
1739 allows confirmation of the final BDT result with a more traditional analysis. The cut-based techniques are
1740 the focus of this chapter, but connections to the BDT result will be illustrated when appropriate.

1741 One important note is that because this analysis is dedicated to the measurement of the VBF pro-
1742 duction mode of the Higgs, events coming from gluon fusion production with the Higgs decaying via
1743 $H \rightarrow WW^* \rightarrow \ell\nu\ell\nu$ are treated as background events. This will be seen throughout the various predic-
1744 tions shown.

1745 5.4.1 COMMON PRE-SELECTION

1746 Both the cut-based and BDT analyses have a common pre-selection that is applied before the main signal
1747 region requirements. The requirements on leptons are common to all n_j bins. The analysis requires two
1748 oppositely charged leptons, with the leading lepton required to have $p_T > 22$ GeV while the subleading
1749 lepton must have $p_T > 10$ GeV. Next, to remove low mass Z/γ^* events, a cut on the dilepton mass
1750 $m_{\ell\ell} > 10$ (12) GeV is applied in the different (same) flavor channel. In the same flavor channels, there is

1751 an additional veto placed on the region around the Z peak, requiring that $|m_{\ell\ell} - m_Z| > 15$ GeV.

1752 There are also requirements on the amount of missing transverse momentum in the event. These are
1753 only applied in the same flavor channels, as in the different flavor channels $t\bar{t}$ is the dominant background
1754 in $n_j \geq 2$. The BDT analysis requires $p_T^{\text{miss}} > 40$ GeV and $E_T^{\text{miss}} > 45$ GeV. The cut-based analysis
1755 must select more tightly on these variables to have maximal sensitivity and thus requires $p_T^{\text{miss}} > 50$ GeV
1756 and $E_T^{\text{miss}} > 55$ GeV.

1757 Finally, because this analysis is focused on VBF, a requirement on the jet multiplicity is placed, with
1758 $n_j \geq 2$. Additionally, the analysis requires that there are no jets identified as b-quarks in the event, or
1759 $n_b = 0$.

1760 5.4.2 CUT-BASED SELECTION

1761 The cut-based selection places sequential requirements on variables reconstructed from the VBF jets in
1762 order to increase the signal to background ratio.

1763 GENERAL BACKGROUND REDUCTION

1764 Top pair production is the primary background in the $n_j \geq 2$ bin. Even though $n_b = 0$ is required, an
1765 additional variable is constructed to further suppress the top background. There is often additional QCD
1766 radiation that accompanies the $t\bar{t}$ system when it is produced. Therefore, a variable which tests for the
1767 presence of this additional radiation, p_T^{sum} , is constructed. It is defined in equation 5.1.

$$p_T^{\text{sum}} = p_T^{\ell\ell} + p_T^{\text{miss}} + \sum p_T^j \quad (5.1)$$

1768 The first cut after pre-selection in the cut-based analysis requires $p_T^{\text{sum}} < 15$ GeV to further suppress $t\bar{t}$
1769 production.

1770 In the different flavor channels, a cut is made to reduce the contamination from $Z \rightarrow \tau\tau$ decays.
1771 The di- τ invariant mass, $m_{\tau\tau}$, is constructed by assuming that the neutrinos from the τ decays were
1772 collinear with the leptons [80]. The analysis requires that this mass not be consistent with a Z by requiring
1773 $m_{\tau\tau} < m_Z - 25$ GeV.

1774 VBF TOPOLOGICAL CUTS

1775 The characteristic feature of VBF production of the Higgs is the presence of two additional forward
1776 jets coming from the incoming partons which radiate the vector bosons that make the Higgs. These jets
1777 are forward because the outgoing partons still carry the longitudinal momentum of the incoming partons.
1778 Figure 5.2 shows the distribution of the η for the leading jet in a VBF event compared to a background top
1779 pair production event. As can be seen, the VBF jets tend to be more forward in η , while the $t\bar{t}$ jets are more
1780 central.

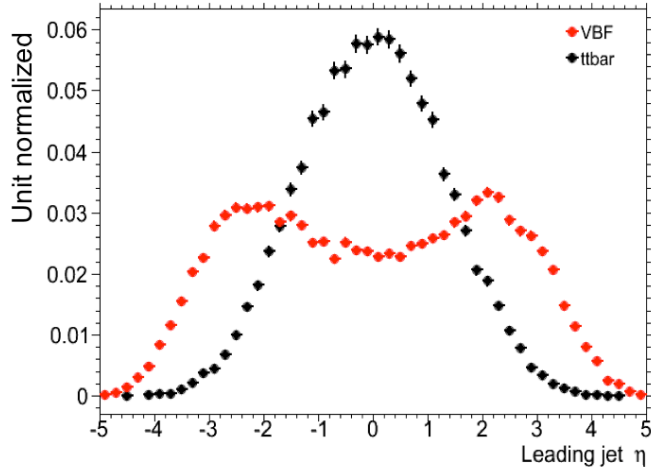


Figure 5.2: Leading jet η in VBF $H \rightarrow WW^*$ (red) and $t\bar{t}$ (black)

1781 Because the cross section for VBF production is an order of magnitude smaller than gluon fusion pro-
1782 duction, these forward jets must be used in order to better reduce background and achieve a good signal to
1783 background ratio. The dedicated VBF search selection requirements are constructed to maximally exploit
1784 the features of the unique VBF topology.

1785 Requirements on the VBF jets are collectively referred to as the “VBF topological cuts”. First, a require-
1786 ment on the dijet invariant mass of the VBF jets, m_{jj} , is placed, requiring $m_{jj} > 600$ GeV. Next, the
1787 event is required to have a large gap in rapidity between the two VBF jets, or $\Delta y_{jj} > 3.6$. Both of these
1788 cuts put tight requirements on the presence of two forward, high p_T jets moving in opposite directions in

1789 the longitudinal plane.

1790 Beyond requiring the presence of the two forward VBF jets, the analysis also vetoes on the presence
1791 of any additional jets that fall between the two VBF jets. This cut is referred to as the central jet veto, or
1792 CJV. Any events with a third jet with $p_T > 20$ GeV whose rapidity is between the region defined by the
1793 two VBF jets are vetoed. This can be expressed in terms of a variable called the jet centrality, defined in
1794 equation 5.2.

$$C_{j3} = \left| \eta_{j3} - \frac{\eta_{j1} + \eta_{j2}}{2} \right| / \frac{|\eta_{j1} - \eta_{j2}|}{2}, \quad (5.2)$$

1795 Here, η_{j1} and η_{j2} are the pseudorapidities of the leading and subleading jets, respectively, while η_{j3} is
1796 the pseudorapidity of the extra jet in the event (if one exists). Intuitively, C_{j3} is zero when η_{j3} is directly
1797 centered between the two jets and unity when η_{j3} is aligned with either of the VBF jets. Thus, the CJV
1798 can be expressed as a requirement that $C_{j3} > 1$.

1799 The decay products of the Higgs tend to be central as well. Thus, the analysis also requires that both
1800 leptons in the analysis fall within the rapidity gap defined by the jets. This cut is referred to as the outside
1801 lepton veto, or OLV. A quantitative way to define the cut is to require that the centrality of each lepton
1802 (defined analogously to that of the third jet in equation 5.2) correspond to the lepton being within the jet
1803 rapidity gap, or $C_\ell < 1$ for both leptons.

1804 Figure 5.3a-c shows the m_{jj} , Δy_{jj} , and $C_{\ell 1}$ variables at the stage where all previous cuts in the sequence
1805 have been made. The agreement between data and Monte Carlo is good, and the bottom panels show their
1806 power in discriminating the VBF signal from the background processes.

1807 The final signal region is also split into two bins of m_{jj} , with the first bin corresponding to $600 \text{ GeV} <$
1808 $m_{jj} < 1 \text{ TeV}$ and the second bin corresponding to $m_{jj} > 1 \text{ TeV}$. The first bin has more statistics but
1809 also a larger contribution from background, while the second bin has lower statistics but a 1:1 signal to
1810 background ratio.

1811 HIGGS TOPOLOGICAL CUTS

1812 The final state leptons will exhibit unique correlations due to the fact that they are arising from the
1813 decay of a spin zero resonance. In particular, the spins of the final state leptons and neutrinos must all

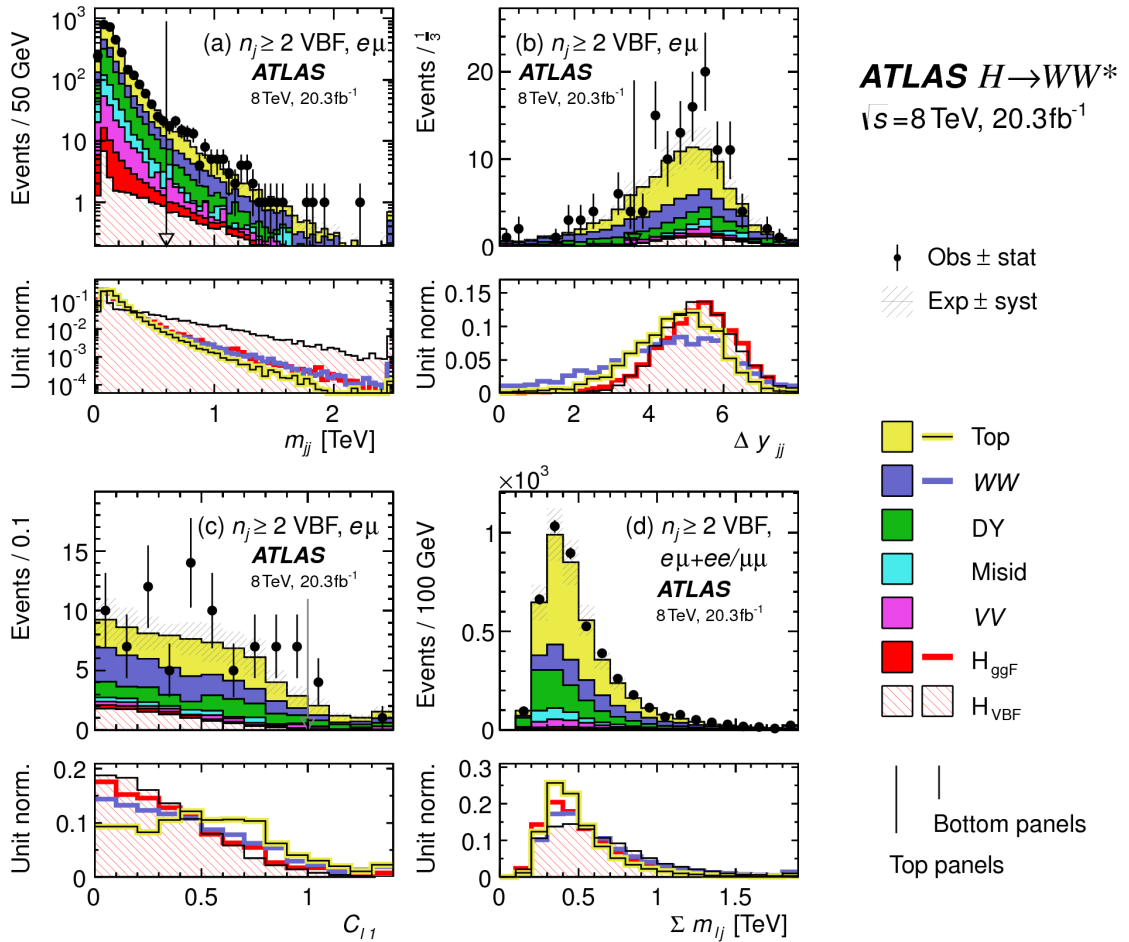


Figure 5.3: Distributions of (a) m_{jj} , (b) Δy_{jj} , (c) $C_{\ell 1}$, and (d) $\Sigma m_{\ell j}$, for the VBF analysis. The top panels compare simulation and data, while the bottom panels show normalized distributions for all background processes and signal [61].

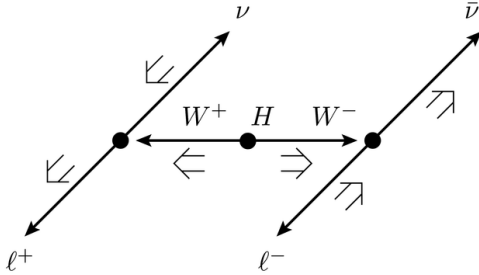


Figure 5.4: A cartoon of the WW final state. Momenta are represented with thin arrows, spins with thick arrows.
[61]

cancel, as shown in figure 5.4. Because the neutrino has a left handed chirality and the anti-neutrino has a right handed chirality (in the massless neutrino approximation), the spin and momentum of the particles will be anti-aligned and aligned, respectively. In the transverse plane, the momenta of all four final state objects must cancel as well. With the constraint of having both the momenta and the spin alignments cancel, the final state kinematics strongly prefer having a small angle between the leptons in the transverse plane (low $\Delta\phi_{\ell\ell}$). This angular correlation will also lead to low values of the di-lepton invariant mass $m_{\ell\ell}$. These unique signal final state kinematic correlations will be exploited to define the ultimate signal region.

The analysis places additional requirements on the final state leptons. Two requirements on dilepton kinematics are made that are common with lower multiplicity jet bins as well. The angle between leptons in the transverse plane, $\Delta\phi_{\ell\ell}$, is required to be less than 1.8 radians. Additionally, the dilepton mass $m_{\ell\ell}$ is required to be less than 50 GeV.

The cut-based analysis uses m_T as the final discriminating variable as in the ggF focused analysis. The optimal number of bins in m_T was found to be three bins, with the bin boundaries at 80 and 130 GeV.

Table 5.7 shows a summary of the data and estimated signal and background yields from simulation as each requirement described above is made. The table shows how the overall signal to background ratio grows through the various selection requirements. Table 5.8 shows the background composition after each selection requirement, illustrating which backgrounds are reduced most by certain requirements. Figure 5.5 shows an ATLAS event display of a candidate event in the final signal region.

Selection	Summary					
	$N_{\text{obs}}/N_{\text{bkg}}$	N_{obs}	N_{bkg}	N_{signal}		
				N_{ggF}	N_{VBF}	N_{VH}
$e\mu$ sample	1.00 ± 0.00	61434	61180	85	32	26
$n_b = 0$	1.02 ± 0.01	7818	7700	63	26	16
$p_T^{\text{sum}} < 15$	1.03 ± 0.01	5787	5630	46	23	13
$m_{\tau\tau} < m_Z - 25$	1.05 ± 0.02	3129	2970	40	20	9.9
$m_{jj} > 600$	1.31 ± 0.12	131	100	2.3	8.2	—
$\Delta y_{jj} > 3.6$	1.33 ± 0.13	107	80	2.1	7.9	—
$C_{j3} > 1$	1.36 ± 0.18	58	43	1.3	6.6	—
$C_{\ell 1} < 1, C_{\ell 2} < 1$	1.42 ± 0.20	51	36	1.2	6.4	—
$m_{\ell\ell}, \Delta\phi_{\ell\ell}, m_T$	2.53 ± 0.71	14	5.5	0.8	4.7	—
$ee/\mu\mu$ sample	0.99 ± 0.01	26949	27190	31	14	10.1
$n_b, p_T^{\text{sum}}, m_{\tau\tau}$	1.03 ± 0.03	1344	1310	13	8.0	4.0
$m_{jj}, \Delta y_{jj}, C_{j3}, C_\ell$	1.39 ± 0.28	26	19	0.4	2.9	0.0
$m_{\ell\ell}, \Delta\phi_{\ell\ell}, m_T$	1.63 ± 0.69	6	3.7	0.3	2.2	0.0

Table 5.7: Summary of event selection for the $n_j \geq 2$ VBF analysis in the 8 TeV cut-based analysis [61].

	Composition of N_{bkg}								
	N_{WW}		N_{top}		N_{misid}		N_{VV}	$N_{\text{Drell-Yan}}$	
	N_{WW}^{QCD}	N_{WW}^{EW}	$N_{t\bar{t}}$	N_t	N_{Wj}	N_{jj}	N_{VV}	$N_{ee/\mu\mu}^{\text{QCD}}$	$N_{\tau\tau}^{\text{EW}}$
$e\mu$ sample	1350	68	51810	2970	847	308	380	51	3260
$n_b = 0$	993	43	3000	367	313	193	273	35	2400
$p_T^{\text{sum}} < 15$	781	38	1910	270	216	107	201	27	2010
$m_{\tau\tau} < m_Z - 25$	484	22	1270	177	141	66	132	7.6	627
$m_{jj} > 600$	18	8.9	40	5.3	1.8	2.4	5.1	0.1	15
$\Delta y_{jj} > 3.6$	11.7	6.9	35	5.0	1.6	2.3	3.3	—	11.6
$C_{j3} > 1$	6.9	5.6	14	3.0	1.3	1.3	2.0	—	6.8
$C_{\ell 1} < 1, C_{\ell 2} < 1$	5.9	5.2	10.8	2.5	1.3	1.3	1.6	—	5.7
$m_{\ell\ell}, \Delta\phi_{\ell\ell}, m_T$	1.0	0.5	1.1	0.3	0.3	0.3	0.6	—	0.5
$ee/\mu\mu$ sample	594	37	23440	1320	230	8.6	137	690	679
$n_b, p_T^{\text{sum}}, m_{\tau\tau}$	229	12.0	633	86	26	0.9	45	187	76
$m_{jj}, \Delta y_{jj}, C_{j3}, C_\ell$	3.1	3.1	5.5	1.0	0.2	0.0	0.7	3.8	0.7
$m_{\ell\ell}, \Delta\phi_{\ell\ell}, m_T$	0.4	0.2	0.6	0.2	0.2	0.0	0.1	1.5	0.3

Table 5.8: Background composition after each requirement in the $n_j \geq 2$ VBF analysis in the 8 TeV cut-based analysis [61].

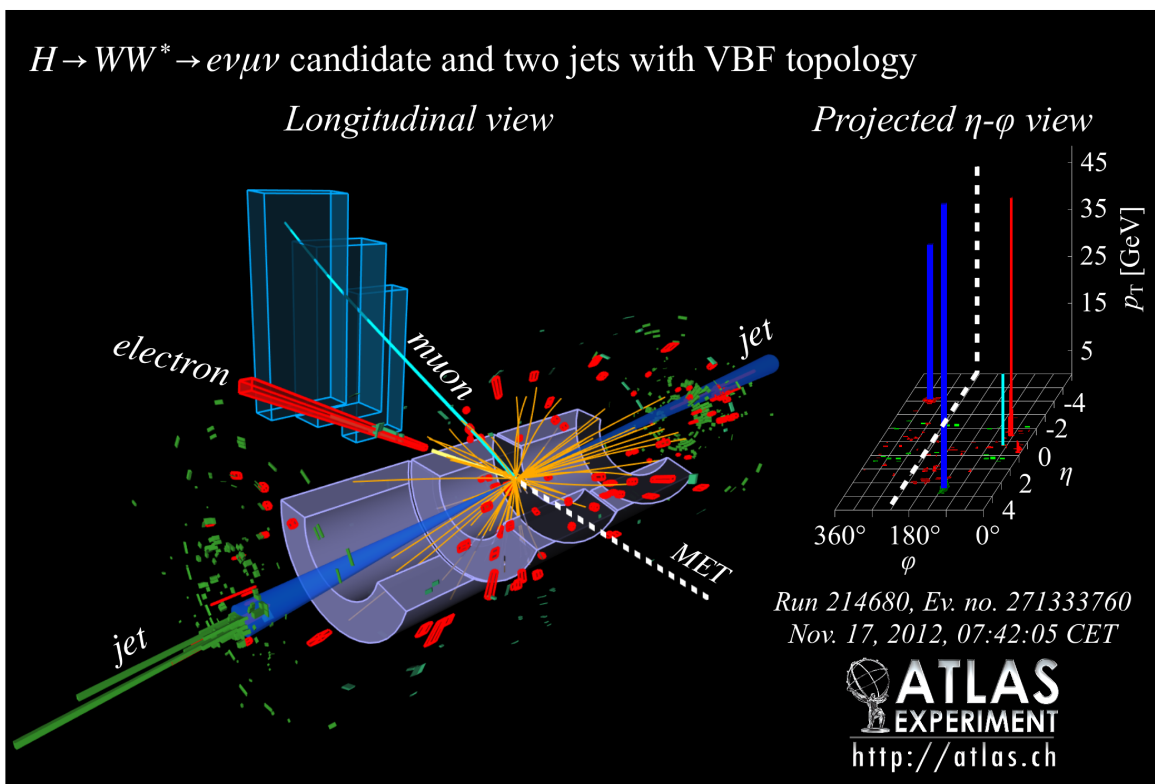


Figure 5.5: Event display of a VBF candidate event [61].

1832 5.4.3 BDT-BASED SELECTION

1833 The boosted decision tree based analysis takes a different philosophy compared to the cut-based. Rather
 1834 than cutting sequentially on many variables, the BDT analysis uses many of these variables as inputs to
 1835 the BDT and the output BDT score (O_{BDT}) as the final discriminant. The BDT is trained with the
 1836 VBF $H \rightarrow WW^*$ simulation as the signal samples and all other processes as background, including ggF
 1837 $H \rightarrow WW^*$ production. While the BDT based analysis is treated as a separate result, it has significant
 1838 overlap with the cut-based selection.

1839 PRE-TRAINING SELECTION AND BDT INPUTS

1840 Before training, the common pre-selection cuts described in section 5.4.1 are applied. Additionally, the
 1841 central jet veto and outside lepton veto described in section 5.4.2 are applied. The BDT has eight input
 1842 variables, six of which are also variables that are used in the cut-based analysis. The six shared variables

1843 are p_T^{sum} , m_{jj} , Δy_{jj} , $m_{\ell\ell}$, $\Delta\phi_{\ell\ell}$, and m_T . The seventh variable input in the BDT is a combination of
 1844 the variables used to do the OLV in the cut-based analysis. The BDT uses as input the sum of lepton
 1845 centralities, or $\sum C_\ell = C_{\ell 1} + C_{\ell 2}$. The final BDT input variable, $\Sigma m_{\ell j}$, is constructed to account for
 1846 the correlations between the jets and leptons in the event. It is the sum of the invariant masses of all four
 1847 possible lepton-jet combinations.

1848 Figure 5.3d shows the agreement between data and simulation for the $\Sigma m_{\ell j}$ variable, as well as showing
 1849 its discriminating power. Figure 5.6 shows the distributions of the Higgs topological variables that are
 1850 shared between the cut-based and BDT analyses. Figure 5.7 shows the distributions of the VBF topological
 1851 variables shared between the cut-based and BDT analyses. In both cases, the VBF yield has been scaled by
 1852 a factor of 50 to better show the shape difference compared to the backgrounds.

1853 Table ?? summarizes the cuts applied for the cut-based and analyses, as well as which variables are used
 1854 as input to the BDT.

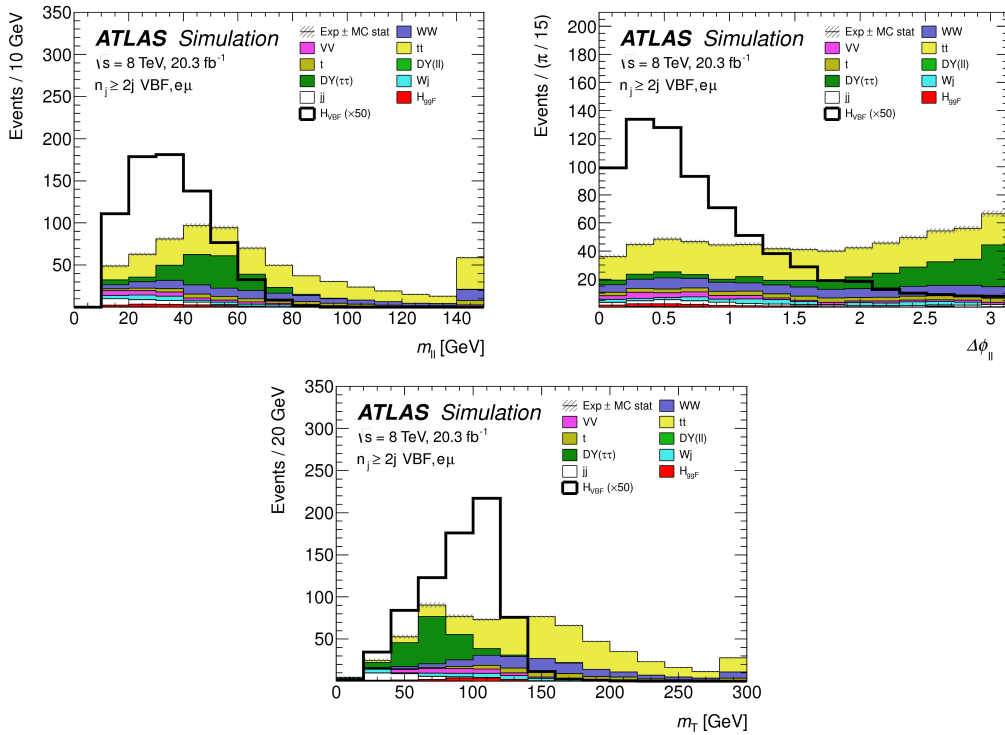


Figure 5.6: Distributions of $m_{\ell\ell}$ (top left), $\Delta\phi_{\ell\ell}$ (top right), and m_T (bottom), Higgs topology variables used in the selection requirements of the cut-based signal region and as inputs to the BDT result. These are plotted after all of the BDT pre-training selection cuts [61].

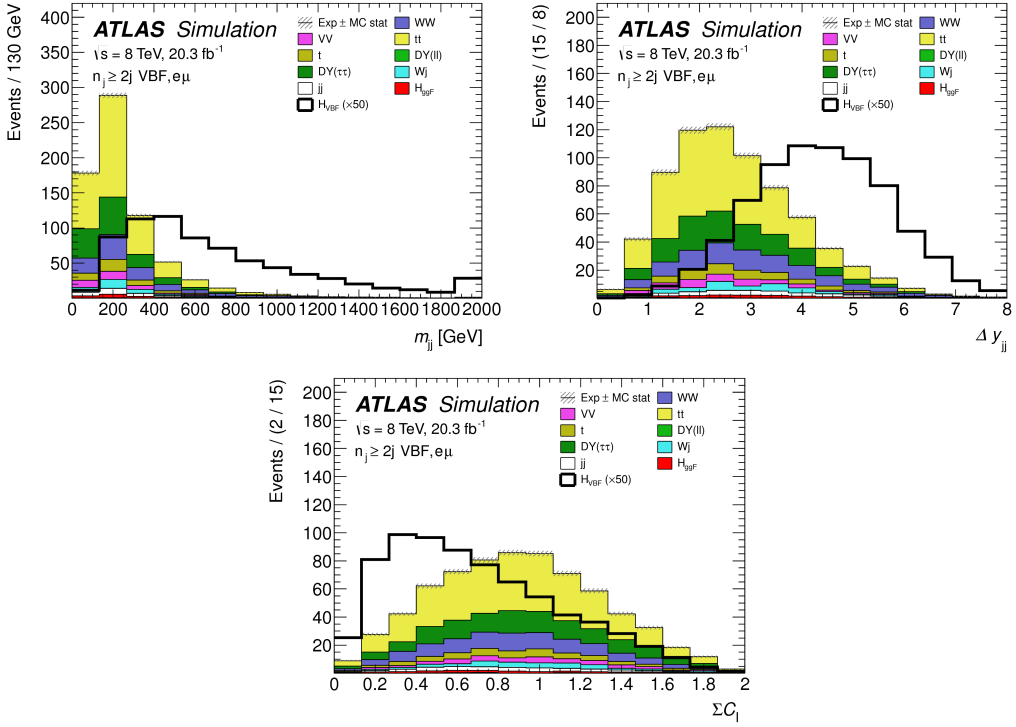


Figure 5.7: Distributions of m_{jj} (top left), Δy_{jj} (top right), $\sum C_\ell$ (bottom), VBF topology variables used in the selection requirements of the cut-based signal region and as inputs to the BDT result. These are plotted after all of the BDT pre-training selection cuts [61].

1855 5.5 BACKGROUND ESTIMATION

1856 This section describes the procedures used to estimate backgrounds for the VBF analysis in both the
 1857 cut-based and BDT analyses.

1858 5.5.1 GENERAL STRATEGY

1859 Most of the backgrounds in the VBF analysis have shapes estimated from Monte Carlo simulation but
 1860 normalizations derived from control regions in data. In essence, a normalization factor (denoted with β
 1861 or abbreviated as NF) is derived by scaling the MC yield in the control region to the corresponding yield
 1862 in data. Once this factor is derived, it can be used to scale the MC estimate of the background in the signal

1863 region. This is illustrated in equation 5.3.

$$B_{\text{SR}}^{\text{est}} = B_{\text{SR}} \times \frac{N_{\text{CR}}}{B_{\text{CR}}} \equiv B_{\text{SR}} \times \beta \quad (5.3)$$

1864 Here, B denotes the MC yield prediction in the denoted region, while N denotes the observed number of
1865 events in data in the denoted region.

1866 Another way of writing the same equation, in terms of an extrapolation factor α rather than a normal-
1867 ization factor β . The overall calculation is exactly the same. However, when phrased in this way, it shows
1868 how the uncertainty on the background estimation can be reduced. This is shown in equation 5.4.

$$B_{\text{SR}}^{\text{est}} = N_{\text{CR}} \times \frac{B_{\text{SR}}}{B_{\text{CR}}} \equiv N_{\text{CR}} \times \alpha \quad (5.4)$$

1869 Phrased this way, the equation shows that with enough statistics in the control region, a large theoretical
1870 uncertainty on the overall background yield in the signal region can be replaced by a small statistical un-
1871 certainty coming from the number of data events in the CR and a smaller theoretical uncertainty on the
1872 extrapolation from the control region to the signal region.

1873 5.5.2 TOP BACKGROUND

1874 The normalization factor β_t for the top background in the VBF analysis is derived in a region required
1875 to have one b-tagged jet, or $n_b = 1$. In the cut-based analysis, normalization factors are computed at every
1876 stage of the cutflow by applying the appropriate cuts in the CR. These NF are then applied to the $t\bar{t}$ and
1877 single top event yields in the SR. In the BDT analysis, a single normalization factor is computed for each
1878 bin of O_{BDT} after applying the BDT pre-training cuts described previously. The computed normaliza-
1879 tion factors are derived with all flavor combinations combined in order to decrease statistical uncertainty.
1880 Additionally, in the BDT analysis, BDT bins 2 and 3 are merged for the same reason.

1881 Table 5.9 shows the evolution of the β_t through the cut-based selection. Table 5.10 shows the value of
1882 the β_t in each bin of O_{BDT} . In all cases, the computed factors are relatively consistent with unity, with
1883 the largest discrepancy coming in bin 1 of O_{BDT} . The normalization factors in the bins of O_{BDT} are also

1884 consistent with those derived in teh cut-based sisgnal region, increasing confidence in the BDT estimation.

Cut	β_t
$p_T^{\text{sum}} < 15 \text{ GeV}$	1.03 ± 0.01
$m_{\tau\tau} < m_Z - 25$	1.05 ± 0.01
$m_{jj} > 600 \text{ GeV}$	0.96 ± 0.06
$\Delta y_{jj} > 3.6$	1.02 ± 0.08
CJV	1.13 ± 0.16
OLV	1.01 ± 0.19
$m_{jj} < 1 \text{ TeV}$	0.94 ± 0.19
$m_{jj} > 1 \text{ TeV}$	1.48 ± 0.66

Table 5.9: Top normalization factors computed at each stage of the cut-based selection. Uncertainties are statistical only.

O_{BDT}	β_t
Bin0	1.09 ± 0.02
Bin1	1.58 ± 0.15
Bin2	0.95 ± 0.31
Bin3	0.95 ± 0.31

Table 5.10: Top normalization factors computed for each bin of O_{BDT} . Uncertainties are statistical only.

1885 Figure 5.8 shows the m_{jj} and O_{BDT} distributions in the top control region. Overall the modeling looks
1886 consistent with the data.

1887 While these normalization factors can be computed and applied to the expected background yields listed
1888 in tables like table ??, in the end the normalization of the top background is profiled (meaning there is a
1889 dedicated Poisson constraint) and allowed to float in the final statistical fit.

1890 5.5.3 $Z/\gamma^* \rightarrow \tau\tau$ BACKGROUND

1891 In the different flavor channels, the $Z/\gamma^* \rightarrow \tau\tau$ background is an important one. Di-tau production
1892 can produce an $e\mu$ final state if each τ lepton decays to a different flavor lepton.

1893 In the BDT analysis, a single normalization factor for the background is derived. A control region
1894 is defined using the pre-training selection cuts, except requiring that $|m_{\tau\tau} - m_Z| < 25 \text{ GeV}$ so that
1895 the region is enriched in $Z/\gamma^* \rightarrow \tau\tau$ background. Additional requirements of $m_{\ell\ell} < 80(75) \text{ GeV}$

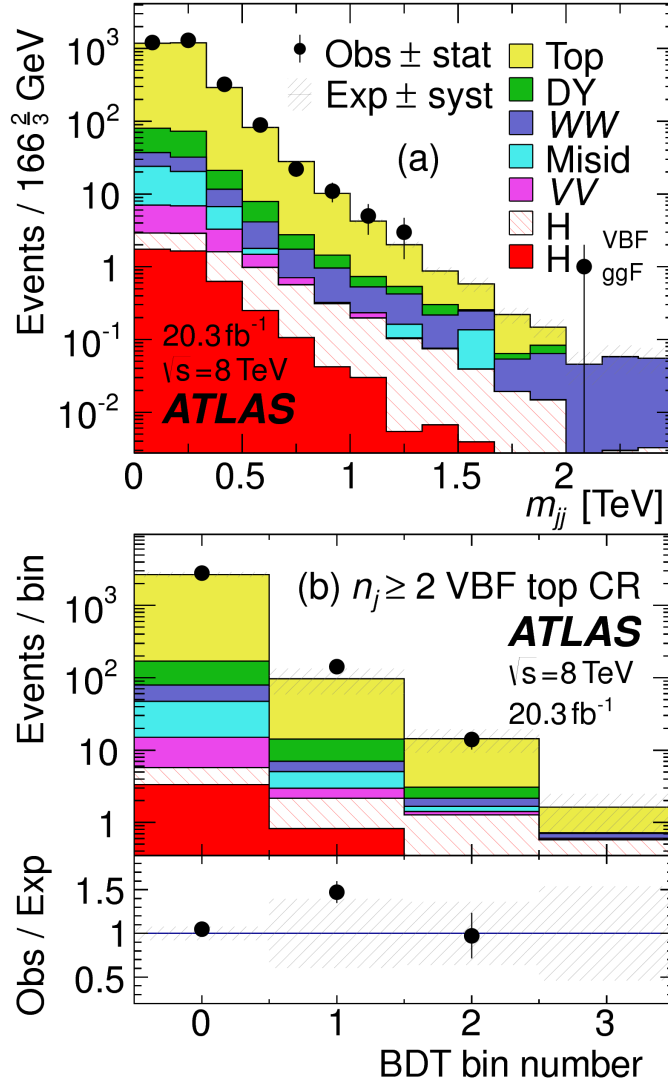


Figure 5.8: Distributions of m_{jj} (a) and O_{BDT} (b) in the VBF $n_b = 1$ top CR [61].

in the different (same) flavor channel, as well as $O_{\text{BDT}} > -0.48$ are applied to increase the purity of the region. The final $\beta_{Z/\gamma^* \rightarrow \tau\tau}$ is calculated to be 0.9 ± 0.3 (statistical uncertainty only). Because of the small contribution of this background in the BDT analysis and the large statistical uncertainty, no additional systematics are calculated. The final SR estimate is scaled by this β and not allowed to float in the fit.

The cut-based corrections are a bit more involved because they need to be applied selection by selection, as well as in the final signal region for the fit. The region is defined including all SR cuts up to the $Z/\gamma^* \rightarrow \tau\tau$ veto, which is instead made into a Z mass peak requirement as for the BDT region. The $m_{\ell\ell}$ cut from

1903 the BDT region is included as well. The cut-based approach aims to correct the normalization of the
 1904 $Z/\gamma^* \rightarrow \tau\tau$ background in two ways. First, an overall normalization factor is computed from the control
 1905 region. However, the VBF topological cuts are not included in this region, and applying them as is done in
 1906 the top CR is not feasible due to limited statistics. So, instead, correction factors (CF) to the cut efficiencies
 1907 of the VBF cuts are derived in a same flavor $Z \rightarrow \ell\ell$ control region, which has significantly more statistics.
 1908 The CF is simply the ratio of the cut efficiencies in data and MC derived in this region. In the end, the
 1909 overall background estimate is given by equation 5.5.

$$N_{Z/\gamma^* \rightarrow \tau\tau}^{\text{est}} = B_{Z/\gamma^* \rightarrow \tau\tau}^{\text{SR}} \times \beta_{\tau\tau} \times \frac{\epsilon_{\text{VBF cuts}}^{\text{data}}}{\epsilon_{\text{VBF cuts}}^{\text{MC}}} \quad (5.5)$$

1910 The hypothesis is that while the normalization correction must be derived in a dedicated region, the ef-
 1911 ficiency of the VBF cuts should not be sensitive to the type of Z/γ^* process and thus the larger control
 1912 region can be exploited to derive the CF. Figure 5.9 shows a shape comparison for the m_{jj} variable in
 1913 $Z \rightarrow \tau\tau$ events in the signal region and $Z \rightarrow \ell\ell$ events in the control region. The figure shows that the
 1914 shapes are indeed comparable and thus any CF derived in the same flavor control region can reliably be
 1915 applied in the signal region.

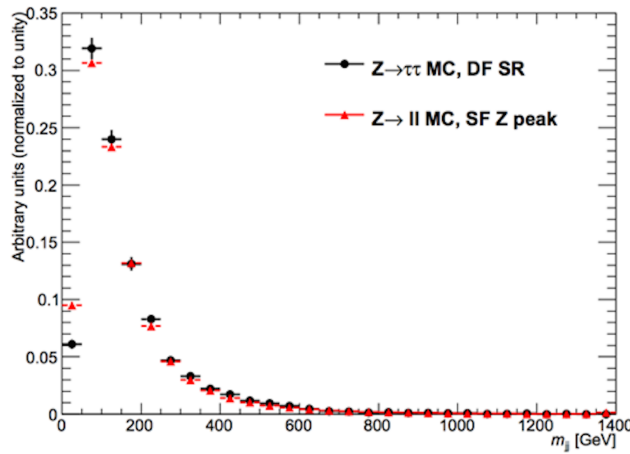


Figure 5.9: Comparison of m_{jj} shape in a same flavor $Z \rightarrow \ell\ell$ control region and the VBF cut-based signal region.

1916 Table 5.11 shows the overall normalization factor $\beta_{\tau\tau}$ and the efficiency correction factors for the various
 1917 VBF topological cuts. In general, the statistical uncertainties on the cut efficiency corrections are quite

¹⁹¹⁸ good, and the MC tends to underestimate the efficiency of the VBF cuts for the $Z/\gamma^* \rightarrow \tau\tau$ background.
¹⁹¹⁹ The overall normalization factor is also consistent with that calculated for the BDT analysis.

$\beta_{\tau\tau}$	0.97 ± 0.04
Cut	Correction factors
$m_{jj} > 600 \text{ GeV}$	1.09 ± 0.01
$\Delta y_{jj} > 3.6$	1.14 ± 0.02
CJV	1.20 ± 0.02
OLV	1.17 ± 0.03
$m_{jj} < 1 \text{ TeV}$	1.17 ± 0.06
$m_{jj} > 1 \text{ TeV}$	1.18 ± 0.13

Table 5.II: $Z/\gamma^* \rightarrow \tau\tau$ correction factors for the VBF cut-based analysis. Uncertainties are statistical only.

¹⁹²⁰ **5.5.4 $Z/\gamma^* \rightarrow \ell\ell$ BACKGROUND**

¹⁹²¹ In the same flavor channels, the $Z/\gamma^* \rightarrow \ell\ell$ background is dominant and thus must be estimated cor-
¹⁹²² rectly. In both the BDT and cut-based analyses, the background is estimated using the so-called “ABCD”
¹⁹²³ method. The ABCD method creates four different regions by defining cuts on two variables. One of the
¹⁹²⁴ regions (A) is the signal region, while the other regions are defined by inverting one of both of the cuts.
¹⁹²⁵ in this case, the two variables used are $m_{\ell\ell}$ and E_T^{miss} , because inverting either of the SR cuts on these
¹⁹²⁶ variables will give regions rich in the $Z/\gamma^* \rightarrow \ell\ell$ background. Figure 5.10 illustrates the general strategy
¹⁹²⁷ for each region.

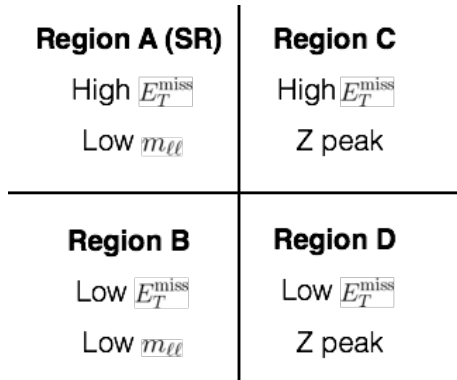


Figure 5.10: General illustration of the ABCD region definitions for $Z/\gamma^* \rightarrow \ell\ell$ background estimation.

¹⁹²⁸ In both of the cut-based and BDT analyses, the Z peak region is defined with $|m_{\ell\ell} - m_Z| < 15 \text{ GeV}$.

1929 In the cut-based analysis, low $m_{\ell\ell}$ corresponds to $m_{\ell\ell} < 50$ GeV (this defines the cut-based SR) while
 1930 in the BDT it is $m_{\ell\ell} < 75$ GeV. In the cut-based, high and low E_T^{miss} are defined as opposite ends of
 1931 the 55 GeV cut applied for the signal region definition. The BDT low E_T^{miss} region is between 25 and
 1932 45 GeV, while the high E_T^{miss} region is $E_T^{\text{miss}} > 45$ GeV.

1933 Once the regions are defined, the final signal region background estimate is done by taking the estimate
 1934 in region B and extrapolating it to the signal region (A) by multiplying it by the ratio of regions C and
 1935 D. Effectively, the Z peak region is used to estimate the efficiency of the E_T^{miss} cut in data, and then this
 1936 efficiency is applied in the low $m_{\ell\ell}$ region. An additional correction is also applied for the non-closure of
 1937 the method in MC. This is summarized in equations 5.6 and 5.7.

$$N_{Z/\gamma^* \rightarrow \ell\ell}^{\text{SR}} = N_{Z/\gamma^* \rightarrow \ell\ell}^B \times \frac{N_{Z/\gamma^* \rightarrow \ell\ell}^C}{N_{Z/\gamma^* \rightarrow \ell\ell}^D} \times f_{\text{corr}} \quad (5.6)$$

$$f_{\text{corr}} = \frac{B_{\text{MC}}^A / B_{\text{MC}}^B}{B_{\text{MC}}^C / B_{\text{MC}}^D} \quad (5.7)$$

1938 Here, the N refer to data yields in each region with the non Z/γ^* backgrounds subtracted, while B
 1939 refer to the Z/γ^* yields in MC in each region.

1940 A normalization factor $\beta_{\ell\ell}$ is computed for each analysis as the ratio of the predicted data yield to the
 1941 MC yield in the SR. The shape of the BDT distribution is taken from data region B, while the shape of
 1942 the m_T distribution in the cut-based analysis is taken from Z/γ^* MC in the SR. The values of the $\beta_{\ell\ell}$ in
 1943 the cut-based and BDT analyses from this method are summarized in table 5.12. They are quite consistent
 1944 with one another within the statistical uncertainties. In the cut-based analysis, the same cut efficiency
 1945 correction factors shown in table 5.11 are also applied (in product with the $\beta_{\ell\ell}$) in the same flavor channels
 1946 to this background, as they were derived in the Z peak region.

	$\beta_{\ell\ell}$
BDT Bin 1	1.01 ± 0.15
BDT Bin 2	0.89 ± 0.28
Cut-based	0.81 ± 0.21

Table 5.12: $Z/\gamma^* \rightarrow \ell\ell$ normalization factors for cut-based and BDT analyses. Uncertainties are statistical only.

1947 **5.5.5 WW AND OTHER DIBOSON BACKGROUNDS**

1948 The WW and other diboson backgrounds have both their shape and normalization taken from MC
 1949 simulation. They are validated in dedicated control regions and found to agree with data well.

1950 As WW is the largest of these backgrounds and is irreducible, validating the estimate is of particular
 1951 importance. The validation region is constructed by requiring the pre-selection cuts on leptons and $m_{\ell\ell}$,
 1952 $n_b = 0$, and $m_T > 100$ GeV. The m_{T2} variable [81] is an additional discriminant that will isolate
 1953 the WW background, and a requirement of $m_{T2} > 160$ GeV is placed to define the WW validation
 1954 region. This cut gives a 60% purity for the validation region. The derived normalization factor in the
 1955 region is 1.15 ± 0.19 and is thus consistent with unity. Figure 5.11 shows the m_{T2} distribution and how it
 1956 distinguishes the WW background.

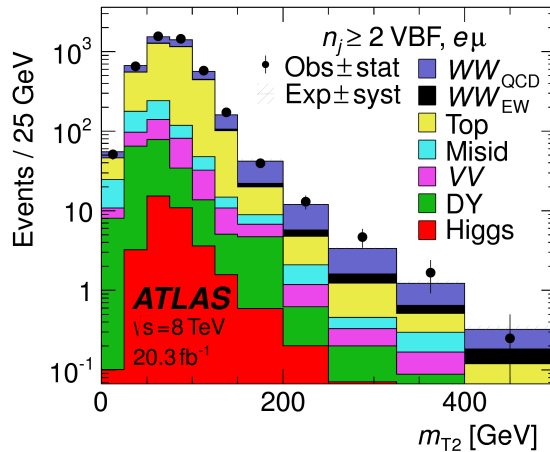


Figure 5.11: Distribution of m_{T2} in the WW validation region of the VBF analysis [61].

1957 **5.5.6 HIGGS PRODUCTION VIA GLUON-GLUON FUSION**

1958 Because this analysis is dedicated to measuring the VBF contribution to Higgs production, the compo-
 1959 nent of Higgs production from gluon-gluon fusion is treated as a background. The shape is taken directly
 1960 from simulation, using the generators described in table 5.4. In the final combined fit of all different signal
 1961 regions, the normalization is controlled by either a combined signal strength parameter μ , which controls
 1962 the normalization of both ggF and VBF production, or a separate parameter μ_{ggF} depending on the in-

1963 terpretation being presented in the final results.

1964 5.5.7 BACKGROUNDS WITH MISIDENTIFIED LEPTONS

1965 As discussed previously, the $W + \text{jets}$ and QCD multijet backgrounds are derived with fully data-driven
1966 methods. These backgrounds do not make a large contribution to the final VBF signal region but their
1967 estimation methods are discussed briefly here.

1968 $W + \text{jets}$ BACKGROUND

1969 The $W + \text{jets}$ background enters the signal region by having one of the jets mis-reconstructed as a lep-
1970 ton. The background is estimated by constructing a control sample with two leptons, where one lepton
1971 passes the usual lepton quality cuts but the second lepton fails one of those cuts (also known as the “anti-
1972 identified” lepton). This control region is rich in the $W + \text{jets}$ contribution because if a second lepton is
1973 reconstructed in a $W + \text{jets}$ event it is likely to be poor quality. The purity of this $W + \text{jets}$ control sample is
1974 85% to 90% depending on the exact configuration of leptons in the final state.

1975 The signal region estimate of $W + \text{jets}$ is estimated by extrapolation from the control sample to the sig-
1976 nal region using extrapolation factors derived in a $Z + \text{jets}$ control sample in data. The extrapolation factor
1977 is the ratio of the number of lepton candidates satisfying all quality criteria to the number of lepton can-
1978 didates anti-identified. This ratio is measured in bins of p_T and η . Thus, the final signal region estimate
1979 (binned as the extrapolation factor is binned) is simply the number of events in the anti-identified lepton
1980 control sample multiplied by the extrapolation factor derived from the $Z + \text{jets}$ control sample. Figure 5.12
1981 shows the extrapolation factors derived for electrons and muons.

1982 QCD MULTIJET BACKGROUND

1983 The method for estimating the multijet background is very similar to the $W + \text{jets}$ estimation method.
1984 The control sample in this case has two anti-identified leptons but otherwise satisfies all signal region re-
1985 quirements. The extrapolation factor is estimated from a multijet sample and applied twice to the control
1986 sample.

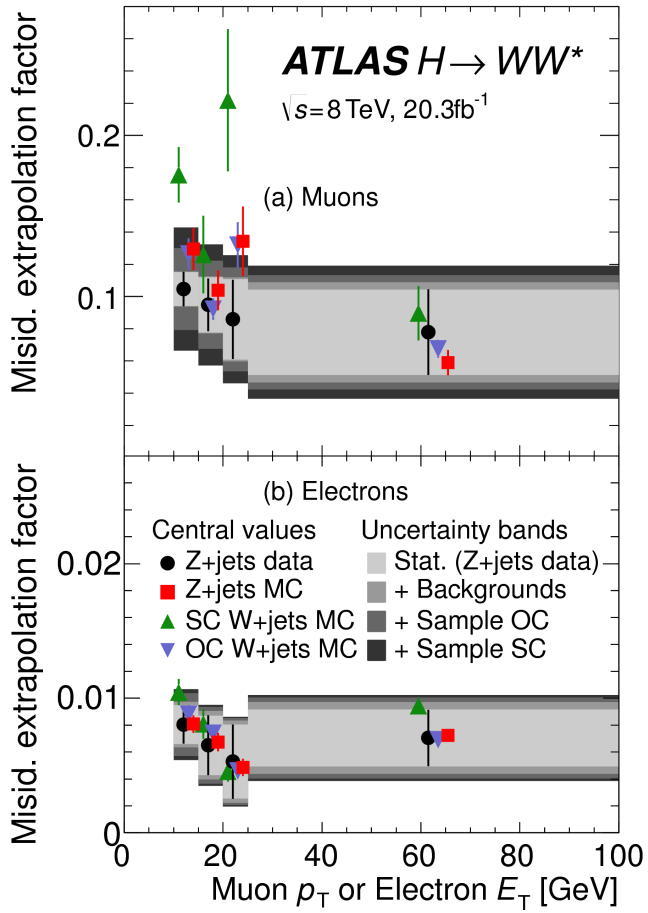


Figure 5.12: Extrapolation factors for the $W + \text{jets}$ estimate derived for muons (a) and electrons (b) as a function of lepton p_T [61].

1987 5.5.8 BACKGROUND COMPOSITION IN FINAL SIGNAL REGION

1988 After all of these estimation procedures, the final signal region composition can be calculated. The esti-
 1989 mated yields are all shown in table ???. Figure 5.13 shows the relative percentages of the different background
 1990 for the different flavor and same flavor final states. In $e\mu$, the leading backgrounds are top backgrounds,
 1991 ggF Higgs, and SM WW production. In $ee/\mu\mu$, the leading background is Drell-Yan, followed by top
 1992 and ggF Higgs.

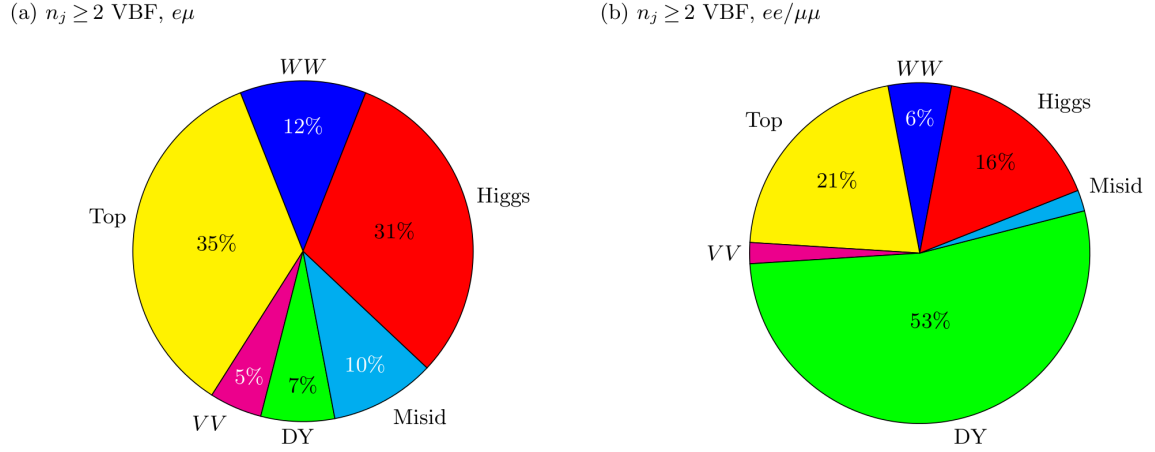


Figure 5.13: Background composition in final VBF signal region [61].

1993 5.6 SYSTEMATIC UNCERTAINTIES

1994 There are two main types of systematic uncertainties that are assessed for the analysis. First, theoretical
 1995 uncertainties associated with the various signal and background yield estimates are discussed. Then, exper-
 1996 imental uncertainties due to detector effects are shown. Normalization uncertainties refer to uncertainties
 1997 that affect the cross section of the process in question in the signal region being probed. Shape uncertain-
 1998 ties refer to systematic uncertainties that affect the shape of the final discriminating variable (either m_T or
 1999 O_{BDT}).

2000 5.6.1 THEORETICAL UNCERTAINTIES

2001 There are four main components to theoretical uncertainties assigned to signal and background pro-
 2002 cesses taken from Monte Carlo. Each one is a different source of variation in the overall acceptance for
 2003 that process. The first involves variation of the QCD renormalization and factorization scales used in the
 2004 calculation. In this case, the two scales are varied independently and simultaneously by factors of two high
 2005 or low and quantifying the resulting variation in normalization and shape for the process. This approx-
 2006 imates the correction to the cross section that would come from including the next order of the QCD
 2007 calculation (referred to as scale uncertainty). Next, there is an uncertainty associated with the PDF set
 2008 used in generating the events. The uncertainty eigenvectors for the given PDF set are studied, and the en-

2009 envelope of maximal variation is taken as an uncertainty. Finally, there are two uncertainties associated with
 2010 the choice of MC software (referred to as PDF uncertainty). An uncertainty associated with the generator
 2011 chosen for the hard scattering process is evaluated by keeping the parton showering software constant but
 2012 varying the matrix element generator and taking the maximal variation as an uncertainty (referred to as
 2013 the generator uncertainty). The converse variation can also be done, where the matrix element generator
 2014 remains constant and the generator used for the underlying event/parton shower modeling is varied (re-
 2015 ferred to as the UE/PS uncertainty). In cases where the background is normalized in a control region, the
 2016 systematic uncertainty arises from variations of the extrapolation factor α between the CR and the SR,
 2017 which can affect the normalization of the background in the SR.

2018 There are two additional uncertainties that are applied to the Higgs processes as well. First, there are
 2019 uncertainties assigned to the Higgs total production cross section. Then, there are uncertainties assigned
 2020 based on the fact that the analysis is done in exclusive jet bins and it is possible for signal events to migrate
 2021 from one bin to the next depending on the presence or absence of jets. These are assigned using the Jet
 2022 Veto Efficiency (JVE) procedure [18, 82] for ggF events and the Stewart-Tackmann (ST) method [83] for
 2023 VBF production.

2024 Table 5.13 shows the total theory uncertainties on the backgrounds in the cut-based analysis. These are
 2025 the sum in quadrature of the uncertainties from each of the variations described above.

Process	Theory syst. (%)
ggF H	48
Top	26
QCD WW	37
$Z/\gamma^* \rightarrow \tau\tau$	6.1

Table 5.13: Systematic uncertainties for various processes in the cut-based VBF analysis, given in units of % change
in yield. Values are given for the low m_{jj} signal region.

2026 Figures 5.14 and 5.15 show the variations in the extrapolation factor from the PDF and QCD uncertain-
 2027 ties on the top background estimate, binned in m_T , for the cut-based analysis. In both cases, there was
 2028 no significant shape uncertainty but normalization uncertainties were assigned according to the maximal
 2029 variation. These uncertainties enter into the 26% total uncertainty on top quoted in table 5.13

2030 While the estimate for the same-flavor $Z/\gamma^* \rightarrow \ell\ell$ background is data-driven, there is still a systematic
 2031 uncertainty taken for the non-closure of the method in Monte Carlo. This is taken as the maximum of the
 2032 deviation of the non-closure factor f_{corr} from unity and its uncertainty, or $\max(|1 - f_{\text{corr}}|, \delta f_{\text{corr}})$. For
 2033 the cut-based analysis this non-closure uncertainty 23%, while for the BDT analysis it is 17%.

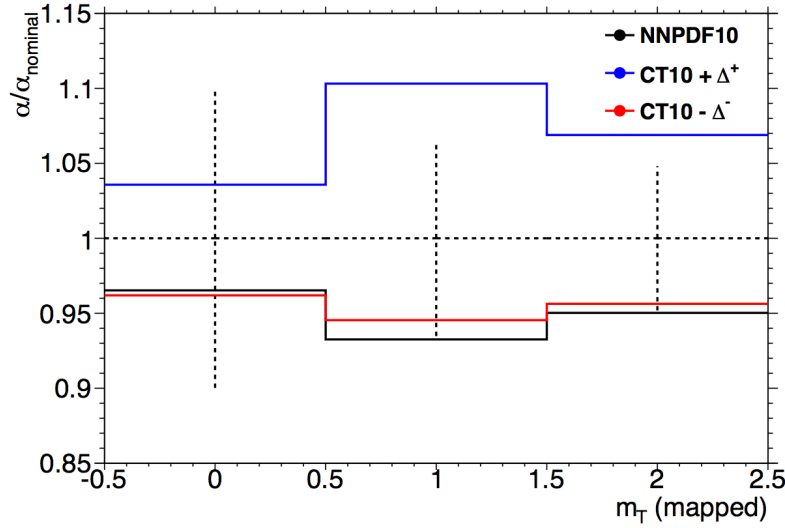


Figure 5.14: Variations in the top background extrapolation factor in the cut-based analysis due to PDF uncertainties, binned in m_T .

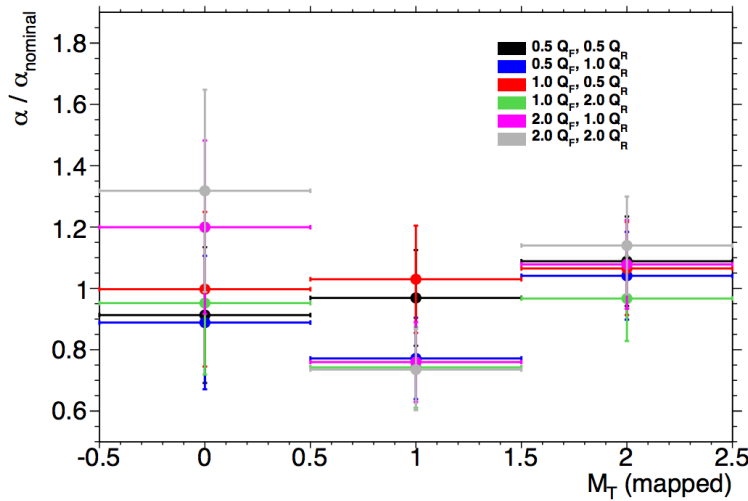


Figure 5.15: Variations in the top background extrapolation factor in the cut-based analysis due to QCD scale uncertainties, binned in m_T .

2034 5.6.2 EXPERIMENTAL UNCERTAINTIES

2035 In this analysis, the theoretical uncertainties end up being the most dominant, but there are some ex-
2036 perimental uncertainties that make a contribution as well. The first is the uncertainty on the measured
2037 integrated luminosity, which affects backgrounds whose normalization is taken from MC and is measured
2038 to be 2.8% in the 8 TeV dataset [84]. The dominant sources of uncertainty overall are uncertainties on the
2039 jet energy scale and resolution and the b -tagging efficiency. Additional sources include lepton uncertain-
2040 ties on identification, resolution, and trigger efficiency, as well as uncertainties on the missing transverse
2041 momentum .

2042 The jet energy scale uncertainty is split into several independent components, including jet-flavor de-
2043 pending calorimeter response uncertainties, uncertainties on modeling of pile-up interactions, uncertain-
2044 ties on extrapolation from the central to forward detector regions, and MC non-closure [85]. The uncer-
2045 tainty on energy scale for jets used in this analysis ranges from 1% to 7% depending on the jet p_T and η .
2046 The jet energy resolution varies from 5% to 20%, with uncertainties ranging from 2% to 40% (the largest
2047 uncertainties occurring at the selection threshold).

2048 The b -tagging efficiency is independently measured in data samples enriched in dileptonic decays of $t\bar{t}$
2049 events or in events where a muon is reconstructed in the vicinity of a jet [86, 87]. The efficiencies and
2050 their uncertainties are binned in p_T and decomposed into uncorrelated components using an eigenvector
2051 method [88]. Uncertainties on the efficiency range from 1% to 7.8%. The uncertainty on the rate of
2052 misidentification of c -jets as b -jets ranges from 6-14%, while the uncertainty on the rate of light jet mis-
2053 tagging ranges from 9-19% depending on p_T and η .

2054 The total experimental uncertainties on different signal and background components are summarized
2055 in table 5.14. They are compared to the level of other statistical and systematic uncertainties as well. Overall,
2056 the experimental uncertainties are sub-dominant compared to the statistical and theoretical uncertainties.

2057 5.7 RESULTS

2058 While the combined results of all the $H \rightarrow WW^*$ sub-analyses will be discussed in the next chapter,
2059 this section presents the results of the VBF specific analysis and interpretations. As table ?? shows, the final

Sample	Total error	Stat. error	Expt. syst. err.	Theo. syst. err.
$n_j \geq 2$ VBF-enriched				
N_{sig}	13	—	6.8	12
N_{bkg}	9.2	4.7	6.4	4.5
N_{WW}	32	—	14	28
N_{top}	15	9.6	7.6	8.5
N_{misid}	22	—	12	19
N_{VV}	20	—	12	15
$N_{\tau\tau}$ (DY)	40	25	31	2.9
$N_{ee/\mu\mu}$ (DY)	19	11	15	—

Table 5.14: Composition of the post-fit uncertainties (in %) on the total signal (N_{sig}), total background (N_{bkg}), and individual background yields in the VBF analysis [61].

2060 cut-based signal region contains 20 events in data with $m_T < 150$ GeV, 14 coming from the $e\mu$ channel
 2061 and 6 coming from the $ee + \mu\mu$ channel. The BDT analysis has many more candidates due to its looser
 2062 selection, and the yields in each bin of O_{BDT} are shown in table 5.15.

(a) Before the BDT classification

Selection	Summary						Composition of N_{bkg}										
	$N_{\text{obs}}/N_{\text{bkg}}$	N_{obs}	N_{bkg}	N_{signal}			N_{WW}^{QCD}	N_{WW}^{EW}	N_{tt}	N_t	N_{Wj}	N_{jj}	N_{VV}	$N_{\text{Drell-Yan}}$	$N_{ee/\mu\mu}^{\text{QCD}}$	$N_{\tau\tau}^{\text{QCD}}$	$N_{\tau\tau}^{\text{EW}}$
				N_{ggF}	N_{VBF}	N_{VH}											
$e\mu$ sample	1.04 ± 0.04	718	689	13	15	2.0	90	11	327	42	29	23	31	2.2	130	2	
$ee/\mu\mu$ sample	1.18 ± 0.08	469	397	6.0	7.7	0.9	37	3	132	17	5.2	1.2	10.1	168	23	1	

(b) Bins in O_{BDT}

$e\mu$ sample																
Bin 0 (not used)	1.02 ± 0.04	661	650	8.8	3.0	1.9	83	9	313	40	26	21	28	2.2	126	1
Bin 1	0.99 ± 0.16	37	37	3.0	4.2	0.1	5.0	1.0	17	3.1	3.3	1.8	2.6	—	4.0	0.2
Bin 2	2.26 ± 0.63	14	6.2	1.2	4.2	—	1.5	0.5	1.8	0.3	0.4	0.3	0.8	—	0.3	0.3
Bin 3	5.41 ± 2.32	6	1.1	0.4	3.1	—	0.3	0.2	0.3	0.1	—	—	0.1	—	0.1	0.1
$ee/\mu\mu$ sample																
Bin 0 (not used)	1.91 ± 0.08	396	345	3.8	1.3	0.8	33	2	123	16	4.1	1.1	8.8	137	20.5	0.5
Bin 1	0.82 ± 0.14	53	45	1.5	2.2	0.1	3.0	0.5	10.4	1.8	0.8	0.2	0.9	26	1.7	0.1
Bin 2	1.77 ± 0.49	14	7.9	0.6	2.5	—	0.8	0.3	1.1	0.2	0.2	—	0.3	4.4	0.3	0.1
Bin 3	6.52 ± 2.87	6	0.9	0.2	1.7	—	0.1	0.2	0.2	—	—	—	—	0.7	—	—

Table 5.15: Event selection for the VBF BDT analysis. The event yields in (a) are shown after the pre-selection and the additional requirements applied before the BDT classification (see text). The event yields in (b) are given in bins in O_{BDT} after the classification [61].

2063 Figure 5.16(a) shows the final distribution of data candidates compared to the expected m_T distribution
 2064 for signal and background. The data are very consistent with a VBF Higgs hypothesis. Figure 5.16(b) shows

2065 where the data candidates fall in the two-dimensional binning of m_T and m_{jj} used in the fit for the cut-
 2066 based analysis.

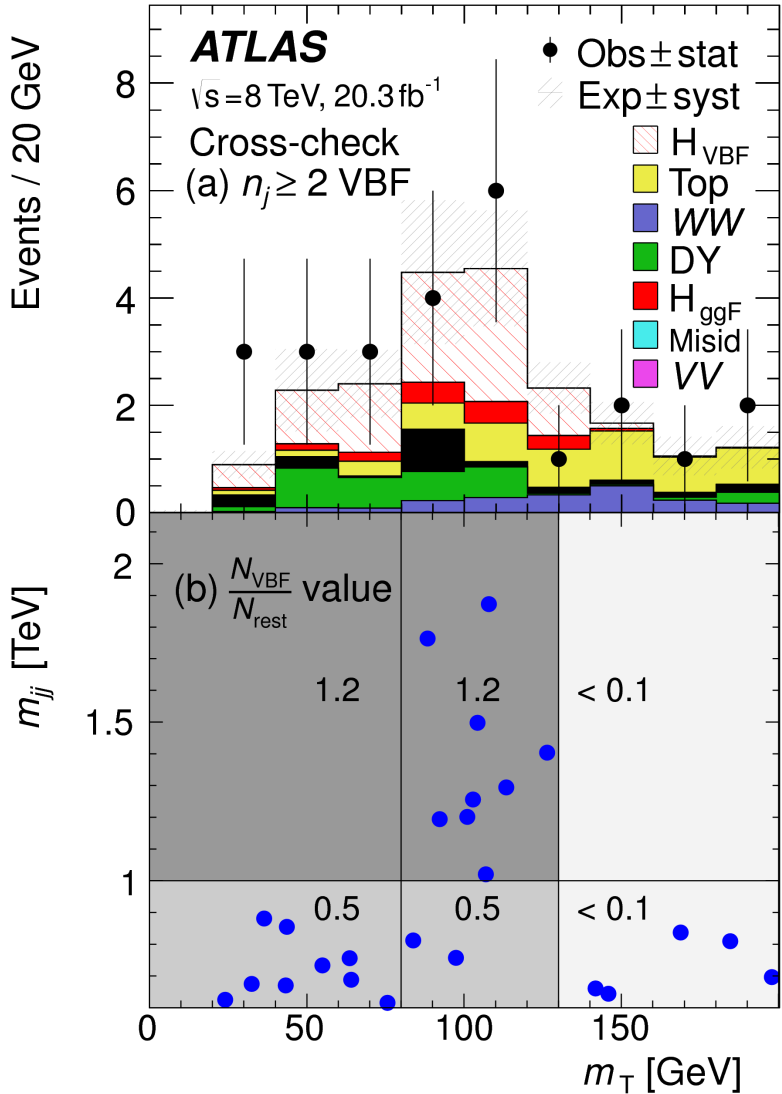


Figure 5.16: Post-fit distributions in the cut-based VBF analysis. Panel (a) shows the one-dimensional m_T distribution, while (b) shows the data candidates split into the bins of m_T and m_{jj} used in the final fit [61].

2067 Figure 5.17 shows the distributions of O_{BDT} and m_T in the VBF BDT analysis. Again the data are quite
 2068 consistent with a VBF Higgs hypothesis.

2069 Because the cut-based result is used as a validation for the BDT analysis and the two signal regions are
 2070 not fully orthogonal, it is interesting to explore which events overlap between the two analyses. Of the

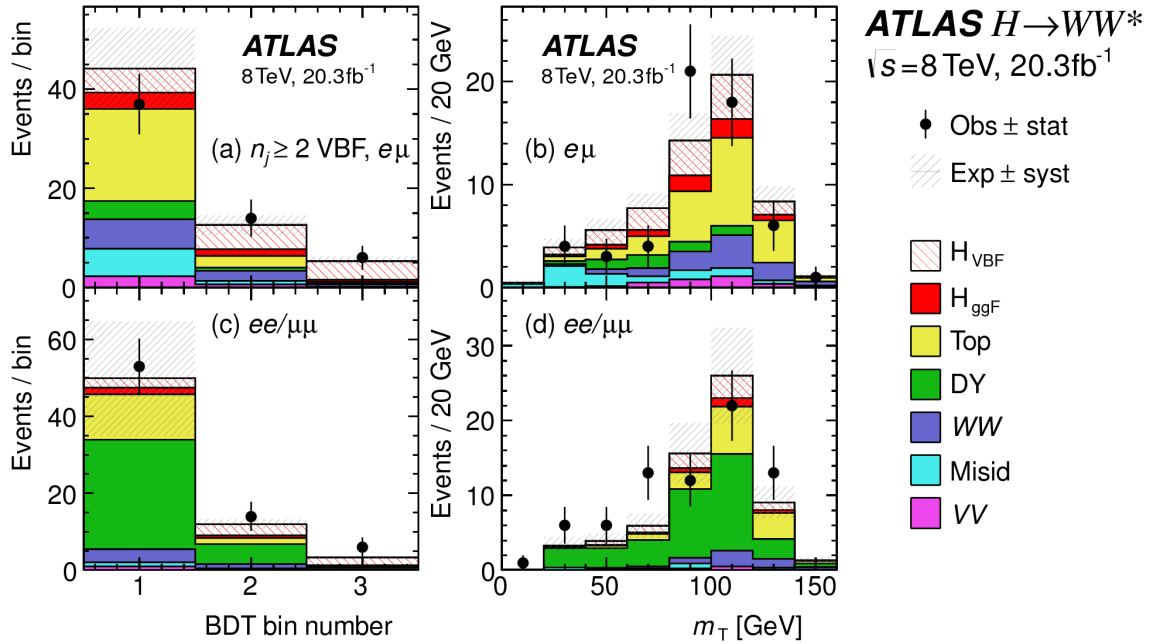


Figure 5.17: Postfit distributions in the BDT VBF analysis [61].

2071 twenty events in the cut-based signal region, only seven were not selected by the BDT analysis, while the
 2072 other thirteen also enter the BDT signal region. Figure 5.18 shows where the different analysis candidates
 2073 lie in the m_{jj} - m_T plane. This shows clearly that the advantage of the BDT analysis is that it can extract
 2074 signal candidates lower m_{jj} region due to its ability to recognize correlations with other variables.

2075 While the context of these results in the broader $H \rightarrow WW^*$ statistical analysis will be presented in
 2076 the next chapter, the significance of the VBF observation can be shown here. In the BDT analysis, the
 2077 expected signal significance was 2.7σ , while the observed significance was 3.1σ . In the cut-based analysis,
 2078 the expected significance was 2.1σ and the observed significance was 3.0σ . The compatibility between
 2079 these two results can be evaluated by computing the probability of observing a larger difference in Z_0 values
 2080 than the one measured. Using toy Monte Carlo with the ggF signal strength fixed to unity and considering
 2081 only statistical uncertainties, this probability is computed to be 79%, indicating good agreement between
 2082 the analyses. This result represents the first observation of the vector boson fusion production of a Higgs
 2083 boson.

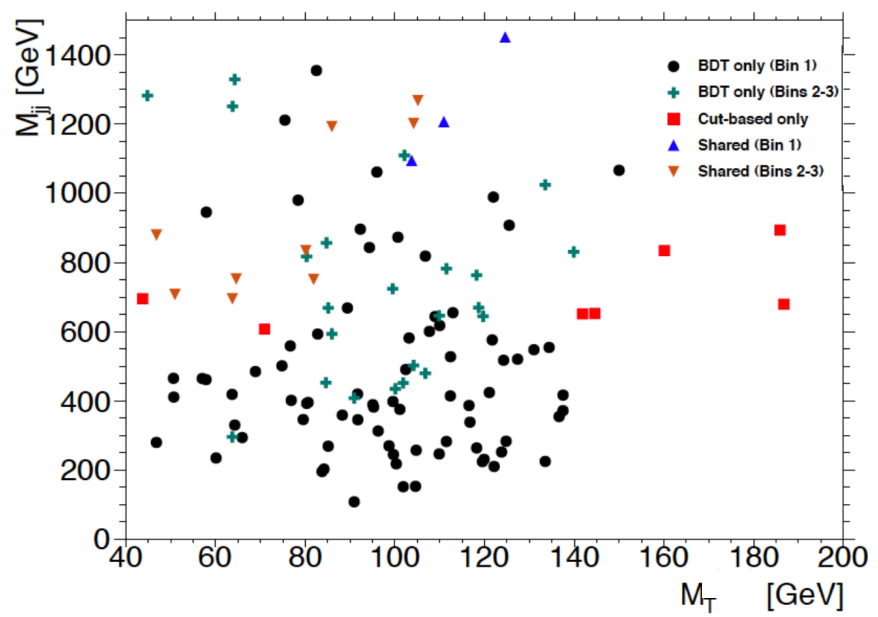


Figure 5.18: Overlap between cut-based and BDT VBF signal region candidates in the m_{jj} - m_T plane.

*The feeling is less like an ending than just another starting
point.*

Chuck Palahniuk

6

2084

2085

Combined Run I $H \rightarrow WW^* \rightarrow \ell\nu\ell\nu$

2086

results

2087

6.1 INTRODUCTION

2088

In the final statistical analysis of $H \rightarrow WW^* \rightarrow \ell\nu\ell\nu$, the dedicated gluon-gluon fusion and vector boson fusion sensitive signal regions are all combined into a single fit to determine the main parameters of interest, the Higgs signal strength μ and mass m_H . Therefore, while the specific requirements applied for the VBF sensitive analysis are discussed in chapter 5, the final measurement of these parameters can only be discussed in combination with the results of the ggF dedicated analysis. For example, because ggF Higgs production is considered a background in the VBF analysis, the ggF dedicated signal regions can actually constrain the normalization of this background in the VBF dedicated region.

2094

This chapter presents the combined interpretation of results in the $H \rightarrow WW^* \rightarrow \ell\nu\ell\nu$ analysis

SR category i				Fit var.	
n_j , flavor	$\otimes m_{\ell\ell}$	$\otimes p_T^{\ell 2}$	$\otimes \ell_2$		
$n_j = 0$	$e\mu$	$\otimes [10, 30, 55]$	$\otimes [10, 15, 20, \infty]$	$\otimes [e, \mu]$	m_T
	$ee/\mu\mu$	$\otimes [12, 55]$	$\otimes [10, \infty]$		m_T
$n_j = 1$	$e\mu$	$\otimes [10, 30, 55]$	$\otimes [10, 15, 20, \infty]$	$\otimes [e, \mu]$	m_T
	$ee/\mu\mu$	$\otimes [12, 55]$	$\otimes [10, \infty]$		m_T
$n_j \geq 2$ ggF	$e\mu$	$\otimes [10, 55]$	$\otimes [10, \infty]$		m_T
$n_j \geq 2$ VBF	$e\mu$	$\otimes [10, 50]$	$\otimes [10, \infty]$		O_{BDT}
	$ee/\mu\mu$	$\otimes [12, 50]$	$\otimes [10, \infty]$		O_{BDT}

Table 6.1: All signal regions definitions input into final statistical fit [61].

for gluon fusion and vector boson fusion Higgs production. First, the results of the dedicated gluon fusion search are presented. Then, a comparison of the individual production mode signal strengths (μ_{ggF} and μ_{VBF}) and a measurement of the combined signal strength (μ) are shown. Subsequently, the measured values of the Higgs couplings to fermions and vector bosons is presented. Finally, the cross section measurement for ggF and VBF production are shown.

6.2 RESULTS OF DEDICATION GLUON FUSION $H \rightarrow WW^* \rightarrow \ell\nu\ell\nu$ SEARCH

The details of the dedicated gluon fusion $H \rightarrow WW^* \rightarrow \ell\nu\ell\nu$ search are not discussed in this thesis and instead left to more comprehensive sources [61]. However, a brief summary of the results are essential for describing the results of the full analysis and interpreting the results of the dedicated VBF search in this broader context.

Table 6.1 shows the individual signal regions that were input into the final statistical fit. The ggF dedicated bins use m_T as their discriminating variable and are separated into bins of p_T of the subleading lepton as well. The VBF dedicated bin uses the O_{BDT} distribution as its final discriminant.

Table 6.2 shows the yields in the various signal regions in both data and expected signal and back-

2110 grounds. The yields for signal and background are all scaled according to the final normalizations cal-
2111 culated in the fit.

	N_{obs}	N_{bkg}	N_{ggF}	N_{VBF}
$n_j = 0$	3750	3430 ± 90	300 ± 50	8 ± 4
$n_j = 1$	1596	1470 ± 40	102 ± 26	17 ± 5
$n_j \geq 2, \text{ggF } e\mu$	1017	960 ± 40	37 ± 11	13 ± 1.4
$n_j \geq 2, \text{VBF}$	130	99 ± 9	7.7 ± 2.6	21 ± 3

Table 6.2: Post-fit yields in the different ggF and VBF dedicated signal regions [61].

2112 Figure 6.1 shows the final post-fit m_T distribution in the $n_j \leq 1$ regions. The data are very consistent with the hypothesis of ggF Higgs production. These yields are used as input, along with the VBF results

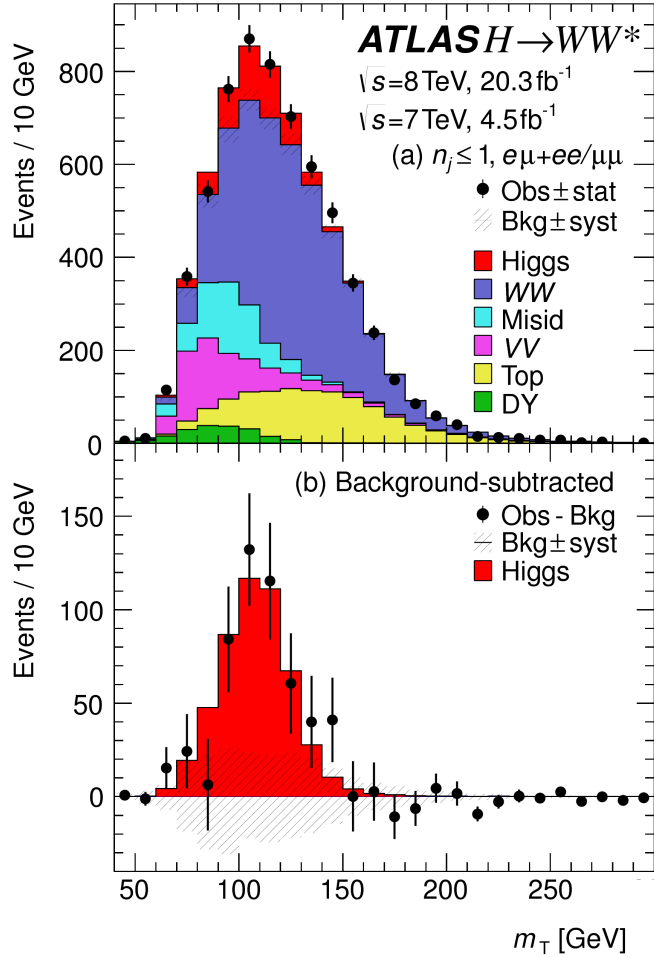


Figure 6.1: Post-fit m_T distribution in the $n_j \leq 1$ regions [61].

2113

2114 in chapter 5, for the physical interpretation of results presented in subsequent sections.

2115 **6.3 SIGNAL STRENGTH MEASUREMENTS IN ggF AND VBF PRODUCTION**

2116 When all of the signal regions are combined in the fit, there can be a combined measurement of the
 2117 signal strength as well as the individual ggF and VBF signal strengths. The combined signal strength is the
 2118 ratio of the sum of the gluon fusion and VBF cross sections to the theory prediction, or a signal strength
 2119 for the total Higgs production cross section that this analysis is sensitive to. The final measured combined
 2120 signal strength μ is measured shown in equation 6.1.

$$\begin{aligned} \mu &= 1.09 \quad {}^{+0.16}_{-0.15} \text{ (stat.)} \quad {}^{+0.08}_{-0.07} \left(\begin{array}{l} \text{expt} \\ \text{syst} \end{array} \right) \quad {}^{+0.15}_{-0.12} \left(\begin{array}{l} \text{theo} \\ \text{syst} \end{array} \right) \quad \pm 0.03 \left(\begin{array}{l} \text{lumi} \\ \text{syst} \end{array} \right) \\ &= 1.09 \quad {}^{+0.16}_{-0.15} \text{ (stat)} \quad {}^{+0.17}_{-0.14} \text{ (syst)} \\ &= 1.09 \quad {}^{+0.23}_{-0.21}. \end{aligned} \tag{6.1}$$

2121 Figure 6.2 gives the best fit signal strength $\hat{\mu}$ as a function of the hypothesized Higgs mass. The value
 2122 at 125.36 GeV corresponds to the μ quoted in equation 6.1. This value of the Higgs mass is used because it
 2123 is the most precise mass measurement from ATLAS, a result of the combined $\gamma\gamma$ and ZZ mass measure-
 2124 ments [89].

2125 As explained in chapter 3, a probability p_0 can be computed using the test statistic q_0 to quantify the
 2126 probability that the background could fluctuate to produce an excess at least as large as the one observed
 2127 in the data. The local p_0 value is shown in figure 6.3 as a function of m_H . The minimum p_0 value is at
 2128 $m_H = 130$ GeV and corresponds to a significance of 6.1σ . The curve is relatively flat and the significance
 2129 is the same at 125.36 GeV within the quoted precision. The expected significance for a signal with strength
 2130 $\mu = 1.0$ is 5.8σ . This represents the first discovery level significance measurement in the $H \rightarrow WW^* \rightarrow$
 2131 $\ell\nu\ell\nu$ analysis.

2132 All the results presented so far in this section have been for the combined gluon fusion and VBF pro-
 2133 duction modes. However, each signal strength can be calculated separately in the likelihood as well. There
 2134 are two ways to do this. First, the likelihood can be parameterized in terms of a single parameter, the ratio

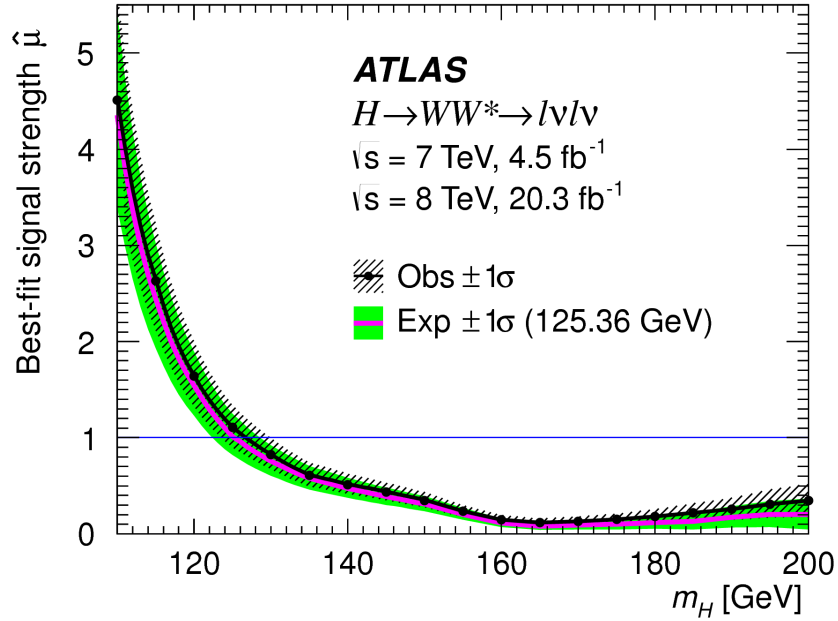


Figure 6.2: Best fit signal strength $\hat{\mu}$ as a function of hypothesized m_H [61].

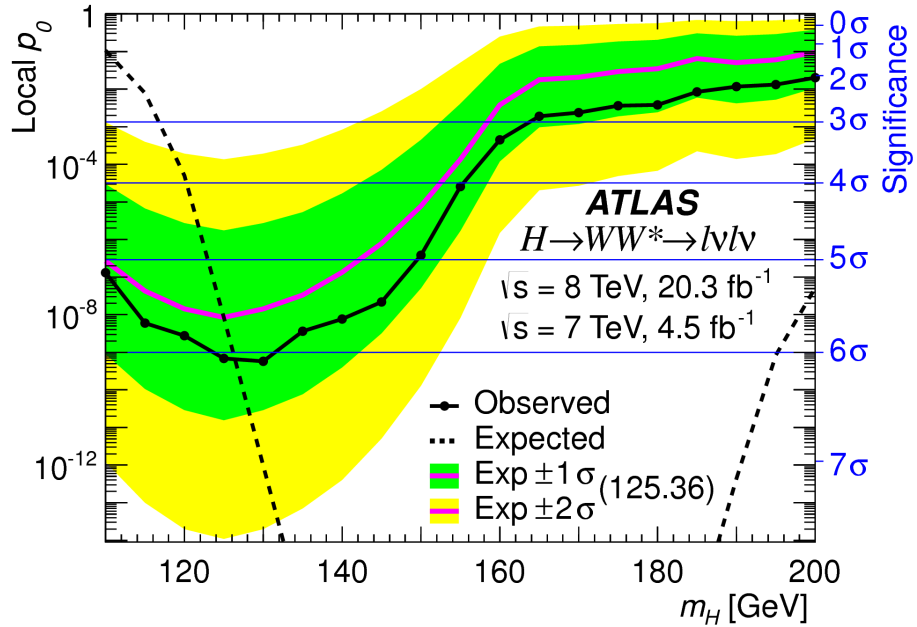


Figure 6.3: Local p_0 as a function of m_H [61].

of the VBF and gluon fusion signal strengths. With this method, the significance of the VBF observation can be evaluated. Figure 6.4 shows the likelihood as a function of the ratio $\mu_{\text{VBF}}/\mu_{\text{ggF}}$.

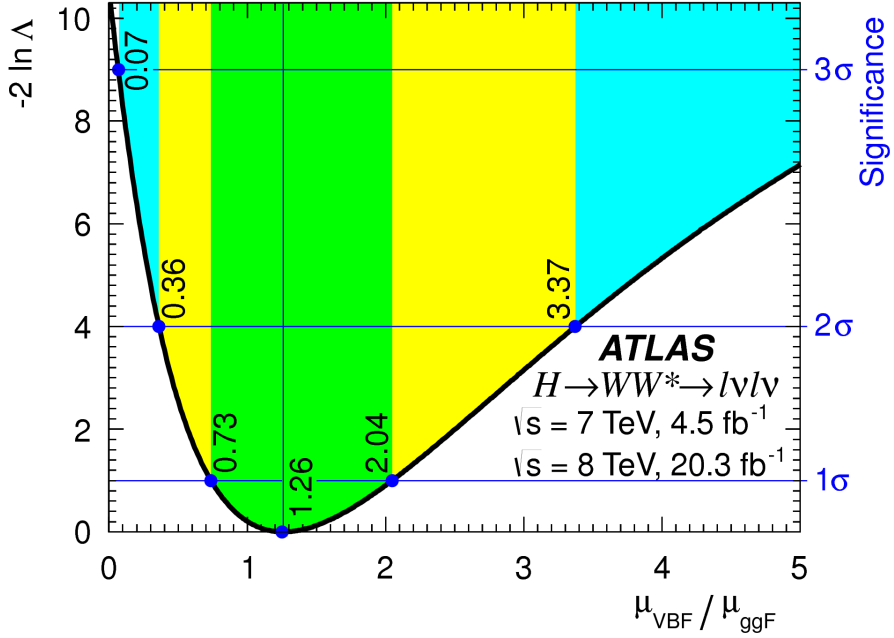


Figure 6.4: Likelihood as a function of $\mu_{\text{VBF}} / \mu_{\text{ggF}}$ [61].

2137 The best fit value of the ratio of signal strengths is shown in equation 6.2. Within the quoted uncer-
 2138 tainties, it is consistent with a ratio of unity.

$$\frac{\mu_{\text{VBF}}}{\mu_{\text{ggF}}} = 1.26^{+0.61}_{-0.45} (\text{stat.})^{+0.50}_{-0.26} (\text{syst.}) = 1.26^{+0.79}_{-0.53} \quad (6.2)$$

2139 The null hypothesis for VBF production corresponds to a ratio of $\mu_{\text{VBF}} / \mu_{\text{ggF}} = 0$. The likelihood in
 2140 figure 6.4 gives a significance of 3.2σ at $\mu_{\text{VBF}} / \mu_{\text{ggF}} = 0$, as quoted in chapter 5.

2141 In addition to the ratio of signal strengths, each signal strength can be varied independently in the like-
 2142 lihood as well. Figure 6.5 shows the two dimensional likelihood scan in the $\mu_{\text{ggF}}-\mu_{\text{VBF}}$ plane. The best fit
 2143 values of the two signal strengths are shown in equation 6.3. Both are consistent with unity within their
 2144 uncertainties.

$$\begin{aligned} \mu_{\text{ggF}} &= 1.02 \pm 0.19^{+0.22}_{-0.18} = 1.02^{+0.29}_{-0.26} \\ \mu_{\text{VBF}} &= 1.27 \pm 0.40^{+0.44}_{-0.21} = 1.27^{+0.53}_{-0.45}. \end{aligned} \quad (6.3)$$

(stat.) (syst.)

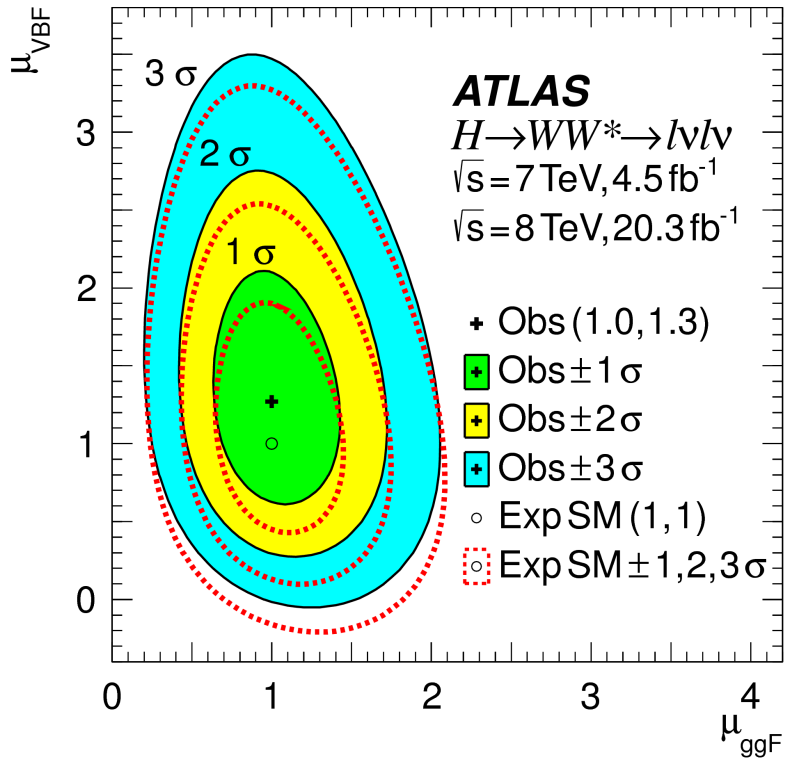


Figure 6.5: Likelihood scan as a function of μ_{VBF} and μ_{ggF} [61].

2145 6.4 MEASUREMENT OF HIGGS COUPLINGS TO VECTOR BOSONS AND FERMIONS

2146 Similar to the parameterization of signal strength, the couplings of the Higgs to fermions and bosons
 2147 can also be parameterized. The parameter of interest in this case is κ , or the ratio of the measured coupling
 2148 to the standard model expectation. Both the fermion and boson couplings have these so-called scale factors,
 2149 κ_F for fermions and κ_V for bosons. Gluon fusion production is sensitive to the fermion couplings through
 2150 the top quark loops in its production, while VBF production is sensitive to the vector boson couplings in
 2151 its production. Both modes are sensitive to the vector boson couplings in their decays. The signal strengths
 2152 will have dependence on the coupling scale factors as described in equation 6.4 [18].

$$\begin{aligned}\mu_{\text{ggF}} &\propto \frac{\kappa_F^2 \cdot \kappa_V^2}{(\mathcal{B}_{H \rightarrow f\bar{f}} + \mathcal{B}_{H \rightarrow gg}) \kappa_F^2 + (\mathcal{B}_{H \rightarrow VV}) \kappa_V^2} \\ \mu_{\text{VBF}} &\propto \frac{\kappa_V^4}{(\mathcal{B}_{H \rightarrow f\bar{f}} + \mathcal{B}_{H \rightarrow gg}) \kappa_F^2 + (\mathcal{B}_{H \rightarrow VV}) \kappa_V^2}.\end{aligned}\quad (6.4)$$

2153 Figure 6.6 shows the two-dimensional likelihood scan of κ_F and κ_V . The best-fit values are given in equa-
 2154 tion 6.5. The best-fit values are consistent with unity within their uncertainties.

$$\begin{aligned} \kappa_F &= 0.93 & +0.24 & +0.21 & = 0.93 & +0.32 \\ \kappa_V &= 1.04 & +0.07 & +0.07 & = 1.04 & \pm 0.11. \end{aligned} \quad (6.5)$$

(stat.) (syst.)

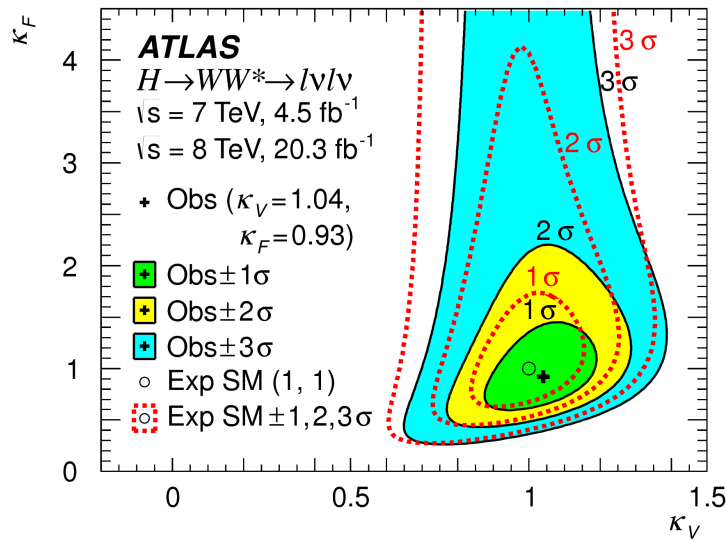


Figure 6.6: Likelihood scan as a function of κ_F and κ_V [61].

2155

2156 6.5 HIGGS PRODUCTION CROSS SECTION MEASUREMENT

2157 Another measurement that comes naturally from the signal strength numbers quoted earlier is the pro-
 2158 duction cross section and 7 and 8 TeV for both gluon fusion and VBF production. The general equation
 2159 for calculating the cross section is given in equation 6.6.

$$\begin{aligned} (\sigma \cdot \mathcal{B}_{H \rightarrow WW^*})_{\text{obs}} &= \frac{(N_{\text{sig}})_{\text{obs}}}{\mathcal{A} \cdot \mathcal{C} \cdot \mathcal{B}_{WW \rightarrow \ell\nu\ell\nu}} \cdot \frac{1}{\int L dt} \\ &= \hat{\mu} \cdot (\sigma \cdot \mathcal{B}_{H \rightarrow WW^*})_{\text{exp}} \end{aligned} \quad (6.6)$$

2160 $(N_{\text{sig}})_{\text{obs}}$ is the number of events observed in data. \mathcal{A} is the geometric and kinematic acceptance of the
 2161 detector, while \mathcal{C} is the efficiency of the signal region selection for events that are reconstructed in the
 2162 detector. The branching ratio of a WW system to leptons must also be divided out. The production
 2163 cross section depends on the center of mass energy and the production mode desired (gluon fusion or
 2164 VBF), and so three separate cross section measurements are quoted in equation 6.7.

$$\begin{aligned}
 \sigma_{\text{ggF}}^{\text{7TeV}} \cdot \mathcal{B}_{H \rightarrow WW^*} &= 2.0 \pm 1.7^{+1.2}_{-1.1} = 2.0^{+2.1}_{-2.0} \text{ pb} \\
 \sigma_{\text{ggF}}^{\text{8TeV}} \cdot \mathcal{B}_{H \rightarrow WW^*} &= 4.6 \pm 0.9^{+0.8}_{-0.7} = 4.6^{+1.2}_{-1.1} \text{ pb} \\
 \sigma_{\text{VBF}}^{\text{8TeV}} \cdot \mathcal{B}_{H \rightarrow WW^*} &= 0.51^{+0.17}_{-0.15} {}^{+0.13}_{-0.08} = 0.51^{+0.22}_{-0.17} \text{ pb.}
 \end{aligned} \tag{6.7}$$

(stat.) (syst.)

2165 The predicted cross section values for gluon fusion are 3.3 ± 0.4 pb at 7 TeV and 4.2 ± 0.5 pb at 8 TeV,
 2166 consistent with the measured values within their uncertainties. For vector boson fusion, the predicted
 2167 cross section is 0.35 ± 0.02 pb, again consistent with the measured value.

2168 6.6 CONCLUSION

2169 The combined analysis of the gluon fusion and vector boson fusion processes in $H \rightarrow WW^* \rightarrow \ell\nu\ell\nu$
 2170 in the 7 and 8 TeV datasets has yielded the first discovery level significance for Higgs production in this
 2171 decay channel. Additionally, precise measurements of the couplings to vector bosons and fermions are
 2172 given. Finally, signal strengths and cross sections for each production mode are measured. Figure 6.7 shows
 2173 the $H \rightarrow WW^* \rightarrow \ell\nu\ell\nu$ measurements in comparison with other Higgs decay channels in ATLAS. The
 2174 measurement of signal strength from this channel remains the most sensitive in both the gluon fusion and
 2175 VBF production modes for the Run 1 dataset.

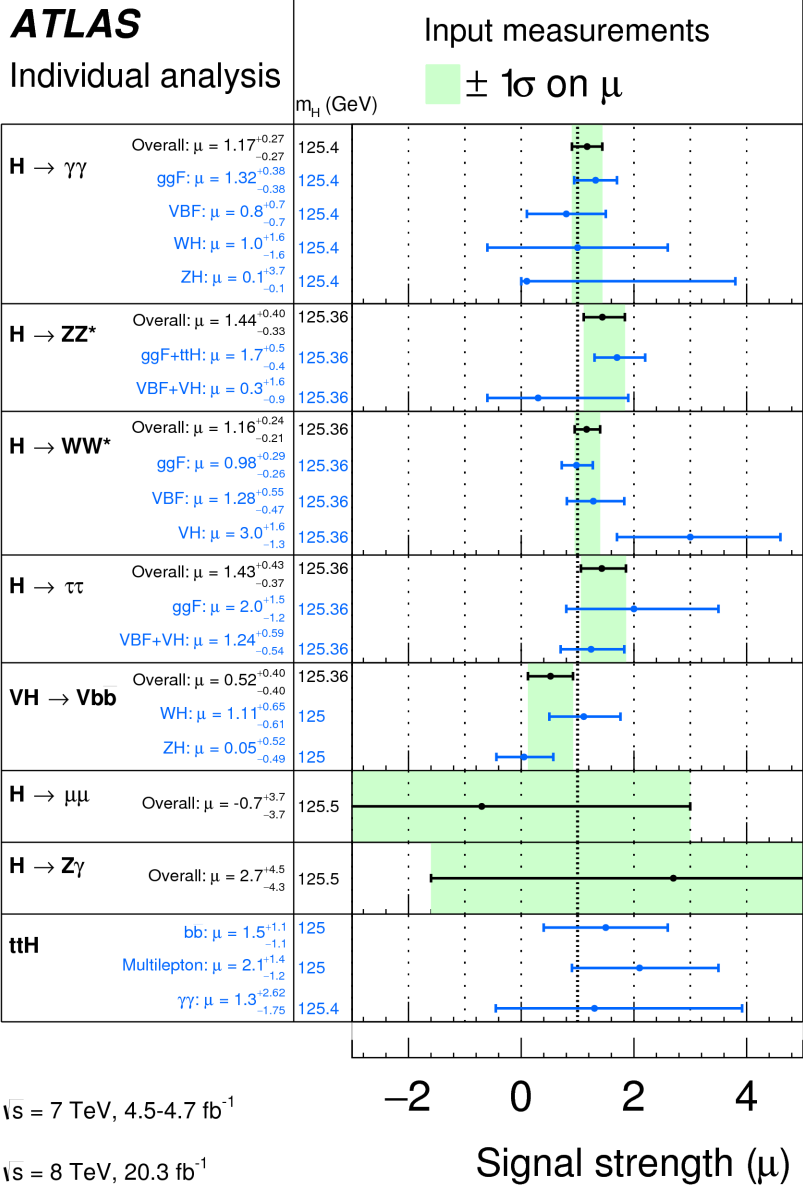


Figure 6.7: Comparison of signal strength measurements in different Higgs decay channels on ATLAS [90].

2176

Part III

2177

Search for Higgs pair production in the

2178

$HH \rightarrow b\bar{b}b\bar{b}$ channel in LHC Run 2 at $\sqrt{s} =$

2179

13 TeV

Passion is in all great searches and is necessary to all creative endeavors.

W. Eugene Smith

7

2180

2181 Search for Higgs pair production in boosted 2182 $b\bar{b}b\bar{b}$ final states

2183 7.1 INTRODUCTION

2184 After the discovery of the Higgs boson in the ATLAS Run 1 dataset and the subsequent measurements
2185 of its properties, the Higgs transformed into a potential tool in searches for physics beyond the Standard
2186 Model. The pair production cross section of the Higgs can be enhanced through BSM physics. Studying
2187 di-Higgs production also probes the Higgs self-coupling, shedding light on the structure of the Higgs po-
2188 tential. This chapter presents a search for resonant production of a Higgs pair in the $X \rightarrow HH \rightarrow b\bar{b}b\bar{b}$
2189 final state in 3.2 fb^{-1} of data collected at $\sqrt{s} = 13 \text{ TeV}$. In particular, this chapter focuses on a search for
2190 this final state in the regime where m_X is large ($\gtrsim 1 \text{ TeV}$) and the Higgs bosons in the decay are signifi-
2191 cantly boosted. A tailored selection for this boosted selection, using novel techniques in jet substructure

and b -tagging, is discussed. Then, the data-driven background estimate is presented. Finally, the results of the search are shown. The signal models used as benchmarks are a spin-2 Randall Sundrum graviton (RSG) and a narrow width spin-0 resonance. These models are described in more detail in Chapter 1. Limits on signal models are reserved for the next chapter where the results of this chapter are combined with the results of a separate selection dedicated to the lower m_X regime.

7.2 MOTIVATION

With the center of mass energy increase from $\sqrt{s} = 8$ TeV to $\sqrt{s} = 13$ TeV, the LHC and ATLAS are able to probe new resonances at higher mass scales than previously accessible in Run 1. This is a powerful motivator for searching for a new resonance in the early 13 TeV data. Figure 7.1 shows the ratios of parton luminosities between 8 and 13 TeV for different resonance masses. For a resonance of $M_X = 2$ TeV, the cross section at $\sqrt{s} = 13$ TeV is roughly a factor of 10 larger than at $\sqrt{s} = 8$ TeV.

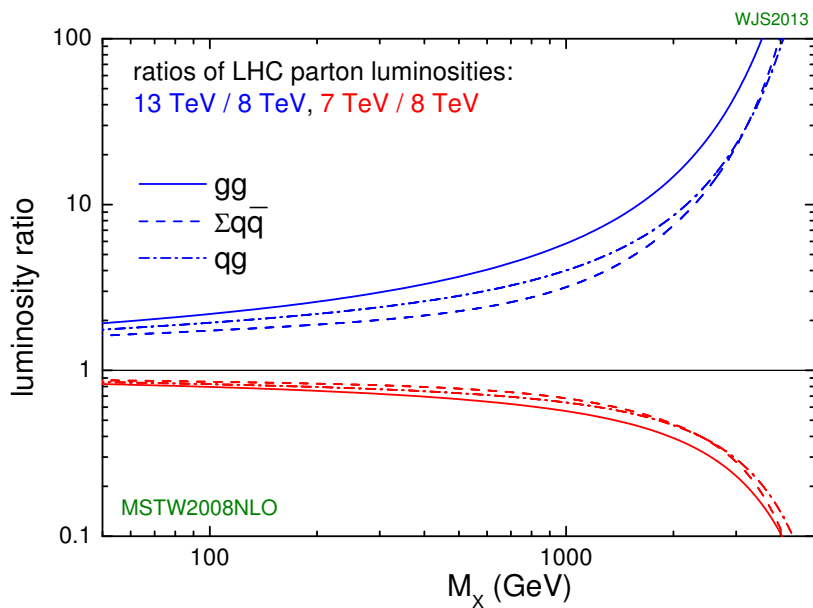


Figure 7.1: Parton luminosity ratios as a function of resonance mass M_X for 13/8 TeV and 7/8 TeV [91].

Higgs pair production offers a vast array of unprobed regions of phase space where searches for BSM physics can be made. Chapter 1 discusses some possibilities for both resonant and non-resonant enhance-

ment of the di-Higgs production cross section. Given the increased mass reach of the LHC in Run 2, it is particularly important to focus on resonant searches at high m_X . One consideration when conducting a search in the HH final state is which decay modes of the Higgs to consider. Figure 7.2 shows the branching ratio of the HH final state for different combinations of decays of each individual Higgs. As the largest branching ratio for the 125 GeV Higgs is $H \rightarrow b\bar{b}$, the $HH \rightarrow b\bar{b}b\bar{b}$ branching ratio is also the largest at 33%.

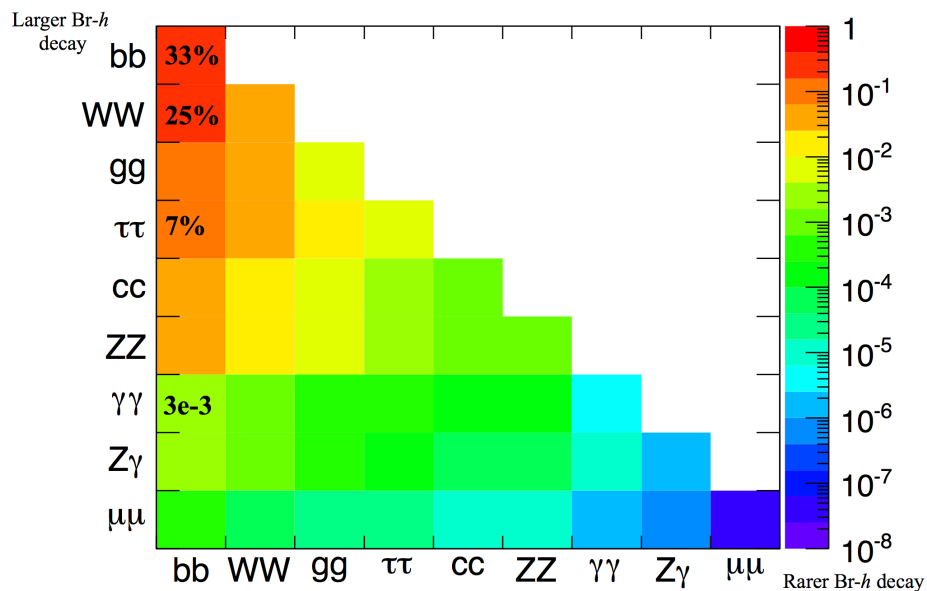


Figure 7.2: Summary of HH branching ratios [92].

At high m_X , the Higgs bosons resulting from the decay of a heavy resonance will have large p_T ¹. The ΔR between the decay products of the Higgs is inversely proportional to the Higgs p_T , as shown in equation 7.1.

$$\Delta R \approx \frac{2m}{p_T} \quad (7.1)$$

Figure 7.3 shows the minimum ΔR between truth level B decay vertices in simulation samples for Randall-Sundrum gravitons of different masses. The figure shows that as the mass of the graviton increases, the ΔR distribution between the b quarks in the Higgs decay tends to shift to lower values. Because of this effect, it is necessary to tailor a selection to target these merged b -jets.

¹In the limit that $m_H \ell \ell m_X$, the Higgs p_T is roughly $m_X/2$.

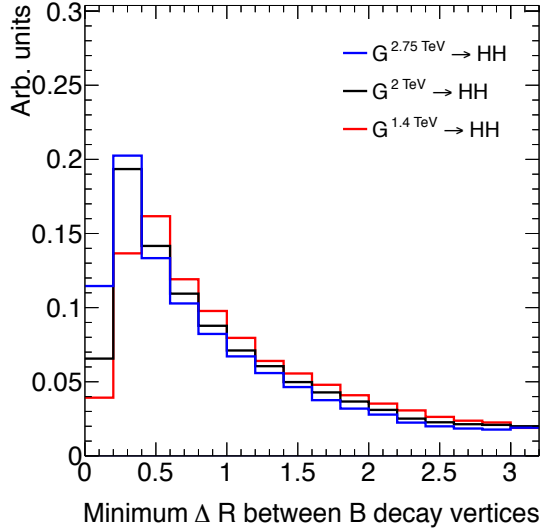


Figure 7.3: Minimum ΔR between B decay vertices for different RSG masses in a $G_{KK}^* \rightarrow HH \rightarrow 4b$ sample with $c = 1$

2218 7.3 DATA AND SIMULATION SAMPLES

2219 7.3.1 SIGNAL MODELS

2220 While the resonance search is by its nature generic (as it is a simple search for a peak in the $4b$ invariant mass spectrum), there are two signal models that the selection requirements have been optimized for.
 2221 The first is Randall-Sundrum (RSG) model, where a tower of massive spin-2 Kaluza-Klein gravitons is
 2222 predicted. The second is a heavy narrow spin-0 resonance, the so-called “heavy Higgs”. This type of res-
 2223 onance arises, for example, in the two Higgs doublet model (2HDM). More details about the physics of
 2224 these models and their motivation is given in chapter 1.

2226 Signal graviton (G_{KK}^*) events are generated at leading order (LO) with **MADGRAPH5 v2.2.2** [93]. The
 2227 PDF set used is the **NNPDF2.3 LO** set [94]. For modeling parton shower and hadronization in jets, **PYTHIA**
 2228 8.186 is used with the A14 tune [73, 95]. The free parameters in the RSG model are the graviton mass and
 2229 the coupling constant $c \equiv k/\bar{M}_{\text{Pl}}^2$. Both the production cross section and width of the graviton are
 2230 proportional to c^2 . Samples are generated at both $c = 1$ and $c = 2$ for a variety of mass points between

² k is the curvature constant for the warped extra dimension and \bar{M}_{Pl} is the Planck mass divided by 8π

2231 300 GeV and 3 TeV.

2232 The second signal sample is a heavy spin-0 resonance H with a fixed width of $\Gamma_H = 1$ GeV. This
2233 is generated with **MADGRAPH5** and uses the **CT10** PDF set [76]. The parton shower and hadronization
2234 are handled by **HERWIG ++** with the **CTEQ6L1** PDF set and the **UEEE5** event tune [77, 96, 97]. Because
2235 the width and branching ratios depend on 2HDM parameters, each mass point generated with this fixed
2236 width corresponds to a different point in the 2HDM parameter phase space. Mass points are generated
2237 between 300 GeV and 1 TeV as with the RSG signal samples.

2238 **7.3.2 BACKGROUND SAMPLES**

2239 While the dominant **QCD** multijet background is estimated with a fully data-driven method, the sub-
2240 dominant backgrounds $t\bar{t}$ and Z +jets are modeled with some input from simulation.

2241 $t\bar{t}$ events are simulated at next-to-leading order (NLO) with the **POWHEG-BOX** version 1 generator us-
2242 ing the **CT10** PDF set [98]. The parton shower, hadronization, and underlying event are simulated with
2243 **PYTHIA 6.428** with the **CTEQ6L1** PDF set [72]. The Perugia 2012 tune is used [99]. NNLO QCD cor-
2244 rections to the cross sections are computed in **Top++ 2.0** [100]. The top quark mass is set to 172.5 GeV.
2245 The shapes of distributions in $t\bar{t}$ are taken from MC while the normalization is taken from data.

2246 Finally, the Z +jets background is simulated with **PYTHIA 8.186** and the **NNPDF2.3** LO PDF set. This
2247 background is negligible compared to the others and is taken fully from MC.

2248 **7.3.3 DATA SAMPLE AND TRIGGER**

2249 This analysis is done on 3.2 fb^{-1} of data taken in 2015 at $\sqrt{s} = 13$ TeV. The details of the machine
2250 conditions during this time can be found in Chapter 2. Only data which was taken during stable beam con-
2251 ditions with all detectors functioning is used. Events must pass a trigger which requires a single 360 GeV
2252 large radius ($R = 1.0$) jet to be reconstructed in the HLT. Figure 7.4 shows the trigger efficiency for vari-
2253 ous trigger options as a function of graviton mass. Above $m_G > 1$ TeV, the single large radius jet trigger
2254 is 99% efficient for events passing the signal selection.

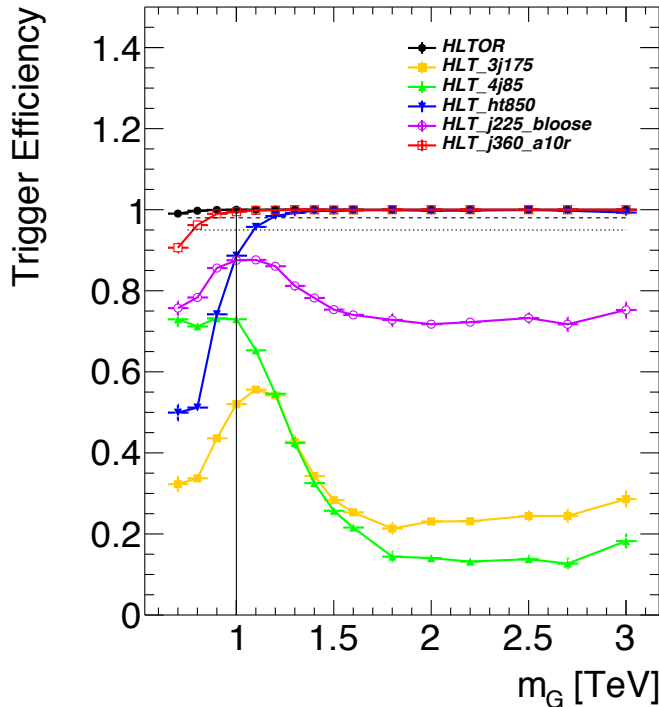


Figure 7.4: Trigger efficiency for events passing all signal region selections as a function of mass in $G_{\text{KK}}^* \rightarrow HH \rightarrow 4b$ samples with $c = 1$ [101]. In the trigger names, “ j ” refers to a jet or jets. “ht” refers to H_T , the scalar sum of transverse momenta in the event. “bloose” refers to a loose b -tagging requirement applied to the jet. “a10r” refers to anti- k_T jets with $R = 1.0$. The numbers at the end are the thresholds on the given quantity in GeV.

2255 7.4 EVENT RECONSTRUCTION AND OBJECT SELECTION

2256 The boosted selection first begins by defining a unique set of objects that can be exploited to increase
 2257 signal efficiency in the kinematic regime where the final state b -jets are very merged.

2258 7.4.1 LARGE RADIUS ($R = 1.0$) JETS

2259 The first step towards reconstructing the final state is to define objects that can be used to measure the
 2260 kinematics of the Higgs bosons. In the boosted selection anti- k_T jets with a radius parameter of 1.0 are
 2261 used. These jets are much larger in angular size than the typical $R = 0.4$ jets and are intended to encompass
 2262 both jets resulting from the Higgs decay³. The jets are built from clusters in the calorimeter calibrated with

³This is in contrast to the resolved selection, which uses two $R = 0.4$ anti- k_T jets for each Higgs

local calibration weighting [56].

Because of the large extent of these jets, great care must be taken to remove potential contributions of calorimeter clusters from pile-up. This is done using a technique called jet trimming [102]. With trimming, the constituents of the large radius jet are re-clustered with a smaller radius with the k_T algorithm. Then, these so-called subjets are removed from the larger jet if $p_T^{\text{subjett}}/p_T^{\text{jet}} < f_{\text{cut}}$. In this analysis, the subjet radius is $R = 0.2$ and $f_{\text{cut}} = 0.05$. Trimming has been shown to improve the mass resolution of large radius jets. Figure 7.5 shows the effect of trimming on the large radius jet mass (M_J). Because the large radius jet fully contains the higgs decay products, its invariant mass should correspond to the 125 GeV mass of the Higgs. The trimming algorithm brings the jet mass much closer to the expected Higgs mass and improves the mass resolution.

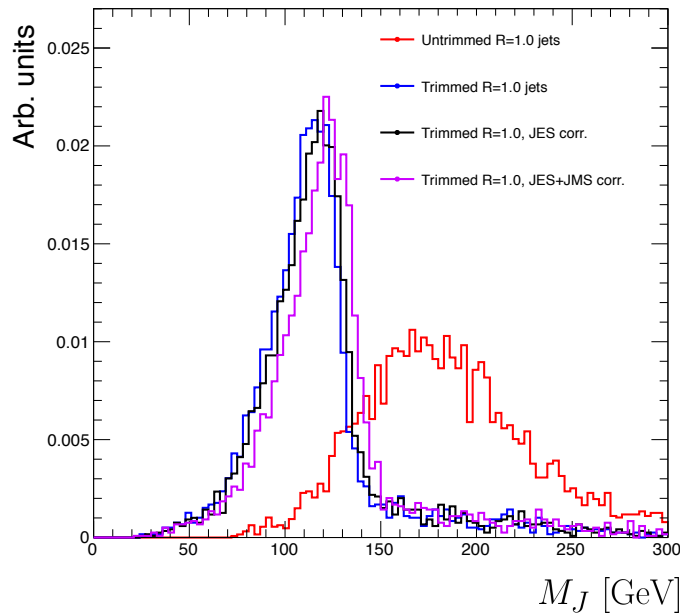


Figure 7.5: Comparison of untrimmed and trimmed jet masses for large radius jets in a RSG sample with $m_{G_{KK}^*} = 1$ TeV. JES (JMS) refers to the standard jet energy (mass) scale calibration for ATLAS [56].

The large radius jets are required to satisfy $250 < p_T < 1500$ GeV. They must also be within $|\eta| < 2.0$ in order to ensure that the full jet is within the inner detector tracking volume. Finally, they are required to have $M_J > 50$ GeV. The upper p_T cut and lower threshold on mass are applied to correspond to the kinematic range where uncertainties are available in ATLAS calibrations [103, 104].

2277 7.4.2 TRACK JETS AND b -TAGGING

2278 Because the b -jets from boosted Higgs decays are so close together (as illustrated in figure 7.3), narrow ra-
2279 dius jets are required to fully resolve both b -jets. The minimum radius feasible for jets based on calorimeter
2280 deposits is determined by the calorimeter granularity. However, because b -tagging relies on information
2281 from the inner detector, it is possible to define another type of jet that can have a smaller radius and better
2282 b -tagging resolution. These jets are called “track jets” [104, 105].

2283 Track jets are formed by applying the usual anti- k_T clustering algorithm to tracks that are required to be
2284 consistent with the primary vertex. After the jet axis has been determined using these tracks, a second step
2285 of track association is also performed to add tracks that can be useful for b -tagging [105]. In this analysis,
2286 the tracks are clustered with a radius parameter of $R = 0.2$. This radius has been shown to give good
2287 performance in boosted Higgs tagging [104, 105]. Figure 7.6 shows a comparison among different track jet
2288 radii of the efficiency for reconstructing two b -jets from each Higgs in a RSG sample as a function of mass.
Track jets with radius of 0.2 give the best performance, especially at high mass. In this analysis, track jets

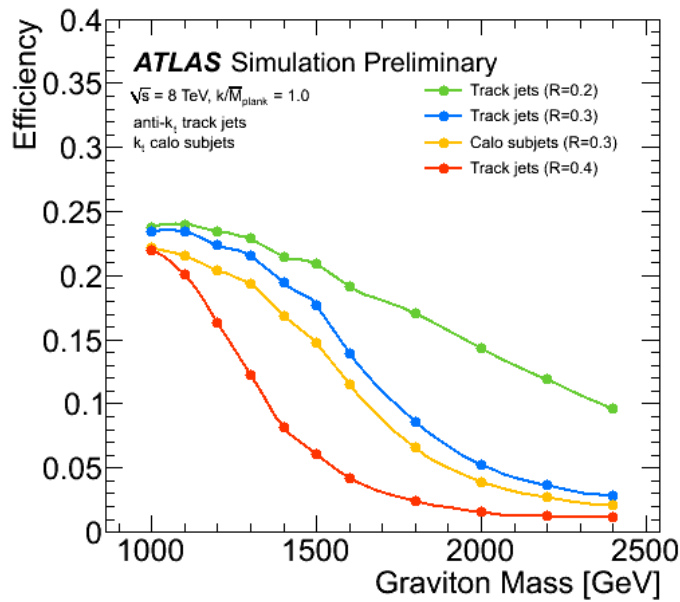


Figure 7.6: Efficiency of finding two b -jets from each Higgs in an RSG event using calorimeter jets with $R = 0.3$ or
2289 different track jet radii [105]

2290 are required to have $p_T > 10$ GeV and $|\eta| < 2.5$. They must also have at least two tracks.

2291 7.4.3 MUONS

2292 Muons are used in this study to correct the four-momenta of calorimeter jets by accounting for semi-
2293 leptonic b decays. The muons used are combined ID and MS muons which must satisfy tight identification
2294 requirements [52]. The muons must have $p_T > 4 \text{ GeV}$ and $|\eta| < 2.5$. Table 7.1 summarizes the object
2295 requirements described in this section.

	R	p_T	$ \eta $	M
Calorimeter jets	1.0	$250 < p_T < 1500 \text{ GeV}$	< 2.0	$> 50 \text{ GeV}$
Track jets	0.2	$> 10 \text{ GeV}$	< 2.5	-
Muons	-	4 GeV	< 2.5	-

Table 7.1: Summary of requirements on objects used in the $X \rightarrow HH \rightarrow b\bar{b}b\bar{b}$ search

2296 7.5 EVENT SELECTION

2297 The first requirement in the boosted selection is for ≥ 2 large radius jets satisfying the selections out-
2298 lined above. The two highest momentum large-R jets in the event are referred to as “Higgs candidates”.
2299 The leading jet is required to have $p_T > 350 \text{ GeV}$.

2300 Track jets satisfying the object selections are matched to Higgs candidate jets via ghost association [106].
2301 Each Higgs candidate must have at least 2 track jets associated with it. These basic requirements are illus-
2302 trated in figure 7.7.

2303 The QCD multijet background produces less central jets than high mass resonances, so there is an ad-
2304 dditional requirement that the two Higgs candidates be close together in η . The large-R jets are required to
2305 satisfy $|\Delta\eta(JJ)| < 1.7$.

2306 7.5.1 MASS REQUIREMENTS

2307 The final set of requirements ensures that the Higgs candidates are consistent with expected properties
2308 of the 125.0 GeV Higgs. First, a variable (X_{hh}) is defined to measure the consistency of both of the Higgs

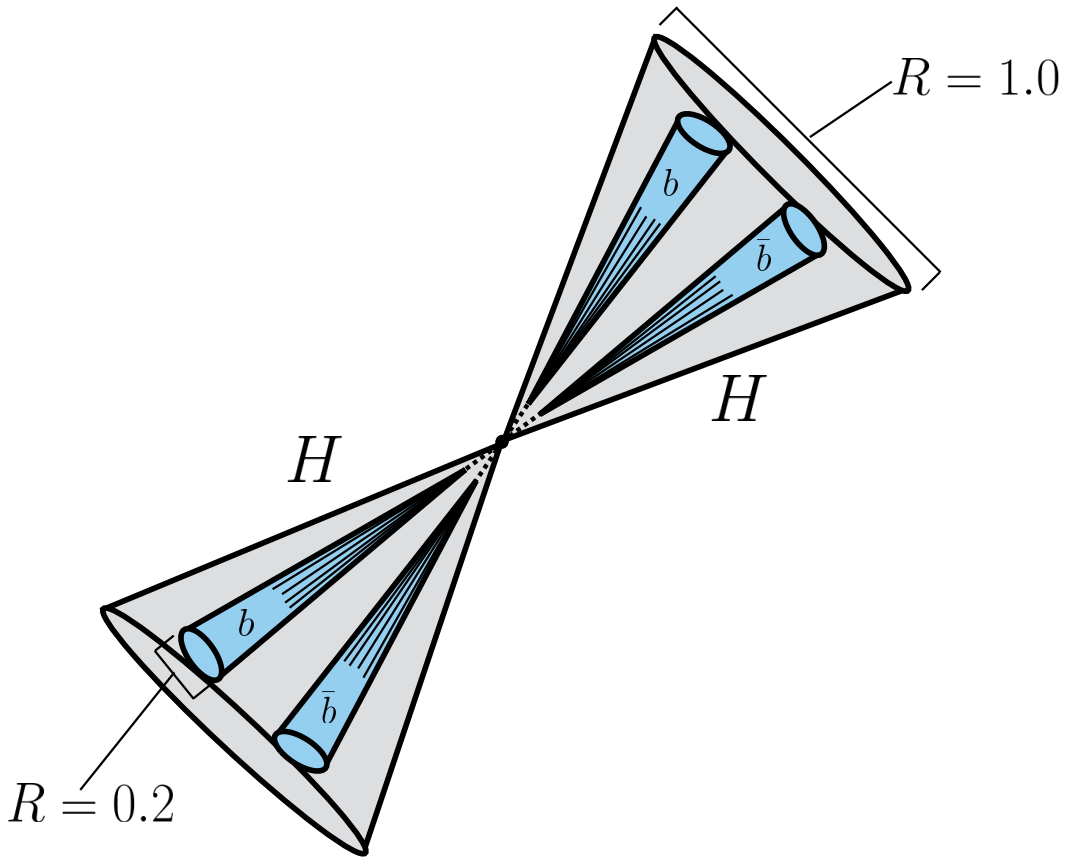


Figure 7.7: Illustration of the boosted selection requirements on Higgs candidates. Each large-radius calorimeter jet (Higgs candidate) must contain two track jets

²³⁰⁹ candidate jets with the SM Higgs mass. This is shown in equation 7.2.

$$X_{hh} = \sqrt{\left(\frac{M_J^{\text{lead}} - 124 \text{ GeV}}{0.1 M_J^{\text{lead}}}\right)^2 + \left(\frac{M_J^{\text{sublead}} - 115 \text{ GeV}}{0.1 M_J^{\text{sublead}}}\right)^2} \quad (7.2)$$

²³¹⁰ The mass values in the X_{hh} formula are optimized to maximize signal efficiency. The sub-leading jet
²³¹¹ typically has a lower mass due to semi-leptonic b decays and final state radiation. X_{hh} effectively acts as
²³¹² a χ^2 measurement of the consistency of the two Higgs candidate masses with the signal hypothesis. The
²³¹³ denominators of each term ($0.1M$) give the uncertainty on the mass measurement for the large radius jets.
²³¹⁴ Events are required to satisfy $X_{hh} < 1.6$.

²³¹⁵ Before making the requirement on X_{hh} , the masses of the Higgs candidates are corrected for semi-

leptonic b decays using muons with the criteria outlined in the previous section. Any muons within a $\Delta R < 0.2$ of a b -tagged track jet (as described in the next section) have their four-momenta added to the four-momentum of the Higgs candidate. This correction does not affect the pre-selection requirements but does affect the X_{hh} requirement and the final invariant mass distribution used.

7.5.2 b -TAGGING REQUIREMENTS

The last requirement applied is on the number of b -tagged track jets. There are two signal regions defined. The first requires exactly four b -tagged track jets, two in each Higgs candidate (known as the $4b$ signal region). At high resonance masses, this requirement is inefficient, so an additional signal region requiring only three b -tagged track jets is also defined (known as the $3b$ signal region). While this has a larger background it is also more efficient for high resonance masses. For both signal regions, the MV2c20 algorithm, where the training sample for the algorithm has 20% charm events is used. More details for this algorithm can be found in Chapter 2.

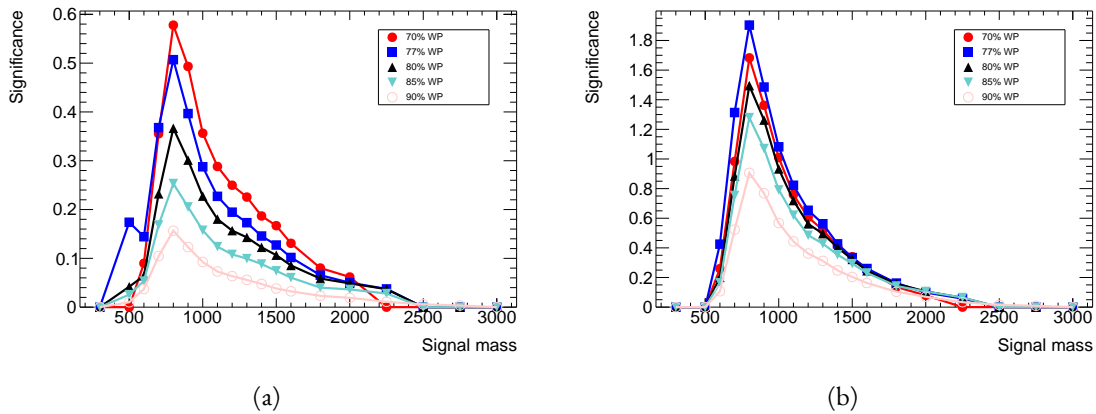


Figure 7.8: Estimated significance as a function of signal mass for RSG $c = 1$ models in the $3b$ (a) and $4b$ (b) regions for different b -tagging efficiency working points

Once the algorithm is selected, an efficiency working point must also be chosen. This working point defines the efficiency with which true b -jets are tagged and also fixes the overall background rejection of the algorithm. Higher efficiency working points accept more true b -jets but also allow for more background. Five different working points (70%, 77%, 80%, 85%, 90%) are tested. With each working point, the full data driven background estimation method is run to quantify the amount of background that will be

present in the final signal region. The significance is quantified using the median discovery significance for signal and background with Poisson errors, given in equation 7.3 [107].

$$Z = \sqrt{2 \left((s + b) \ln \left(1 + \frac{s}{b} \right) - s \right)} \quad (7.3)$$

Here, s is the expected number of signal events and b is the expected number of background events. This formula is derived using Poisson statistics with errors on both the signal and background. It is used because it is valid in the regime where s and b are of the same order. Note that in the limit where s is much smaller than b , this equation reduces to the more well known s/\sqrt{b} . Figure 7.8 shows the estimated significance as a function of signal mass in RSG $c = 1$ models for the $3b$ and $4b$ signal regions. The 77% working point gives the best performance over a wide range of masses in the $4b$ signal region. As this is the region which contributes the most to the total discovery significance, the 77% efficiency working point is chosen for the analysis.

7.5.3 SELECTION EFFICIENCY

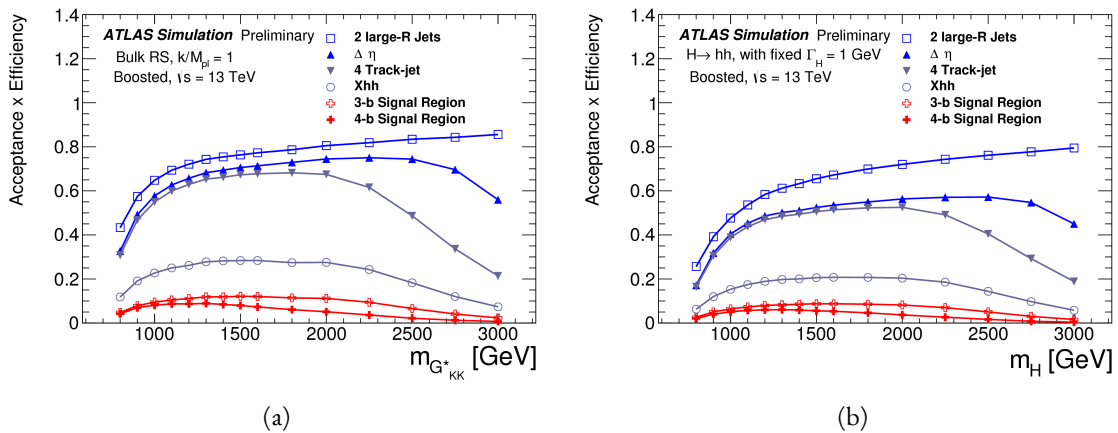


Figure 7.9: Acceptance \times efficiency as a function of mass for (a) RSG and (b) narrow heavy scalar signal models [108].

Figure 7.9 shows the product of acceptance and efficiency as a function of mass for both the RSG and narrow heavy scalar resonance signal models. After $m_X > 1$ TeV, the efficiency of the $4b$ requirement begins to decline. After $m_X > 2$ TeV, the efficiency of requiring two track jets in each Higgs candidate

begins to decline as well. Both of these behaviors illustrate the difficulty of resolving the merged decay products at high mass. Figure 7.10 shows a more detailed comparison of the signal efficiency in the $3b$ vs $4b$ signal regions for the RSG model. The efficiencies shown here are relative to all prior selection requirements. It can be seen there that at high masses the $3b$ signal region is more efficient for signal.

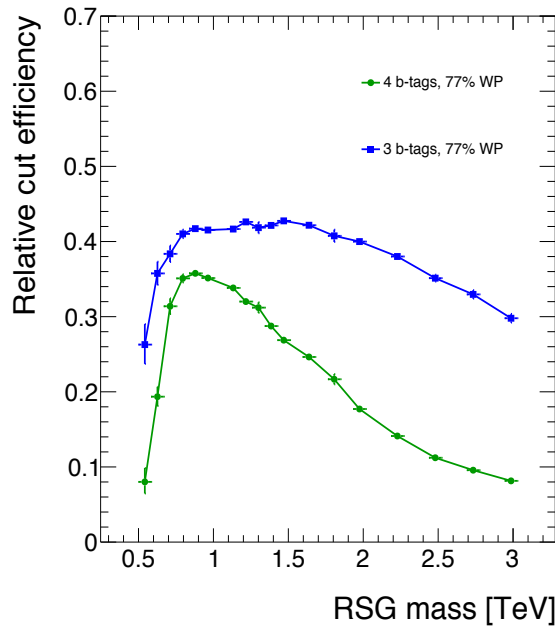


Figure 7.10: Efficiency of requiring 3 or 4 b -tagged track jets vs. RSG mass. The efficiency quoted is relative to the previous selection requirements (rather than an absolute efficiency).

To investigate the degradation of b -tagging efficiency at high p_T , the individual jet tagging efficiencies can be compared as a function of signal mass. This is shown in figure 7.11. The figure shows that the leading jet tagging efficiency in both calorimeter jets degrades heavily, while the sub-lead jet tagging efficiency remains relatively constant. More details on the cause of this degradation are shown in appendix A.

The final discriminating variable used in the boosted analysis is M_{2J} , the invariant mass of the two Higgs candidates. In order to improve the mass resolution, the four-momenta of each Higgs candidate are scaled by m_h/M_J . The effect of this correction is small in the boosted analysis but is done for consistency with the resolved selection. Table 7.2 shows the effect of the selection requirements on signal and background simulations as well as data.

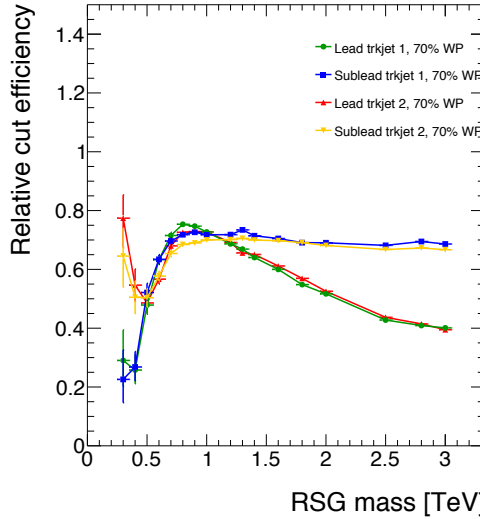


Figure 7.11: MV2c20 b -tagging efficiency for each of the four track jets in the boosted $4b$ selection as a function of RSG mass for $c = 1$ models.

Selection	Data	$m_{G_{KK}^*} = 1\text{TeV}$	$m_{G_{KK}^*} = 2\text{TeV}$	$t\bar{t}$	$Z + \text{jets}$
$N(\text{fiducial large-R jets}) \geq 2$	2202396	23.3	0.48	32345.2	4255.7
leading large-R jet $p_T > 350\text{ GeV}$	1873741	22.9	0.48	26511.7	3649.9
Both large-R jet $m > 50\text{ GeV}$	1854625	21.2	0.47	24369.8	3575.8
Both large-R jet $p_T < 1500\text{ GeV}$	1853601	21.2	0.46	24346.5	3572.9
$ \Delta\eta(JJ) < 1.7$	1435273	20.8	0.44	20751.0	3265.8
≥ 2 track-jets per large-R jet	1224727	19.8	0.40	18234.5	2692.6
3 b -tags, $X_{hh} < 1.6$	316	3.4	0.067	46.7	2.0
4 b -tags, $X_{hh} < 1.6$	20	2.9	0.030	1.4	0.0

Table 7.2: Effect of boosted selection on data, RSG signal models, $t\bar{t}$, and $Z + \text{jets}$. The numbers from simulation are normalized with the MC generator cross section and do not take into account the data driven estimates described in section 7.6 [109].

2360 7.6 DATA-DRIVEN BACKGROUND ESTIMATION

2361 The largest background to this final state is QCD multijet production, constituting 80-90% of the to-
 2362 total background. Because of the difficulties in modeling higher order QCD processes, this background is
 2363 estimated with a fully data-driven method. The only other non-negligible background is $t\bar{t}$, constituting
 2364 the other 10-20%⁴. Due to the presence of $t\bar{t}$ in the sideband region where the QCD background will be

⁴The $Z + \text{jets}$ background is a sub-percent level contribution

2365 estimated, the normalization of the QCD and $t\bar{t}$ backgrounds are simultaneously estimated.

2366 **7.6.1 MASS REGION DEFINITIONS**

2367 The first step in the data-driven background estimate is to define a sideband mass region where the
2368 background normalization can be derived. Additionally, a control region is defined where the background
2369 estimate can be validated. The control (CR) and sideband (SB) regions are defined using a radial distance
2370 in the two-dimensional large-R jet mass plane, R_{hh} , which is defined in equation 7.4.

$$R_{hh} = \sqrt{(M_J^{\text{lead}} - 124 \text{ GeV})^2 + (M_J^{\text{sublead}} - 115 \text{ GeV})^2} \quad (7.4)$$

2371 Events in the sideband region are required to fail the signal region $X_{hh} < 1.6$ requirement and have
2372 $R_{hh} > 35.8 \text{ GeV}$. The control region consists of those events which are not in the signal or sideband
regions. Figure 7.12 shows the definition of the signal, control, and sideband mass regions. Table 7.3 sum-

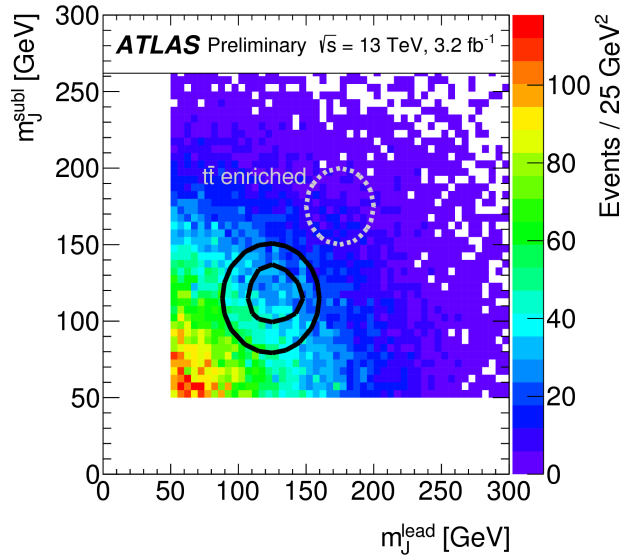


Figure 7.12: M_J^{sublead} vs. M_J^{lead} in a 2 b -tag data sample. The signal region is defined by the inner black contour ($X_{hh} < 1.6$) and the sideband region is defined by the outer contour ($R_{hh} > 35.8 \text{ GeV}$). The region between the black contours is the control region. The mass region which is enriched in $t\bar{t}$ background is also shown for illustration. [108]

2373

2374 summarizes the mass region selections for the three different regions used in the analysis.

Region	Requirement	Notes
Signal Region (SR)	$X_{hh} < 1.6$	-
Control Region (CR)	$R_{hh} < 35.8 \text{ GeV}$ and $X_{hh} > 1.6$	Used for validation of background estimates
Sideband Region (SB)	$R_{hh} > 35.8 \text{ GeV}$	Used to derive background normalization

Table 7.3: Mass region definitions used for background estimation

2375 7.6.2 BACKGROUND ESTIMATION

2376 The method for estimating the background in this analysis is similar to the ABCD method presented in
 2377 Chapter 5. In this case, the two handles used to define different regions for the estimate are the number of
 2378 b -tagged track jets and the mass regions. A region requiring exactly two b -tagged track jets in one large-R
 2379 jet (referred to as the 2-tag or $2b$ region) is defined for use in the background estimate. The number of
 2380 expected background events in the $3b$ and $4b$ signal regions is then given by equation 7.5.

$$N_{\text{bkg}}^{3(4)-\text{tag},\text{SR}} = \mu_{\text{Multijet}} N_{\text{Multijet}}^{2-\text{tag},\text{SR}} + \beta_{t\bar{t}} N_{t\bar{t}}^{3(4)-\text{tag},\text{SR}} + N_{Z+\text{jets}}^{3(4)-\text{tag},\text{SR}} \quad (7.5)$$

2381 In this equation, $N_{\text{bkg}}^{3(4)-\text{tag}}$ is the expected number of background events in the $3b$ or $4b$ signal regions.
 2382 $N_{\text{Multijet}}^{2-\text{tag}}$ is the number of multijet events in the 2-tag region. $N_{t\bar{t}}^{3(4)-\text{tag}}$ is the number of $t\bar{t}$ events pre-
 2383 dicted in the MC for the $3b$ or $4b$ signal region, and the variable is similarly defined for the $Z+\text{jets}$ back-
 2384 ground. The $\beta_{t\bar{t}}$ parameter is a scale factor used to correct the normalization of the $t\bar{t}$ estimate in the signal
 2385 region. μ_{Multijet} is an extrapolation factor that is derived in the sideband region and used to estimate the
 2386 ratio of 2-tag events to 3(4)-tag events in the signal region. It is defined in equation 7.6.

$$\mu_{\text{Multijet}} = \frac{N_{\text{Multijet}}^{3(4)-\text{tag},\text{SB}}}{N_{\text{Multijet}}^{2-\text{tag},\text{SB}}} = \frac{N_{\text{data}}^{3(4)-\text{tag},\text{SB}} - \beta_{t\bar{t}} N_{t\bar{t}}^{3(4)-\text{tag},\text{SB}} - N_{Z+\text{jets}}^{3(4)-\text{tag},\text{SB}}}{N_{\text{data}}^{2-\text{tag},\text{SB}} - \beta_{t\bar{t}} N_{t\bar{t}}^{2-\text{tag},\text{SB}} - N_{Z+\text{jets}}^{2-\text{tag},\text{SB}}} \quad (7.6)$$

2387 The $t\bar{t}$ scale factor ($\beta_{t\bar{t}}$) and the QCD multijet extrapolation factor (μ_{Multijet}) are estimated together in
 2388 a simultaneous fit in the sideband region. Then, the number of events in the 2-tag signal region is used,
 2389 along with the $t\bar{t}$ estimate in the $3b$ and $4b$ signal regions and μ_{Multijet} , to estimate the total number
 2390 of background events in the two final signal regions. The shape of the final discriminant M_{2J} is also

2391 taken from the 2-tag signal region where there are more statistics. This method is illustrated graphically in
2392 figure 7.13.

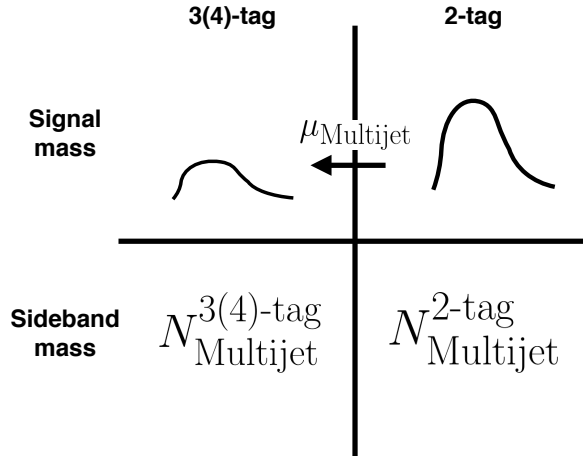


Figure 7.13: An illustration of the data-driven background estimation technique for the boosted analysis

2393 In the $3b$ region, the fit yields values of $\mu_{\text{Multijet}} = 0.160 \pm 0.03$ and $\beta_{t\bar{t}} = 1.02 \pm 0.09$. In the $4b$
2394 region, the fit gives $\mu_{\text{Multijet}} = 0.0091 \pm 0.0007$ and $\beta_{t\bar{t}} = 0.82 \pm 0.39$. The uncertainties quoted are
2395 statistical only. The larger uncertainties in the $4b$ values indicate the lower statistics available in that region.

2396 Figure 7.14 shows the distributions of data and background estimates in the $3b$ and $4b$ sideband regions
2397 after the background fit has been done. The normalizations are constrained from the fit to match that of
2398 the data, but good modeling of the shape of the mass of the leading large-R jet is seen as well. The shapes
2399 of the kinematic distributions in the $4b$ region are taken from the $3b$ region due to the better MC statistics
2400 in that region.

2401 7.6.3 BACKGROUND SHAPE FIT

2402 As mentioned in the previous section, the background shape in the 3-tag and 4-tag signal regions is
2403 taken from the 2-tag signal mass region. Due to the limited statistics available, the background shapes are
2404 additionally smoothed after being extrapolated to the 3-tag and 4-tag signal regions. Only the data in the
2405 range $900 < M_{2J} < 2000$ GeV is included in the fit due to the limited statistics available above 2 TeV.
2406 Both the $t\bar{t}$ and QCD multijet background are independently fit with an exponential shape, $y = e^{ax+b}$.

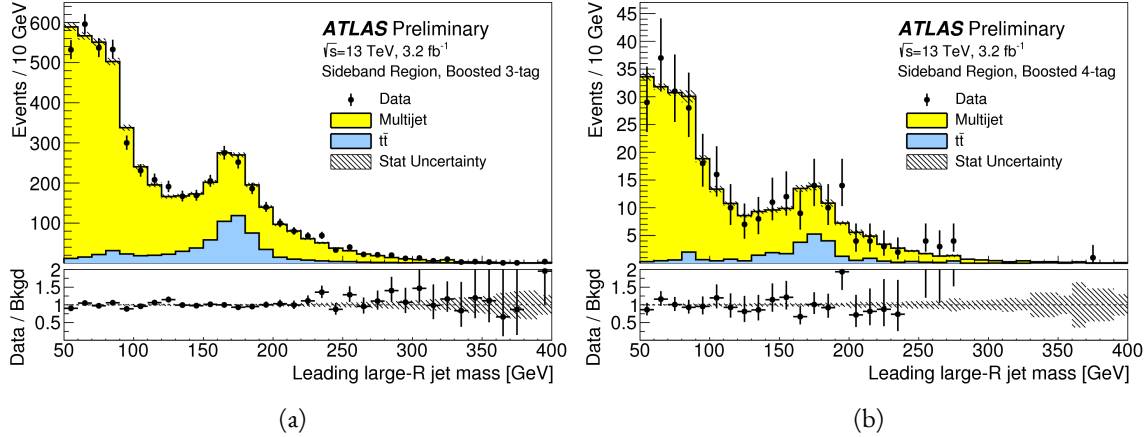


Figure 7.14: Leading large-R jet mass in the $3b$ (a) and $4b$ (b) sideband regions. The multijet and $t\bar{t}$ backgrounds are estimated using the data-driven methods described above. Because their normalizations are derived in the sideband region, the total background normalization is constrained by default to match the normalization of the data [108].

2407 Other shapes are considered and used for the systematic uncertainties. Table 7.4 shows the fit values for
 2408 the parameters. Because both the $3b$ and $4b$ QCD shapes come from the 2-tag region, the slopes derived
 2409 are very similar.

	a	b
QCD ($4b$)	0.00545 ± 0.00021	5.44 ± 0.24
$t\bar{t}$ ($4b$)	0.00746 ± 0.00021	4.88 ± 0.36
QCD ($3b$)	0.00545 ± 0.00021	8.30 ± 0.24
$t\bar{t}$ ($3b$)	0.00746 ± 0.00021	8.58 ± 0.36

Table 7.4: Parameters derived for exponential fit to background M_{2J} shape in the $3b$ and $4b$ signal regions [109]

2410 7.6.4 VALIDATION OF BACKGROUND ESTIMATE

2411 The background estimate can be validated by using the method to estimate the number of events in the
 2412 control mass region rather than the signal mass region. Figure 7.15 shows the M_{2J} distribution in the $3b$
 2413 and $4b$ control regions, comparing data and background estimates. In both cases, both the background
 2414 shape and normalization are consistent with the data, indicating good agreement. The ratio of data to the
 2415 background estimates is also fit to a line in the figure to test for any shape difference. The slope of the
 2416 line is within 1σ (from the fit uncertainties) of flat, further indicating that the data is consistent with the
 2417 background estimate in the control region.

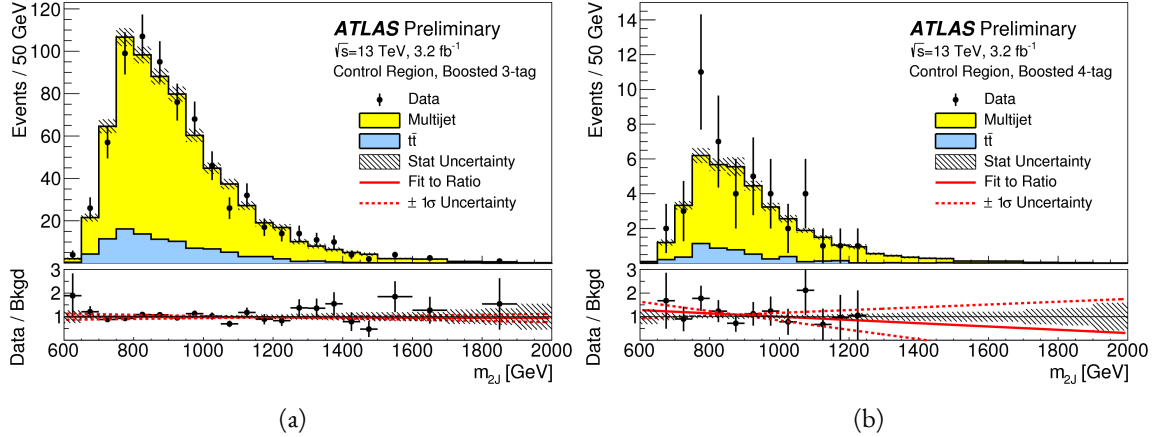


Figure 7.15: Di-jet invariant mass (M_{2J}) in the 3b (a) and 4b (b) control regions. The multijet and $t\bar{t}$ backgrounds are estimated using the data-driven methods described above [108].

Table 7.5 shows the yields in data and background estimates in the 3-tag and 4-tag sideband and control regions. Again, here, it can be seen that the total number of predicted background events from the data driven method is consistent with the number of data events in the region.

Sample (3-tag)	Sideband Region	Control Region
Multijet	4328 ± 27	607 ± 10
$t\bar{t}$	683.5 ± 8.1	99.6 ± 3.1
Z+jets	31.8 ± 3.7	7.7 ± 1.8
Total	5043 ± 28	715 ± 11
Data	5043	724
Sample (4-tag)	Sideband Region	Control Region
Multijet	247.4 ± 1.5	34.7 ± 0.6
$t\bar{t}$	28.4 ± 1.5	5.1 ± 0.7
Z+jets	3.4 ± 1.2	0.6 ± 0.5
Total	279.2 ± 2.5	40.3 ± 1.0
Data	279	45

Table 7.5: The number of events in data and predicted background events in the boosted 3-tag and 4-tag sideband and control regions. The uncertainties shown are statistical only. [108]

2421 7.7 SYSTEMATIC UNCERTAINTIES

2422 The systematic uncertainties in this analysis can be divided into two broad categories. The first type
2423 is uncertainties associated with the modeling of the signal processes. The second type of uncertainty is
2424 associated with both the shape and normalization of the background prediction.

2425 7.7.1 SIGNAL MODELING UNCERTAINTIES

2426 The signal modeling uncertainty has three main components: theoretical uncertainty on the acceptance,
2427 experimental uncertainties on the large-R jets, and experimental uncertainties on the track jets related to
2428 b -tagging. In this analysis the experimental uncertainties are the most significant.

2429 The first uncertainty on signal modeling is the theoretical uncertainty on the acceptance. As explained
2430 in section 5.6.1, there are four components to this uncertainty. The first is related to missing higher order
2431 terms from the matrix element calculations which is estimated by varying the QCD renormalization and
2432 factorization scales. The second is uncertainty due to the PDF set used. The third is a generator uncer-
2433 tainty which is estimated by modifying the generator used to model the underlying event and hadroniza-
2434 tion. Finally, there is an uncertainty associated with the modeling of the initial state and final state radia-
2435 tion (ISR/FSR). The total theoretical uncertainty on the signal yield is 3%, and this is dominated by the
2436 ISR/FSR modeling.

2437 There are uncertainties on the large-R jets in both the jet energy scale (JES) and jet energy resolution
2438 (JER) as well as the jet mass scale (JMS) and jet mass resolution (JMR). These are evaluated using $\sqrt{s} =$
2439 8 TeV data from Run 1 of ATLAS and extrapolated to the Run 2 beam and detector conditions using
2440 MC^s. The details of these uncertainties can be found in reference [110].

2441 Uncertainties on the track jets are related to the b -tagging efficiency. The total uncertainty on the signal
2442 yield due to b -tagging is evaluated by propagating variations of the b -tagging efficiency through the boosted
2443 selection requirements. The uncertainties are calculated jet-by-jet and parameterized as a function of b -jet
2444 p_T and η [88]. For high p_T b -jets (with $p_T > 300$ GeV), the uncertainties are extrapolated using MC
2445 simulation from the lower p_T b -jets [111].

^sThe uncertainties are correspondingly larger due to the uncertainty of this extrapolation.

2446 Table 7.6 shows the systematic uncertainties on the signal normalization for models with $m_{G_{\text{KK}}^*} =$
2447 1.5 TeV and both $c = 1$ and $c = 2$ as well as a narrow width heavy scalar. The dominant uncertainty
2448 comes from b -tagging and this uncertainty is larger in the 4-tag region than the 3-tag region.

Source	Background	G_{KK}^*		H
		$c = 1$	$c = 2$	
Luminosity	-	5.0	5.0	5.0
3-tag				
JER	< 1	< 1	< 1	< 1
JES	2	< 1	< 1	< 1
JMR	1	12	12	11
JMS	5	14	13	17
b -tagging	1	23	22	23
Theoretical	-	3	3	3
Multijet Normalization	3	-	-	-
Statistical	2	1	1	1
Total	7	31	30	33
4-tag				
JER	< 1	< 1	< 1	< 1
JES	< 1	< 1	< 1	< 1
JMR	4	12	13	13
JMS	5	13	13	14
b -tagging	2	36	36	36
Theoretical	-	3	3	3
Multijet Normalization	14	-	-	-
Statistical	3	1	1	1
Total	15	42	42	43

Table 7.6: Summary of systematic uncertainties in the total background and signal event yields (expressed in %) in the boosted 3-tag and 4-tag signal regions. Systematic uncertainties on the signal normalization are shown for models with $m_{G_{\text{KK}}^*} = 1.5$ TeV and both $c = 1$ and $c = 2$ as well as a narrow width heavy scalar.

2449 **7.7.2 BACKGROUND UNCERTAINTIES**

2450 Uncertainties on the QCD multijet background normalization and shape are estimated using the con-
2451 trol mass region. As shown previously, the background predictions in the control region match with the

2452 data yields within the statistical uncertainty in both the 3-tag and 4-tag control regions. As an additional
 2453 protection, the statistical uncertainty on the background prediction in the control region is assigned as a
 2454 systematic uncertainty on the normalization of the QCD background.

2455 Additional robustness tests are done by varying the definition of the control mass region and the b -
 2456 tagging requirements used to define the 2-tag sample. In all cases, the effect of the variations is found to be
 2457 within the statistical uncertainties on the background normalization in the control region.

2458 Shape uncertainties on the background are evaluated using two techniques. First, as shown in fig-
 2459 ure 7.15, the ratio between the data and background prediction is fit with a linear function. The uncer-
 2460 tainties on the slope of this fit are assigned as shape uncertainties. An additional uncertainty is assigned by
 2461 using alternate power law fit functions for the smoothing of the background shape. Table 7.7 shows the
 2462 alternate shapes used. The largest difference between the nominal fit function and the alternates, taking
 2463 into account the 1σ uncertainty band on each fit as well, is taken as a shape uncertainty.

Functional Form
$f_1(x) = p_0(1 - x)^{p_1}x^{p_2}$
$f_2(x) = p_0(1 - x)^{p_1}e^{p_2 x^2}$
$f_3(x) = p_0(1 - x)^{p_1}x^{p_2}x$
$f_4(x) = p_0(1 - x)^{p_1}x^{p_2} \ln x$
$f_5(x) = p_0(1 - x)^{p_1}(1 + x)^{p_2}x$
$f_6(x) = p_0(1 - x)^{p_1}(1 + x)^{p_2} \ln x$
$f_7(x) = \frac{p_0}{x}(1 - x)^{p_1-p_2} \ln x$
$f_8(x) = \frac{p_0}{x^2}(1 - x)^{p_1-p_2} \ln x$

Table 7.7: Alternate fit functions used to model the M_{2J} distribution in the QCD multijet background. In the equations, $x = M_{2J}/\sqrt{s}$.

2464 The uncertainties on the $t\bar{t}$ background are obtained by propagating the various experimental variations
 2465 (JES, JER, JMS, JMR, b -tagging) through the analysis selection requirements. Table 7.6 summarizes the
 2466 background uncertainties in the 3-tag and 4-tag regions.

2467 7.8 RESULTS

2468 Table 7.8 shows the observed yields in the 3-tag and 4-tag signal regions for the boosted analysis com-
 2469 pared to the predicted number of background events. In the 3-tag region, 316 events are observed with
 2470 a predicted background of 285 ± 19 . In the 4-tag region, 20 events are observed with a predicted back-
 2471 ground of 14.6 ± 2.4 . Figure 7.16 shows the M_{2J} distribution in the 3-tag and 4-tag regions. There are
 2472 some small excesses in the data, in particular in the 3-tag region around $M_{2J} \approx 900$ GeV and in the region
 2473 of $1.6 < M_{2J} < 2.0$ TeV. The significance of these excesses will be evaluated in the next chapter in the
 2474 statistical combination with the resolved results.

Sample	Signal Region (3-tag)	Signal Region (4-tag)
Multijet	235 ± 14	13.5 ± 2.4
$t\bar{t}$	48 ± 22	1.2 ± 1.0
$Z + \text{jets}$	2.0 ± 2.2	-
Total	285 ± 19	14.6 ± 2.4
Data	316	20
G_{KK}^* (1000 GeV), $c = 1$	3.4 ± 0.9	2.9 ± 1.1

Table 7.8: Observed yields in the 3-tag and 4-tag signal regions for the boosted analysis compared to the predicted number of background events Errors correspond to the total uncertainties in the predicted event yields. The yields for a graviton with $m_{G_{\text{KK}}^*} = 1$ TeV and $c = 1$ are also shown. [108]

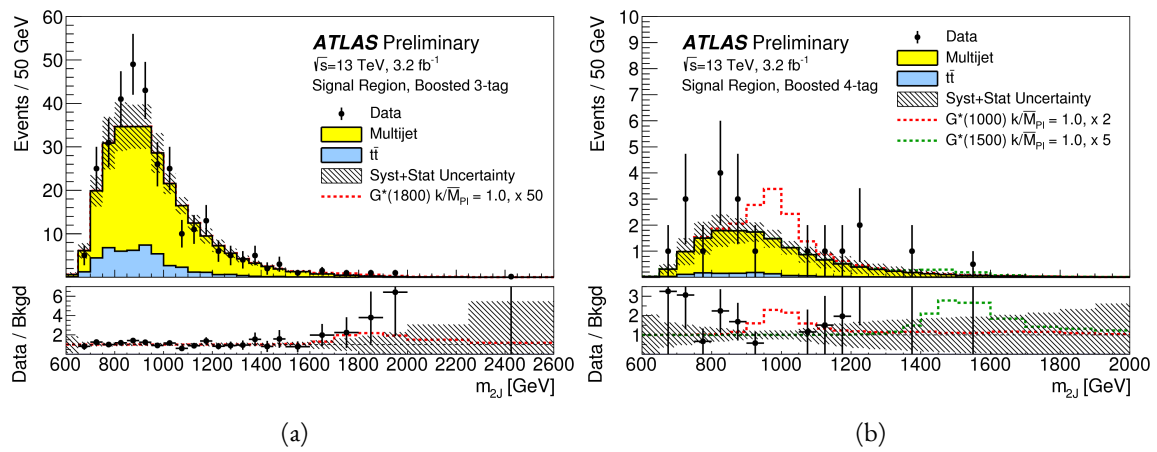


Figure 7.16: Di-jet invariant mass (M_{2J}) in the $3b$ (a) and $4b$ (b) signal regions. The multijet and $t\bar{t}$ backgrounds are estimated using the data-driven methods described above. In the $3b$ region, a graviton signal with $m_{G_{KK}^*} = 1.8$ TeV and $c = 1$ is overlaid, with the cross section multiplied by a factor of 50 so that the signal is visible. In the $4b$ region, signals with $m_{G_{KK}^*} = 1.0$ TeV and $m_{G_{KK}^*} = 1.5$ TeV are overlaid, both with $c = 1$ and the yields multiplied by factors of 2 and 5 respectively [108].

*There is no real ending. It's just the place where you stop
the story.*

Frank Herbert

8

2475

2476

Combined limits from boosted and resolved searches

2477

2478

8.1 INTRODUCTION

2479 In order to cover the full mass range of possible resonances decaying to di-Higgs final states, two distinct
2480 tailored selections were produced. The resolved selection is more sensitive in the mass range of $400 < m_X < 1100$ GeV while the boosted selection is more sensitive to masses in the range $1100 < m_X <$
2481 3000 GeV. Chapter 7 presents the details of the boosted selection and results. In setting limits on spin-2
2482 Randall-Sundrum graviton (RSG) and narrow width heavy scalar (H) models, the results of the boosted
2483 selection are combined with the results of the resolved selection to cover the full mass range.
2484

2485 This chapter presents limits on signal models resulting from the $X \rightarrow HH \rightarrow b\bar{b}b\bar{b}$ search in both
2486 the resolved and boosted selections. It first presents a brief overview of the resolved results that go into

2487 the limit setting. Then, an overview of the statistical methods used for the search and limit setting is given.
2488 Finally, limits on the RSG and heavy scalar models are presented.

2489 **8.2 RESOLVED RESULTS**

2490 The details of the resolved selection will not be presented here and can be found in reference [108]. In
2491 basic terms, the selection searches for four $R = 0.4$ b-tagged calorimeter jets (where each pair of jets is
2492 one Higgs candidate). This is distinct from the boosted methodology which searches for merged decay
2493 products. The backgrounds to the resolved selection are the same as those presented in Chapter 7 for the
2494 boosted analysis.

2495 Table 8.1 shows the results for data yields and expected background in the resolved signal region. Fig-
2496 ure 8.1 shows the M_{2J} distribution in the resolved signal region. The total number of events is consistent
2497 with the prediction and no significant excess is seen. One event in the boosted 4-tag signal is shared with
2498 the resolved signal region and has a mass of 852 GeV.

Sample	Signal Region Yield
Multijet	43.3 ± 2.3
$t\bar{t}$	4.3 ± 3.0
$Z + \text{jets}$	-
Total	47.6 ± 3.8
Data	46
SM hh	0.25 ± 0.07
$G_{\text{KK}}^*(800 \text{ GeV}), c = 1$	5.7 ± 1.5

Table 8.1: Observed yields in the resolve selection 4-tag signal region compared to the predicted number of background events Errors correspond to the total uncertainties in the predicted event yields. The yields for a graviton with $m_{G_{\text{KK}}^*} = 800$ GeV and $c = 1$ are also shown. [108]

2499 **8.3 SEARCH TECHNIQUE AND RESULTS**

2500 The statistical technique used for the search in this analysis is the same as that used in the $H \rightarrow WW^*$
2501 analysis presented in section 3.6.2. The test statistic q_0 is used to define the p -values which measure the

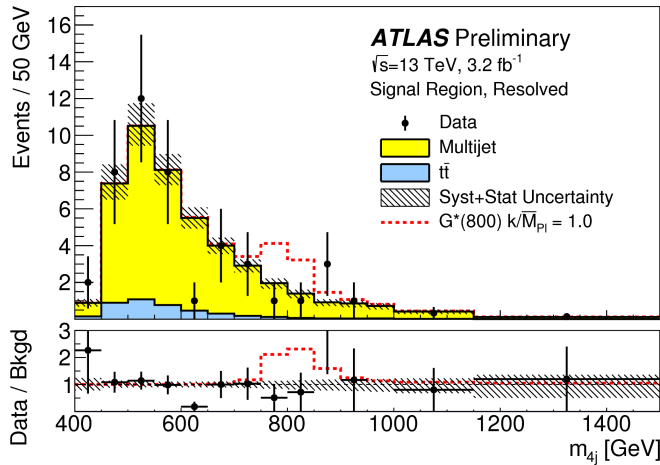


Figure 8.1: Di-jet invariant mass (M_{2J}) in the resolved signal region. A graviton signal with $m_{G_{KK}^*} = 800$ GeV and $c = 1$ is overlaid. [108].

compatibility of the data with the background-only hypothesis corresponding to a signal strength $\mu = 0$.

Local p_0 values are computed to quantify the probability that the background could produce a fluctuation greater than or equal to the one observed in the data. In the resolved analysis, no significant excesses are observed. The largest discrepancy with respect to the background only hypothesis occurs near a resonance mass of 900 GeV and is found to be less than 2σ in significance.

In the boosted selection, the largest local excess is a broad excess in the $3b$ signal region that begins near $M_{2J} \approx 1.7$ GeV. Assuming a G_{KK}^* with this mass and $c = 1.0$, the local significance of this excess is 2.0σ .

8.4 LIMIT SETTING

In the absence of any significant excess observed in the data, limits on different signal models can be set. This section describes the limit setting procedure and presents combined results of the resolved and boosted analyses.

8.4.1 LIMIT SETTING PROCEDURE

The procedure used for setting exclusion limits in this analysis is the CL_s method [112]. The first step in setting the limits is to define a test statistic which will be used. For limit setting, the test statistic is shown

2517 in equation 8.1.

$$\tilde{q}_\mu = \begin{cases} -2 \ln \frac{L(\mu, \hat{\theta}(\mu))}{L(0, \hat{\theta}(0))} & \hat{\mu} < 0 \\ -2 \ln \frac{L(\mu, \hat{\theta}(\mu))}{L(\hat{\mu}, \hat{\theta})} & 0 \leq \hat{\mu} < \mu \\ 0 & \hat{\mu} > \mu \end{cases} \quad (8.1)$$

2518 In the above equation, μ is the value of the signal strength under test, $\hat{\mu}$ is the best fit μ , $\hat{\theta}$ is the
2519 best fit value of the nuisance parameters, $\hat{\theta}$ is the best fit value of the nuisance parameters under the fixed
2520 μ value, and L is the Poisson likelihood of the data (as described in section 3.6.2).

2521 The test statistic \tilde{q}_μ is constructed to protect against two interesting corner cases when setting the upper
2522 limit on the cross section. First, it protects against negative signal strengths μ which are unphysical. Second,
2523 it does not count excesses in the data larger than those expected by a signal strength μ as evidence against
2524 the μ hypothesis.

2525 The CL_s statistic is constructed by taking a ratio of two probabilities. CL_{s+b} is the probability that the
2526 signal+background hypothesis would produce a value of the test statistic that is less than or equal to the
2527 observed value¹. CL_b is the probability that the background only hypothesis will produce a value
2528 of the test statistics less than or equal to the observed. The CL_s statistic is then the ratio CL_{s+b}/CL_b . A
2529 95% upper limit on the cross section is set at the value of μ that makes the CL_s statistic less than 5%.

2530 In practice, the limits are computed numerically within an asymptotic approximation for the distribu-
2531 tion of the test statistic \tilde{q}_μ . The details of this approximation can be found in reference [63].

2532 The resolved and boosted analyses are combined using a very simple procedure rather than a full statis-
2533 tical combination. For each mass point tested, the limit which gives the most stringent constraint is used.
2534 This means that for mass points below 1.1 TeV the resolved signal region is used, while at and above this
2535 point the combination of the orthogonal 3b and 4b boosted signal regions is used.

2536 8.4.2 LIMIT SETTING RESULTS

2537 Figure 8.2 shows the combined 95% upper bounds as a function of mass for three different models:
2538 G_{KK}^* with $c = 1$, G_{KK}^* with $c = 2$, and a narrow heavy scalar H .

¹Lower values of \tilde{q}_μ mean better compatibility

2539 The cross section of $\sigma(pp \rightarrow G_{\text{KK}}^* \rightarrow hh \rightarrow b\bar{b}b\bar{b})$ with $c = 1$ is constrained to be less than 70 fb
2540 for masses in the range $600 < m_{G_{\text{KK}}^*} < 3000$ GeV. For the RSG model with $c = 2$, cross sections limits
2541 between 40 fb and 200 fb are set for the mass range of $500 < m_{G_{\text{KK}}^*} < 3000$ GeV. Masses in the range
2542 of $475 < m_{G_{\text{KK}}^*} < 785$ GeV are excluded with $c = 1$ (with an exclusion of the range 465 to 745 GeV
2543 expected). Masses less than 980 GeV are excluded with $c = 2$ (with an exclusion for masses less than
2544 1 TeV expected).

2545 In the heavy Higgs model, the cross section upper limits for $\sigma(pp \rightarrow H \rightarrow hh \rightarrow b\bar{b}b\bar{b})$ ranges from
2546 30 to 300 fb in the mass range of $500 < m_H < 3000$ GeV. The resolved analysis can also set an upper
2547 limit on the Standard Model di-Higgs production cross section discussed in chapter 3. The upper limit on
2548 $\sigma(pp \rightarrow hh \rightarrow b\bar{b}b\bar{b})$ in the Standard Model is constrained to be less than 1.22 pb.

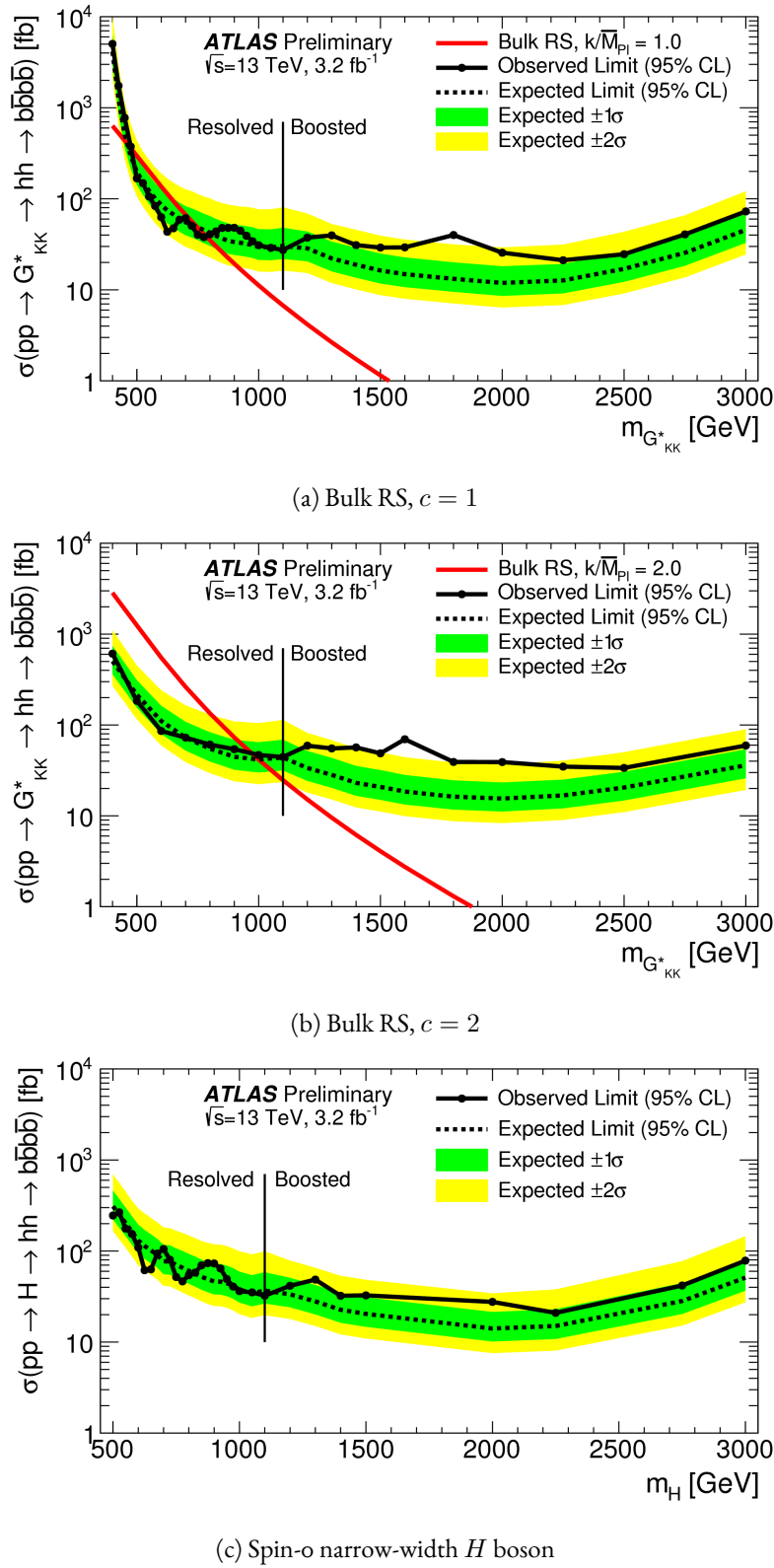


Figure 8.2: Expected and observed upper limit as a function of mass for G^*_{KK} in the RSG model with (a) $c = 1$ and (b) $c = 2$, as well as (c) H with fixed $\Gamma_H = 1$ GeV, at the 95% confidence level in the CL_s method. [108]

2549

Part IV

2550

Looking ahead

9

2551

2552

Conclusion

2553 After being sought for many years at different collider experiments, the Higgs boson was discovered by
2554 the ATLAS and CMS experiments in 2012, confirming the leading theory for the source of electroweak
2555 symmetry breaking and filling in the last missing piece of the Standard Model. After its discovery, mea-
2556 surements of the particle's detailed properties and searches for new particles decaying to Higgs final states
2557 were both extremely important in constraining physics beyond the Standard Model. This dissertation
2558 presented this evolution through two results: the observation and measurement of the Higgs boson in the
2559 $H \rightarrow WW^* \rightarrow \ell\nu\ell\nu$ channel at $\sqrt{s} = 7$ TeV and $\sqrt{s} = 8$ TeV and a search for Higgs pair production
2560 in the $HH \rightarrow b\bar{b}b\bar{b}$ channel at $\sqrt{s} = 13$ TeV with the ATLAS detector in pp collisions at the Large
2561 Hadron Collider.

2562 In the $H \rightarrow WW^* \rightarrow \ell\nu\ell\nu$, results from both the discovery of the Higgs boson and the full ATLAS
2563 Run 1 dataset were presented. The Higgs boson was discovered with a 6.1σ significance in a combina-
2564 tion of the $H \rightarrow \gamma\gamma$, $H \rightarrow ZZ4\ell$, $H \rightarrow WW^* \rightarrow \ell\nu\ell\nu$ with 4.2 fb^{-1} at $\sqrt{s} = 7$ TeV and

2565 5.2 fb^{-1} at $\sqrt{s} = 8 \text{ TeV}$. With the full 20.3 fb^{-1} at $\sqrt{s} = 8 \text{ TeV}$ and 4.2 fb^{-1} at $\sqrt{s} = 7 \text{ TeV}$,
2566 ATLAS achieved discovery level significance in the $H \rightarrow WW^*$ channel alone and obtained the first ob-
2567 servation of vector boson fusion production in that channel. The combined signal strength is measured
2568 to be $\mu = 1.09^{+0.23}_{-0.21}$. The total observed significance of the $H \rightarrow WW^*$ process is observed to be 6.1σ
2569 (with 5.8σ expected). Advanced methods for background reduction and estimation, particularly in same-
2570 flavor lepton final states, are shown. The VBF signal strength is measured to be $\mu_{\text{VBF}} = 1.27^{+0.53}_{-0.45}$ with
2571 an observed significance of 3.2σ (with 2.7σ expected).

2572 These results required many novel innovations. The increase of pileup interactions in the higher in-
2573 stantaneous luminosity LHC conditions of 2012 led to a degradation of missing transverse momentum
2574 resolution. As a result, the prominent $Z/\gamma^* + \text{jets}$ background of the same flavor $H \rightarrow WW^* \rightarrow \ell\nu\ell\nu$
2575 final states increased greatly. New variables, including a track-based missing transverse momentum and a
2576 measurement of the balance between the dilepton system and recoiling jets, allowed for significant reduc-
2577 tion of this background. In the VBF channel, selections were optimized to exploit the unique VBF final
2578 state topology. Incorporating these variables into a boosted decision tree technique allowed the analysis
2579 to exceed the 3σ observation threshold.

2580 After the end of Run 1, the results of Higgs measurements from ATLAS were combined with those
2581 from CMS to produce the most precise measurements of the Higgs boson so far [113]. Figure 9.1 shows the
2582 combination of ATLAS and CMS data for the Higgs signal strength in and coupling measurements. In the
2583 signal strength measurements of gluon fusion and vector boson fusion, the $H \rightarrow WW^*$ channel provides
2584 the tightest constraints. Additionally, the Higgs coupling to W bosons is the most precisely measured with
2585 a relative uncertainty of 10%.

2586 With the discovery of the Higgs firmly established and its properties measured, a natural next step was
2587 to search for new physics with Higgs final states. At $\sqrt{s} = 13 \text{ TeV}$, a search for Higgs pair production
2588 in the $b\bar{b}b\bar{b}$ final state with 3.2 fb^{-1} was conducted. A signal region optimized for the boosted final states
2589 arising from high mass resonances was constructed. This signal region utilized large-radius calorimeter jets
2590 and b -tagging with small radius track jets to maximize the signal acceptance. No significant excesses were
2591 observed, and upper limits on cross sections are placed for spin-2 Randall Sundrum gravitons (RSG) and

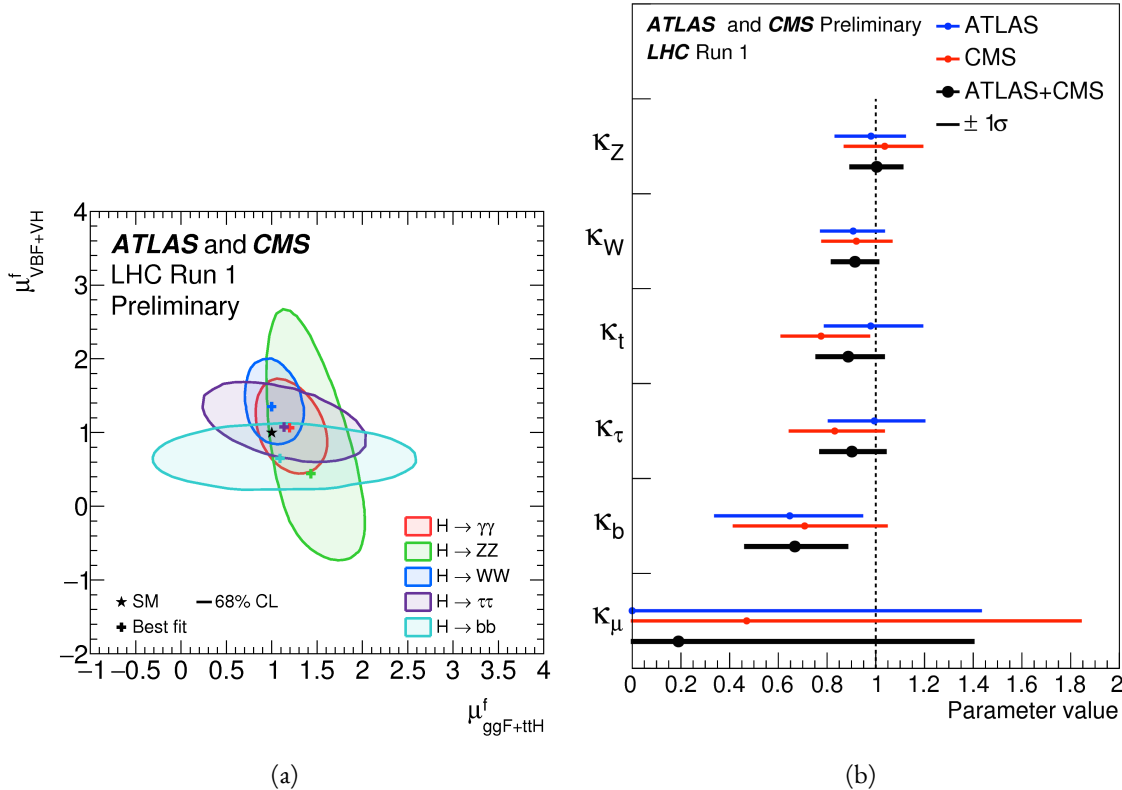


Figure 9.1: Combined ATLAS and CMS measurements in Run 1 for (a) Higgs signal strength in gluon fusion and VBF and (b) Higgs couplings normalized to their SM predictions

narrow spin-0 resonances. The increase in center of mass energy in Run 2 allowed this analysis to extend upper limits up to 3 TeV, while previous results from ATLAS in Run 1 only quotes limits up to 2 TeV. The cross section of $\sigma(pp \rightarrow G_{KK}^* \rightarrow hh \rightarrow b\bar{b}b\bar{b})$ with $k/\bar{M}_{\text{Pl}} = 1$ is constrained to be less than 70 fb for masses in the range $600 < m_{G_{KK}^*} < 3000$ GeV. For the RSG model with $k/\bar{M}_{\text{Pl}} = 2$, cross sections limits between 40 fb and 200 fb are set for the mass range of $500 < m_{G_{KK}^*} < 3000$ GeV. The cross section upper limits for $\sigma(pp \rightarrow H \rightarrow hh \rightarrow b\bar{b}b\bar{b})$ ranges from 30 to 300 fb in the mass range of $500 < m_H < 3000$ GeV.

While there has been a rigorous program of measurements and searches involving the Higgs, there is still much room for improvement at the High Luminosity LHC (HL-LHC) and beyond. The measured signal strength for VBF production in $H \rightarrow WW^*$ still has a relative error at the level of 40%, largely dominated by statistical uncertainty. Projections for the HL-LHC show that the uncertainty on the VBF signal strength can be reduced to approximately 15% with 3000 fb^{-1} [114, 115]. This uncertainty also

2604 assumes that theoretical uncertainties on the signal, which would be the largest contribution in this dataset,
 2605 remain as they are now. Improvements in the theoretical understanding of the Higgs signal would also
 2606 reduce the signal strength uncertainty dramatically. Such precision measurements allow for measurements
 2607 of the Higgs coupling to vector bosons precise to the few percent level, therefore giving much power to
 2608 constrain or discover new physics.

2609 The prospects for detection of beyond the Standard Model resonant di-Higgs production at the HL-
 2610 LHC are also quite promising. Figure 9.2 shows projections for the discovery significance of RSG signals at
 2611 the HL-LHC in the $X \rightarrow HH \rightarrow b\bar{b}b\bar{b}$ search [115]. In all detector budget scenarios, a 1.5 TeV resonance
 is above or near 5σ significance, while a 2 TeV resonance is between $4-5\sigma$ except for the lowest budget.

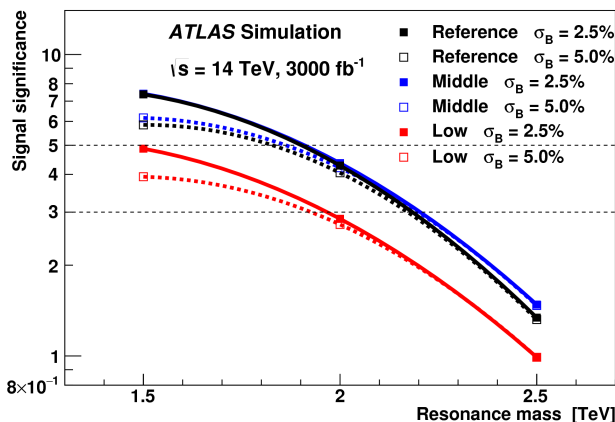


Figure 9.2: Discovery significance for RSG models at the HL-LHC in three different budget scenarios [115]. Systematic uncertainties on the background prediction (σ_B) of 2.5% and 5.0% are both tested.

2612
 2613 The Higgs will continue to be an incredibly powerful tool in the understanding of nature at the HL-
 2614 LHC and beyond. Through both precision measurements and searches, the nature of electroweak symme-
 2615 try breaking will be better understood and the potential for the discovery of physics beyond the Standard
 2616 Model has never been greater.

A

2617

2618

b-tagging performance at high p_T

2619 One of the limiting factors of the signal acceptance in the $X \rightarrow HH \rightarrow b\bar{b}b\bar{b}$ search at high resonance
2620 masses is the degradation of the *b*-tagging efficiency for high p_T jets. This appendix presents a study of the
2621 underlying causes of this degradation.

2622 A.I CHANGES IN MV₂ SCORE AT HIGH p_T

2623 The degradation of *b*-tagging at high p_T was studied in particular in the context of RSG models at high
2624 mass. Figure A.I shows the p_T of the leading track jet inside of the leading calorimeter jet in RSG events.
2625 At high $m_{G_{KK}^*}$, the p_T spectrum of track jets is much harder than at lower masses due to the increased
2626 Higgs p_T .

2627 Figure A.2 shows the MV_{2c20} algorithm score for the leading and subleading track jets inside of the
2628 leading calorimeter jet. In both cases, it can be seen that at higher RSG masses the MV₂ score shifts towards
2629 more background like (negative) values. Additionally, this effect is more pronounced in the leading track

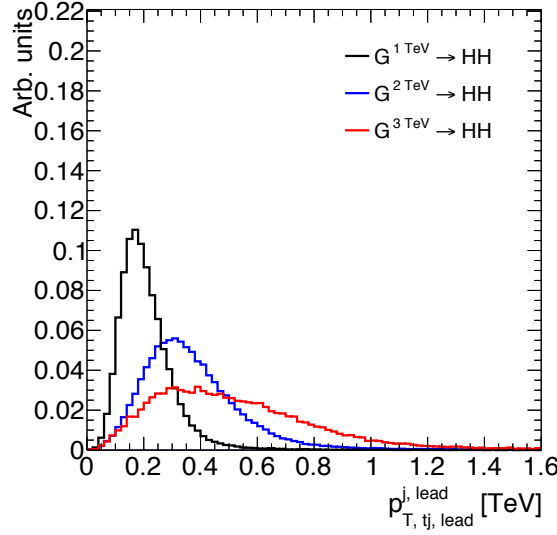


Figure A.1: p_T of the leading track jet in the leading calorimeter jet for different signal masses in RSG $c = 1$ models

jet than the subleading.

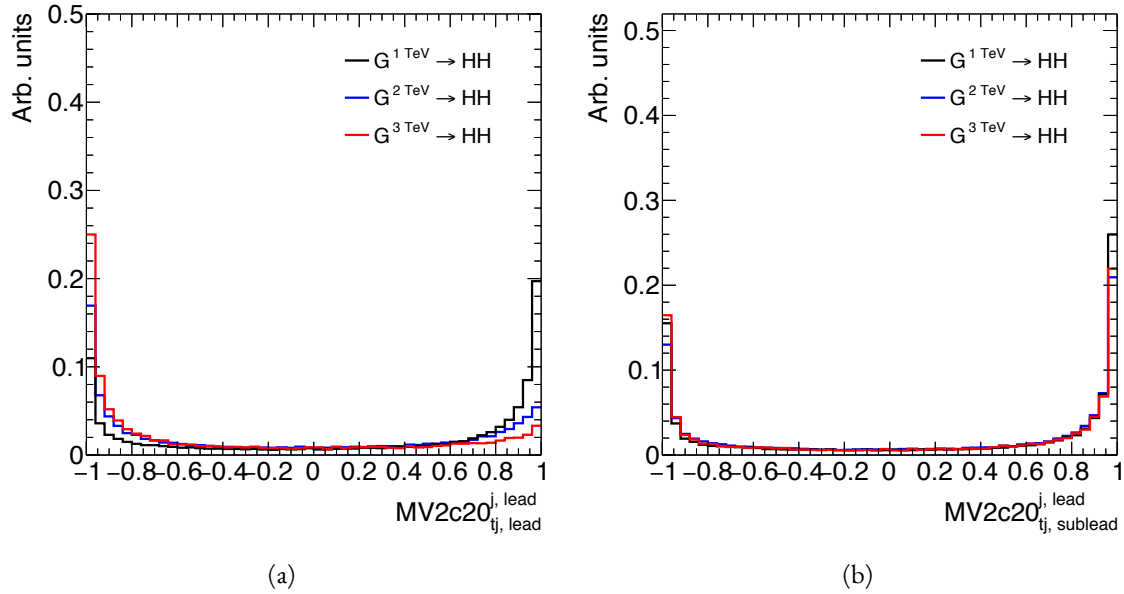


Figure A.2: MV2c20 score for the leading track jet (a) and subleading track jet (b) of the leading calorimeter jet for different signal masses in RSG $c = 1$ models

To understand what is causing this change in the MV2c20 score, the same comparisons can be made for the input variables of MV2c20. The focus in these comparisons will be on the leading track jet as this is the one seen to have the largest difference in MV2 score. Figure A.3 shows the log likelihood ratio $\log(p_b/p_u)$

from the IP₃D (three dimensional impact parameter) algorithm. At higher masses, the IP₃D likelihood ratio distribution does become more background-like.

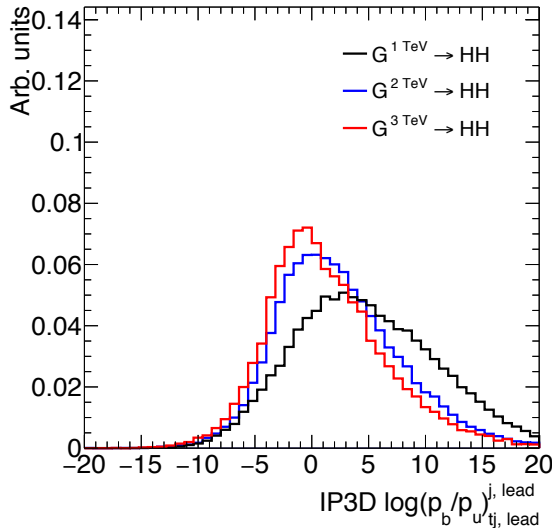


Figure A.3: IP₃D log-likelihood ratio ($\log(p_b/p_u)$) of the leading track jet in the leading calorimeter jet for different signal masses in RSG $c = 1$ models

Figure A.4 shows the mass and number of tracks at the secondary vertex computed by the SV1 algorithm. When there is no secondary vertex found, the algorithm assigns a default negative value for these quantities. Both of these distributions show that there is a significantly larger fraction of jets where no secondary vertex is found in the high mass samples compared to the $m_{G_{KK}^*} = 1$ TeV sample. The SV1 algorithm's inability to find a secondary vertex could be an important factor in the overall MV₂ score shift, as this eliminates eight of the input variables that would normally contribute information to the algorithm.

Figure A.5 shows the same quantities for the JetFitter algorithm. In this case, there is also a change in the fraction of jets which have their secondary vertices successfully reconstructed, but this change is not as drastic as that seen in SV1. There is also an increase in the number of jets which have high values of mass.

A.2 EFFECT OF MULTIPLE b -QUARKS INSIDE ONE JET

One hypothesis for why the efficiency of b -tagging the leading track jet degrades is that at high masses, the b quarks get close enough together that both of them are inside of the leading track jet. Because MV₂

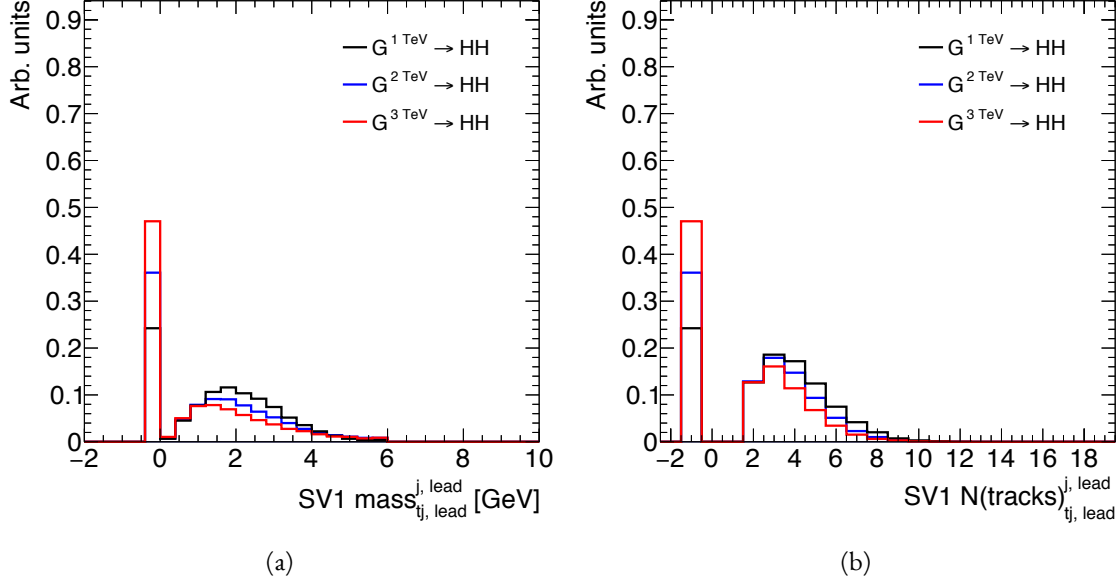


Figure A.4: Mass (a) and number of tracks (b) for the secondary vertices computed with the SV1 algorithm. When no secondary vertex is found, the quantities are assigned to default negative values.

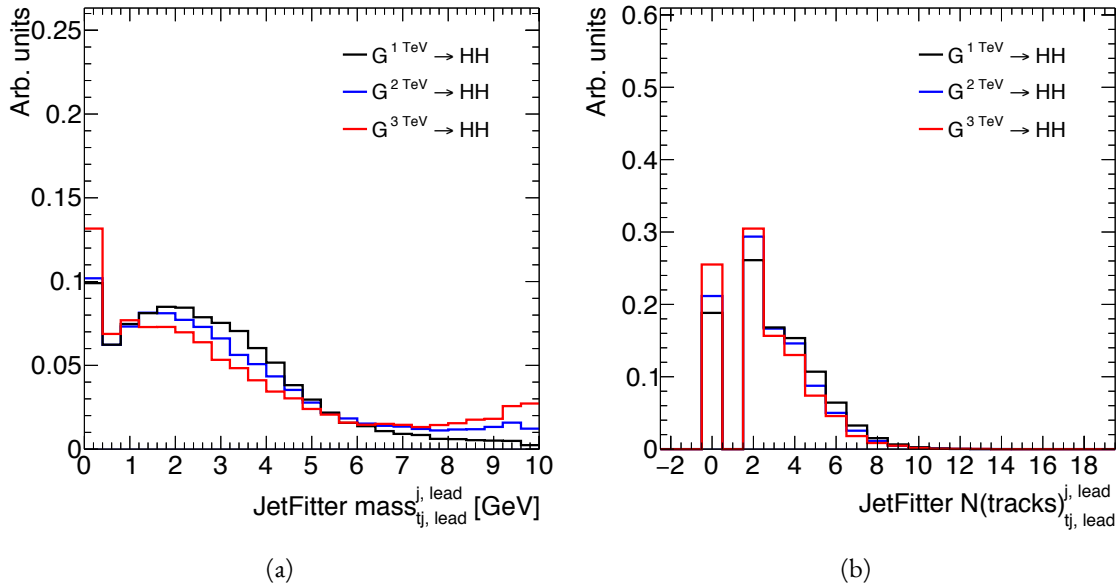


Figure A.5: Mass (a) and number of tracks (b) for vertices computed with the JetFitter algorithm. When no vertices are found, the quantities are assigned to default negative values.

2648 is not tuned for tagging multiple b quarks inside one jet, the tagging efficiency could degrade. Figure A.6
 2649 shows MV₂ scores and SV1 mass for cases where there are two b quarks at truth level within the radius of

the leading track jet compared to cases where there is only one true b^l . This figure suggests that the presence

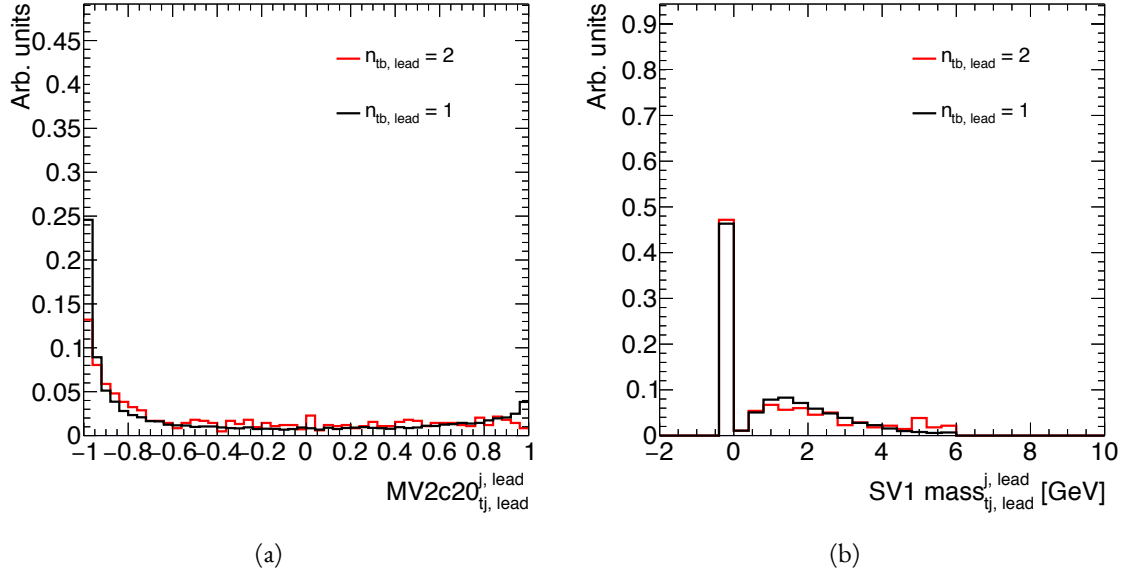


Figure A.6: MV₂c20 score (a) and SV1 mass (b) for leading track jets with two truth b quarks ($n_{tb,\text{lead}} = 2$) compared to those with only one truth b ($n_{tb,\text{lead}} = 1$).

of two b -quarks inside the leading jet is not the cause of the degradation in efficiency. There is a change in the shape of the MV₂ score distribution, but it is not nearly as pronounced as that seen in A.2 at higher masses. Additionally, the fraction of jets with no secondary vertex found is nearly identical in the track jets with two truth b -quarks.

A.3 CHANGES IN TRACK QUALITY AT HIGH p_T

Another hypothesis for the degradation of the b -tagging efficiency is a decrease in track quality for high p_T b jets. One way to check the overall quality of the tracking inside the jet is to investigate quantities related to the leading track inside of the track jet. Figure A.7 shows the fit χ^2/n_{DOF} and number of hits in the pixel detector for the leading track of the leading track jet. In both cases, the figure shows that in higher mass samples, the quality of the leading track inside of the track jet degrades substantially. The fit quality is lessened and the tracks have less hits in the pixel detector. This is likely due to the fact that at higher p_T ,

¹When two truth b quarks are required in the leading jet, the subleading jet is required to have zero. When one is required for the leading, one is also required for the subleading.

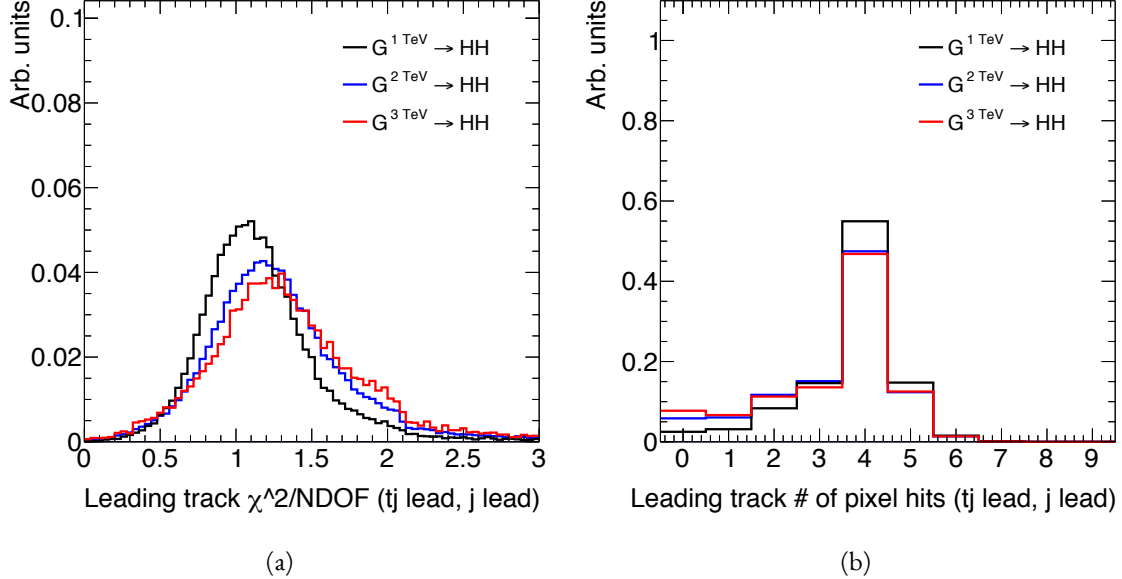


Figure A.7: Track fit χ^2/nDOF (a) and number of pixel detector hits (b) for the leading track of the leading track jet in different mass RSG $c = 1$ samples

the B -hadron will sometimes live long enough to miss the IBL and first pixel layer, thus decreasing the number of hits on the track.

To check whether this is the cause for the shift in the MV_2 score and the higher difficulty in reconstructing secondary vertices, jets whose leading track have at least four pixel hits are compared with those whose tracks have less than four pixel hits. The results for the MV_2 score and SV_1 mass are shown in figure A.8. Track jets where the leading track does not have at least four pixel hits are more likely to not have a secondary vertex reconstructed. Additionally, their MV_{2c2o} score is shifted more significantly to background-like values. This seems to confirm the hypothesis that degrading track quality is responsible for the lowered b -tagging efficiency at high p_T .

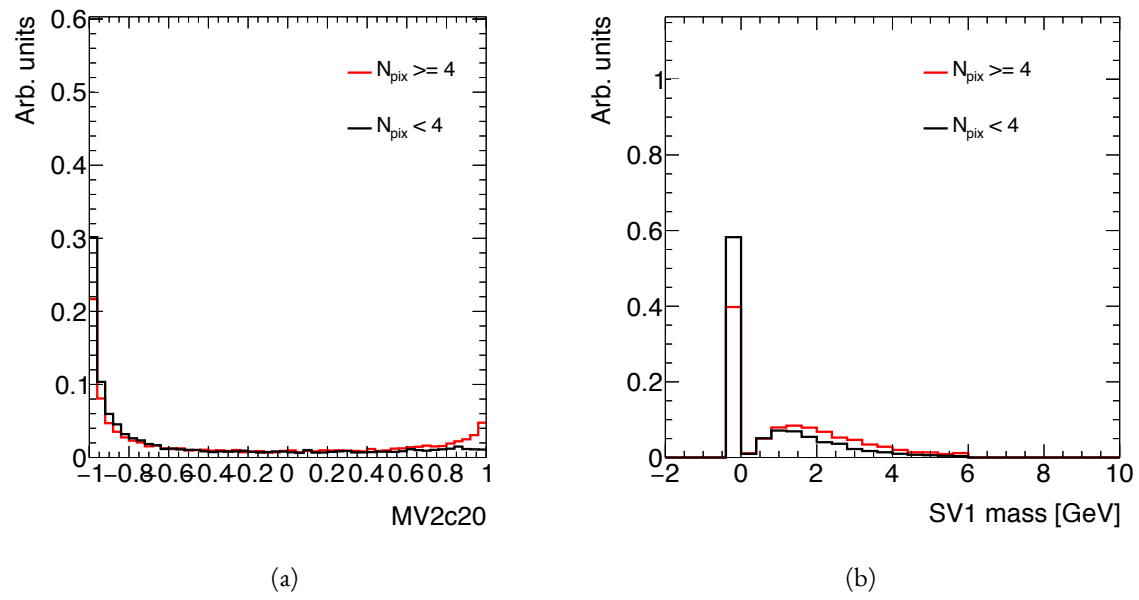


Figure A.8: MV₂c₂₀ score (a) and SV₁ mass (b) for leading track jets whose leading track jet has at least four pixel hits ($N_{\text{pix}} \geq 4$) compared to those which do not ($N_{\text{pix}} < 4$).

References

2671

- [1] Georges Aad et al. Observation of a new particle in the search for the Standard Model Higgs boson with the ATLAS detector at the LHC. *Phys. Lett.*, B716:1–29, 2012. doi: 10.1016/j.physletb.2012.08.020.
- [2] Serguei Chatrchyan et al. Observation of a new boson at a mass of 125 GeV with the CMS experiment at the LHC. *Phys. Lett.*, B716:30–61, 2012. doi: 10.1016/j.physletb.2012.08.021.
- [3] David Griffiths. *Introduction to elementary particles*. 2008.
- [4] F. Halzen and Alan D. Martin. *QUARKS AND LEPTONS: AN INTRODUCTORY COURSE IN MODERN PARTICLE PHYSICS*. 1984. ISBN 0471887412, 9780471887416.
- [5] Christopher G. Tully. *Elementary particle physics in a nutshell*. 2011.
- [6] K. A. Olive et al. Review of Particle Physics. *Chin. Phys.*, C38:090001, 2014. doi: 10.1088/1674-1137/38/9/090001.
- [7] Matthew D. Schwartz. *Quantum Field Theory and the Standard Model*. Cambridge University Press, 2014. ISBN 1107034736, 9781107034730. URL <http://www.cambridge.org/us/academic/subjects/physics/theoretical-physics-and-mathematical-physics/quantum-field-theory-and-standard-model>.
- [8] S. Dawson. Introduction to electroweak symmetry breaking. In *High energy physics and cosmology. Proceedings, Summer School, Trieste, Italy, June 29-July 17, 1998*, pages 1–83, 1998. URL <http://alice.cern.ch/format/showfull?sysnb=0301862>.
- [9] S. L. Glashow. Partial Symmetries of Weak Interactions. *Nucl. Phys.*, 22:579–588, 1961. doi: 10.1016/0029-5582(61)90469-2.
- [10] Steven Weinberg. A Model of Leptons. *Phys. Rev. Lett.*, 19:1264–1266, 1967. doi: 10.1103/PhysRevLett.19.1264.
- [11] A. Salam. *Elementary Particle Theory*. Almqvist and Wiksell, Stockholm, 1968.
- [12] J. Iliopoulos S.L. Glashow and L. Maiani. *D2:1285*, 1970.
- [13] R. Keith Ellis, W. James Stirling, and B. R. Webber. *QCD and collider physics*. *Camb. Monogr. Part. Phys. Nucl. Phys. Cosmol.*, 8:1–435, 1996.

- 2698 [14] P. W. Higgs. Broken symmetries and the masses of gauge bosons. *13*:508, 1964.
- 2699 [15] P. W. Higgs. Spontaneous symmetry breakdown without massless bosons. *145*:1156, 1966.
- 2700 [16] F. Englert and R. Brout. Broken symmetry and the mass of gauge vector mesons. *13*:321, 1964.
- 2701 [17] G. S. Guralnik, C. R. Hagen, and T. W. .B. Kibble. Global conservation laws and massless particles. *Phys. Rev. Lett.*, *13*:585, 1964. doi: [10.1103/PhysRevLett.13.585](https://doi.org/10.1103/PhysRevLett.13.585).
- 2703 [18] LHC Higgs Cross Section Working Group, S. Heinemeyer, C. Mariotti, G. Passarino, and
2704 R. Tanaka (Eds.). Handbook of LHC Higgs Cross Sections: 3, Higgs Properties. 2013.
- 2705 [19] J. Baglio, A. Djouadi, R. Gröber, M. M. Mühlleitner, J. Quevillon, and M. Spira. The mea-
2706 surement of the Higgs self-coupling at the LHC: theoretical status. *JHEP*, *04*:151, 2013. doi:
2707 [10.1007/JHEP04\(2013\)151](https://doi.org/10.1007/JHEP04(2013)151).
- 2708 [20] Matthew J. Dolan, Christoph Englert, and Michael Spannowsky. New Physics in LHC Higgs boson
2709 pair production. *Phys. Rev.*, *D87*(5):055002, 2013. doi: [10.1103/PhysRevD.87.055002](https://doi.org/10.1103/PhysRevD.87.055002).
- 2710 [21] Roberto Contino, Margherita Ghezzi, Mauro Moretti, Giuliano Panico, Fulvio Piccinini, and An-
2711 drea Wulzer. Anomalous Couplings in Double Higgs Production. *JHEP*, *08*:154, 2012. doi:
2712 [10.1007/JHEP08\(2012\)154](https://doi.org/10.1007/JHEP08(2012)154).
- 2713 [22] R. Grober and M. Mühlleitner. Composite Higgs Boson Pair Production at the LHC. *JHEP*, *06*:
2714 020, 2011. doi: [10.1007/JHEP06\(2011\)020](https://doi.org/10.1007/JHEP06(2011)020).
- 2715 [23] Lisa Randall and Raman Sundrum. A Large mass hierarchy from a small extra dimension. *Phys.*
2716 *Rev. Lett.*, *83*:3370–3373, 1999. doi: [10.1103/PhysRevLett.83.3370](https://doi.org/10.1103/PhysRevLett.83.3370).
- 2717 [24] Kaustubh Agashe, Hooman Davoudiasl, Gilad Perez, and Amarjit Soni. Warped Gravitons at the
2718 LHC and Beyond. *Phys. Rev.*, *D76*:036006, 2007. doi: [10.1103/PhysRevD.76.036006](https://doi.org/10.1103/PhysRevD.76.036006).
- 2719 [25] A. Liam Fitzpatrick, Jared Kaplan, Lisa Randall, and Lian-Tao Wang. Searching for the Kaluza-
2720 Klein Graviton in Bulk RS Models. *JHEP*, *09*:013, 2007. doi: [10.1088/1126-6708/2007/09/013](https://doi.org/10.1088/1126-6708/2007/09/013).
- 2721 [26] Julien Baglio, Otto Eberhardt, Ulrich Nierste, and Martin Wiebusch. Benchmarks for Higgs Pair
2722 Production and Heavy Higgs boson Searches in the Two-Higgs-Doublet Model of Type II. *Phys.*
2723 *Rev.*, *D90*(1):015008, 2014. doi: [10.1103/PhysRevD.90.015008](https://doi.org/10.1103/PhysRevD.90.015008).
- 2724 [27] G. C. Branco, P. M. Ferreira, L. Lavoura, M. N. Rebelo, Marc Sher, and Joao P. Silva. Theory and
2725 phenomenology of two-Higgs-doublet models. *Phys. Rept.*, *516*:1–102, 2012. doi: [10.1016/j.physrep.2012.02.002](https://doi.org/10.1016/j.physrep.2012.02.002).
- 2727 [28] Howard E. Haber and Oscar Stål. New LHC benchmarks for the \mathcal{CP} -conserving two-Higgs-
2728 doublet model. *Eur. Phys. J.*, *C75*(10):491, 2015. doi: [10.1140/epjc/s10052-015-3697-x](https://doi.org/10.1140/epjc/s10052-015-3697-x).

- 2729 [29] Jose M. No and Michael Ramsey-Musolf. Probing the Higgs Portal at the LHC Through Resonant
 2730 di-Higgs Production. *Phys. Rev.*, D89(9):095031, 2014. doi: 10.1103/PhysRevD.89.095031.
- 2731 [30] Johan Alwall, Michel Herquet, Fabio Maltoni, Olivier Mattelaer, and Tim Stelzer. MadGraph
 2732 5:Going Beyond. *JHEP*, 1106:128, 2011. doi: 10.1007/JHEP06(2011)128.
- 2733 [31] Lyndon R Evans and Philip Bryant. LHC Machine. *J. Instrum.*, 3:S08001. 164 p, 2008. URL
 2734 <https://cds.cern.ch/record/1129806>. This report is an abridged version of the LHC De-
 2735 sign Report (CERN-2004-003).
- 2736 [32] ATLAS Collaboration. The ATLAS experiment at the CERN Large Hadron Collider. *JINST*, 3:
 2737 S08003, 2008. doi: 10.1088/1748-0221/3/08/S08003.
- 2738 [33] CMS Collaboration. The cms experiment at the cern lhc. *Journal of Instrumentation*, 3(08):S08004,
 2739 2008. URL <http://stacks.iop.org/1748-0221/3/i=08/a=S08004>.
- 2740 [34] LHCb Collaoration. The LHCb Detector at the LHC. *JINST*, 3:S08005, 2008. doi: 10.1088/
 2741 1748-0221/3/08/S08005.
- 2742 [35] ALICE Collaboration. The alice experiment at the cern lhc. *Journal of Instrumentation*, 3(08):
 2743 S08002, 2008. URL <http://stacks.iop.org/1748-0221/3/i=08/a=S08002>.
- 2744 [36] Lyndon Evans. The Large Hadron Collider. In Holstein, BR and Haxton, WC and Jawah-
 2745 ery, A, editor, *ANNUAL REVIEW OF NUCLEAR AND PARTICLE SCIENCE, VOL*
 2746 *61*, volume 61 of *Annual Review of Nuclear and Particle Science*, pages 435–466. 2011. doi:
 2747 {10.1146/annurev-nucl-102010-130438}.
- 2748 [37] ATLAS Collaboration. Luminosity Determination in pp Collisions at $\sqrt{s} = 7$ TeV Using the
 2749 ATLAS Detector at the LHC. *Eur. Phys. J.*, C 71:1630, 2011. doi: 10.1140/epjc/s10052-011-1630-5.
- 2750 [38] Mike Lamont for the LHC team. The First Years of LHC Operation for Luminosity Production.
 2751 International Particle Accelerator Conference, 2013. URL <https://accelconf.web.cern.ch/>
 2752 accelconf/IPAC2013/talks/moyab101_talk.pdf.
- 2753 [39] Paul Collier for the LHC team. LHC Machine Status. CERN Resource Review Board, 2015. URL
 2754 <https://cds.cern.ch/record/2063924/files/CERN-RRB-2015-119.PDF>.
- 2755 [40] Track Reconstruction Performance of the ATLAS Inner Detector at $\sqrt{s} = 13$ TeV. Technical
 2756 Report ATL-PHYS-PUB-2015-018, CERN, Geneva, Jul 2015. URL <http://cds.cern.ch/>
 2757 [record/2037683](https://cds.cern.ch/record/2037683).

- 2758 [41] M Capeans, G Darbo, K Einsweiller, M Elsing, T Flick, M Garcia-Sivieres, C Gemme, H Perneg-
2759 ger, O Rohne, and R Vuillermet. ATLAS Insertable B-Layer Technical Design Report. Techni-
2760 cal Report CERN-LHCC-2010-013. ATLAS-TDR-19, CERN, Geneva, Sep 2010. URL <https://cds.cern.ch/record/1291633>.
- 2761
- 2762 [42] ATLAS Collaboration. ATLAS Trigger Operations Public Results. 2015. URL <https://twiki.cern.ch/twiki/bin/view/AtlasPublic/TriggerOperationPublicResults>.
- 2763
- 2764 [43] ATLAS Collaboration. ATLAS Luminosity Public Results, Run 1. 2012. URL <https://twiki.cern.ch/twiki/bin/view/AtlasPublic/LuminosityPublicResults>.
- 2765
- 2766 [44] ATLAS Collaboration. ATLAS Luminosity Public Results, Run 2. 2015. URL <https://twiki.cern.ch/twiki/bin/view/AtlasPublic/LuminosityPublicResultsRun2>.
- 2767
- 2768 [45] T Kawamoto, S Vlachos, L Pontecorvo, J Dubbert, G Mikenberg, P Iengo, C Dallapiccola,
2769 C Amelung, L Levinson, R Richter, and D Lellouch. New Small Wheel Technical Design Re-
2770 port. Technical Report CERN-LHCC-2013-006. ATLAS-TDR-020, CERN, Geneva, Jun 2013.
2771 URL <https://cds.cern.ch/record/1552862>. ATLAS New Small Wheel Technical Design
2772 Report.
- 2773
- 2774 [46] Y. Giomataris, Ph. Rebours, J.P. Robert, and G. Charpak. Micromegas: a high-granularity
2775 position-sensitive gaseous detector for high particle-flux environments. *Nuclear Instruments
2776 and Methods in Physics Research Section A: Accelerators, Spectrometers, Detectors and As-
2777 sociated Equipment*, 376(1):29 – 35, 1996. ISSN 0168-9002. doi: [http://dx.doi.org/10.1016/0168-9002\(96\)00175-1](http://dx.doi.org/10.1016/0168-9002(96)00175-1). URL <http://www.sciencedirect.com/science/article/pii/0168900296001751>.
- 2775
- 2776
- 2777
- 2778
- 2779 [47] T. Alexopoulos, J. Burnens, R. de Oliveira, G. Glonti, O. Pizzirussi, V. Polychronakos, G. Sekhni-
2780 aidze, G. Tsipolitis, and J. Wotschack. A spark-resistant bulk-micromegas chamber for high-
2781 rate applications. *Nuclear Instruments and Methods in Physics Research Section A: Acceler-
2782 ators, Spectrometers, Detectors and Associated Equipment*, 640(1):110 – 118, 2011. ISSN 0168-9002.
2783 doi: <http://dx.doi.org/10.1016/j.nima.2011.03.025>. URL <http://www.sciencedirect.com/science/article/pii/S0168900211005869>.
- 2784
- 2785
- 2786 [48] Joao Pequenao and Paul Schaffner. An computer generated image representing how ATLAS de-
2787 tects particles. Jan 2013. URL <https://cds.cern.ch/record/1505342>.
- 2788
- 2789 [49] Improved electron reconstruction in ATLAS using the Gaussian Sum Filter-based model for
bremsstrahlung. Technical Report ATLAS-CONF-2012-047, CERN, Geneva, May 2012. URL
<https://cds.cern.ch/record/1449796>.

- 2790 [50] Electron efficiency measurements with the ATLAS detector using the 2012 LHC proton-proton
 2791 collision data. Technical Report ATLAS-CONF-2014-032, CERN, Geneva, Jun 2014. URL
 2792 <https://cds.cern.ch/record/1706245>.
- 2793 [51] Georges Aad et al. Electron and photon energy calibration with the ATLAS detector using LHC
 2794 Run 1 data. *Eur. Phys. J.*, C74(10):3071, 2014. doi: 10.1140/epjc/s10052-014-3071-4.
- 2795 [52] Georges Aad et al. Measurement of the muon reconstruction performance of the ATLAS detector
 2796 using 2011 and 2012 LHC proton–proton collision data. *Eur. Phys. J.*, C74(11):3130, 2014. doi:
 2797 10.1140/epjc/s10052-014-3130-x.
- 2798 [53] W Lampl, S Laplace, D Lelas, P Loch, H Ma, S Menke, S Rajagopalan, D Rousseau, S Snyder,
 2799 and G Unal. Calorimeter Clustering Algorithms: Description and Performance. Technical Re-
 2800 port ATL-LARG-PUB-2008-002. ATL-COM-LARG-2008-003, CERN, Geneva, Apr 2008. URL
 2801 <https://cds.cern.ch/record/1099735>.
- 2802 [54] Georges Aad et al. Topological cell clustering in the ATLAS calorimeters and its performance in
 2803 LHC Run 1. 2016.
- 2804 [55] Matteo Cacciari, Gavin P. Salam, and Gregory Soyez. The Anti- $k(t)$ jet clustering algorithm. *JHEP*,
 2805 04:063, 2008. doi: 10.1088/1126-6708/2008/04/063.
- 2806 [56] Monte Carlo Calibration and Combination of In-situ Measurements of Jet Energy Scale, Jet Energy
 2807 Resolution and Jet Mass in ATLAS. Technical Report ATLAS-CONF-2015-037, CERN, Geneva,
 2808 Aug 2015. URL <http://cds.cern.ch/record/2044941>.
- 2809 [57] Georges Aad et al. Performance of b -Jet Identification in the ATLAS Experiment. 2015.
- 2810 [58] Expected performance of the ATLAS b -tagging algorithms in Run-2. Technical Report
 2811 ATL-PHYS-PUB-2015-022, CERN, Geneva, Jul 2015. URL <http://cds.cern.ch/record/2037697>.
- 2812 [59] Georges Aad et al. Performance of Missing Transverse Momentum Reconstruction in Proton-
 2813 Proton Collisions at 7 TeV with ATLAS. *Eur. Phys. J.*, C72:1844, 2012. doi: 10.1140/epjc/
 2814 s10052-011-1844-6.
- 2815 [60] Performance of Missing Transverse Momentum Reconstruction in ATLAS studied in Proton-
 2816 Proton Collisions recorded in 2012 at 8 TeV. Technical Report ATLAS-CONF-2013-082, CERN,
 2817 Geneva, Aug 2013. URL <http://cds.cern.ch/record/1570993>.
- 2818 [61] ATLAS Collaboration. Observation and measurement of Higgs boson decays to WW^* with the
 2819 ATLAS detector. *Phys. Rev. D*, 92(012006), 2015.

- 2821 [62] Aaron James Armbruster. Discovery of a Higgs Boson with the ATLAS detector. 2013. CERN-
2822 THESIS-2013-047.
- 2823 [63] G. Cowan, K. Cranmer, E. Gross, and O. Vitells. Asymptotic formulae for likelihood-based tests
2824 of new physics. *Eur. Phys. J.*, C 71:1554, 2011. doi: 10.1140/epjc/s10052-011-1554-0.
- 2825 [64] ATLAS Collaboration. Limits on the production of the Standard Model Higgs Boson in pp
2826 collisions at $\sqrt{s} = 7$ TeV with the ATLAS detector. *Eur. Phys. J.*, C 71:1728, 2011. doi:
2827 10.1140/epjc/s10052-011-1728-9.
- 2828 [65] ATLAS Collaboration. Performance of the ATLAS muon trigger in pp collisions at $\sqrt{s} = 8$ TeV.
2829 *Eur. Phys. J. C*, (arXiv:1408.3179. CERN-PH-EP-2014-154):75, 19 p, Aug 2014. URL <https://cds.cern.ch/record/1749694>.
- 2831 [66] ATLAS collaboration. Electron trigger performance in 2012 ATLAS data, 2015. ATLAS-COM-
2832 DAQ-2015-091.
- 2833 [67] Paolo Nason. A new method for combining NLO QCD with shower Monte Carlo algorithms.
2834 *JHEP*, 11:040, 2004.
- 2835 [68] B. P. Kersevan and E. Richter-Was. The Monte Carlo event generator AcerMC version 2.0 with
2836 interfaces to PYTHIA 6.2 and HERWIG 6.5. 2004.
- 2837 [69] Nikolas Kauer and Giampiero Passarino. Inadequacy of zero-width approximation for a light Higgs
2838 boson signal. 2012.
- 2839 [70] T. Gleisberg, Stefan Hoeche, F. Krauss, M. Schonherr, S. Schumann, et al. Event generation with
2840 SHERPA 1.1. *JHEP*, 0902:007, 2009. doi: 10.1088/1126-6708/2009/02/007.
- 2841 [71] Michelangelo L. Mangano et al. ALPGEN, a generator for hard multiparton processes in hadronic
2842 collisions. *JHEP*, 0307:001, 2003. doi: 10.1088/1126-6708/2003/07/001.
- 2843 [72] Torbjorn Sjostrand, Stephen Mrenna, and Peter Z. Skands. PYTHIA 6.4 Physics and Manual.
2844 *JHEP*, 0605:026, 2006. doi: 10.1088/1126-6708/2006/05/026.
- 2845 [73] Torbjorn Sjostrand, Stephen Mrenna, and Peter Z. Skands. A Brief Introduction to PYTHIA 8.1.
2846 *Comput.Phys.Commun.*, 178:852–867, 2008. doi: 10.1016/j.cpc.2008.01.036.
- 2847 [74] G. Corcella et al. HERWIG 6: An event generator for hadron emission reactions with interfering
2848 gluons (including super-symmetric processes) . *JHEP*, 01:010, 2001. doi: 10.1088/1126-6708/2001/
2849 01/010.
- 2850 [75] J. M. Butterworth, Jeffrey R. Forshaw, and M. H. Seymour. Multiparton interactions in photo-
2851 production at HERA. *Z. Phys.*, C 72:637, 1996. doi: 10.1007/s002880050286.

- 2852 [76] Jun Gao, Marco Guzzi, Joey Huston, Hung-Liang Lai, Zhao Li, et al. The CT10 NNLO Global
 2853 Analysis of QCD. *Phys. Rev.*, D89:033009, 2014. doi: [10.1103/PhysRevD.89.033009](https://doi.org/10.1103/PhysRevD.89.033009).
- 2854 [77] P. M. Nadolsky. Implications of CTEQ global analysis for collider observables. *Phys. Rev.*, D 78:
 2855 013004, 2008. doi: [10.1103/PhysRevD.78.013004](https://doi.org/10.1103/PhysRevD.78.013004).
- 2856 [78] A. Sherstnev and R. S. Thorne. Parton distributions for the LHC. *Eur. Phys. J.*, C 55:553, 2009. doi:
 2857 [10.1140/epjc/s10052-008-0610-x](https://doi.org/10.1140/epjc/s10052-008-0610-x).
- 2858 [79] S. Agostinelli et al. GEANT4, a simulation toolkit. *Nucl. Instrum. Meth.*, A 506:250, 2003. doi:
 2859 [10.1016/S0168-9002\(03\)01368-8](https://doi.org/10.1016/S0168-9002(03)01368-8).
- 2860 [80] R.K. Ellis, I. Hinchliffe, M. Soldate, and J.J. Van Der Bij. Higgs decay to $\tau+\tau$ —a possible signature
 2861 of intermediate mass higgs bosons at high energy hadron colliders. *Nuclear Physics B*, 297(2):221
 2862 – 243, 1988. ISSN 0550-3213. doi: [http://dx.doi.org/10.1016/0550-3213\(88\)90019-3](http://dx.doi.org/10.1016/0550-3213(88)90019-3). URL <http://www.sciencedirect.com/science/article/pii/0550321388900193>.
- 2864 [81] Eilam Gross and Ofer Vitells. Transverse mass observables for charged Higgs boson searches at
 2865 hadron colliders. *Phys. Rev.*, D81:055010, 2010. doi: [10.1103/PhysRevD.81.055010](https://doi.org/10.1103/PhysRevD.81.055010).
- 2866 [82] J. R. Andersen et al. Les Houches 2013: Physics at TeV Colliders: Standard Model Working Group
 2867 Report. 2014.
- 2868 [83] I. Stewart and F. Tackmann. Theory uncertainties for Higgs mass and other searches using jet bins.
 2869 *Phys. Rev.*, D 85:034011, 2012. doi: [10.1103/PhysRevD.85.034011](https://doi.org/10.1103/PhysRevD.85.034011).
- 2870 [84] ATLAS Collaboration. Luminosity Determination in pp Collisions at $\sqrt{s} = 7$ TeV Using the
 2871 ATLAS Detector at the LHC. *Eur. Phys. J.*, C 71:1630, 2011. doi: [10.1140/epjc/s10052-011-1630-5](https://doi.org/10.1140/epjc/s10052-011-1630-5).
- 2872 [85] Jet energy scale and its systematic uncertainty in proton-proton collisions at $\sqrt{s} = 7$ tev with atlas
 2873 2011 data. *ATLAS-CONF-2013-004*, 2013.
- 2874 [86] Calibrating the b -tag efficiency and mistag rate in 35 pb^{-1} of data with the atlas detector. *ATLAS-*
 2875 *CONF-2011-089*, 2011.
- 2876 [87] ATLAS Collaboration. Measurement of the b -tag Efficiency in a Sample of Jets Containing Muons
 2877 with 5 fb^{-1} of Data from the ATLAS Detector. *ATLAS-CONF-2012-043*, 2012. URL <http://cdsweb.cern.ch/record/1435197>.
- 2879 [88] ATLAS Collaboration. Calibration of b -tagging using dileptonic top pair events in a combinatorial
 2880 likelihood approach with the ATLAS experiment. (ATLAS-CONF-2014-004), 2014. URL <http://cds.cern.ch/record/1664335>.

- 2882 [89] Georges Aad et al. Measurement of the Higgs boson mass from the $H \rightarrow \gamma\gamma$ and $H \rightarrow ZZ^* \rightarrow$
 2883 4ℓ channels with the ATLAS detector using 25 fb^{-1} of pp collision data. *Phys. Rev.*, D90(5):052004,
 2884 2014. doi: 10.1103/PhysRevD.90.052004.
- 2885 [90] Georges Aad et al. Measurements of the Higgs boson production and decay rates and coupling
 2886 strengths using pp collision data at $\sqrt{s} = 7$ and 8 TeV in the ATLAS experiment. *Eur. Phys. J.*,
 2887 C76(1):6, 2016. doi: 10.1140/epjc/s10052-015-3769-y.
- 2888 [91] W.J. Stirling. $7/8$ and $13/8$ TeV LHC luminosity ratios. 2013. URL http://www.hep.ph.ic.ac.uk/~wstirlin/plots/lhclumi7813_2013_v0.pdf.
- 2890 [92] J Alison. Experimental Studies of hh. Oct 2014. URL <http://cds.cern.ch/record/1952581>.
- 2891 [93] J. Alwall et al. The automated computation of tree-level and next-to-leading order differential cross
 2892 sections, and their matching to parton shower simulations. *JHEP*, 07:079, 2014.
- 2893 [94] Richard D. Ball et al. Parton distributions with LHC data. *Nucl. Phys. B*, 867:244, 2013.
- 2894 [95] ATLAS Collaboration. ATLAS Run 1 Pythia8 tunes. (ATL-PHYS-PUB-2014-021), Nov 2014.
 2895 URL <https://cds.cern.ch/record/1966419>.
- 2896 [96] M. Bahr et al. Herwig++ Physics and Manual. *Eur. Phys. J. C*, 58:639–707, 2008. doi: 10.1140/
 2897 epjc/s10052-008-0798-9.
- 2898 [97] Stefan Gieseke, Christian Rohr, and Andrzej Siodmok. Colour reconnections in Herwig++. *Eur.*
 2899 *Phys. J. C*, 72:2225, 2012. doi: 10.1140/epjc/s10052-012-2225-5.
- 2900 [98] Simone Alioli, Paolo Nason, Carlo Oleari, and Emanuele Re. A general framework for implement-
 2901 ing NLO calculations in shower Monte Carlo programs: the POWHEG BOX. *JHEP*, 06:043,
 2902 2010.
- 2903 [99] Peter Zeiler Skands. Tuning Monte Carlo Generators: The Perugia Tunes. *Phys. Rev. D*, 82:074018,
 2904 2010. doi: 10.1103/PhysRevD.82.074018.
- 2905 [100] Michal Czakon and Alexander Mitov. Top++: A Program for the Calculation of the Top-Pair
 2906 Cross-Section at Hadron Colliders. 2011.
- 2907 [101] Baojia (Tony) Tong. Private communication.
- 2908 [102] D. Krohn, J. Thaler, and L.-T. Wang. Jet Trimming. *JHEP*, 02:084, 2010. doi: 10.1007/
 2909 JHEP02(2010)084.
- 2910 [103] ATLAS Collaboration. Identification of Boosted, Hadronically Decaying W Bosons and Compar-
 2911 isons with ATLAS Data Taken at $\sqrt{s} = 8$ TeV. 2015.

- 2912 [104] Expected Performance of Boosted Higgs ($\rightarrow b\bar{b}$) Boson Identification with the ATLAS Detector
 2913 at $\sqrt{s} = 13$ TeV. Technical Report ATL-PHYS-PUB-2015-035, CERN, Geneva, Aug 2015. URL
 2914 <https://cds.cern.ch/record/2042155>.
- 2915 [105] Flavor Tagging with Track Jets in Boosted Topologies with the ATLAS Detector. Technical Report
 2916 ATL-PHYS-PUB-2014-013, CERN, Geneva, Aug 2014. URL <https://cds.cern.ch/record/1750681>.
- 2918 [106] Matteo Cacciari and Gavin P. Salam. Pileup subtraction using jet areas. *Phys. Lett. B*, 659:119, 2008.
 2919 doi: [10.1016/j.physletb.2007.09.077](https://doi.org/10.1016/j.physletb.2007.09.077).
- 2920 [107] Glen Cowan, Eilam Gross. Discovery significance with statistical uncertainty in the background
 2921 estimate. 2008. URL <http://www.pp.rhul.ac.uk/~cowan/stat/notes/SigCalcNote.pdf>.
- 2923 [108] Search for pair production of Higgs bosons in the $b\bar{b}b\bar{b}$ final state using proton-proton collisions
 2924 at $\sqrt{s} = 13$ TeV with the ATLAS detector. Technical Report ATLAS-CONF-2016-017, CERN,
 2925 Geneva, Mar 2016. URL <https://cds.cern.ch/record/2141006>.
- 2926 [109] Qi Zeng. Private communication.
- 2927 [110] ATLAS Collaboration. Identification of boosted, hadronically-decaying W and Z bosons in
 2928 $\sqrt{s} = 13$ TeV Monte Carlo Simulations for ATLAS. (ATL-PHYS-PUB-2015-033), Aug 2015. URL
 2929 <https://cds.cern.ch/record/2041461>.
- 2930 [111] ATLAS Collaboration. Performance of b -Jet Identification in the ATLAS Experiment. 2015.
- 2931 [112] Alexander L. Read. Presentation of search results: The CL(s) technique. *J. Phys. G*, 28:2693, 2002.
 2932 doi: [10.1088/0954-3899/28/10/313](https://doi.org/10.1088/0954-3899/28/10/313).
- 2933 [113] Measurements of the Higgs boson production and decay rates and constraints on its couplings
 2934 from a combined ATLAS and CMS analysis of the LHC pp collision data at $\sqrt{s} = 7$ and 8 TeV.
 2935 Technical Report ATLAS-CONF-2015-044, CERN, Geneva, Sep 2015. URL <http://cds.cern.ch/record/2052552>.
- 2937 [114] Projections for measurements of Higgs boson signal strengths and coupling parameters with the
 2938 ATLAS detector at a HL-LHC. Technical Report ATL-PHYS-PUB-2014-016, CERN, Geneva,
 2939 Oct 2014. URL <http://cds.cern.ch/record/1956710>.
- 2940 [115] ATLAS Phase-II Upgrade Scoping Document. Technical Report CERN-LHCC-2015-020. LHCC-
 2941 G-166, CERN, Geneva, Sep 2015. URL <http://cds.cern.ch/record/2055248>.



2942

THIS THESIS WAS TYPESET using \LaTeX , originally developed by Leslie Lamport and based on Donald Knuth's \TeX . The body text is set in 11 point Egenolff-Berner Garamond, a revival of Claude Garamont's humanist typeface. The above illustration, *Science Experiment 02*, was created by Ben Schlitter and released under [CC BY-NC-ND 3.0](#). A template that can be used to format a PhD dissertation with this look & feel has been released under the permissive [AGPL](#) license, and can be found online at github.com/asm-products/Dissertate or from its lead author, Jordan Suchow, at suchow@post.harvard.edu.